

SYNTHESIS AND CHARACTERIZATION OF
BORON-DOPED GRAPHITIC CARBON
FOR ENERGY STORAGE APPLICATIONS

by

Devin Gray McGlamery

A dissertation submitted in partial fulfillment
of the requirements for the degree

of

Doctor of Philosophy

in

Chemistry

MONTANA STATE UNIVERSITY
Bozeman, Montana

July 2023

©COPYRIGHT

by

Devin Gray McGlamery

2023

All Rights Reserved

DEDICATION

I dedicate this work to my partner, Hannah. Your unwavering support, kindness, and stability has brought immeasurable joy to my life. Along this winding and ever-changing route, you have been my rock and my best friend. Your persistence, courage, and drive for adventure has filled me with the strength needed to face all of life's challenges head-on. Thank you for traveling with me into the unknown along the unbeaten path.

To my mother, Orien, I am forever grateful for the sacrifices you have made to provide me with the best life possible. Your unconditional love and endless encouragement fuels my pursuit for knowledge. You have sown the seeds of wonder harboring a curiosity about the universe. Thank you for instilling in me a thirst for understanding, I carry your wisdom and spirit with me as I continue to travel along my scholarly road.

To my father, Matthew, thank you for the lessons and experiences you have shared with me over the years. Although sometimes it may have felt like I wasn't listening, your words of wisdom return to me when I need them most. Your constant push for excellence motivates me to be the best possible version of myself and has shaped me into the man I am today. The dedication and love you have for our family, the strength you embody, and your wisdom inspires me to reach new heights.

Finally, I extend my heartfelt appreciation to my brother, Logan, for keeping me grounded and for offering unfiltered truths that only a brother can provide. Your honesty and perspective serve as a compass, helping me navigate the complexities of life. The bond we share, and your well-rounded mindset inspires me to push past my limitations and embrace new possibilities.

Each of you has played an indispensable role in shaping the person I am today. I will be forever grateful for your love, support, and influence. This dissertation is dedicated to you, as a testament to our bond and the immeasurable impact you have had on my life.

ACKNOWLEDGEMENTS

First, I would like to thank my advisor and friend Dr. Nicholas P. Stadie, it has been a remarkable journey establishing a research group with you, starting from an empty room, and growing into a multifaceted and thriving lab. The space you have developed has harbored curiosity, creativity, and productivity for everyone who enters. You have given me freedom, allowing for the struggles necessary for personal and professional growth, yet have always been involved in my progress. Thank you for pushing me to produce consistent and honest results, for never taking the easy road, and for the excellence that you have imparted in every aspect of my professional life.

I would like to thank my committee for their support and guidance over the years, Dr. Rob Walker, Dr. Erik Grumstrup, and Dr. Michael Mock for your insightful and thought-provoking questions, as well as for your assistance in developing my experimental technique and scientific thinking.

I would also like to thank my first scientific mentor Dr. Kate Marshall who was instrumental in my evolution as a scientist. You introduced me to the fundamentals of experimental chemistry, guided my curiosity, and instilled in me the habits needed to be a well-rounded, thorough, and safe scientist. Thank you for taking the time to guide me.

Though there are many others who have contributed to my success, I would also like to thank Cassie, the kind owner of Columbus Pizzeria for being a shining light in our community. You have always shown me kindness, lent helpful life advice, shared delicious pizza and a refreshing beverage when I needed it most. Thank you for the joy you have shared with me over the years.

TABLE OF CONTENTS

1. INTRODUCTION	1
Overview	1
Objectives	3
Technical Challenges	5
References	11
2. BACKGROUND	15
Energy Storage	15
Boron-Doped Graphitic Carbon	21
Hydrogen Storage in BC_3'	21
Historical Synthes of BC_3'	23
References	27
3. HYDROGEN-TYPE BINDING SITES IN CARBONACEOUS ELECTRODES FOR RAPID LITHIUM INSERTION	30
Contribution of Authors	30
Manuscript Information	31
Abstract	32
Introduction	33
Results and Discussion	34
Conclusions	45
Experimental Section	46
Materials Synthesis	46
Commercial Reference Materials	46
Materials Characterization	46
Electrochemical Characterization	47
Associated Content	48
Acknowledgments	48
Supporting Information	48
References	62
4. PHONON DISPERSION RELATION OF BULK BORON-DOPED GRAPHITIC CARBON	66
Contribution of Authors	66
Manuscript Information	67
Abstract	68
Introduction	69
Experimental Methods	75
Direct Synthesis of Bulk C' , CBr_x' , and BC_x'	75

TABLE OF CONTENTS CONTINUED

Powder XRD	76
Raman Spectroscopy	76
X-ray Absorption Spectroscopy	76
Elemental Analysis	77
Phonon Structure Calculations	77
Results	78
Structural Characterization	78
Chemical Composition	82
Boron Chemical Environments	83
Discussion	86
X-ray Diffraction	86
Raman Spectroscopy	89
Temperature and Graphitic Structure	91
Boron Content and Graphitic Structure	92
Phonon Dispersion Relation	93
Conclusions	97
Associated Content	98
Supporting Information	98
Corresponding Author	110
Authors	110
Acknowledgments	110
References	111
5. PRECURSOR DECOMPOSITION COMPATIBILITY AS THE KEY TO THE HALIDE-FREE SYNTHESIS OF METASTABLE BC ₃ '	116
Contribution of Authors	116
Manuscript Information	117
Abstract	118
Introduction	119
Results and Discussion	120
Conclusions	126
Associated Content	127
Supporting Information	127
Funding Sources	161
Acknowledgments	161
References	162
6. CONCLUSIONS	168
Summary of Results	168
Objective 1	169

TABLE OF CONTENTS CONTINUED

Objective 2	170
Objective 3	171
Future Work	172
H-Type Binding Sites.....	173
Diborane-Derived BC_3'	174
References	176
APPENDIX A:.....	178
AMPOLES AND SCHLENK LINE.....	178
Ampule Fabrication.....	179
Ampule synthesis	181
Sample Collection	183
APPENDIX B:.....	186
HYDROGEN UPTAKE MEASUREMENTS IN BC_3'	186
References	189
REFERENCES.....	191

LIST OF TABLES

Table	Page
Chapter Two	
1. Historical developments to the synthesis of boron doped carbons.	26
Chapter Three	
1. Structural properties of Cor800 and three standard materials of comparison, as determined using XRD, Raman spectroscopy, N ₂ adsorption at 77 K, combustion analysis, and electrochemical lithiation.	39
S1. Structural properties of all materials investigated herein, as determined using XRD, Raman spectroscopy, N ₂ adsorption at ~77 K, combustion analysis, and electrochemical lithiation.	60
Chapter Five	
S1. Elemental composition (as determined by EDX) of each morphology of the BC _x products of synthesis routes I–V.	147
S2. Raman D peak dispersion as a function of Reaction number and boron reagent utilized in the pyrolysis reaction.	155
S3. Decomposition energies (ΔE^{SFC}), experimental decomposition temperatures, and corresponding references for small molecules of interest in co-pyrolysis reactions to produce boron- and carbon-containing products.	160

LIST OF FIGURES

Figure	Page
Chapter One	
1. The boron–carbon binary phase diagram.....	6
2. Reaction coordinate diagram of metastable states. The hypothetical metastable material A is kinetically trapped in a local energy well, B is an unstable state, and the thermodynamic product C is shown in the lowest energy state of the system.....	8
Chapter Two	
1. Components of a pressurized hydrogen storage tank. (Adapted from reference 10).....	16
2. Liquid hydrogen storage vessel containing an inner storage tank with heat exchangers and cooling system that is wrapped in insulation to maintain a cryogenic environment. (Adapted from reference 11).....	17
3. Hydrogen H ₂ phase diagram. The ambient temperature and pressure lines are highlighted.	18
4. Overview of hydrogen storage methods.	19
5. Schematic reaction coordinate diagram of hydrogen binding in BC ₃ '. Hydrogen in the initial state (IS) is placed within the slit pore of two BC ₃ ' sheets where it coordinates to adjacent boron atoms through the vacant boron p _z orbitals. In the transition state (TS) the hydrogen–hydrogen bond dissociates, and the individual hydrogen atoms coordinate to either side of the slit pore. In the final state (FS) the hydrogen bonds to the neighboring carbon atom with a C-C-H dihedral angle of ~106°, and neighboring boron atoms deflect out of plane to accommodate the rehybridization of the system (denoted with blue arrows). Binding of a second hydrogen molecule would alleviate the formal charges depicted in the FS. ¹⁷	22
6. Boron–carbon phase diagram at low boron concentrations.....	24

LIST OF FIGURES CONTINUED

Figure	Page
Chapter Three	
1. Representative SEM images of (a) graphite (AG20), (b) graphitic carbon with hydrogen-type sites (Cor800), (d) hard carbon (Super P), and (e) ordered porous carbon with no stacking (ZTC). The main image in each panel shows a 20 μm scale bar, and the inset shows a 500 nm scale bar. (c) XRD patterns of AG20, Cor800, Super P, and ZTC with the graphite (002) and (004) reflections indicated as dashed gray lines. The (111) and (220) reflections characteristic of the cubic pore-to-pore ordering in ZTC are indicated with open diamonds. (f) Raman spectra of AG20, Cor800, Super P, and ZTC, collected using a 532 nm excitation source.	37
2. CV analysis of (a,e) AG20, (b,f) Cor800, (c,g) Super P, and (d,h) ZTC at scan rates between 0.1-15 mV s^{-1} . (a-d) Select CV profiles and (e-h) R-S analysis showing the presence of numerous lithiation environments: reductive stage 3-4 intercalation (R3-4), wide interlayer intercalation (R-I), hydrogen-type site binding (R-H), and adsorption (R-A), and oxidative stage 1, 2, or 3-4 intercalation (O1, O2, and O3-4), wide interlayer intercalation (O-I), hydrogen-type site binding (O-H), and adsorption (O-A).....	41
3. (a, c) Reversible GCD profiles of (a) AG20 and Cor800, and (c) Super P and ZTC at 25 mA g^{-1} (~ 0.1 C). (b) Cycling stability and rate capability of all materials at current rates between 0.4-30 A g^{-1} (~ 1 -80 C, as shown). (d) Materials-specific Ragone plot assuming use of an anode against a range of standard cathodes (see Supporting Information for details). (e) Allocation of reversible charge storage capacity in all materials as per the type of lithiation environment (indicated by color) as a function of charging rate at select rates of 1 C, 10 C, 20 C, 40 C, and 60 C (indicated above each bar).	42
S1. Representative fitting profile for the Raman spectrum of graphitic carbon. One Lorentzian(*C-H) is used to account for hydrogen edge character, a second Lorentzian (D) accounts for the D mode, and a BWF lineshape (G) accounts for the G mode.	52
S2. Equilibrium adsorption isotherms of N_2 on ZTC, Super P, AG20, and Cor800 at ~ 77 K.....	53

LIST OF FIGURES CONTINUED

Figure	Page
S3. N ₂ -accessible pore size distributions of (a) AG20, (b) Cor800, (c) Super P, and (d) ZTC.	54
S4. Atomistic depictions of (a) graphite (AG20), (b) graphitic carbon with hydrogen-type sites (Cor800), (d) hard carbon (Super P), and (e) ordered porous carbon with no stacking (ZTC).	55
S5. (a) XRD and (b) Raman spectra (collected using a 532 nm excitation source) of Ben800, Nap800, Pyr800, and Cor800.	59
S6. (a) CV profiles (at a 0.1 mV s ⁻¹ scan rate) and (b) GCD rate capability (between 0.4-30 A g ⁻¹ or ~1-60 C) of Ben800, Nap800, Pyr800, and Cor800.	61
S7. CV profiles (at a 0.02 mV s ⁻¹ scan rate) of AG20, Cor800, ZTC, and Super P between 0.05-0.4 V vs. Li/Li ⁺ (a) during the first cycle and (b) after extended cycling.	62

Chapter Four

1. Schematic depiction of the pyrolysis products of boron tribromide and benzene depending on synthesis temperature and nominal composition (C/B ratio, x). Solid solutions of boron in turbostratic graphitic carbon are referred to as BC _x ', while pure turbostratic graphitic carbon is referred to as C'.	74
2. Structural characterization as a function of temperature. (a) XRD patterns and (b) Raman spectra (E _L = 532 nm) of CBr _x ' (bottom, magenta), C' (middle, black), and BC ₃ ' (top, green). Samples were synthesized by the direct method in 50 °C increments between 750 and 1100 °C.	80
3. Structural characterization as a function of boron content. (a) XRD patterns and (b) Raman spectra (EL = 532 nm) of BC _x ' (x = 3, 5, 10, 20, 30, and ∞) synthesized by the direct method at 800 °C.	81

LIST OF FIGURES CONTINUED

Figure	Page
4. Elemental analysis. Boron content of BC_x' as measured by AES (circles) and EDX (squares) as a function of nominal composition determined by the B/C ratio of the initial reaction mixture.	83
5. Boron chemical environment. XAS spectra near the B Kedge of BC_x' synthesized by the direct method and related materials: (a) boron oxide, amorphous boron, and hexagonal boron nitride, chosen as standards, and thin film BC_3 (TF- BC_3) for reference ⁴³ , (b) BC_x' composition series, and (c) BC_3' temperature series. The near-edge region is expanded for (d) BC_x' composition and (e) BC_3' temperature series.	85
6. Interlayer spacing and crystallite size. The development of (a) d_{002} , (b) L_c , and (c) L_a as a function of synthesis temperature within the BC_3', C' , and CBr_x' temperature series. The development of (d) d_{002} , (e) L_c , and (f) L_a as a function of boron content measured by AES within the BC_x' composition series.....	87
7. Raman spectroscopy analysis ($E_L = 532$ nm). The (a) $I(D)/I(G)$ ratio, (b) $Pos(G)$, (c) $fwhm(D)$, and (d) $fwhm(G)$ as a function of synthesis temperature within the BC_3', C' , and CBr_x' temperature series. The (e) $I(D)/I(G)$ ratio, (f) $Pos(G)$, (g) $fwhm(D)$, and (h) $fwhm(G)$ as a function of measured boron content by AES within the BC_x' composition series.	90
8. Phonon dispersion of the D mode. (a) $Disp(D)$ as a function of synthesis temperature for BC_3', C' , and CBr_x' temperature series materials. (b) $Disp(D)$ as a function of the measured boron content within the BC_x' composition series synthesized at 800 °C.....	95
S1. XRD pattern analysis. (a) The raw data (RD), measured background data (BGD), and background-subtracted data (BGSD) of BC_3' synthesized at 800 °C as a representative graphitic carbon material. (b) The BGSD fitted to the combination of a linear background (BG), a single Lorentzian (L_1) for the (002) reflection, and two Lorentzians for the (10) family of reflections (L_2 and L_3).....	98

LIST OF FIGURES CONTINUED

Figure	Page
S2. Raman spectrum analysis. (a) The raw data (RD) fitted to the combination of a linear background (BG), a single Lorentzian (L_4) for the D peak, and a single BWF for the G peak. The Raman spectrum of BC_3' synthesized at 800 °C (analyzed at $E_L = 532$ nm) is shown as a representative example. (b) The E_L dependence of $Pos(D)$ used to calculate $Disp(D)$ for two materials: (c) BC_3' synthesized at 800 °C and (d) C' synthesized at 1100 °C.....	101
S3. Carbon chemical environment. XAS spectra near the C K-edge of the BC_3' temperature series (Black), and HOPG (Blue) as a standard.	103
S4. EDX spectrum analysis. (a) EDX spectra of the BC_x' composition series. (b) The boron content was determined for the BC_x' composition series as well as a boron carbide standard.	104
S5. AES spectrum analysis. Raw AES spectra for the (a) B K-LL, (b) C K-LL, and (c) O K-LL transitions of the BC_x' composition series. (b) The boron content was determined for the BC_x' composition series as well as a boron carbide standard.....	105
S6. Scanning electron microscopy. SEM images of BC_3' (a) and (b), as well as SEM images of C' material (c) and (d).....	106
S7. Calculated phonon dispersion diagrams for (a) graphene, (b) single-layer BC_7 , and (c) single-layer BC_3 . The optical modes (possibly) contributing to the D peak in the Raman spectrum of BC_x' are shown in the red, purple, and blue circles, respectively.	108
S8. Vibrational modes corresponding to phonon branches of (a) graphene, (b) single-layer BC_7 , and (c-d) single-layer BC_3 at near the measured D peak frequency in graphitic BC_x' materials, at frequencies of 1281, 1289, 1363, and 1304 cm^{-1} , respectively. Carbon is shown in black, boron in green, and the 8-atom cell used for calculations in gray.	109

LIST OF FIGURES CONTINUED

Figure	Chapter Five	Page
1.	(a) Binary phase diagram of the boron-carbon system. ³⁰ The region of interest for the formation of metastable BC ₃ is highlighted. (b) The proposed in-plane structure and unit cell of BC ₃ . ^{7,10} (c) Thermochemical ranking of boron and carbon precursors based on their estimated temperature of decomposition (T _d).	121
2.	SEM images of the graphitic BC _x pyrolysis products resulting from five different synthesis routes: (a) route I via boron tribromide, (b) route II via diborane, (c) route III via decaborane, (d) route IV via NDB, and (e) route V via sodium borohydride.	123
3.	Materials characterization of borohydride-derived BC ₃ compared to graphite: (a) XRD patterns, (b) EDX spectra, (c) XAS spectra at the B K-edge, and (d) Raman spectra at 532 nm. (e-f) Dispersion relation of the D peak as revealed by multi-wavelength Raman spectroscopy.	125
S1.	Gas evolution during pyrolysis in a custom metal reactor. (a) Change in amount of gaseous species present as a function of reaction time during the co-pyrolysis of B ₂ H ₆ and C ₆ H ₆ (route II) or pure C ₆ H ₆ , under closed, inert conditions and (b) the corresponding temperature profile.....	130
S2.	Experimental apparatus for filling and sealing the custom metal reactor within a glovebox: the reactor body affixed to a vise (center), the head of the reactor (bottom center), and the split-ring sealing cuff (top right) are shown.	131
S3.	Experimental apparatus for storage and delivery of diborane: lecture bottle containing the B ₂ H ₆ /H ₂ mixture (center) within a freezer held at -20 °C, a purgeable regulator (right), pressure transducer controller (top center), and purge, vent, and delivery gas lines (right and top right) inside a fume hood.....	131
S4.	Experimental apparatus for diborane abatement: two Dreschel flasks (left and right) filled with methanol (clear liquid) showing exhaust flow from right to left. In contact with methanol, diborane is converted into trimethoxyborane and hydrogen is evolved (small bubbles are shown in both flasks, but less evolution occurs in the downstream flask on the left).....	132

LIST OF FIGURES CONTINUED

Figure	Page
S5. Experimental apparatus for diborane/benzene co-pyrolysis reactions (route II): custom metal reactor (center), furnace (center right), freezer containing the B ₂ H ₆ /H ₂ mixture (left), purgeable regulator (center left), gas manifold (Teflon and stainless steel), vacuum outlet (right), and abatement system (top center). The reactor is shown submerged in an acetone and dry ice bath at -78 °C.	132
S6. Custom metal reactor removed from the furnace, shown post reaction and prior to opening.	133
S7. Custom metal reactor head and thermowell, shown post reaction (benzene pyrolysis at 700 °C) and after opening.	133
S8. Custom metal reactor head and thermowell, shown post reaction (diborane/benzene pyrolysis at 700 °C) and after opening.	134
S9. Synthesis of 1,8-Naphthalic Boronic Acid Anhydride, 1.	136
S10. Synthesis of 1,8-Naphthalenediyl-Bridged Diborane(6) (NDB).	137
S11. ¹ H NMR spectrum of NDB dissolved in C ₆ D ₆ (*) using a 500 MHz spectrometer.	138
S12. ¹³ C NMR spectrum of NDB dissolved in C ₆ D ₆ (*) using a 500 MHz spectrometer.	138
S13. Two solid products generated by the pyrolysis of B ₂ C ₁₀ H ₁₄ (NDB) at 800 °C (route IV) can be seen: a suspension of flakes (left) and the remaining mound of the majority solid (right).	140
S14. XRD patterns of the as-collected solid products generated by the co-pyrolysis of NaBH ₄ , I ₂ , and C ₆ H ₆ under inert conditions within a quartz ampule at 800 °C (route V), and of the solid recovered after concentrating wash water from processing the graphitic material.	141
S15. EDX maps of the as-collected solid products generated by the co-pyrolysis of NaBH ₄ , I ₂ , and C ₆ H ₆ at 800 °C (route V). The color-coded maps are generated from the signals of (a) boron and carbon, (b) sodium, (c) carbon, sodium, and silicon, (d) silicon, (e) iodine and sodium, and (f) oxygen.	142

LIST OF FIGURES CONTINUED

Figure	Page
S16. Representative fitting profile for the Raman spectrum of graphitic carbon. One Lorentzian (*C-H) is used to account for hydrogen edge character, a second Lorentzian (D) accounts for the D mode, and a BWF lineshape (G) accounts for the G mode.	144
S17. Compositional analysis of decaborane-derived BC _x (route III). Three morphologies can be seen: (1) low-boron content flakes with a grey metallic luster, (2) high-boron content flakes with a colorful metallic luster, and (3) microsphere-covered surfaces that appear dull black.	149
S18. (a) SEM image and (b) EDX elemental map of decaborane-derived BC _x (route III). The same heterogeneity observed by eye (Figure S17) can be quantifiably differentiated in terms of boron content.	149
S19. Structural analysis of the pyrolysis products from routes I-V. (a) XRD patterns and (b) Raman spectra (E _L = 532 nm) of boron tribromide- (I), diborane- (II), decaborane- (III), NDB- (IV), and sodium borohydride-(V) derived BC _x	151
S20. XAS spectra near the B K-edge of the pyrolysis products from routes I-V and related reference materials. The samples shown are boron tribromide- (I), diborane- (II), decaborane- (III), NDB- (IV), and sodium borohydride- (V) derived BC _x , hexagonal boron nitride, amorphous boron, boron carbide, and boron oxide. TEY spectra (surface) are shown as dashed lines, and TFY spectra (bulk) as solid lines.	153
S21. Raman analysis of the D peak dispersion of the product of the co-pyrolysis of BBr ₃ and C ₆ H ₆ at 800 °C (route I). (a) Representative Raman spectra at 532 nm, 633 nm, and 785 nm. (b) D peak position as a function of excitation wavelength, and the least-squares fit dispersion relation.....	155
S22. Raman analysis of the D peak dispersion of the product of the co-pyrolysis of B ₂ H ₆ and C ₆ H ₆ at 700 °C (route II). (a) Representative Raman spectra at 532 nm, 633 nm, and 785 nm. (b) D peak position as a function of excitation wavelength, and the least-squares fit dispersion relation.....	156

LIST OF FIGURES CONTINUED

Figure	Page
S23. Raman analysis of the D peak dispersion of the product of the co-pyrolysis of B ₁₀ H ₁₄ and C ₆ H ₆ at 800 °C (route III). (a) Representative Raman spectra at 532 nm, 633 nm, and 785 nm. (b) D peak position as a function of excitation wavelength, and the least-squares fit dispersion relation.....	156
S24. Raman analysis of the D peak dispersion of the product of the pyrolysis of B ₂ C ₁₀ H ₁₄ (NDB) at 800 °C (route IV). (a) Representative Raman spectra at 532 nm, 633 nm, and 785 nm. (b) D peak position as a function of excitation wavelength, and the least-squares fit dispersion relation.....	157
S25. Raman analysis of the D peak dispersion of the product of the co-pyrolysis of NaBH ₄ and C ₆ H ₆ at 800 °C (route V). (a) Representative Raman spectra at 532 nm, 633 nm, and 785 nm. (b) D peak position as a function of excitation wavelength, and the least-squares fit dispersion relation.....	157
S26. Thermochemical decomposition energy/temperature correlation. Calculated decomposition energy (ΔE^{SCF}), normalized to the number of atoms of relevance (B or C), as a function of experimental decomposition temperature (T _d), showing an expectable correlation that passes close to the origin. The precursors explored in this work are circled in red and indicated with their molecular formula. Note: the “decomposition temperature” of any species is highly dependent on the experimental method/apparatus used, as well as the definition of decomposition itself.	159

Chapter Six

1. Retrosynthetic analysis of graphitic BC ₃	169
--	-----

Appendix A

A1. Oxy-Hydrogen torch flame intensity. (a) The flame should be relatively intense to effectively soften and move the quartz. (b) the ratio of hydrogen to oxygen should be adjusted so the flame forms a sharp inner cone.	180
--	-----

LIST OF FIGURES CONTINUED

Figure	Page
A2. The evolution of a quartz tube into a finished large ampule. The top tube is a cut segment of the stock tubing, below that is a partially generated ampule where the bottom has been closed off. Third from the top is an ampule with a neck that has not been cleaned, note the white silicone dioxide dust around the neck and base. Bottom is a synthesis ready ampule that has been washed and dried.....	181
A3. Male $\frac{3}{4}$ inch Schlenk adapter. The assembled Schlenk adapter can be seen on top and the exploded view on bottom. The O-rings often need to be replaced to achieve an acceptable seal. The small stem O-ring (k-EP-70-OR-008, Swagelok) can be seen on the left, and the two Ultra-Torr O-rings (VT-7-OR-116, Swagelok) can be seen on the right of the assembly.....	182
A4. Female Schlenk adapter. The assembled Schlenk adapter can be seen on the top and the exploded view on bottom. The O-rings often need to be changed to achieve an acceptable seal; from left to right the valve O-ring (VT-7-OR-012, Swagelok), insert O-ring (K-FC-75-OR-015, Swagelok), and stem seal O-ring (VT-7-OR-014, Swagelok) can be seen.	182
A5. Ampule opening procedure. a) The workspace is clean and prepared with the ampule sitting in the center of the fume hood. b) The ampule has been carefully scored with a diamond bladed saw. c) After cleaning the ampule, it is prepared to be placed within the nitrile enclosure. d) The ampule is secured within the vise with the score line resting on the knife edge that is affixed to the right side of the vise. e) The ampule releases its gaseous byproducts into the fume hood after it has been snapped open. (Note the white fumes exiting the nitrile enclosure) f) The nitrile enclosure is cut open and the contents of the ampule are wetted to assist in collection.....	184
A6. Collection and washing of synthesized material. (a–b) The material is collected with deionized water. (c–d) the collected material is washed over a filter frit.	185
Appendix B	
B1. (a) Gravimetric hydrogen uptake, and (b) hydrogen uptake normalized to the materials surface area, BC ₃ ' collected at 87°C, and CNS-201, MSC-30, and ZTC collected at 25 °C ^{8,9}	188

ABSTRACT

Carbonaceous materials offer great utility as a medium for electrochemical energy storage of ions or for the storage of chemical fuels. The low molecular weight of the second-row element carbon affords access to materials that express remarkably high gravimetric energy densities, and the robust nature of carbon–carbon bonds allow for good cyclability and longevity of carbon-based materials for use in energy storage applications. With the growing popularity and recent advancement of electric vehicles, current battery technologies are pushed to their limits in terms of capacities as well as in minimizing charging times. This has motivated great efforts to discover new lightweight materials that outperform what has traditionally been used in these applications. Alternative energy carriers, such as hydrogen, are also critical for the development of our energy landscape yet are plagued with their own technical challenges; mainly low volumetric energy densities and safety concerns associated with high pressure gas storage systems. Chapter 2 reviews hydrogen storage in today’s society as well as provides a review of past synthetic methods to generate high boron content graphite (BC_3'); being a promising metastable material for the storage of alkali metal ions as well as for solid state hydrogen storage at near ambient conditions. Chapter 3 focuses on the discovery of a new lithium storage mechanism within a novel carbon-based material possessing a high hydrogen content that is tolerant of extremely fast charging, yet still expresses high reversible capacities. Chapter 4 presents a systematic investigation for the detection of chemical environments within BC_3' through an examination of unique spectroscopic properties that originate from the materials phonon structure. Chapter 5 explores the generation of boron and carbon binary phases by the co-pyrolysis of molecular precursors and establishes a density functional theory based approach to align the cracking temperatures of molecular feedstocks; affording access to bulk metastable materials that contain a homogeneous distribution of chemical environments. This work is concluded with an assessment of the materials investigated herein from the perspective of energy storage, as well as provides directions for future work.

CHAPTER ONE

INTRODUCTION

Overview

The work presented in this dissertation addresses the synthesis and characterization of metastable boron-doped graphitic materials that have applications ranging from electrochemical energy storage of alkali metals to the solid-state storage of hydrogen at near-ambient conditions. While select examples of material applications towards the forms of energy storage are presented, the primary focus of this work is to systematically investigate the bottom-up synthesis of metastable, high boron content graphitic systems and to thoroughly characterize their resulting structural/chemical environments. We begin by outlining the primary objectives of the work, and highlight the technical challenges associated with addressing these objectives. Chapter 2 motivates the need for alternative energy carriers in our rapidly evolving society, reviews metastable graphitic materials, and introduces high boron content graphite, especially (BC_3') in terms of its metastability, energy storage applications, and past synthetic efforts to access this elusive material.

While the synthesis and characterization of boron-doped graphitic carbon up to the composition BC_3' is the focus of this work, Chapter 3 is a slight digression, arising from a systematic investigations of low temperature pyrolysis reactions of hydrocarbons relevant to the synthesis of BC_3' . We present the investigation of a novel, high hydrogen content graphitic material that expresses a previously unreported form of lithium binding. We arrived serendipitously at this discovery through a systematic investigation of the low temperature (800 °C) pyrolysis products of a series of polycyclic aromatic hydrocarbons (PAHs) of increasing ring

count starting from benzene (1 ring) up to coronene (7 rings). This was conducted to investigate the decomposition mechanisms of carbon precursor molecules in the temperature range of relevance for the formation of the metastable material BC_3' , where the system is not driven to its thermodynamic products. Through electrochemical lithiation experiments of the pyrolysis products derived from various PAH precursors we noticed a unique lithiation event of a coronene-derived carbon referred to herein as Cor800. This material presents a unique redox couple upon lithiation/delithiation occurring at 0.5 V vs. Li/Li^+ and exhibits minimal hysteresis between intercalation and deintercalation of lithium as seen in galvanostatic charge/discharge experiments. Notably this unique type of lithium interaction is not observed in the pyrolysis products of PAH precursors with ring counts less than 7. The lithiation of Cor800 is distinctly different from previously reported lithium interactions in high hydrogen content carbons that have been previously reported by Dahn and coworkers where insertion occurs at ~ 0.1 V vs. Li/Li^+ and a large voltage hysteresis occurs between lithiation and delithiation.^{1,2}

Chapter 4 transitions into a systematic investigation of the binary boron and carbon system with a study of the previously established direct synthesis of BC_3' by the pyrolysis of boron tribromide and benzene under inert conditions.³ This study examines the effect of synthesis temperature on phase separation between 750–1100 °C as well as the effect of boron content on the materials structure and chemical environments. We present for the first time a convenient method for the detection of graphitic BC_3 (g- BC_3) chemical environments through an examination of the Raman spectrum of this material, where the D peak becomes non-dispersive with respect to the incident wavelength. This is distinctly different from the highly dispersive D peak found in

disordered carbon systems.⁴⁻⁶ These results are validated by comparisons with direct measurements of boron chemical environments through X-ray absorption spectroscopy (XAS).

Chapter 5 explores the bottom-up synthesis of binary boron and carbon phases via the co-pyrolysis of several different molecular precursors. In this we seek a halide free route to obtain BC_3' by utilizing sodium borohydride, diborane, or decaborane in co-pyrolysis with benzene in the temperature range of 700–800 °C. We also explore the pyrolysis of a novel 1,8-naphthalenediyl-bridged diborane(6) (NDB) tiled precursor to explore the crackability of pre-established boron carbon bonds and the effect precursor tiling ability has on the formation of g- BC_3 environments. This study culminates in the development of a density functional theory (DFT) based approach for determining the thermochemical stability of individual precursors and relates this calculated stability to cracking temperature. These calculations can be used to assess the compatibility of molecular precursors for use in co-pyrolysis reactions for the generation of a homogeneous single-phase product. We theorized that this method is applicable to any molecular reagent containing p-block elements.

In chapter 6 we conclude with a summary of the major findings of these three related yet distinct studies and provide directions for future work in the field of bottom-up synthesis for the generation of metastable binary phases.

Objectives

The objectives of this work are as follows:

1. To explore the relative decomposition mechanisms of carbon precursor molecules in the temperature range of relevance for the formation of BC_3' .

2. To develop methods for identifying g-BC₃ chemical environments that are accessible by benchtop characterization methods, mainly Raman spectroscopy.
3. To discover new synthetic routes to access bulk BC₃' that circumvent the use of boron halide reagents such as boron tribromide (BBr₃) or boron trichloride (BCl₃).

This work addresses these objectives by focusing on the development of bottom-up synthetic routes to systematically generate materials with varying structures and chemical environments. These materials are generated by the systematic variation of molecular reagents, molar ratios of reagents in the starting mixture, as well as pyrolysis temperature. The various series of materials generated by systematic perturbations of the synthetic system are then investigated with a suite of complementary characterization techniques, each of which provides a unique and complementary view of the material's structure and/or chemical environments. X-ray diffraction (XRD) is employed to investigate the underlying crystalline structure of the materials; spacings between diffraction planes are determined according to Bragg's law, and the relative length scales of crystallites are estimated through Scherrer broadening.⁷ This technique assesses the long-range order that is present within the solid phases yet provides little or no information as to the identity or structure of any amorphous constituents within the system. Raman spectroscopy is utilized in two-fold: first, to assist in the identification of various phases (including amorphous) that are present within the solid materials, and second, to elucidate contributions that defects express on the graphitic lattice, mainly in the form of edge site character as well as substitutional doping; both act as defects in the graphitic phase.^{4-6,8-10} Energy dispersive X-ray spectroscopy (EDS),¹¹ Auger electron spectroscopy (AES),¹² as well as flame combustion elemental analysis (EA)¹³ are used in

conjunction to determine elemental composition of the synthesized materials. XAS is used to determine both the surface and bulk chemical environments of specific elements that are present within the materials.¹⁴⁻¹⁷ The nitrogen accessible surface area of the materials was determined from N₂ adsorption measurements at ~77 K.¹⁸ By combining the unique information gleaned from these complementary characterization techniques, a comprehensive assessment of the various series of materials can be made, allowing for a detailed understanding of the individual material's structure, chemical composition, and chemical environments that result from systematic synthetic perturbations to the system.

Technical Challenges

From a synthetic perspective, the main challenge associated with incorporating boron into the graphitic lattice is phase separation between the boron and carbon system. The thermodynamic limit of boron incorporation within graphite, carbons thermodynamic allotrope at standard state, was established by Lowell in 1976 and found to be 2.35 at. % boron,¹⁹ this is found at the eutectic temperature between 2350–2375 °C (see Figure 1). At these elevated temperatures the solid solution of boron in the graphitic lattice results in a relatively large quantity of boron substitutionally doped into the stable thermodynamic phase. This relatively large amount of “allowed” boron substitution diminishes to negligible values of incorporation by the time the system is cooled to below 1000 °C. The phase diagram indicates that if more boron is added to the system and the temperature remains below the eutectic line, such as at 25 at. % boron and 800 °C, then the system will phase segregate into the low boron content solid solution of graphite mixed with boron carbide (of composition B₄C). The exact atomic compositions of each phase can be determined by the intercepts of the horizontal tie line at a specified temperature that connects the

two pure phases; the relative abundance of the individual phases in the mixture is determined by the ratio of the two phases that produces an overall atomic ratio that is consistent with total boron content.²⁰ In our example of the point at 25 at. % boron and 800 °C, the thermodynamic composition of the mixed phase would be 31 at. % graphite (C) and 69 at. % boron carbide (B₄C) (see Figure 1). Thus, the metastable material BC₃' is not a thermodynamic product of the boron and carbon binary system and is not shown on the systems thermodynamic phase diagram.

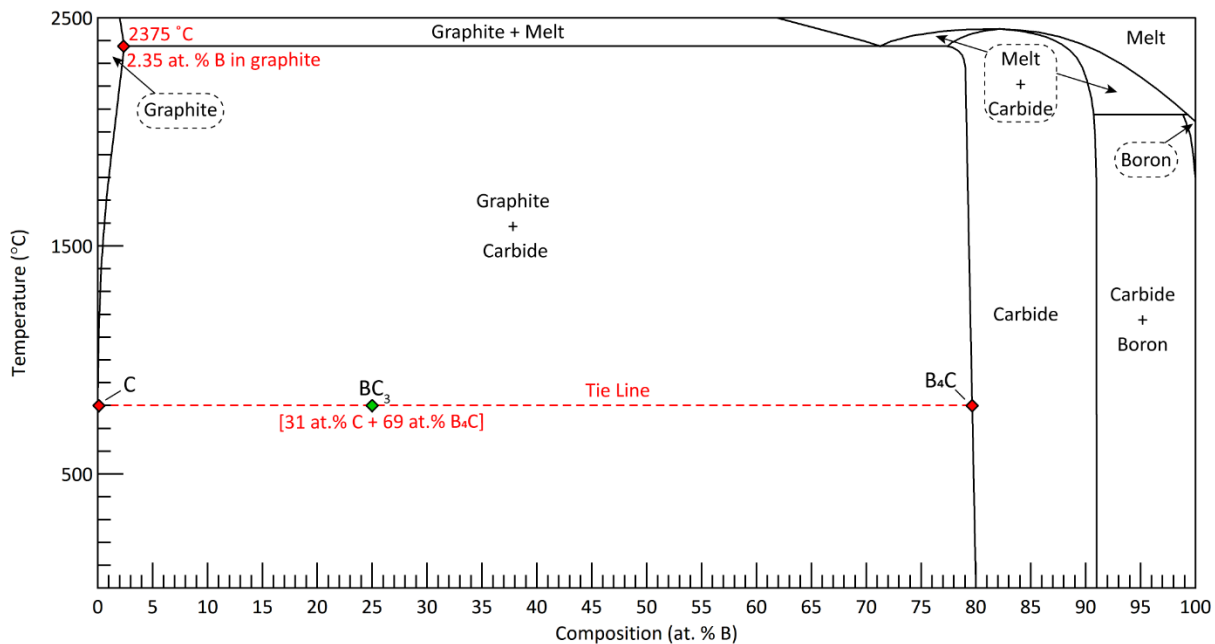


Figure 1. The boron–carbon binary phase diagram.

Metastable materials, also referred to as kinetically trapped phases, are ubiquitous throughout nature and in many cases have desirable properties compared to their equilibrium state counterparts. Functional metastable materials include ionic-conductors²¹, photovoltaics^{22,23}, catalysts²⁴, and sorbents^{25,26}, just to name a few. Even though these metastable materials exhibit a positive free energy above their equilibrium state, many can be isolated and utilized for a variety of practical applications; in fact, we owe our existence to metastable states.²⁷ Cellulose is a

metastable phase of the ternary carbon–oxygen–hydrogen system; fortunately, cellulose does not spontaneously decompose into its lowest energy state.²⁸ Given enough time, this transition will occur according to thermodynamics. However, because cellulose, and numerous other metastable materials exist in a local energy minimum on the energy landscape, they can persist for relatively long timescales. That is until a perturbation lifts them high enough in energy to overcome an activation energy allowing for a cascade down to either another local minimum, or the global minimum where they will remain indefinitely as their respective thermodynamic products. The distribution and evolution of the possible states described above is shown schematically on a two-dimensional reaction coordinate diagram in Figure 2, where the metastable material A is kinetically trapped by the activation energy that separates its local energy well from the global minimum. Material B is an unstable state that will either fall into the kinetically trapped well or convert to C at the global minimum, the stable thermodynamic product C. The shapes used to depict these hypothetical materials are related to one another; this concept has driven the rational design of metastable materials through chemical intuition from a synthetic perspective. Historically, metastable materials that are structurally similar to other thermodynamic products have been good candidates for synthetic endeavors.^{29,30} This allows for minimal structural and chemical modifications that lead to new metastable materials that are still relatively low in energy when compared to the global stability of their thermodynamic counterpart. BC₃' is a perfect example of this concept, where the underlying crystal structure is nearly identical to that of the thermodynamically stable carbon allotrope: graphite.

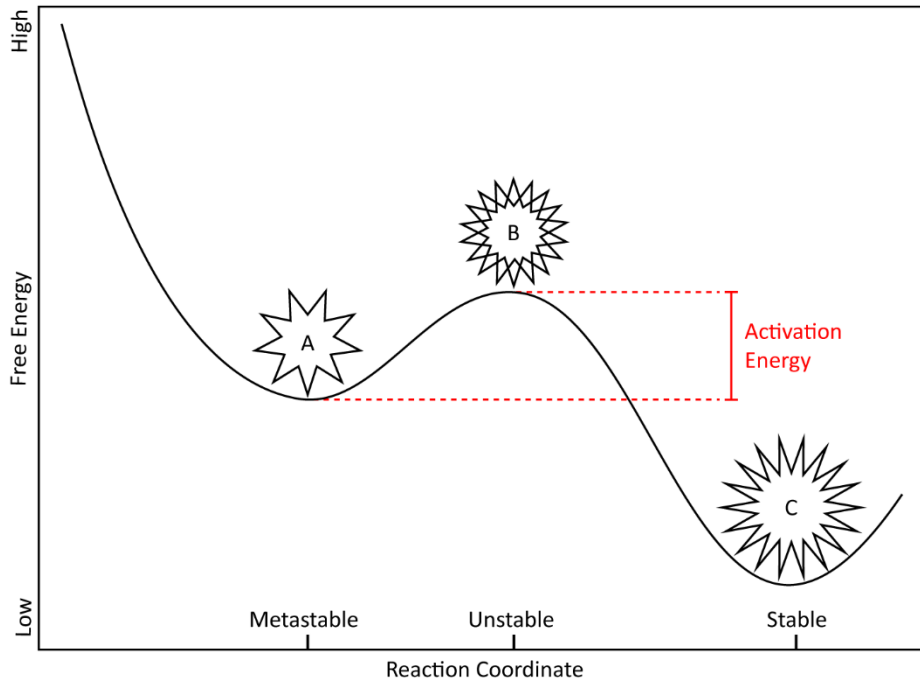


Figure 2. Reaction coordinate diagram of metastable states. The hypothetical metastable material A is kinetically trapped in a local energy well, B is an unstable state, and the thermodynamic product C is shown in the lowest energy state of the system.

Structural characterization of nanocrystalline metastable materials presents a wide array of technical challenges arising from the low degree of long-range crystalline order in these systems. The bulk materials investigated herein are nanocrystalline in nature and exhibit a high degree of turbostratic disorder between the individual graphene sheets that make up the bulk graphitic material. This low level of crystallinity complicates materials characterization due to the lack of a single, well-defined structure within the solid; instead, the materials are dominated by defects and the presence of edge sites that do not reflect the idealized structure and resulting properties that theory predicts. In the context of XRD, this manifests into low signal intensity and large peak breadth, with signals that are often convoluted with other reflections. In order to glean structural information from diffraction experiments, careful assessment of the subtle features in the

diffraction patterns is paramount to deconvoluting the underlying crystalline structure despite the presence of defects, secondary phases, and nanoscale ordering within the solid phases. Raman spectroscopy of nanocrystalline materials is also challenging compared to that of single crystals. Raman spectroscopy is especially sensitive to the highly polarizable carbon-carbon bonding in graphite, allowing for the sensitive determination of chemical and structural environments within these carbonaceous systems.^{4,6,8} The spectra produced by these low temperature pyrolysis products often express a convolution of material and molecular features that complicate not only the collection of spectral data, but also its interpretation. The molecular character that persists in some nanocrystalline graphitic crystallites can lead to large contributions from fluorescence, resulting in a prohibitively intense background that can hide the underlying Raman signals.¹⁰ Thus, care must be taken when collecting spectral data to minimize the fluorescence background, as well as when interpreting the spectral features in order to determine the contributions from the underlying graphitic material as well as those of the molecular fragments that persist through the pyrolysis reaction.

Quantification of boron in carbon systems has also proven to be a challenge due to the similarities in size and scattering cross section between the two neighboring elements. Historically, the quantification of boron in carbon systems has been accomplished using AES^{9,15,31}, elastic recoil detection analysis (ERDA),³ electron probe microanalysis,³² digestion coupled with volumetric titration,¹⁹ or by combustion with fluorine gas followed by quantitative detection of BF_3 and CF_4 by infrared spectroscopy.³³ Classically, the detection of boron has not been possible by EDS techniques owing to the low X-ray yield and energy of the light element boron, coupled with the use of borosilicate windows in line with energy discriminating X-ray detectors. However, in recent

years great advancements have been made in detector sensitivity and configuration, as in the XFlash 6|10 from Bruker Corp., permitting the detection of boron.³⁴ The improved sensitivity and energy resolution of these modern windowless detectors permits accurate quantification with a detection limit of 1-3 at. % boron within mixed boron and carbon systems.³⁵

Characterization of boron chemical environments within nanocrystalline solids presents unique challenges. While the individual chemical environments within highly crystalline systems are well defined, many such systems often exhibit a low concentration of boron within the crystalline phase, hindering their detection. In contrast, the disorder that is often present in high boron content carbons, coupled with the relatively high degree of solubility of boron and carbon in these systems results in a wide range of chemical environments. The surface of boron containing materials always shows evidence for oxide species; fortunately, this robust oxide coating protects the bulk boron environments from further environmental oxidation. The wide range of solubility of boron and carbon, especially in the carbide structure also leads to a multitude of unique bonding motifs often involving nonclassical three-centered two-electron bonds ($3c-2e$).³⁶ While substitutional incorporation of boron into graphite results in trigonal planar BC_3 local environments, these environments can be arranged in a random distribution (a- BC_3) or in ordered arrays (e.g., g- BC_3) leading to distinct materials properties for the two types of boron incorporation.³⁷ XAS is typically used to elucidate the identities and relative contributions from the wide array of boron chemical environments found in these materials.^{14-17,37} While XAS provides direct information regarding the bonding environment and geometries, it requires the use of synchrotron radiation with tunable monochromatic incident X-rays, limiting its accessibility and thus utility. More accessible techniques such as solid-state ^{11}B NMR spectroscopy,^{3,38} electron

energy-loss spectroscopy,³⁹ and X-ray photoelectron spectroscopy^{38,40,41} have also historically been used to determine bulk and surface boron chemical environments. Work presented in this dissertation establishes a new method based on detecting altered phonon dispersion properties of the D peak in the Raman spectrum of high boron content graphite to detect the presence of hexagonally ordered graphitic boron environments (g-BC₃).³⁷

References

- (1) Dahn, J. R.; Zheng, T.; Liu, Y.; Xue, J. S. Mechanisms for Lithium Insertion in Carbonaceous Materials. *Science* **1995**, *270* (5236), 590–593.
- (2) Stevens, D. A.; Dahn, J. R. The Mechanisms of Lithium and Sodium Insertion in Carbon Materials. *J. Electrochem. Soc.* **2001**, *148* (8), A803.
- (3) Stadie, N. P.; Billeter, E.; Piveteau, L.; Kravchyk, K. V.; Döbeli, M.; Kovalenko, M. V. Direct Synthesis of Bulk Boron-Doped Graphitic Carbon. *Chem. Mater.* **2017**, *29* (7), 3211–3218.
- (4) Ferrari, A. C.; Robertson, J. Interpretation of Raman Spectra of Disordered and Amorphous Carbon. *Phys. Rev. B* **2000**, *61* (20), 14095–14107.
- (5) Dresselhaus, M. S.; Jorio, A.; Saito, R. Characterizing Graphene, Graphite, and Carbon Nanotubes by Raman Spectroscopy. *Annu. Rev. Condens. Ma. P.* **2010**, *1* (1), 89–108.
- (6) Ferrari, A. C.; Basko, D. M. Raman Spectroscopy as a Versatile Tool for Studying the Properties of Graphene. *Nature Nanotech.* **2013**, *8* (4), 235–246.
- (7) Langford, J. I.; Wilson, A. J. C. Seherrer after Sixty Years: A Survey and Some New Results in the Determination of Crystallite Size. *J. Appl. Cryst.* **1978**, No. 11, 102–113.
- (8) Yamada, Y.; Kawai, M.; Yorimitsu, H.; Otsuka, S.; Takanashi, M.; Sato, S. Carbon Materials with Zigzag and Armchair Edges. *ACS Appl. Mater. Interfaces* **2018**, *10* (47), 40710–40739.
- (9) Naeini, J. G.; Way, B. M.; Dahn, J. R.; Irwin, J. C. Raman Scattering from Boron-Substituted Carbon Films. *Phys. Rev. B* **1996**, *54* (1), 144–151.
- (10) Cloutis, E.; Szymanski, P.; Applin, D.; Goltz, D. Identification and Discrimination of Polycyclic Aromatic Hydrocarbons Using Raman Spectroscopy. *Icarus* **2016**, *274*, 211–230.

- (11) Ingemarsson, L.; Halvarsson, M. SEM/EDX Analysis of Boron, 2011.
- (12) Madden, H. H.; Nelson, G. C. Auger-Electron Spectra from Boron Carbide. *Phys. Rev. B* **1985**, *31* (6), 3667–3671.
- (13) Matejovic, I. Determination of Carbon, Hydrogen, and Nitrogen in Soils by Automated Elemental Analysis (Dry Combustion Method). *Commun. Soil Sci. Plant Anal.* **1993**, *24*, 213–2222.
- (14) Ravel, B. *Introduction to X-ray Absorption Spectroscopy*. Synchrotron Science Group National Institute of Standards and Technology & Beamline for Materials Measurements National Synchrotron Light Source II.
- (15) Way, B. M.; Dahn, J. R.; Tiedje, T.; Myrtle, K.; Kasrai, M. Preparation and Characterization of B_xC_{1-x} Thin Films with the Graphite Structure. *Phys. Rev. B* **1992**, *46* (3), 1697–1702.
- (16) Pallier, C.; Leyssale, J.-M.; Truflandier, L. A.; Bui, A. T.; Weisbecker, P.; Gervais, C.; Fischer, H. E.; Sirotti, F.; Teyssandier, F.; Chollon, G. Structure of an Amorphous Boron Carbide Film: An Experimental and Computational Approach. *Chem. Mater.* **2013**, *25*, 2618–2629.
- (17) Caretti, I.; Gago, R.; Albella, J. M.; Jiménez, I. Boron carbides formed by coevaporation of B and C atoms: Vapor reactivity, B_xC_{1-x} composition, and bonding structure. *Phys. Rev. B: Condens. Matter Mater. Phys.* **2008**, *77*, 174109.
- (18) Islamoglu, T.; Idrees, K. B.; Son, F. A.; Chen, Z.; Lee, S.-J.; Li, P.; Farha, O. K. Are You Using the Right Probe Molecules for Assessing the Textural Properties of Metal–Organic Frameworks? *J. Mater. Chem. A* **2021**, *10* (1), 157–173.
- (19) Lowell, C. E. Solid Solution of Boron in Graphite. *J. Am. Ceram. Soc.* **1967**, *50* (3), 142–144.
- (20) McQuarrie, D. A.; Simon, J. D. *Physical Chemistry: A Molecular Approach*; University Science Books, 1997.
- (21) Sanna, S.; Esposito, V.; Andreasen, J. W.; Hjelm, J.; Zhang, W.; Kasama, T.; Simonsen, S. B.; Christensen, M.; Linderoth, S.; Pryds, N. Enhancement of the Chemical Stability in Confined δ - Bi_2O_3 . *Nat. Mater.* **2015**, *14* (5), 500–504.
- (22) Nagabhushana, G. P.; Shivaramaiah, R.; Navrotsky, A. Direct Calorimetric Verification of Thermodynamic Instability of Lead Halide Hybrid Perovskites. *P. Natl. Acad. Sci. USA* **2016**, *113* (28), 7717–7721.
- (23) Kuech, T. F.; Babcock, S. E.; Mawst, L. Growth Far from Equilibrium: Examples from III-V Semiconductors. *Appl. Phys. Rev.* **2016**, *3* (4), 040801.

- (24) Sclafani, A.; Herrmann, J. M. Comparison of the Photoelectronic and Photocatalytic Activities of Various Anatase and Rutile Forms of Titania in Pure Liquid Organic Phases and in Aqueous Solutions. *J. Phys. Chem.* **1996**, *100* (32), 13655–13661.
- (25) Davis, M. E.; Lobo, R. F. Zeolite and Molecular Sieve Synthesis. *Chem. Mater.* **1992**, *4* (4), 756–768.
- (26) Stadie, N. P.; Murialdo, M.; Ahn, C. C.; Fultz, B. Anomalous Isosteric Enthalpy of Adsorption of Methane on Zeolite-Templated Carbon. *J. Am. Chem. Soc.* **2013**, *135* (3), 990–993.
- (27) Sun, W. Theoretical Advancements towards Understanding Crystalline Metastability during Materials Synthesis. Thesis, Massachusetts Institute of Technology, 2016.
- (28) Ribeiro, T. R.; Ferreira Neto, J. B.; Takano, C.; Pocolo, J. G. R.; Kolbeinsen, L.; Ringdalen, E. C-O-H₂ Ternary Diagram for Evaluation of Carbon Activity in CH₄-Containing Gas Mixtures. *Materials Research and Technology* **2021**, *13*, 1576–1585.
- (29) Parija, A.; Waetzig, G. R.; Andrews, J. L.; Banerjee, S. Traversing Energy Landscapes Away from Equilibrium: Strategies for Accessing and Utilizing Metastable Phase Space. *J. Phys. Chem. C* **2018**, *122* (45), 25709–25728.
- (30) Sun, W.; Dacek, S. T.; Ong, S. P.; Hautier, G.; Jain, A.; Richards, W. D.; Gamst, A. C.; Persson, K. A.; Ceder, G. The Thermodynamic Scale of Inorganic Crystalline Metastability. *Science Advances* **2016**, *2* (11), e1600225.
- (31) Kouvetakis, J.; McElfresh, M. W.; Beach, D. B. Chemical vapor deposition of highly conductive boron-doped graphite from triphenyl boron. *Carbon* **1994**, *32*, 1129–1132.
- (32) Shirasaki, T.; Derré, A.; Ménerier, M.; Tressaud, A.; Flandrois, S. Synthesis and characterization of boron-substituted carbons. *Carbon* **2000**, *38*, 1461–1467.
- (33) Kouvetakis, J.; Kaner, R. B.; Sattler, M. L.; Bartlett, N. A novel graphite-like material of composition BC₃, and nitrogen–carbon graphites. *J. Chem. Soc., Chem. Commun.* **1986**, 1758–1759.
- (34) *XFlash 6-10 detector*. <https://www.bruker.com/en/products-and-solutions/elemental-analyzers/eds-wds-ebds-SEM-Micro-XRF/detectors/xflash-6-10-detector.html> (accessed 2023-05-11).
- (35) Statham, P. J. Prospects for Improvement in EDX Microanalysis. *J. Microsc.-Oxford* **1983**, *130* (2), 165–176.
- (36) Parkin, G. Representation of Three-Center–Two-Electron Bonds in Covalent Molecules with Bridging Hydrogen Atoms. *J. Chem. Educ.* **2019**, *96* (11), 2467–2475.

- (37) McGlamery, D.; Baker, A. A.; Liu, Y.-S.; Mosquera, M. A.; Stadie, N. P. Phonon Dispersion Relation of Bulk Boron-Doped Graphitic Carbon. *J. Phys. Chem. C* **2020**, *124* (42), 23027–23037.
- (38) King, T. C.; Matthews, P. D.; Glass, H.; Cormack, J. A.; Holgado, J. P.; Leskes, M.; Griffin, J. M.; Scherman, O. A.; Barker, P. D.; Grey, C. P.; et al. Theory and practice: bulk synthesis of C3B and its H₂- and Li-storage capacity. *Angew. Chem., Int. Ed.* **2015**, *54*, 5919–5923.
- (39) Serin, V.; Brydson, R.; Scott, A.; Kihn, Y.; Abidate, O.; Maquin, B.; Derré, A. Evidence for the solubility of boron in graphite by electron energy loss spectroscopy. *Carbon* **2000**, *38*, 547–554.
- (40) Kim, Y. A.; Fujisawa, K.; Muramatsu, H.; Hayashi, T.; Endo, M.; Fujimori, T.; Kaneko, K.; Terrones, M.; Behrends, J.; Eckmann, A.; et al. Raman Spectroscopy of Boron-Doped Single-Layer Graphene. *ACS Nano* **2012**, *6*, 6293–6300.
- (41) Kim, E.; Oh, I.; Kwak, J. Atomic structure of highly ordered pyrolytic graphite doped with boron. *Electrochem. Commun.* **2001**, *3*, 608–612.

CHAPTER TWO

BACKGROUND

Energy Storage

The need for renewable, safe, and efficient energy carriers motivates interesting chemical and physical problems that must be addressed in order to adapt to the increasing energy demands of modern society. Lithium-ion battery (LIB) technology has improved greatly and the cost has significantly dropped since it was introduced by Sony in the 1990s,¹ facilitating the widespread implementation of electric vehicles (EVs) both in the commercial and private sectors.^{2,3} As of May 2023, Tesla Incorporated's Nevada-based Gigafactory alone has produced 7.3 billion LIB cells (37 GWh annually), 1.5 million battery packs, 3.6 million driving units, and 1 million energy modules (14 GWh total).⁴ With the rapid growth of electrification, the demand for responsibly-mined lithium has increased with it. Many have estimated that this will not be a limitation as new lithium deposits are yet to be tapped into,^{5,6} however others have predicted that the demand for lithium will surpass mining capability in the near future and that it will be necessary to increase recycled lithium recovery from < 1 %, the recovery rate in 2017, to > 90 % in order to meet the global demand for LIBs.⁷ In order to facilitate energy security and sustainability on the global scale, we must develop alternative energy carriers that augment existing technologies in order to diversify the energy landscape.

Hydrogen (H₂) is notable for having an exceptional gravimetric energy density (142 MJ kg⁻¹), nearly three times that of gasoline.⁸ The chemical energy stored within molecular hydrogen can be efficiently converted directly to electrical or mechanical energy by oxidation in a fuel cell

or combustion within an engine; both methods consume oxygen from the atmosphere and produce water as the sole byproduct, making hydrogen an attractive energy carrier for many applications. Unfortunately, the efficient storage of hydrogen in a compact volume remains challenging despite several decades of research at academic, government, and private institutions around the world.

Currently, hydrogen is most effectively stored on board passenger and commercial vehicles in high-pressure composite tanks with a maximum storage pressure of 700 bar. State of the art compressed hydrogen tanks can reach a gravimetric storage capacity of 4.2 wt. % hydrogen with respect to the entire storage system, hence the US Department of Energy (DOE) has set a series of targets ranging from 4.5–6.5 wt. % for next-generation hydrogen storage systems.^{8,9} A schematic of the components of a next-generation, high-pressure hydrogen storage tank is shown in Figure 1.¹⁰ There is further motivation to lower the pressure of storage tanks for both practical reasons (e.g., to accommodate diverse tank shapes and sizes) and safety reasons, making it desirable to seek storage methods that utilize condensed/solid-state phases of hydrogen or hydrogen-rich media.

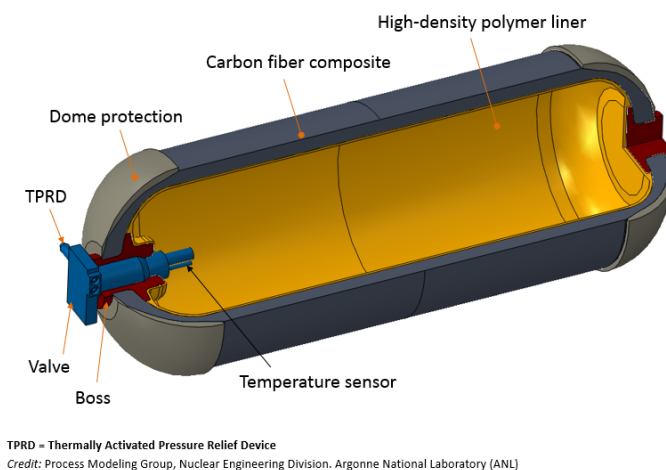


Figure 1. Components of a pressurized hydrogen storage tank. (Adapted from reference 10)

Hydrogen may also be stored as a liquid, which is attractive due to its increased density (71.3 g L^{-1} at 20 K and 1 bar) compared to gaseous hydrogen (39.2 g L^{-1} at 298 K and 700 bar). A schematic of a liquid H_2 storage system is shown in Figure 2.¹¹ Liquefaction only occurs at very low temperatures at ambient pressure ($\sim 20 \text{ K}$, see Figure 3), and requires extensive, energy-inefficient cooling systems to operate, adding weight and complexity to the overall storage system. Furthermore, liquid hydrogen can only be stored safely in open systems to eliminate the risk of overpressure, which makes long-term storage as a liquid unfeasible.¹²

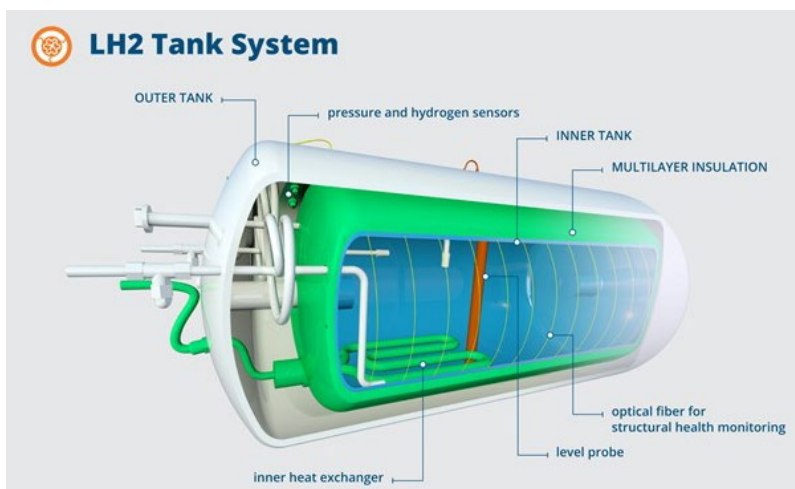


Figure 2. Liquid hydrogen storage vessel containing an inner storage tank with heat exchangers and cooling system that is wrapped in insulation to maintain a cryogenic environment. (Adapted from reference 11)

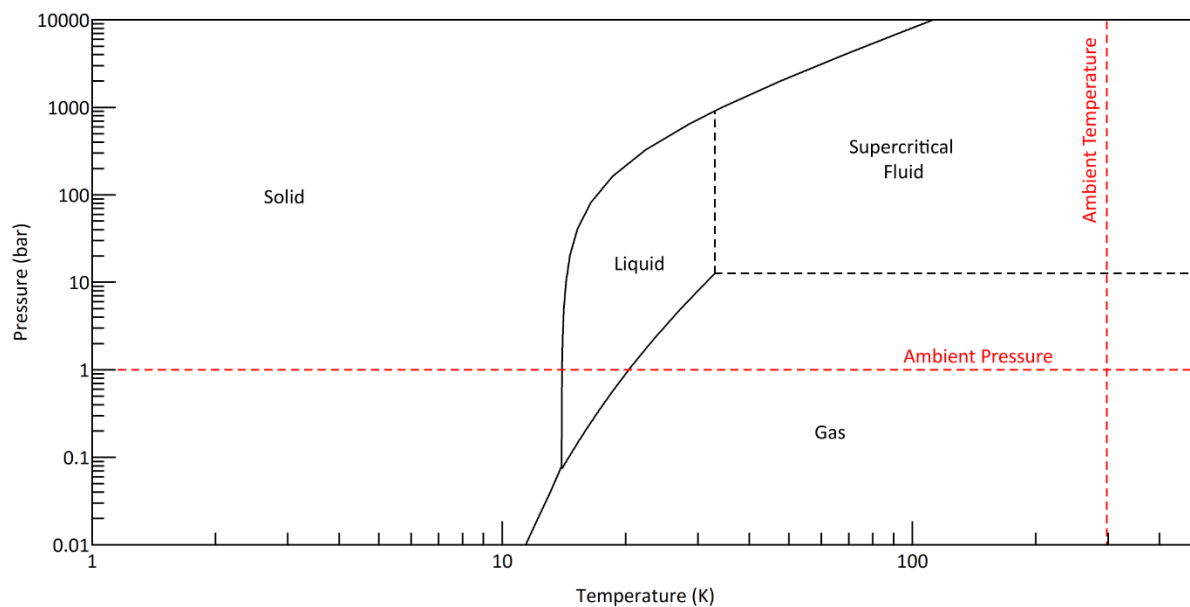


Figure 3. Hydrogen H₂ phase diagram. The ambient temperature and pressure lines are highlighted.

Beyond pure compression and liquefaction, hydrogen can also be stored on or within an appropriate host material through adsorption or absorption, respectively. Adsorption, a surface-specific phenomenon, comprises both physisorption and chemisorption mechanisms of interaction. Physisorption is dictated by the weak dispersion forces present between the H₂ molecule (the adsorbate) and the surface of the host material. These forces are typically on the order of 1-10 kJ mol⁻¹ for adsorbate-sorbent interactions. Adsorption can be represented simplistically by a Lennard-Jones potential well with the depth of the well corresponding to the binding energy; at lower temperatures, the adsorbate is confined to longer residence times on the adsorption site. To maximize gravimetric and volumetric storage capacity, materials with large surface area, narrow pore diameter, and relatively strong binding sites are desired. To date, the maximum gravimetric excess storage capacity of physisorbed hydrogen on high surface area carbons is ~5.5 wt. % at 77 K; this value is typically reduced to ~1 wt. % at 298 K and 300 bar.¹³ State-of-the-art materials for

room temperature physisorptive hydrogen storage are metal-organic frameworks (MOFs) which can achieve up to 1.65 wt. % storage capacities at 298 K and 48 bar.^{9,14} Physisorption is a perfectly reversible and robust method for storing hydrogen, but effective capacities can only be reached at low temperatures as of today. An overview of current hydrogen storage methods is depicted in Figure 4.¹⁵

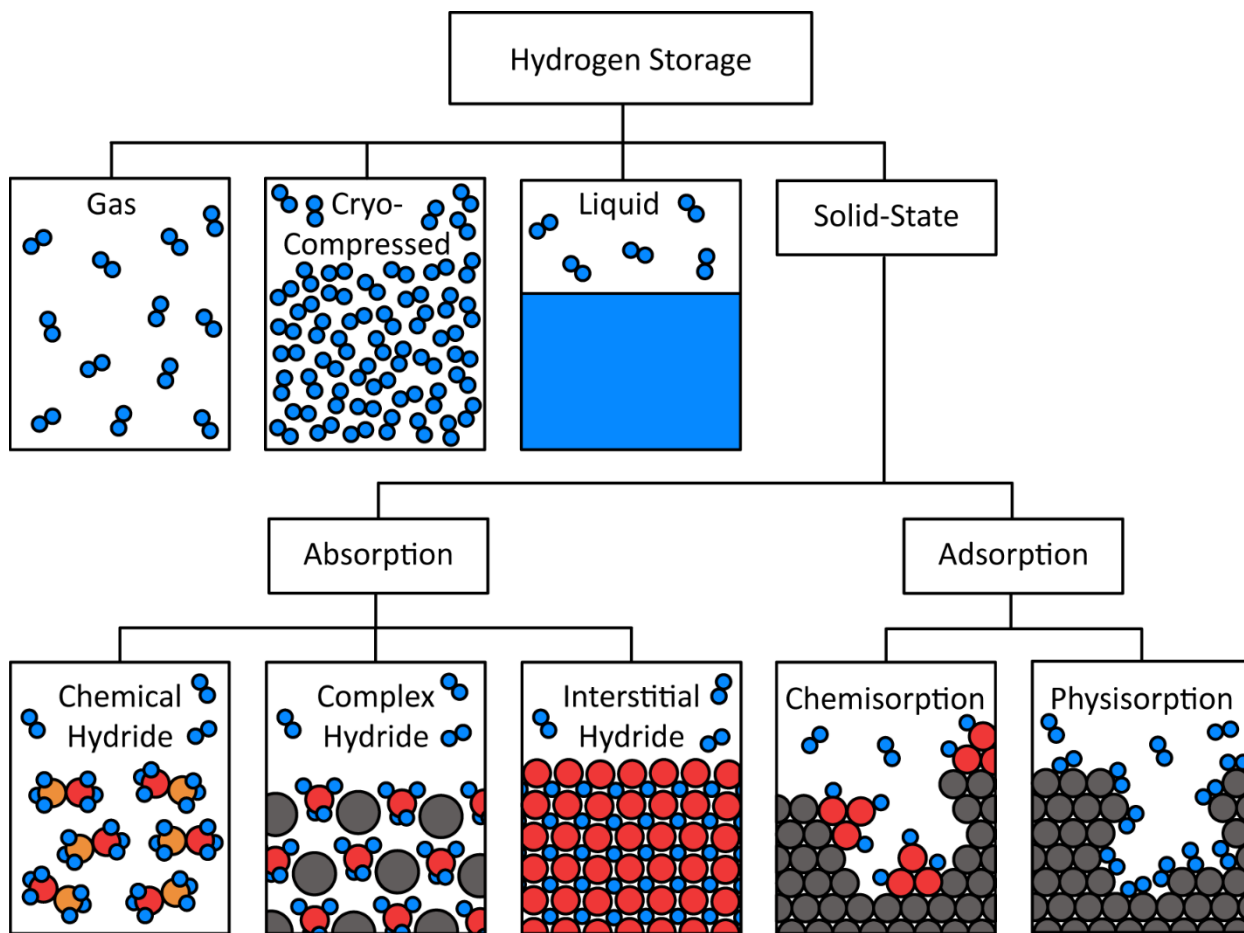


Figure 4. Overview of hydrogen storage methods.

Solid-state hydrogen storage can also be accomplished via chemisorption which occurs when a hydrogen molecule is dissociated into two hydrogen atoms and becomes chemically bound to the host surface or within a molecule or material. Chemisorption is often enhanced at elevated

temperatures due to the activation barrier of the reaction (typically H₂ bond cleavage) and the strength of chemical bonds: typically, 100-1000 kJ mol⁻¹. The mechanism of chemisorption can therefore be crudely described by a simple two-state reaction coordinate diagram; hydrogen uptake and release are increased at higher temperatures to facilitate bond formation and cleavage. This method of hydrogen storage occurs on or within a wide variety of materials ranging from metal hydrides to complex hydrides,¹⁶ as well as hydrogen-rich molecules (e.g., NH₃).¹² Chemisorption typically suffers from reversibility issues associated with strong chemical bonding or the degradation of the host material upon system cycling. Some benchmark hydrogen storage materials such as palladium and LaNi₅ exhibit extremely robust cycling but remain prohibitively expensive and/or heavy.

Due to the various technical limitations mentioned above, current methods cannot provide efficient, reliable, and safe storage of hydrogen at the same time, limiting the practicality of hydrogen as a primary energy carrier. An ideal material for hydrogen storage at ambient conditions would be lightweight, made of earth abundant elements, and have a hydrogen binding energy that is stronger than that typical of physisorption (to allow for higher operating temperatures closer to 298 K) yet weaker than that typical of chemisorption (to allow for lower operating temperatures closer to 298 K and to eliminate reversibility issues). Thus, an ideal material for hydrogen storage would be comprised of lightweight elements and express a hydrogen binding energy on the order of 10-100 kJ mol⁻¹.

Boron-Doped Graphitic Carbon

Hydrogen Storage in BC₃'

In 2007, a first principles study of hydrogen absorption in a bulk graphitic material of composition BC₃' was reported,¹⁷ inspired largely by previous serendipitous observations of enhanced hydrogen release by boron-doped graphitic thin-films at temperatures between 400-1200 K.¹⁸⁻²⁰ These calculations were used to follow H₂ chemisorption, H₂ dissociation, and H absorption/diffusion properties of BC₃', utilizing a plane-wave pseudopotential DFT package (CASTEP). It was predicted that H₂ can dissociate within BC₃' with a barrier of 19 kJ mol⁻¹ and absorb atomic hydrogen with a binding energy of 46-80 kJ mol⁻¹ at low and high hydrogen coverages, respectively (where all molar quantities refer to H₂). The favorable interaction of H₂ within BC₃' as compared to graphite, which does not readily absorb H₂, was ascribed to the softening of the in-plane bonding that results from substitutional boron incorporation into the graphitic lattice. It was shown that if an H₂ molecule could be placed within the interlayer galleries of pure carbon graphite (an unrealistic scenario), the optimal C-C-H bond angle would be unfavorable to the formation of the new sp³ hybridized C-H bond. In BC₃', however, the H was predicted to rest between the carbon and the boron atom on one side of the slit pore; the resulting C-C-H bond angle was found to be 106°, closer to the preferred sp³ geometry of the bound state (see Figure 5).¹⁷ In other words, the soft nature of B-C bonding results in a lower energetic barrier for H chemisorption within the lattice of BC₃' when compared to that in pure graphite.

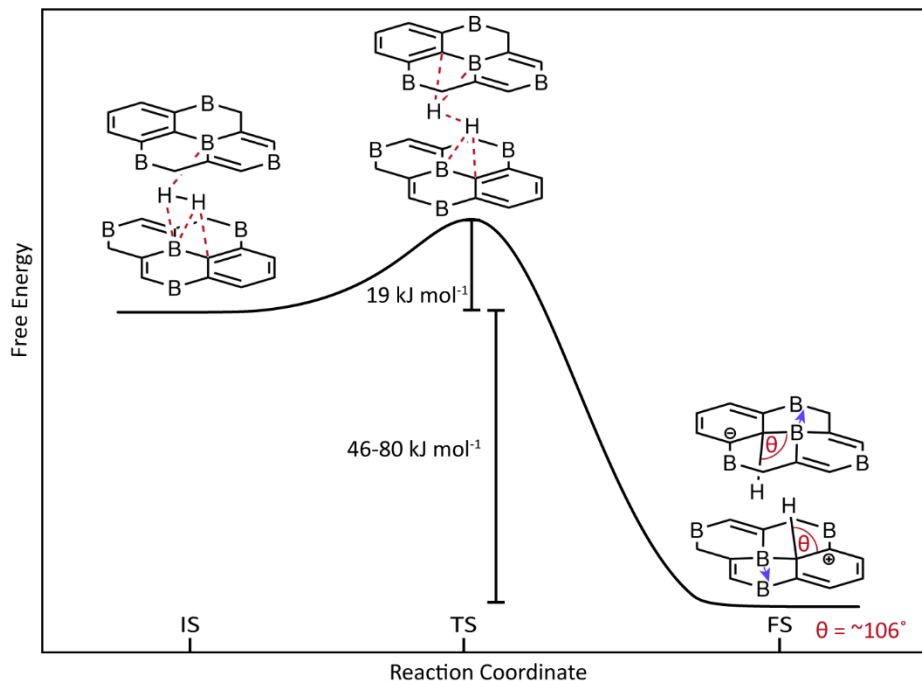


Figure 5. Schematic reaction coordinate diagram of hydrogen binding in BC_3' . Hydrogen in the initial state (IS) is placed within the slit pore of two BC_3' sheets where it coordinates to adjacent boron atoms through the vacant boron p_z orbitals. In the transition state (TS) the hydrogen–hydrogen bond dissociates, and the individual hydrogen atoms coordinate to either side of the slit pore. In the final state (FS) the hydrogen bonds to the neighboring carbon atom with a C-C-H dihedral angle of $\sim 106^\circ$, and neighboring boron atoms deflect out of plane to accommodate the rehybridization of the system (denoted with blue arrows). Binding of a second hydrogen molecule would alleviate the formal charges depicted in the FS.¹⁷

A follow-up study of hydrogen absorption in BC_3' was reported in 2010.²¹ The thermodynamics and kinetics of H_2 dissociation and subsequent H migration were calculated using the projector augmented wave (PAW) method. The overall process was predicted to be slightly endothermic by approximately 46 kJ mol^{-1} . The activation barrier of hydrogen dissociation within BC_3' , including contributions from insertion at a particle edge (not previously considered), was found to be 60 kJ mol^{-1} , slightly higher than previously predicted, yet still significantly lower than that in pure graphite. Therefore, all reported theoretical results suggest that both hydrogen

intercalation and dissociation are thermodynamically and kinetically favorable at near ambient conditions ($\sim 70\text{--}140\text{ }^\circ\text{C}$), with a high storage capacity within bulk single crystal BC_3' .

Historical Synthesis of BC_3'

The history of thermal reactions between various boron species and hydrocarbons began with a systematic investigation by Hurd in 1948, where the low temperature pyrolysis reactions between diborane and a variety of hydrocarbons was studied. These reactions were conducted under inert conditions in the temperature range of $100\text{--}200\text{ }^\circ\text{C}$, resulting in the substitution of boron into the organic precursors yielding a variety of small molecule products.²² Boron substitution into graphite was first systematically investigated by Lowell in 1967; equilibrium solid solutions were prepared by the heating of boron carbide (nominally B_4C) and graphite under reduced pressure up to $2500\text{ }^\circ\text{C}$, followed by rapid quenching.²³ The maximum equilibrium substitution of boron in graphite was determined to be 2.35 at. % at the eutectic temperature of $2350\text{ }^\circ\text{C}$, as shown in Figure 6. The vast region of boron concentration in the B-C system below the eutectic temperature and between $\sim 2\text{--}80$ at. % corresponds to a phase-separated mixture of low boron content graphite and boron carbide.

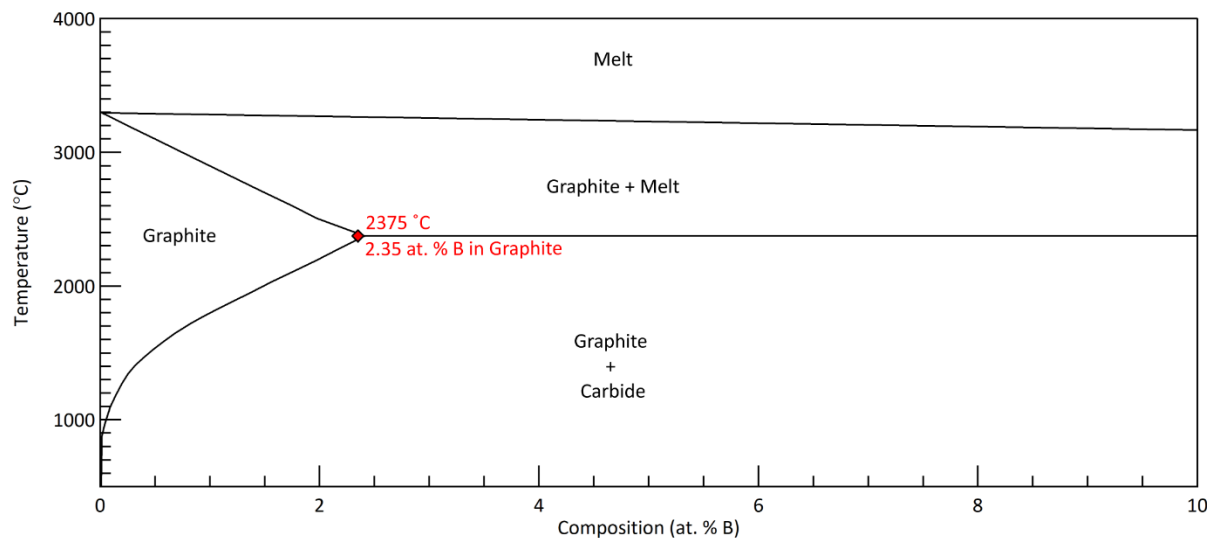


Figure 6. Boron–carbon phase diagram at low boron concentrations.

High boron content graphitic carbon thin films were subsequently synthesized in 1986 by chemical vapor deposition (CVD) of stoichiometric ratios of boron trichloride (BCl_3) and benzene (C_6H_6) at 800 °C.²⁴ The synthesized thin-films exhibited a dark metallic luster and were reported to exhibit a composition of BC_3 (25 at. % boron). Such a high substitutional boron concentration had not previously been reported for graphite or disordered graphitic materials. It was surmised that the low temperatures of synthesis (800 °C) and possibly the presence of the substrate allowed access to a new metastable state of the boron-carbon system, thus avoiding phase separation of boron carbide and graphite. The properties of this new phase, often referred to as BC_3' and later reported to have a stoichiometry closer to BC_5 ,²⁵ have been of great fundamental interest and therefore the subject of numerous computational and physical studies.^{26–28}

A bulk BC_3' material (as opposed to thin-films) remained elusive for the next 30 years. In 2015, a closed “molecular tiling” synthesis route was investigated via the pyrolysis of 1,3-bis(dibromoboryl)benzene at 800 °C.²⁹ The resulting material was found to be highly disordered and contained a significant amount of oxygen within the bulk material. Therefore, hydrogen

storage in the so-obtained samples was found to be negligible. We note that the multistep synthesis of the organic precursor is an important complexity of this work, and likely a source of oxygen contamination; its fixed B:C ratio also prevents the continuous tuning of the boron to carbon ratio within the final material.

Prior to this work, the latest route to bulk high boron content graphitic BC₃' was reported by Stadie et al. in 2017.³⁰ This method bypassed the complicated organic synthesis of 1,3-bis(dibromoboryl)benzene; instead, benzene (C₆H₆) and boron tribromide (BBr₃) were combined directly in the liquid phase at room temperature, both available in high purity as commercial reagents. Continuously variable ratios of benzene and boron tribromide were heated to 800-1050 °C in a closed quartz ampule to produce nanocrystalline graphitic BC_x' of widely tunable composition ($x \geq 3$). Oxygen was effectively reduced as a contaminant in the resulting materials; however, halide contamination was unavoidable due to the use of BBr₃. The hydrogen storage properties of the so-obtained materials remained uncharacterized in the original report, but preliminary results are now presented as part of this work and can be found in Appendix B. Nevertheless, two main synthetic challenges remain: the development of a 1) more crystalline and 2) halide free material, enabling the careful assessment and possible corroboration of the long-standing theoretical predictions of hydrogen storage within the metastable graphitic BC₃' material. A historical summary of the development of boron-doped graphitic systems is given in Table 1, where studies have evolved from a focus on molecular products to thin-films and lastly to bulk materials in recent years.

Table 1. Historical developments to the synthesis of boron-doped carbons.

Year	Reference	Product Classification	Synthesis Method	Reported Composition (at.% B)	Reagents	Synthesis Temperature [Annealing] (°C)
1948	22	Molecular	Low Temperature Thermal	7.69	$C_4H_8 + B_2H_6$	100
1948	22	Molecular	Low Temperature Thermal	14.29	$C_2H_2 + B_2H_6$	100
1948	22	Molecular	Low Temperature Thermal	5.26	$C_6H_6 + B_2H_6$	100
1948	22	Molecular	Low Temperature Thermal	25	$CH_4 + B_2H_6$	180
1948	22	Molecular	Low Temperature Thermal	-	$C_5H_{12} + B_2H_6$	180
1967	23	Bulk Solid Solution	Top-Down, Thermal	2.35	Graphite + B_4C	2375
1981	31	Bulk Solid Solution	Top-Down, Ion-Implantation	-	Graphite + B^+	[950]
1986	24	Thin Film	Bottom-Up, CVD	25	$C_6H_6 + BCl_3$	800
1989	32	Thin Film	Bottom-Up, CVD	25	$C_6H_6 + BCl_3$	800
1992	26	Thin Film	Bottom-Up, CVD	17	$C_6H_6 + BCl_3$	900
1993	33	Thin Film	Bottom-Up, CVD	20	$C_6H_6 + BCl_3$	475-775 [900]
1994	34	Thin Film	Bottom-Up, CVD	5.26	$(C_6H_5)_3B$	800
1995	35	Thin Film	Bottom-Up, CVD	15	$C_6H_6 + BCl_3$	900 [1000-2300]
1996	25	Thin Film	Bottom-Up, CVD	17	$C_6H_6 + BCl_3$	900
1996	36	Thin Film	Bottom-Up, CVD	20	$C_3H_8 + BCl_3$	950
2000	27	Thin Film	Bottom-Up, CVD	20	$C_2H_2 + BCl_3$	1000- 1225
2010	37	Bulk Porous Framework	Bottom-Up, Solution-Phase	7.3	$Cl_2C=CCl_2 + BCl_3$	250-350
2010	37	Bulk Porous Framework	Bottom-Up, Solution-Phase	7.3	$C_6Cl_6 + BCl_3$	250-350
2012	28	Thin Film	Top-Down, Thermal	0.22	Graphite + H_3BO_3	2450
2015	29	Bulk	Bottom-Up, Closed Reactor	20	$(BBr_2)_2C_6H_4$	800
2017	30	Bulk	Bottom-Up, Closed Reactor	25	$C_6H_6 + BBr_3$	800
2020	38	Bulk	Bottom-Up, Closed Reactor	12	$C_6H_6 + BBr_3$	800

References

- (1) *Lithium-Ion Batteries: Science and Technologies*; Yoshio, M., Brodd, R. J., Kozawa, A., Eds.; Springer: New York, NY, 2009.
- (2) Li, M.; Lu, J.; Chen, Z.; Amine, K. 30 Years of Lithium-Ion Batteries. *Adv. Mater.* **2018**, *30* (33), 1800561.
- (3) Kim, T.; Song, W.; Son, D.-Y.; K. Ono, L.; Qi, Y. Lithium-Ion Batteries: Outlook on Present, Future, and Hybridized Technologies. *J. Mater. Chem. A* **2019**, *7* (7), 2942–2964.
- (4) *Continuing Our Investment in Nevada*. Tesla. <https://www.tesla.com/blog/continuing-our-investment-nevada> (accessed 2023-05-12).
- (5) Mohr, S. H.; Mudd, G. M.; Giurco, D. Lithium Resources and Production: Critical Assessment and Global Projections. *Minerals* **2012**, *2* (1), 65–84.
- (6) Gruber, P. W.; Medina, P. A.; Keoleian, G. A.; Kesler, S. E.; Everson, M. P.; Wallington, T. J. Global Lithium Availability. *J. Ind. Ecol.* **2011**, *15* (5), 760–775.
- (7) Swain, B. Recovery and Recycling of Lithium: A Review. *Sep. Purif. Technol.* **2017**, *172*, 388–403.
- (8) Schlapbach, L.; Züttel, A. Hydrogen-Storage Materials for Mobile Applications. *Nature* **2001**, *414* (6861), 353–358.
- (9) Allendorf, M. D.; Hulvey, Z.; Gennett, T.; Ahmed, A.; Autrey, T.; Camp, J.; Cho, E. S.; Furukawa, H.; Haranczyk, M.; Head-Gordon, M.; Jeong, S.; Karkamkar, A.; Liu, D.-J.; Long, J. R.; Meihaus, K. R.; Nayyar, I. H.; Nazarov, R.; Siegel, D. J.; Stavila, V.; Urban, J. J.; Veccham, S. P.; Wood, B. C. An Assessment of Strategies for the Development of Solid-State Adsorbents for Vehicular Hydrogen Storage. *Energy Environ. Sci.* **2018**, *11* (10), 2784–2812.
- (10) *Physical Hydrogen Storage*. Energy.gov. <https://www.energy.gov/eere/fuelcells/physical-hydrogen-storage> (accessed 2023-05-22).
- (11) *Toray Advanced Composites to lead research consortium for development of liquid hydrogen composite tanks for civil aviation - Toray Advanced Composites*. <https://www.toraytac.com/media/news-item/2021/12/14/Toray-Advanced-Composites-to-lead-research-consortium-for-development-of-liquid-hydrogen-composite-tanks-for-civil-aviation> (accessed 2023-05-22).
- (12) Züttel, A. Materials for Hydrogen Storage. *Mater. Today* **2003**, *6* (9), 24–33.

- (13) Stadie, N. P.; Vajo, J. J.; Cumberland, R. W.; Wilson, A. A.; Ahn, C. C.; Fultz, B. Zeolite-Templated Carbon Materials for High-Pressure Hydrogen Storage. *Langmuir* **2012**, *28* (26), 10057–10063.
- (14) Huong, T. T. T.; Thanh, P. N.; Son, D. N. Metal – Organic Frameworks: State-of-the-Art Material for Gas Capture and Storage. *VNU Journal of Science: Mathematics - Physics* **2016**, *32* (1).
- (15) *Hydrogen Storage*. Energy.gov. <https://www.energy.gov/eere/fuelcells/hydrogen-storage> (accessed 2023-05-22).
- (16) Orimo, S.; Nakamori, Y.; Eliseo, J. R.; Züttel, A.; Jensen, C. M. Complex Hydrides for Hydrogen Storage. *Chem. Rev.* **2007**, *107* (10), 4111–4132.
- (17) Zhang, C.; Alavi, A. Hydrogen Absorption in Bulk BC₃: A First-Principles Study. *J. Chem. Phys.* **2007**, *127* (21), 214704.
- (18) Ferro, Y.; Marinelli, F.; Allouche, A.; Brosset, C. Density Functional Theory Investigation of H Adsorption on the Basal Plane of Boron-Doped Graphite. *J. Chem. Phys.* **2003**, *118* (12), 5650–5657.
- (19) Ferro, Y.; Marinelli, F.; Jelea, A.; Allouche, A. Adsorption, Diffusion, and Recombination of Hydrogen on Pure and Boron-Doped Graphite Surfaces. *J. Chem. Phys.* **2004**, *120* (24), 11882–11888.
- (20) Ferro, Y.; Brosset, C.; Allouche, A. Quantum Study of Hydrogen Interaction with Plasma-Facing Graphite and Boron Doped Graphite Surfaces. *Phys. Scr.* **2004**, *2004* (T108), 76.
- (21) Sha, X.; Cooper, A. C.; Bailey, W. H.; Cheng, H. Revisiting Hydrogen Storage in Bulk BC₃. *J. Phys. Chem. C* **2010**, *114*, 3260–3264.
- (22) Hurd, D. T. The Reactions of Diborane with Hydrocarbons. *J. Am. Chem. Soc.* **1948**, *70* (6), 2053–2055.
- (23) Lowell, C. E. Solid Solution of Boron in Graphite. *J. Am. Ceram. Soc.* **1967**, *50* (3), 142–144.
- (24) Kouvetakis, J.; Kaner, R. B.; Sattler, M. L.; Bartlett, N. A novel graphite-like material of composition BC₃, and nitrogen–carbon graphites. *J. Chem. Soc., Chem. Commun.* **1986**, 1758–1759.
- (25) Naeini, J. G.; Way, B. M.; Dahn, J. R.; Irwin, J. C. Raman Scattering from Boron-Substituted Carbon Films. *Phys. Rev. B* **1996**, *54* (1), 144–151.
- (26) Way, B. M.; Dahn, J. R.; Tiedje, T.; Myrtle, K.; Kasrai, M. Preparation and Characterization of B_xC_{1-x} Thin Films with the Graphite Structure. *Phys. Rev. B* **1992**, *46* (3), 1697–1702.

- (27) Shirasaki, T.; Derré, A.; Mé né trier, M.; Tressaud, A.; Flandrois, S. Synthesis and characterization of boron-substituted carbons. *Carbon* **2000**, *38*, 1461–1467.
- (28) Kim, Y. A.; Fujisawa, K.; Muramatsu, H.; Hayashi, T.; Endo, M.; Fujimori, T.; Kaneko, K.; Terrones, M.; Behrends, J.; Eckmann, A.; et al. Raman Spectroscopy of Boron-Doped Single-Layer Graphene. *ACS Nano* **2012**, *6*, 6293–6300.
- (29) King, T. C.; Matthews, P. D.; Glass, H.; Cormack, J. A.; Holgado, J. P.; Leskes, M.; Griffin, J. M.; Scherman, O. A.; Barker, P. D.; Grey, C. P.; et al. Theory and practice: bulk synthesis of C3B and its H₂- and Li-storage capacity. *Angew. Chem., Int. Ed.* **2015**, *54*, 5919–5923.
- (30) Stadie, N. P.; Billeter, E.; Piveteau, L.; Kravchyk, K. V.; Döbeli, M.; Kovalenko, M. V. Direct Synthesis of Bulk Boron-Doped Graphitic Carbon. *Chem. Mater.* **2017**, *29* (7), 3211–3218.
- (31) Elman, B. S.; Dresselhaus, M. S.; Dresselhaus, G.; Maby, E. W.; Mazurek, H. Raman scattering from ion-implanted graphite. *Phys. Rev. B: Condens. Matter Mater. Phys.* **1981**, *24*, 1027–1034.
- (32) Kouvetakis, J.; Sasaki, T.; Shen, C.; Hagiwara, R.; Lerner, M.; Krishnan, K. M.; Bartlett, N. Novel Aspects of Graphite Intercalation by Fluorine and Fluorides and New B/C, C/N and B/C/N Materials Based on the Graphite Network. *Synth. Met.* **1989**, *34* (1), 1–7.
- (33) Fecko, D. L.; Jones, L. E.; Thrower, P. A. The formation and oxidation of BC₃, a new graphitelike material. *Carbon* **1993**, *31*, 637–644.
- (34) Kouvetakis, J.; McElfresh, M. W.; Beach, D. B. Chemical vapor deposition of highly conductive boron-doped graphite from triphenyl boron. *Carbon* **1994**, *32*, 1129–1132.
- (35) Cermignani, W.; Paulson, T. E.; Onneby, C.; Pantano, C. G. Synthesis and Characterization of Boron-Doped Carbons. *Carbon* **1995**, *33*, 367–374.
- (36) Jacques, S.; Guette, A.; Bourrat, X.; Langlais, F.; Guimon, C.; Labrugere, C. LPCVD and Characterization of Boron-Containing Pyrocarbon Materials. *Carbon* **1996**, *34* (9), 1135–1143.
- (37) Jin, Z.; Sun, Z.; Simpson, L. J.; O'Neill, K. J.; Parilla, P. A.; Li, Y.; Stadie, N. P.; Ahn, C. C.; Kittrell, C.; Tour, J. M. Solution-Phase Synthesis of Heteroatom-Substituted Carbon Scaffolds for Hydrogen Storage. *J. Am. Chem. Soc.* **2010**, *132* (43), 15246–15251.
- (38) McGlamery, D.; Baker, A. A.; Liu, Y.-S.; Mosquera, M. A.; Stadie, N. P. Phonon Dispersion Relation of Bulk Boron-Doped Graphitic Carbon. *J. Phys. Chem. C* **2020**, *124* (42), 23027–23037.

CHAPTER THREE

HYDROGEN-TYPE BINDING SITES IN CARBONACEOUS ELECTRODES
FOR RAPID LITHIUM INSERTION

Contribution of Authors

Manuscript in Chapter 3

Author: Devin McGlamery

Contributions: Synthesized materials, collected data, analyzed data, produced figures, and wrote the manuscript.

Co-Author: Charles McDaniel

Contributions: Sample processing, collected data, and assisted in editing the manuscript.

Co-Author: Wei Xu

Contributions: Fabricated electrochemical cells, collected electrochemical data, assisted in analyzing electrochemical data.

Co-Author: Nicholas P. Stadie

Contributions: Oversaw experimental designed, aided in interpretation of results, and assisted in writing and editing the manuscript.

Manuscript Information

Devin McGlamery, Charles McDaniel, Wei Xu, and Nicholas P. Stadie

Department of Chemistry & Biochemistry, Montana State University, Bozeman, Montana 59717,
United States

Status of Manuscript:

Prepared for submission to a peer-reviewed journal

Officially submitted to a peer-reviewed journal

Accepted by a peer-reviewed journal

Published in a peer-reviewed journal

ACS Applied Materials and Interfaces

Abstract

Direct pyrolysis of coronene at 800 °C produces low surface area, nanocrystalline graphitic carbon containing a uniquely high content of a class of lithium binding sites referred to herein as “hydrogen-type” sites. Correspondingly, this material exhibits a distinct redox couple under electrochemical lithiation that is characterized as intermediate-strength, capacitive lithium binding, centered at ~ 0.5 V vs. Li/Li⁺. Lithiation of hydrogen-type sites is reversible and electrochemically distinct from capacitive lithium adsorption and from intercalation type binding between graphitic layers. Hydrogen-type site lithiation can be fully retained even up to ultrafast current rates (e.g., 15 A g⁻¹, ~ 40 C) where intercalation is severely hampered by ion desolvation kinetics; at the same time, the bulk nature of these sites does not require a large surface area and only minimal electrolyte decomposition occurs during the first charge/discharge cycle, making coronene-derived carbon an exceptional candidate for high-energy density battery applications.

Introduction

Graphite remains the de facto anode material for lithium-ion batteries (LIBs) since it was introduced into the commercial market in the 1990s,^{1,2} favored for its low operating potential of ~ 0.1 V vs. Li/Li⁺, high reversible capacity (LiC₆, 372 mAh g⁻¹), and admirable safety compared to metallic lithium.³⁻⁵ However, the demands of next generation LIBs require faster charging than is accessible to the intercalation chemistry native to graphite-based LIB anodes.⁶ At charging rates above 1 C (i.e., a 60 min charging time), the reversible capacity of crystalline graphite is precipitously reduced owing to sluggish desolvation kinetics of lithium from within standard liquid carbonate electrolytes at the surface of the graphite anode.⁷⁻¹¹ Recent work has shown that the rate capability is correlated with specific properties of the chosen type of graphite, including such properties as crystallite size, particle size, and content and type of lattice imperfections; reasonable capacity can be retained in high-performance variants up to roughly 4 C (i.e., a 15 min charging time) but requires a precisely tuned, anode-limited full-cell.¹² Other methods have been shown to elevate the rate capability of graphite through modification strategies such as laser patterning and nanosizing, increasing the complexity of electrode fabrication.¹³⁻¹⁶ On the other hand, high surface area porous carbon materials can effectively store lithium under ultrafast charging rates via the capacitive adsorption of ions and formation of an electric double-layer at their surfaces.¹⁷ The reversible capacity of these materials increases with surface area to far higher than 372 mAh g⁻¹;¹⁸⁻²⁰ however, due to decomposition of electrolyte and the resulting formation of solid electrolyte interphase (SEI) on all exposed surfaces of the electrode, a massive irreversible consumption of electrolyte occurs during the first cycle in standard Li-ion electrolytes, prohibitive to their use in commercial battery applications.²¹

Dahn and coworkers have noted a third type of lithium interaction within carbonaceous materials containing a significant amount of hydrogen.^{22,18} This type of binding is categorized as distinct from strongly bound intercalation and weakly bound capacitive ion adsorption. A distinct charge storage mechanism was surmised to result, via charge transfer between lithium guests and hydrogen terminations at edges in the carbon structure: i.e., the formation of dative covalent bonds.²² Hence, this type of charge storage would be expected to be faradaic but was not definitively characterized. The general effect of hydrogen content on lithium uptake was explored in detail by Dahn and coworkers by lithiation of the pyrolysis products of petroleum pitches, polyvinyl chloride, and polyvinylidene fluoride between 550-1000 °C.²³ These experiments exhaustively supported an increasing reversible lithiation capacity with increasing hydrogen content, and further evidenced atomistic rearrangement of the edge-site carbon upon lithiation/delithiation, as observed by a large voltage hysteresis between the charge and discharge profiles. Interestingly, little more remains understood, even over 20 years later, about the specific atomistic mechanism associated with this type of lithium binding. A hurdle in characterizing any kind of lithiation site or charge storage mechanism lies in obtaining a material which exhibits that site or mechanism in abundance; the work presented herein reveals that coronene-derived carbon pyrolyzed at 800 °C is such a material for hydrogen-type lithiation sites.

Results and Discussion

In this work, we hypothesized that the partial pyrolysis of a large polyaromatic hydrocarbon (PAH) precursor would result in the synthesis of a low surface area, nanocrystalline graphitic carbon containing a high content of confined hydrogen edge sites between adjacent

precursor molecules. A series of PAHs (benzene, naphthalene, pyrene, and coronene) were explored to determine the effects of precursor size and hydrogen content on the structure and composition of the pyrolysis product, and especially on its number and type of lithiation sites available for electrochemical ion storage. The model compound for further in-depth study was obtained via the pyrolysis of neat coronene ($C_{24}H_{12}$) under closed conditions at 800 °C, the product of which is referred to herein as Cor800. While coronene exhibits the lowest initial hydrogen content of all PAHs explored herein, its large size encourages a significant role for precursor stacking prior to and during pyrolysis and reduces the likelihood of perfect tiling of the 2D graphitic plane. Interestingly, upon electrochemical lithiation, a distinct type of lithiation site was observed in high quantity in Cor800 that cannot be classified as either faradaic intercalation within the graphitic layers or as capacitive formation of an electric double layer at the particle surfaces. This was confirmed by systematic comparison with several benchmark types of carbonaceous electrode materials with well-resolved carbon structures: crystalline graphite (AG20) with almost exclusively interlayer-type lithiation sites, high surface-area zeolite-templated carbon (ZTC) with exclusively surface-type lithiation sites, and a standard hard carbon (Super P) that exhibits (widely-spaced) interlayer sites as well as a significant content of surface sites. Scanning electron micrographs of Cor800 and the three benchmark materials of comparison are shown in Figure 1 as indicative of their complementary structure and composition; proposed atomistic depictions of the same materials are shown in the Supporting Information. The novel sites in Cor800, referred to hereafter as “hydrogen-type” sites, were thoroughly characterized using a suite of electrochemical techniques and could still be lithiated reversibly even at ultrafast charging rates up to 40 C (corresponding to a 90 s charging time).

The structure of Cor800 was first investigated using powder X-ray diffraction (XRD) and Raman spectroscopy, for comparison to the three benchmark standards (Figure 1c and 1f). Cor800 exhibits a broad peak indexed as the (002) reflection of the AB-stacked graphite unit cell, corresponding to an interlayer spacing (d_{002}) of 3.42 Å and an average crystallite size along the c-axis (L_c) of 22 Å, ~6 graphitic layers. This contrasts with the XRD pattern of AG20 which exhibits a narrow (002) reflection corresponding to a d_{002} of 3.35 Å and an average L_c of 314 Å (~94 graphitic layers). AG20 is therefore a far more crystalline graphite than Cor800, though its small particle size of 15.2 ± 3.5 µm permits a relatively high-rate capability toward lithiation in standard carbonate electrolytes.¹² Super P, a commercial hard carbon, also shows a weak (002) reflection corresponding to an expanded graphitic structure with a d_{002} spacing of 3.54 Å and an L_c of 21 Å (~6 graphitic layers). The final comparison material, ZTC, is a unique, highly porous carbonaceous framework solid with no (002) peak related to graphitic stacking.²⁴ The long-range order present in the atomistic structure of ZTC originates from the original faujasite (FAU) template; the XRD pattern exhibits an intense (111) reflection at 6.4°, corresponding to a pore-to-pore d-spacing of 14.1 Å and a coherence length of 284 Å (~20 pore-to-pore repeats). Hence, ZTC is a model material for purely capacitive lithium storage since its unique chemical vapor deposition (CVD) synthesis within a microporous zeolite template gives rise to a material that, when templated effectively, cannot have any significant graphitic stacking (all parts of the carbon network are double-sided graphene ribbon fragments).²⁵

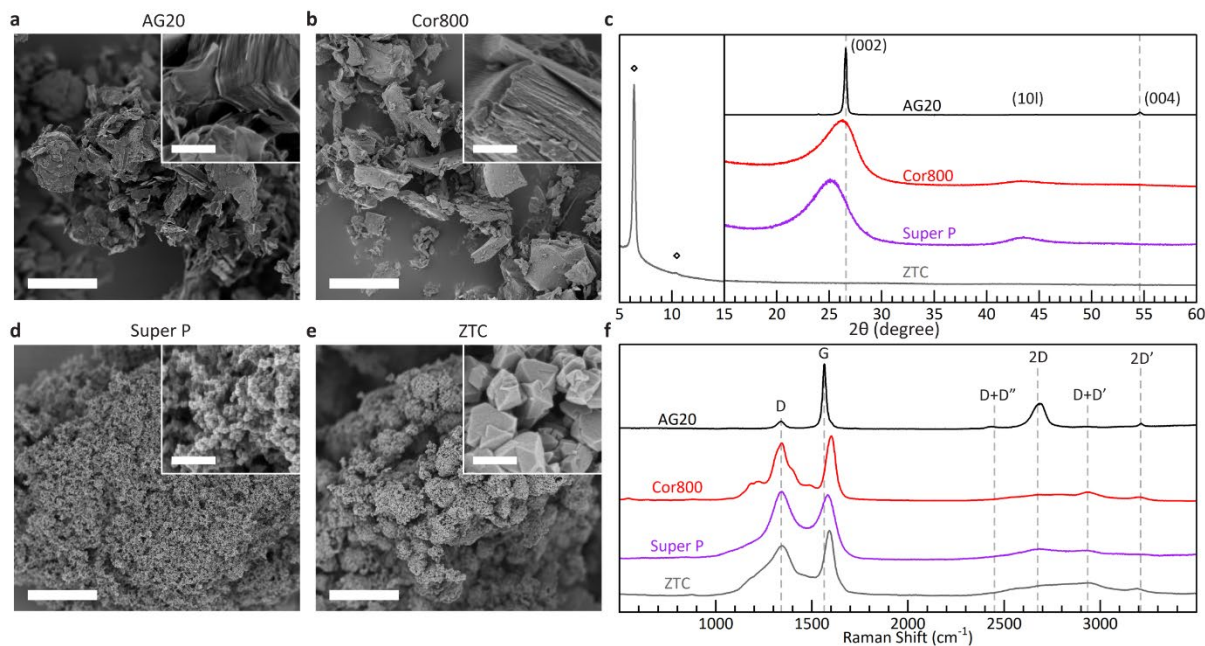


Figure 1. Representative SEM images of (a) graphite (AG20), (b) graphitic carbon with hydrogen-type sites (Cor800), (d) hard carbon (Super P), and (e) ordered porous carbon with no stacking (ZTC). The main image in each panel shows a 20 μm scale bar, and the inset shows a 500 nm scale bar. (c) XRD patterns of AG20, Cor800, Super P, and ZTC with the graphite (002) and (004) reflections indicated as dashed gray lines. The (111) and (220) reflections characteristic of the cubic pore-to-pore ordering in ZTC are indicated with open diamonds. (f) Raman spectra of AG20, Cor800, Super P, and ZTC, collected using a 532 nm excitation source.

Raman spectroscopy reveals additional information about the complementary structural features of Cor800 as compared to AG20, Super P, and ZTC, as shown in Figure 1f. All four materials exhibit the usual features of the in-plane structure associated with graphite/graphene (the regime shown relates exclusively to in-plane phonons): the G and D modes, and their overtones and other defect-induced features.^{26,27} The Raman spectrum of Cor800 exhibits a prominent G mode that is seemingly shifted to higher frequency (1600 cm^{-1}) than that of crystalline graphite (1564 cm^{-1}), indicating the significant presence of the defect induced D' mode (typically found between $1700\text{--}1840\text{ cm}^{-1}$), not the actual change in frequency of G. This specifically signals the presence of electron hole scattering sites in Cor800, which can also be seen in Super P and ZTC.

While Cor800, Super P, and ZTC all exhibit a broad D mode, Cor800 exhibits some unique identifiable features on both shoulders of the D mode. The two features on the low-frequency shoulder at 1182 cm^{-1} and 1285 cm^{-1} correspond to C–H bending modes of armchair and zigzag edges, respectively. The two features on the high frequency shoulder of the D mode at 1395 cm^{-1} and 1462 cm^{-1} correspond to 5,6-ring carbon stretching modes that result from the fusion of coronene molecules during pyrolysis.²⁸ Thus, Cor800 contains a significant amount of C–H edge character within the crystallites and highly imperfect in-plane bonding. As evidenced by N_2 adsorption studies at 77 K, Cor800 has a low surface area of only $\sim 4\text{ m}^2\text{ g}^{-1}$. However, it also has an exceptionally high content of hydrogen as quantified by combustion analysis (roughly 1 hydrogen per 5 carbon atoms); these results are summarized and compared to the three standard materials in Table 1. Hydrogen content is directly correlated with edge sites, a feature that usually gives rise to a higher N_2 -accessible surface area. Together with XRD and Raman analysis, this body of evidence reveals a unique, internal content of hydrogen terminations that is buried within the defected graphitic structure of Cor800. In contrast, the D mode of graphite is minimal (as expected for highly crystalline graphite) and that for Super P is expressed as a single peak indicating low hydrogen content and minimal edge character. The D mode of ZTC is broad and exhibits a modulated low frequency shoulder indicating a mixture of armchair and zigzag edges terminating the network of graphene ribbon-like blades. As expected, the hydrogen content of the three standard materials scales with the N_2 -accessible surface area (Table 1) indicating that their H-terminations are on “outer surfaces,” typical of graphitic and porous carbons. Table 1. Structural properties of Cor800 and three standard materials of comparison, as determined using XRD, Raman spectroscopy, N_2 adsorption at 77 K, combustion analysis, and electrochemical lithiation.

Table 1. Structural properties of Cor800 and three standard materials of comparison, as determined using XRD, Raman spectroscopy, N₂ adsorption at 77 K, combustion analysis, and electrochemical lithiation.

	XRD			Raman Spectroscopy		N ₂ Adsorption	Combustion Analysis	Electrochemical Lithiation
	d ₀₀₂ (Å)	L _c (Å)	L _a (Å)	Pos(G) (cm ⁻¹)	FWHM(G) (cm ⁻¹)	BET SA (m ² g ⁻¹)	H:C (molar ratio)	Total Li Capacity* (mAh g ⁻¹)
Cor800	3.42	22	18	1600	53	4	0.20	297
AG20	3.35	314	43	1564	20	9	0.00	320
ZTC	-	-	-	1592	60	3330	0.20	255
Super P	3.54	21	41	1583	103	59	0.01	265

* - reversible low-rate (25 mA g⁻¹) GCD capacity, measured as the average of the 15th-20th delithiation cycle

The lithiation of Cor800 was investigated by performing a series of electrochemical experiments in half-cell configuration against lithium metal, in the presence of a standard carbonate-based electrolyte (see the Supporting Information for details). First, cyclic voltammetry (CV) at a low scan rate (0.1 mV s⁻¹) was used to deduce the number and type of lithiation mechanism(s) within Cor800 between 0.01-1.5 V vs. Li/Li⁺, by reference to identical experiments using the three standard materials (Figure 2, dark purple traces). Similarly to Super P, a portion of the lithiation of Cor800 proceeds by wide-interlayer intercalation, as evidenced by a broad oxidation peak upon delithiation at 0.2 V vs. Li/Li⁺. Unlike in graphite (which shows numerous intercalation features associated with staging)²⁹ this peak is expressed as a broad, single peak in both Cor800 and Super P, and the corresponding reduction peak in both cases is an intense, asymmetric feature at close to the cutoff voltage of 0.01 V vs. Li/Li⁺. As expected, no such intercalation features exist for ZTC; instead, a box-like profile is observed as is typical for purely capacitive electrode materials (Super P too shows a constant current background associated with the formation of a modest electric double layer on its surface area of 60 m² g⁻¹). However, interestingly, a prominent redox couple is also observed in the profile of Cor800 at around 0.5 V

vs. Li/Li^+ that is not observed in any of the standard materials used herein, nor in any other materials in the reported literature. We attribute this feature to the lithiation/delithiation of hydrogen-type sites within the bulk graphitic structure of Cor800. This is consistent with the adsorption/desorption of lithium in $\text{Li}\cdots\text{H}-\text{C}$ environments at zigzag edges, predicted to occur at between 0.49-0.66 V.³⁰

To explore the relative rates of lithiation of the three above-identified environments, CV was performed at a wide range of scan rates from 0.1-15 mV s^{-1} (select profiles shown in Figure 2a-2d). While the features associated with intercalation broadened significantly and then disappeared as scan rate increased, the box-like profile owing to capacitive lithiation (in Super P and ZTC) and the lithiation event attributed to hydrogen-type sites persisted to extremely high scan rates. The scan rate dependences of these features are summarized in Figure 2e-2h. Randles-Ševčík (R-S) analysis was then performed to determine the extent of diffusion limitation associated with each type of lithiation mechanism.³¹⁻³³ As expected, the staging phenomena associated with intercalation of highly crystalline AG20 (labeled as O1 to O3-4 for the oxidative peaks and R3-4 for the reductive peaks, where the number indicates the stage of intercalation/deintercalation) exhibit a scan rate dependence characteristic of a faradaic charge transfer event (with an R-S slope of ~ 0.5 across the entire range of scan rates).³¹ All other lithiation events were found to exhibit capacitive or pseudocapacitive lithium binding, with R-S slopes significantly greater than 0.5 and approaching 1 at low scan rates. The redox couple associated with intercalation in Cor800 (labeled as O-I and R-I for oxidation and reduction, respectively) persists with an R-S slope of ~ 1 up to a scan rate of 1 mV s^{-1} (corresponding to a charge rate of ~ 2 C), a similar fate as low-stage intercalation in AG20. Beyond 2 C, the CV profile of Cor800 is dominated by the hydrogen-type

interaction which persists until the ultrafast scan rate of 15 mV s^{-1} ($\sim 40 \text{ C}$), and yields an R-S slope of ~ 1 between $0.1\text{-}1 \text{ mV s}^{-1}$, indicating that there are no diffusion limitations to charge transfer or pseudocapacitance in this process.³³ As the scan rate rises above 1 mV s^{-1} , desolvation becomes a limiting factor for lithiation of the hydrogen-type sites, and the R-S slope significantly decreases (its value is no longer meaningful in this region³¹). This analysis reveals that lithium-binding on hydrogen-type sites is likely based on a rapid redox mechanism referred to as pseudocapacitance.³⁴

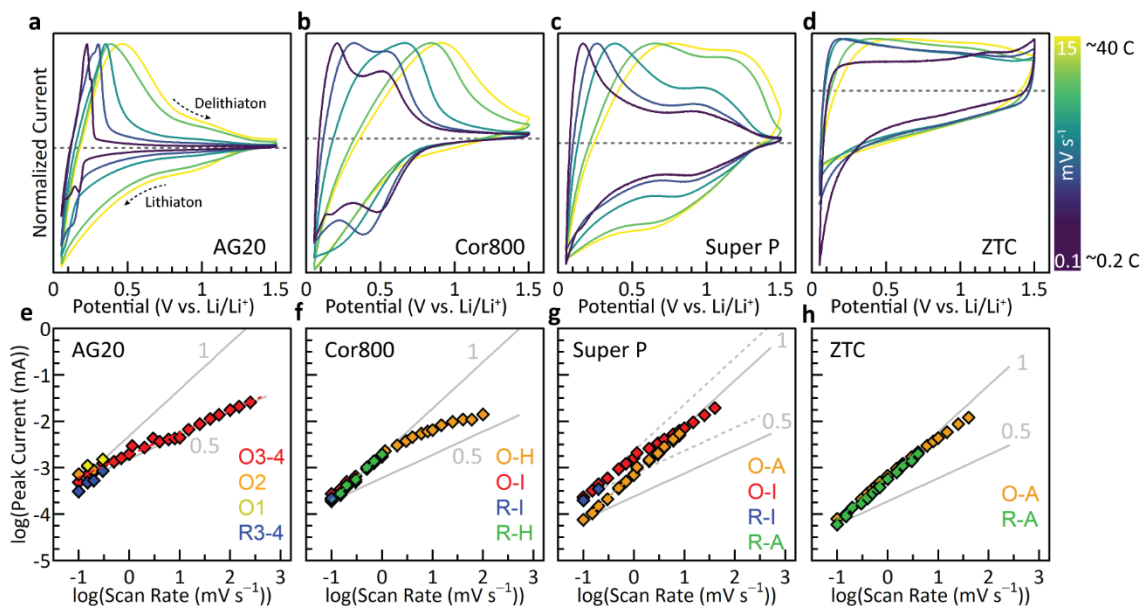


Figure 2. CV analysis of (a,e) AG20, (b,f) Cor800, (c,g) Super P, and (d,h) ZTC at scan rates between $0.1\text{-}15 \text{ mV s}^{-1}$. (a-d) Select CV profiles and (e-h) R-S analysis showing the presence of numerous lithiation environments: reductive stage 3-4 intercalation (R3-4), wide interlayer intercalation (R-I), hydrogen-type site binding (R-H), and adsorption (R-A), and oxidative stage 1, 2, or 3-4 intercalation (O1, O2, and O3-4), wide interlayer intercalation (O-I), hydrogen-type site binding (O-H), and adsorption (O-A).

To best quantify the total lithiation capacity of Cor800, galvanostatic charge/discharge (GCD) cycling was performed between $0.01\text{-}1.5 \text{ V vs. Li/Li}^+$, as shown in Figure 3. The reversible GCD profile of Cor800 at low rate ($\sim 0.1 \text{ C}$, Figure 3a) shows a similar (negligible) lithiation capacity to AG20 between $1.5\text{-}0.75 \text{ V vs. Li/Li}^+$; an indistinct plateau centered at $\sim 0.5 \text{ V vs. Li/Li}^+$

(attributable to hydrogen-type sites) is observed in Cor800, followed by a sloping feature prior to reaching the voltage cutoff, exhibiting a total specific capacity of 300 mAh g⁻¹. A mild voltage hysteresis between charge and discharge is observed, indicating an overpotential associated with the hydrogen-type and wide interlayer intercalation mechanisms. The magnitude of hysteresis in Cor800 is intermediate between Super P (exhibiting a mild hysteresis) and ZTC (exhibiting a large hysteresis), and not as large as that of high H-content materials reported by Dahn et al.²³ Despite that obvious plateaus are not observed for Cor800 under GCD at low-rate conditions, the GCD profile is generally consistent with the CV profiles shown in Figure 2 and remains unique compared to the three reference materials herein.

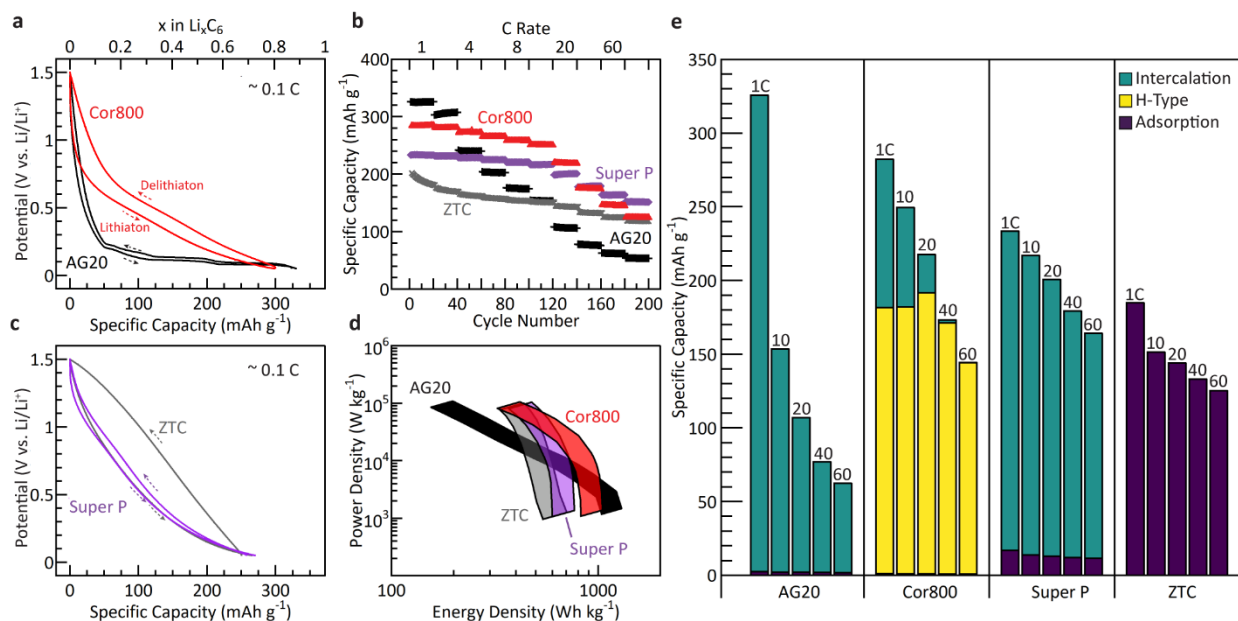


Figure 3. (a, c) Reversible GCD profiles of (a) AG20 and Cor800, and (c) Super P and ZTC at 25 mA g⁻¹ (~0.1 C). (b) Cycling stability and rate capability of all materials at current rates between 0.4-30 A g⁻¹ (~1-80 C, as shown). (d) Materials-specific Ragone plot assuming use of an anode against a range of standard cathodes (see Supporting Information for details). (e) Allocation of reversible charge storage capacity in all materials as per the type of lithiation environment (indicated by color) as a function of charging rate at select rates of 1 C, 10 C, 20 C, 40 C, and 60 C (indicated above each bar).

The effect of charging rate on capacity retention was then assessed via GCD cycling at increasing rates between 0.4-30 A g⁻¹ (~ 0.1-80 C), as shown in Figure 3b. A constant current constant voltage (CCCV) charging protocol was employed at each step in the protocol to ensure that all materials were fairly compared (i.e., the total charging time was held to be the same regardless of performance during the CC phase). These results show, as expected, that while AG20 exhibits the highest capacity at low charging rates, its capacity diminishes significantly at >2 C.¹² Unlike graphite, Cor800 exhibits high capacity retention up to ~10 C, much more akin to Super P and ZTC, both of which benefit from an abundance of surface sites available for capacitive adsorption (which Cor800 does not exhibit). The capacity of Cor800 is the highest among the materials explored herein (under a non-optimized set of cell fabrication conditions, but in an apples-to-apples comparison) until the ultrafast current rate of 60 C is exceeded. The same GCD cycling data are reconfigured as a materials-specific Ragone plot in Figure 3d. To convert the average electrochemical potential during discharge to an energy, an estimate of full-cell voltage was made via pairing with a standard cathode material (assuming an average cathode potential of 4.2 or 3.4 V vs. Li/Li⁺, respectively). The power density was determined according to the CCCV charging time; further details are provided in the Supporting Information. As noted above, AG20 exhibits the highest energy density and is best suited to low power density applications. Meanwhile, Super P and ZTC show the expected behavior of capacitive materials with nearly constant energy density within the range of power densities explored (up to 100 kW kg⁻¹, per mass of active material only). On the other hand, Cor800 exhibits a high energy density even at relatively high-power densities up to ~10 kW kg⁻¹. The relatively high energy density is attributable to the

large number of hydrogen-type sites, while the high-power density is facilitated by only nanoscale crystallinity and the presence of significantly wider interlayer spacing.

In order to decouple the storage mechanisms responsible for the observed reversible capacities of AG20, Cor800, Super P, and ZTC at current rates between 1-60 C, we made a series of reasonable approximations culminating in Figure 3e. The total (GCD-derived) discharge capacity at each rate was assessed as a combination of three mechanism types: intercalation (including staging and wide interlayer types), hydrogen-type interactions, and surface adsorption. The surface adsorption capacity was assessed on the basis of the N₂-accessible surface area of each material and calibrated at each rate according to ZTC. The remaining two mechanisms were distinguished by integration of the CV oxidation profiles (at a scan rate comparable to the given GCD current rate) under two peaks, one for the low-voltage intercalation feature and one for the hydrogen-type feature at ~0.5 V vs Li/Li⁺. Further details related to the estimation of the site type distributions shown in Figure 3e are given in the Supporting Information. From this analysis, two summarizing discoveries about Cor800 are clear: its reversible lithiation capacity cannot be explained by its surface area alone (as shown by the low contribution to capacity from surface adsorption) and that the novel hydrogen-type feature unique to Cor800 persists up to extremely fast lithiation/delithiation rates, even continuing to dominate the overall charge storage mechanism at 60 C. The content of H-type sites in Cor800, almost constant up to 40 C, corresponds to a lithium storage density of ~6.7 mmol g⁻¹ or a stoichiometry of roughly LiH_{2.4}C₁₂. This remarkable capacity of high-power sites is highly relevant for next-generation LIBs since, unlike for the dominantly capacitive materials such as Super P and ZTC, Cor800 exhibits a relatively high first-cycle Coulombic efficiency of 55% and therefore low irreversible capacity loss that is often prohibitive

for high-rate carbon materials. This fact is consistent with our proposed description of Cor800 containing an abundance of internal “hydrogen-type” sites within its bulk that are inaccessible to solvent but still readily lithiable up to ultrahigh current rates. We further propose that the predominance of such sites can be attributed to the imperfect tiling of the 2D plane by the large coronene precursor used to derive Cor800, leading to the formation of pockets where lithium could be trapped in a confined state between H-terminations, a feature not observed in equivalent materials derived from smaller PAHs (see Supporting Information). This lends a rich series of testable hypotheses that can guide future research into the use of PAHs of varying shape and symmetry toward further optimization of the content and characteristic potential of lithiation of H-type sites.

Conclusions

A novel type of lithiation mechanism of carbon materials has been observed and thoroughly characterized for a coronene-derived graphitic carbon material pyrolyzed at 800 °C referred to herein as Cor800. This material is graphitic in nature and exhibits a low surface area akin to graphite. However, it also contains a high content of hydrogen in its elemental composition, implying an extensive edge character embedded within the bulk of the material (not accessible to the N₂ surface area analysis probe). The unique combination of wide interlayer graphitic stacking and internal hydrogen-type sites allows for rapid insertion and de-insertion of lithium at current rates up to 60 C (1 min charging time) with excellent reversibility and stability at ~0.5 V vs. Li/Li⁺. The buried nature of these lithiation sites renders them protected from solvent during the first cycle lithiation, resulting in minimal SEI formation and therefore promising technological relevance.

Whether such hydrogen-type sites can also be sodiated or potassiated in a similar way remains unknown and will be the focus of future work.³⁵

Experimental Section

Materials Synthesis

Cor800 was synthesized by the direct pyrolysis of coronene (Acros Organics, 95%) under inert conditions at 800 °C. ZTC was synthesized via a two-step method, where dry NaY zeolite template (4 g, HSZ 320NAA, Tosoh Corp.) was first impregnated with liquid furfuryl alcohol (FA, 99%, Aldrich) and polymerized at 80 °C, followed by deposition of carbon by flowing 7 mol% propylene in argon (99.99% propylene in 99.999% argon) at 700 °C; finally, the product was annealed at 900 °C. The zeolite template was then removed by dissolution in aqueous hydrofluoric acid (HF, 48-51%, Thermo Scientific) and the product dried in air at 40 °C. Further synthetic details on PAH pyrolysis and ZTC synthesis can be found in the Supporting Information.

Commercial Reference Materials

Two commercially available reference materials were investigated in this study: AG20, a type of artificial graphite (synthetic graphite 282863, nominal particle size: <20 µm, Sigma-Aldrich) and Super P, a type of hard carbon commonly used as a conductive additive (supplied by Timcal Ltd.).

Materials Characterization

Powder XRD diffraction patterns were obtained from hand ground samples using a powder diffractometer (D8 ADVANCE, Bruker) in reflection geometry, equipped with a Cu K $\alpha_{1,2}$ radiation source ($\lambda = 1.54 \text{ \AA}$). Raman spectra were measured with a Raman spectrometer

(LabRAM HR Evolution, Horiba Scientific Ltd.) equipped with a confocal microscope and a 532 nm (2.33 eV) frequency-doubled Nd:YAG laser operating at 45 mW. Scanning electron microscopy (SEM) of the as-synthesized materials was performed using a field emission scanning electron microscope (SUPRA 55VP, ZEISS Group) operating at 1 kV with a working distance of <5 mm. Samples were prepared by mounting onto conductive carbon tape. Surface area was determined via N₂ adsorption measurements performed using a volumetric Sieverts apparatus (3Flex, Micromeritics Corp.) at ~77 K; the data were fitted to a Brunauer-Emmett-Teller (BET) model following standard consistency criteria to yield the BET surface area (BET SA). Elemental analysis was determined by flame combustion (Atlantic Microlab, Inc.). Extensive experimental details as well as data analysis methods for XRD, Raman spectroscopy, N₂ adsorption, and elemental analysis can be found in the Supporting Information.

Electrochemical Characterization

Working electrodes were cast onto copper foil from a slurry containing 80 wt.% active material, 10 wt.% Super P as the conductive additive, and 10 wt.% polyvinylidene fluoride (PVDF) as the binder. The active mass loading was 1.2-1.6 mg cm⁻². Lithium half-cells were then assembled under inert argon conditions, comprising a lithium metal chip (MTI Corp.) as the counter/reference electrode, a glass microfiber separator (GF/D grade, catalogue number 1823–257, Whatman), and a working electrode (∅ 10 mm) within a coin-type cell (316 stainless steel, size 2032, Xiamen AOT Electronics Technology Co.). Prior to sealing, the cell was charged with 125 μL of 1.2 M lithium hexafluorophosphate (LiPF₆) in a 3:7 by weight mixture of ethylene carbonate and ethyl methyl carbonate (with 2 wt.% fluoroethylene carbonate additive) as the electrolyte. GCD profiles were measured using a battery cycler (CT30001A, Landt Instruments).

CV was performed on fresh cells using a potentiostat (VersaSTAT 4-450, Princeton Applied Research). Further details can be found in the Supporting Information.

Associated Content

Acknowledgments

We are very grateful to Harish Banda for insightful discussions. We also thank Erin Taylor for synthesis of the ZTC and Dalton Compton for performing the N₂ adsorption experiments. Funding for this work was provided by the DEVCOM Army Research Laboratory (ARL) under cooperative agreement (W911NF-20-2-0284). We also thank the Center for Biofilm Engineering Imaging Facility for use of their instrumentation, which is supported by funding from the National Science Foundation (DBI-1726561) and the M. J. Murdock Charitable Trust (SR-2017331).

Supporting Information

Direct Synthesis of PAH-Derived Carbons: The primary materials investigated in the present work were synthesized by the pyrolysis of benzene (Sigma-Aldrich, anhydrous 99.8%), naphthalene (Acros Organics, 99+%), pyrene (Acros Organics, 98%), or coronene (Acros Organics, 95%) under inert conditions at 800 °C to produce Ben800, Nap800, Pyr800, and Cor800, respectively. A typical synthesis of Cor800 was performed by adding 420 mg of coronene to a 30 mL quartz ampule within an argon-filled glovebox (<0.5 ppm O₂, <0.5 ppm H₂O). The ampule was then temporarily sealed with a custom Swagelok Ultra-Torr Schlenk line adapter and removed from the glovebox. At this point the ampule contents were frozen by immersing the ampule in liquid nitrogen and evacuation to 10⁻³ mbar within 30 s. In this state the ampule was flame-sealed with an oxyhydrogen torch. The sealed ampule was then placed in the center of a chamber furnace

(RWF 12/13, Carbolite Gero Ltd.) and heated to 800 °C via a 1 °C min⁻¹ ramp. The set temperature was held for 1 h and then allowed to gradually cool to ambient temperature. The ampule was scored with a diamond-bladed saw, the outside washed with deionized water and dried, then snapped open within a nitrile rubber enclosure, releasing the overpressure of gaseous byproducts into a fume hood. The material was collected as large, lustrous flakes; the flakes of Ben800 were quite thin and flexible and this transitioned to thicker, almost glassy flakes for Cor800. A portion of each product was hand-ground for 10 min with a mortar and pestle to produce homogeneous powders for XRD and electrochemical characterization.

Synthesis of ZTC: Zeolite-templated carbon (ZTC) was synthesized via a two-step method, where the NaY zeolite template (4 g, HSZ 320NAA, Tosoh Corp.) was degassed in a glass oven (B-585, Büchi) at 300 °C for 24 h under oil-free vacuum ($<2 \times 10^{-3}$ mbar). The dried zeolite was then transferred under inert conditions into a 2-neck round-bottom flask and impregnated with 40 mL of furfuryl alcohol (FA, 99%, Aldrich) via syringe. The mixture was stirred under passive vacuum at room temperature for 24 h, after which the impregnated solid was collected by vacuum filtration in air, washed three times with 10 mL aliquots of mesitylene (97%, Aldrich), and dried under suction on the filter frit for 10 min. The impregnated and washed zeolite was then split equally into two alumina boats (10 × 30 × 107 mm) and inserted into a quartz tube (ø 45 mm) installed in a horizontal furnace (HST 12/600, Carbolite Gero Ltd.). The tube was purged via dry argon flow (200 sccm) at ambient pressure. Polymerization of FA inside the zeolite pores was achieved by heating to 80 °C at 5 °C min⁻¹ under flowing dry argon for 24 h. The poly-FA was then carbonized by heating to 700 °C at 5 °C min⁻¹, after which further carbon introduction was achieved via chemical vapor deposition (CVD) at 700 °C under flowing 7 mol% propylene in

argon (99.99% propylene in 99.999% argon) at 200 sccm. After ambient-pressure CVD for 5 h, the gas flow was returned to dry argon at 200 sccm. An annealing step was performed by heating the zeolite-carbon composite up to 900 °C at 5 °C min⁻¹ and held for an additional 3 h. The system was allowed to cool overnight, the gas flow was stopped, and the zeolite-carbon composite was collected. The zeolite template was removed via three sequential dissolutions in 35 mL of aqueous hydrofluoric acid (HF, 48-51%, Thermo Scientific), followed by centrifugation and three washes with distilled water. The final ZTC product was then dried in air at 40 °C.

Powder XRD: X-ray diffraction (XRD) was performed on the hand-ground samples using a powder diffractometer (D8 ADVANCE, Bruker) in reflection geometry equipped with a Cu K $\alpha_{1,2}$ radiation source ($\lambda = 1.54 \text{ \AA}$). The sample was placed in the 25 mm diameter well of a circular sample holder, and the excess material was removed to produce a level sampling surface. The sample was rotated at 15 rev min⁻¹ and sampled in 0.02° increments for 0.3 s each from 10° to 60°.

Analysis of the as-measured XRD patterns was accomplished by direct subtraction of the background based on an identical experiment performed without any sample. The resulting pattern was then fitted to the combination of a linear background, a single Lorentzian for the (002) reflection, and two Lorentzian functions for the (10l) region comprised of the (100) and (101) reflections of crystalline graphite.

The peak center of the (002) reflection was related to the d-spacing (d) via Bragg's law, Equation 1, and the full-width at half-maxima (FWHM) of the (002) and (10l) reflections were used to estimate the crystallite size along the c and a axes (L_c and L_a , respectively) via the Scherrer equation, Equation 2. The d-spacing and Scherrer size estimates based on the (002) reflection

correspond to c-axis (layer-to-layer) ordering whereas those based on the (10l) reflections correspond to a-axis (in-plane) ordering.³⁶

$$d = \frac{1.54 \text{ \AA}}{2 \sin \theta} \quad (1)$$

$$L = \frac{0.9 (1.54 \text{ \AA})}{(\text{FWHM}) \cos \theta} \quad (2)$$

The FWHM in the Scherrer equation corresponds to the width of the reflection in 2θ expressed in radians.

Raman Spectroscopy: Room temperature measurements were conducted with a Raman spectrometer (LabRAM HR Evolution, Horiba Scientific Ltd.) equipped with a confocal microscope and a 532 nm (2.33 eV) frequency-doubled Nd:YAG laser with an incident power of 45 mW.

The region containing peaks associated to the D and G modes in each Raman spectrum were fitted using a previously established method based on the combination of a Lorentzian and a Breit-Wigner-Fano (BWF) lineshape.^{37,38} The main D peak was fitted to a single Lorentzian and the low frequency shoulder of the D peak was fitted to another Lorentzian to account for hydrogen edge character and denoted as (*C–H). The G peak was fitted to a single BWF, and the baseline was approximated by a linear background, as shown in Figure S1. The combination of two Lorentzian functions and a BWF provided a profile with minimal fitting parameters that could effectively fit the Raman spectrum of the wide range of carbon materials with varying hydrogen content explored in this work. The BWF lineshape is given by:

$$I(\omega) = I_0 \frac{[1 + (\omega - \omega_0/Q\Gamma)]^2}{1 + [(\omega - \omega_0)/\Gamma]^2} \quad (3)$$

Where I_0 is the peak intensity, ω_0 is the peak position, Γ is the FWHM, and Q is the BWF coupling coefficient. A negative Q value tails the BWF toward lower frequency and helps accounts for residual intensity between the D and G peaks. Due to the asymmetry of the BWF lineshape, ω_0 does not lie at the frequency of the peak maximum (ω_{\max}) as in a simple Lorentzian or Gaussian function. To correct for this, the following equation was applied to determine ω_{\max} :

$$\omega_{\max} = \omega_0 + \frac{\Gamma}{2Q} \quad (4)$$

Since Q is negative, ω_{\max} lies at a lower frequency than ω_0 .

FWHM(D) and FWHM(G) were determined based on FWHM of the Lorentzian associated with the D Peak and BWF fits, respectively. Pos(D) was determined based on ω_0 of the Lorentzian associated with the D Peak, and Pos(G) was determined based on ω_{\max} of the BWF associated with the G peak by applying Equation 4.

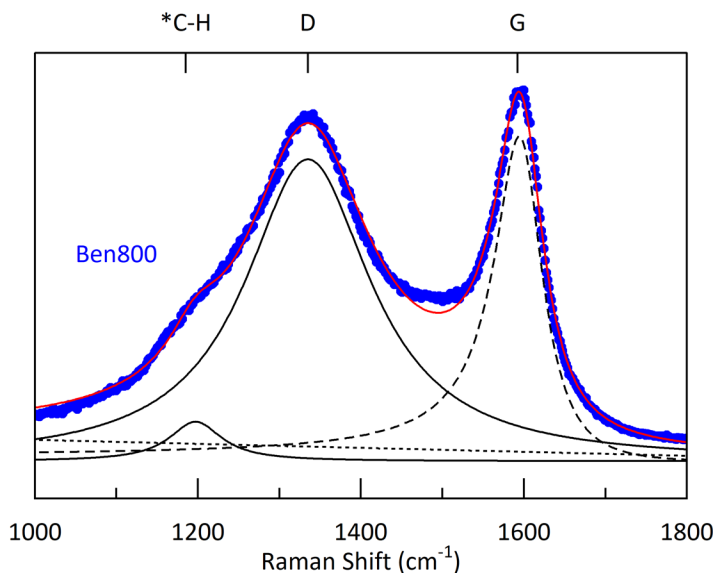


Figure S1. Representative fitting profile for the Raman spectrum of graphitic carbon. One Lorentzian(*C–H) is used to account for hydrogen edge character, a second Lorentzian (D) accounts for the D mode, and a BWF lineshape (G) accounts for the G mode.

Surface Area Measurements: The surface area of each sample was determined by applying Brunauer-Emmett-Teller (BET) analysis to N₂ adsorption equilibria measured using a volumetric apparatus (3Flex, Micromeritics Corp.). In each experiment, 200-300 mg of sample was loaded and degassed at 130 °C for 180 min, and then adsorption and desorption equilibria were measured at liquid nitrogen temperature (~77 K). N₂ adsorption isotherms of AG20, Co800, Super P, and ZTC are shown in Figure S2; the corresponding pore size distributions via non-local density functional theory (NLDFT) methods are shown in Figure S3.

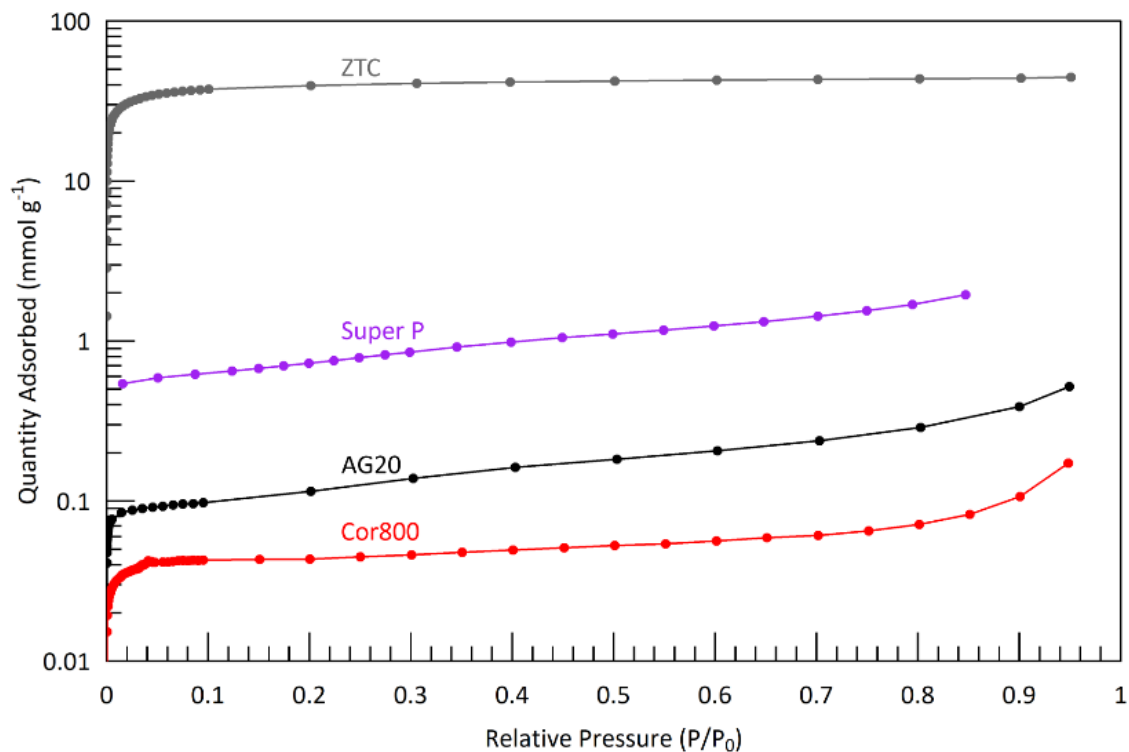


Figure S2. Equilibrium adsorption isotherms of N₂ on ZTC, Super P, AG20, and Cor800 at ~77 K.

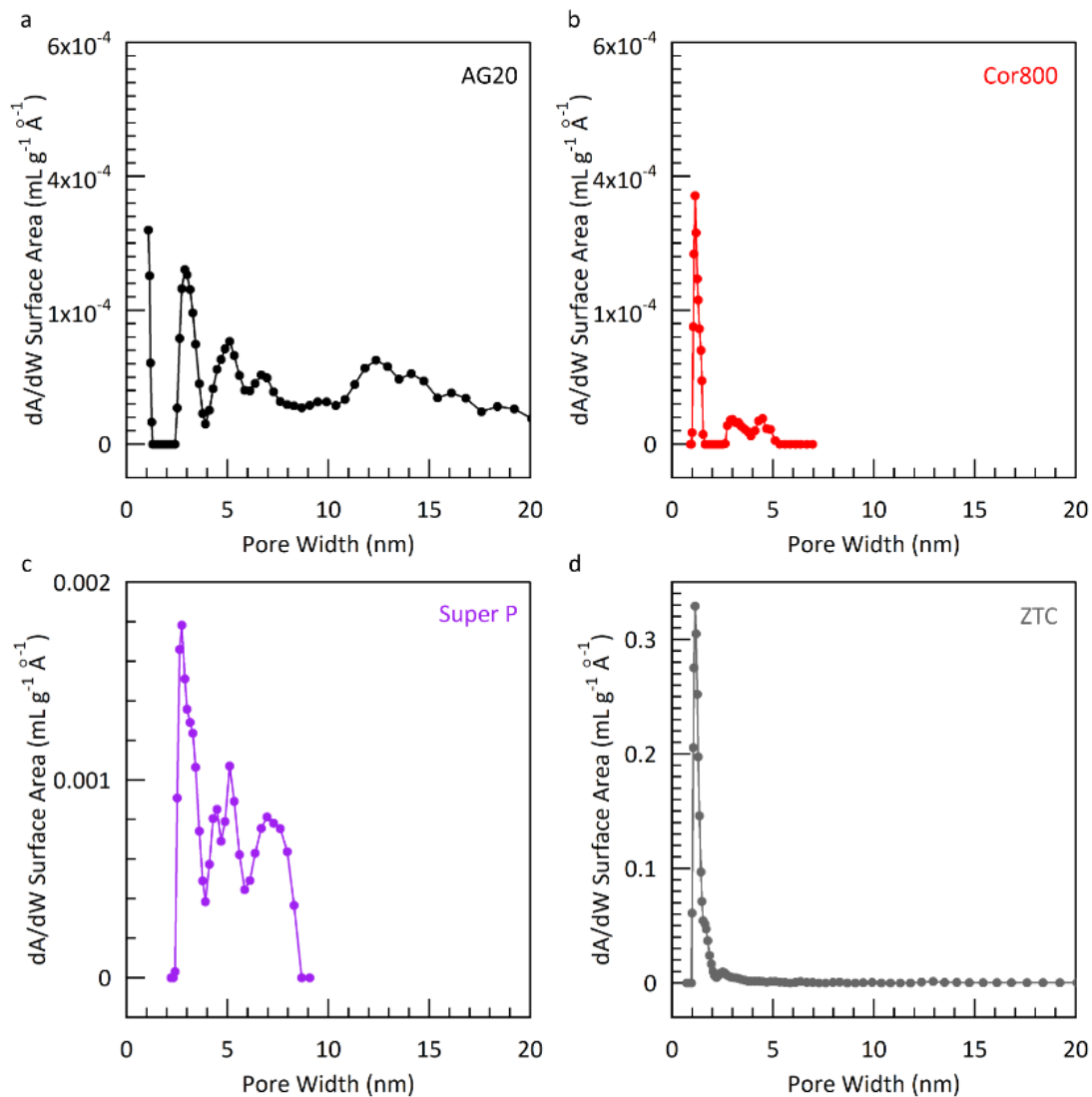


Figure S3. N_2 -accessible pore size distributions of (a) AG20, (b) Cor800, (c) Super P, and (d) ZTC.

Elemental Analysis: The CHO elemental composition of each material was determined in triplicate using flame combustion (Atlantic Microlab, Inc.), and is reported herein as the average and converted to atomic fractions.

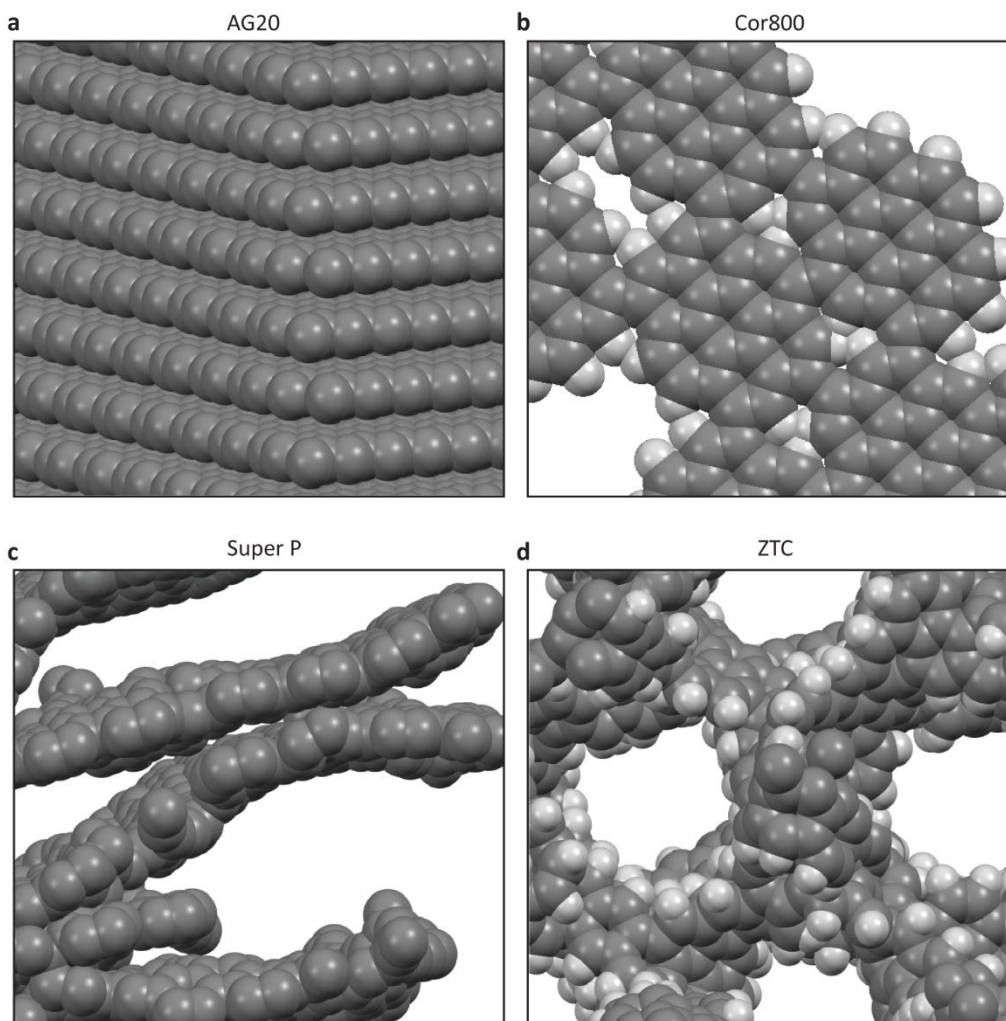
Atomistic Depictions:

Figure S4. Atomistic depictions of (a) graphite (AG20), (b) graphitic carbon with hydrogen-type sites (Cor800), (d) hard carbon (Super P), and (e) ordered porous carbon with no stacking (ZTC).

Electrochemical Characterization: The working electrode slurry was comprised of 80 wt.% active materials, 10 wt.% Super P as a conductive additive, and 10 wt.% polyvinylidene fluoride (PVDF) as a binder, with a total loading mass of $1.5\text{-}2.0\text{ mg cm}^{-2}$ cast onto copper foil; the active mass loading was $1.2\text{-}1.6\text{ mg cm}^{-2}$. The electrode sheet was first dried in a forced-air oven at $80\text{ }^{\circ}\text{C}$ for 12 h and then transferred to a vacuum oven and dried overnight at $100\text{ }^{\circ}\text{C}$ to remove any

moisture and solvent. Coin cells (316 stainless steel, size 2032, Xiamen AOT Electronics Technology Co.) were assembled in an argon-filled glovebox, with a lithium chip used as the counter and reference electrode, and with a glass microfiber separator (GF/D grade, catalogue number 1823–257, Whatman). The electrolyte used was 1.2 M lithium hexafluorophosphate (LiPF₆) in a mixture of ethylene carbonate and ethyl methyl carbonate (EC/EMC, 3:7 by weight) with 2 wt.% fluoroethylene carbonate (FEC) as an additive. Galvanostatic charge and discharge (GCD) profiles were measured using a battery cycler (CT30001A, Landt Instruments) at a constant temperature of 25.0 °C. All cells underwent a conditioning protocol comprising five formation cycles at 0.2 C to establish a stable initial capacity (omitted in Figure 3b). Additional cycles were then carried out at higher current rates (1 C, 2 C, 4 C, 6 C, 8 C, 10 C, 20 C, 40 C, 60 C, and 80 C) to evaluate rapid-charging performance and rate capability. The charge step was performed using a constant current constant voltage (CCCV) protocol wherein a constant current was first applied (according to an idealized capacity of 370 mAh g⁻¹) until the cutoff voltage was reached, and then the voltage was held constant until the total charging time limit was reached (as determined by the desired practical C rate). For example, during a CCCV charge step at 60 C, the cell was first charged at 22.2 A g⁻¹ until the cutoff voltage was reached and then further charged at the cutoff voltage for the remaining time expected in a 60 C charge (taking 1 min total). The discharge step was always performed using a constant current (CC) protocol. The reversible discharge capacity was reported as normalized per mass of active material. Cyclic voltammetry (CV) was performed on separate cells using a dedicated potentiostat (VersaSTAT 4-450, Princeton Applied Research).

Site Type Distribution Calculations: The total electrochemical capacity (Q_{tot}) of each material was assessed as associated with a combination of three types of lithiation sites: capacitive

surface adsorption (Q_A), faradaic interlayer intercalation (Q_I), and H-type sites (Q_H), as shown in Figure 3e. The distribution of these sites within each material was estimated by coupling information gleaned from GCD and CV experiments conducted under equivalent rate conditions. The following equations were used to estimate the contribution from each site type:

$$Q_A(\text{mAh g}^{-1}) = SA(\text{m}^2 \text{g}^{-1}) \times 0.2839 (\text{mAh m}^{-2}) \times F_{\text{rate}} \quad (5)$$

$$Q_I(\text{mAh g}^{-1}) = (Q_{\text{tot}}(\text{mAh g}^{-1}) - Q_A(\text{mAh g}^{-1})) \times \alpha_I \quad (6)$$

$$Q_H(\text{mAh g}^{-1}) = (Q_{\text{tot}}(\text{mAh g}^{-1}) - Q_A(\text{mAh g}^{-1})) \times \alpha_H \quad (7)$$

$$\alpha_I + \alpha_H = 1 \quad (8)$$

In Equation 5, SA is the N_2 -accessible surface area of the material (in $\text{m}^2 \text{g}^{-1}$) and the factor 0.2839 (in mAh m^{-2}) is the theoretical maximum capacity per unit surface area, assuming that a single-sided graphene sheet ($1310 \text{ m}^2 \text{g}^{-1}$) can be lithiated up to 372 mAh g^{-1} (LiC_6). The adsorption capacity fading due to rate (a small but observable effect) is accounted for by F_{rate} , a “fade factor” that is based on the observed capacity fading of ZTC as a function of current rate. In Equations 6 and 7, Q_{tot} is the total reversible discharge capacity of the material in mAh g^{-1} , as determined via GCD analysis at the corresponding rate. The weighting factors α_I and α_H are fractions between 0 and 1 that are determined by integrating the oxidative CV profile of the relevant material (the delithiation scan typically had higher resolution with respect to the different features present) and assigning the total integrated area to two peaks, one for intercalation (at low potentials) and one for H-type sites (at $\sim 0.5 \text{ V}$). The CV scan rate was chosen to be an equivalent overall delithiation rate to that for the corresponding GCD experiment. Note: only the Cor800 was treated by this entire method since Super P and AG20 were assessed as exhibiting only capacitive and intercalative storage ($\alpha_H = 0$), and ZTC was assessed as exhibiting only capacitive storage ($Q_{\text{tot}} = Q_A$).

Energy and Power Calculations: Specific energy and specific power with respect to the active materials investigated herein were used to generate a Ragone plot showing charged power as a function of discharged energy (Figure 3d). Specific energy (E , in Wh kg^{-1}) was determined as:

$$E = Q \times (V_{\text{cat,theo}} - V_{\text{an,avg}}) \quad (9)$$

where Q is the average measured discharge capacity over the last five cycles of a given charging rate step (in mAh g^{-1} , as shown in Figure 3b), $V_{\text{cat,theo}}$ is a fixed theoretical value set herein by the typical (de)lithiation potential of either lithium-iron phosphate (LFP) or nickel-manganese-cobalt oxide (NMC) used as a cathode (4.2 or 3.4 V vs. Li/Li^+ , respectively), and $V_{\text{an,avg}}$ is the average measured half-cell voltage (also averaged over the last five cycles of a given step). The corresponding specific power (P , in W kg^{-1}) was then calculated using:

$$P = I \times (V_{\text{cat,theo}} - V_{\text{an,avg}}) \quad (10)$$

where I is the current rate during the charge step in mA g^{-1} .

It must be stressed that the calculated specific energy and specific power determined in this work are based on the mass of the active material alone and not the mass of a full-cell assembly.

Structural Characterization of PAH-Derived Carbons: XRD patterns of Ben800, Nap800, Pyr800, and Cor800 are shown in a Figure S5a. The XRD patterns of all PAH-derived materials can be indexed to the hexagonal graphite unit cell, with a broad (002) reflection that shifts from $2\theta = 24.9^\circ$ for Ben800 up to 26.2° for Cor800. The FWHM of the (002) reflection of these materials decreases from 6.34° in 2θ for Ben800 down to 3.49° for Cor800. The observed width of these peaks is attributed to Scherrer broadening and the Scherrer crystallite size in the c-axis was determined according to Equation 2. A summary of the structural properties of the PAH-derived

carbons is shown in Table S1. The crystallite size in the c-axis as well as the interlayer distance were found to be correlated to the ring count of the PAH precursor molecule: 1 for benzene, 2 for naphthalene, 4 for pyrene, and 7 for coronene. The correlation between improved crystallinity and PAH ring count is attributed to the significant intermolecular π - π stacking forces present in these planar aromatic molecules. A proxy for assessing the strength of these van der Waals interactions is the melting point of the PAH precursor (e.g., benzene at -5°C and coronene at 412°C , respectively). As a result, larger precursors lead to an enhancement of c-axis stacking and larger crystallites along the c-axis due to the intrinsic π - π stacking strength of the pyrolyzed fragments. A weaker (10l) family of XRD reflections can also be observed at $2\theta = 43^{\circ}$, a convolution of the (100) and (101) reflections of the hexagonal graphite unit cell. This reflection mainly corresponds to ordering along the a-axis of the graphitic unit cell and is found to be relatively unaffected by precursor size.

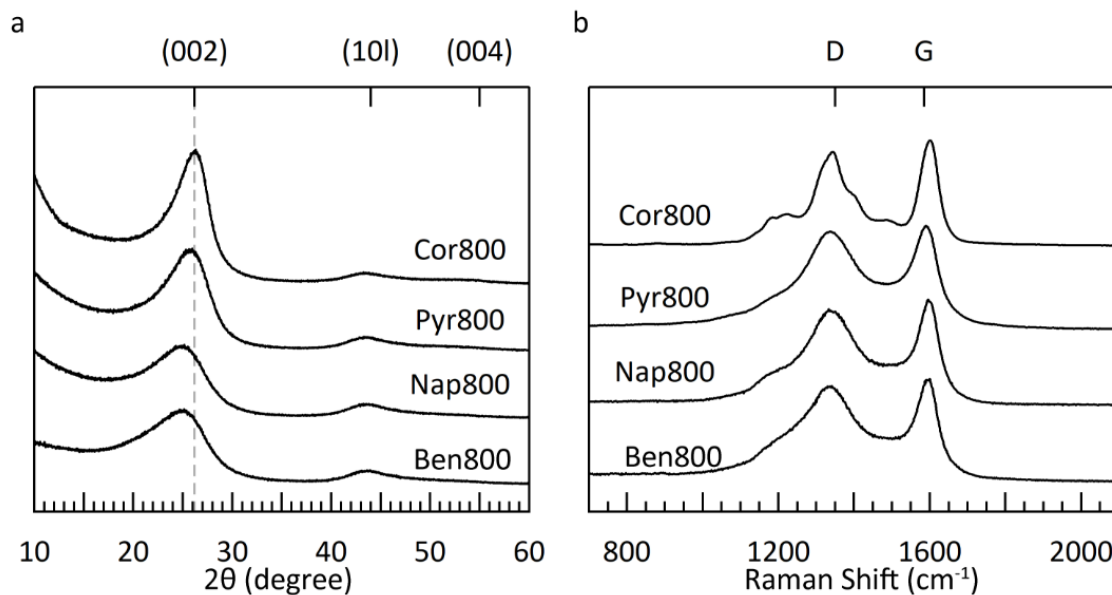


Figure S5. (a) XRD and (b) Raman spectra (collected using a 532 nm excitation source) of Ben800, Nap800, Pyr800, and Cor800.

The Raman spectra of Ben800, Nap800, Pyr800, and Cor800 are shown in Figure S5b. The improved crystallinity achieved with larger precursors observed in XRD is also evident in the Raman spectrum by a narrowing of the G peak. The G mode frequency decreases from 72 cm^{-1} for Ben800 to 53 cm^{-1} for Cor800, corresponding to a more homogeneous distribution of sp^2 carbon environments within the probing region. The narrowing of the G peak with increasing precursor size is evidence for preservation of the C–C bonds within the PAH framework, leading to stronger van der Waals interactions and π - π stacking within the final material.

Table S1. Structural properties of all materials investigated herein, as determined using XRD, Raman spectroscopy, N_2 adsorption at ~ 77 K, combustion analysis, and electrochemical lithiation.

	XRD			Raman Spectroscopy		N_2 Adsorption	Combustion Analysis	Electrochemical Lithiation
	d_{002} (Å)	L_c (Å)	L_a (Å)	Pos(G) (cm^{-1})	FWHM(G) (cm^{-1})	BET SA (m^2g^{-1})	H:C (molar ratio)	Total Li Capacity* (mAh g^{-1})
Ben800	3.58	11	21	1594	72	16	0.11	219
Nap800	3.57	12	20	1597	70	21	0.11	292
Pyr800	3.47	19	20	1590	82	5	0.14	281
Cor800	3.42	22	18	1600	53	4	0.20	297
AG20	3.35	314	43	1564	20	9	0.00	320
ZTC	-	-	-	1592	60	3330	0.20	255
Super P	3.54	21	41	1583	103	59	0.01	265

* - reversible low-rate (25 mA g^{-1}) GCD capacity, measured as the average of the 15th-20th delithiation cycles.

Electrochemical Characterization of PAH-Derived Carbons: Analogous electrochemical characterization to that performed for the primary materials of interest (as shown in Figure 2-3 in the main text) was also carried out for the series of PAH-derived carbons with increasing precursor size from Ben800, Nap800, and Pyr800 to Cor800. Reversible CV scans measured at a scan rate of 0.1 mV s^{-1} (~ 0.2 C) are shown in Figure S6a. An increase in the relative intensity of the turbostratic intercalation event at ~ 0.1 V is observed. This is attributed to the increase in crystallite size and decrease in d_{002} as a result of improved stacking order imparted by the larger precursors.

Interestingly, only Cor800 exhibits the unique redox event present at ~ 0.5 V vs Li/Li⁺, attributed herein as “hydrogen-type” sites. The specific discharge capacity under GCD cycling of each PAH-derived carbon is shown in Figure S6b, as a function of increasing current rate. An increase in reversible capacity as a function of increasing precursor size is observed at all current rates explored in this work.

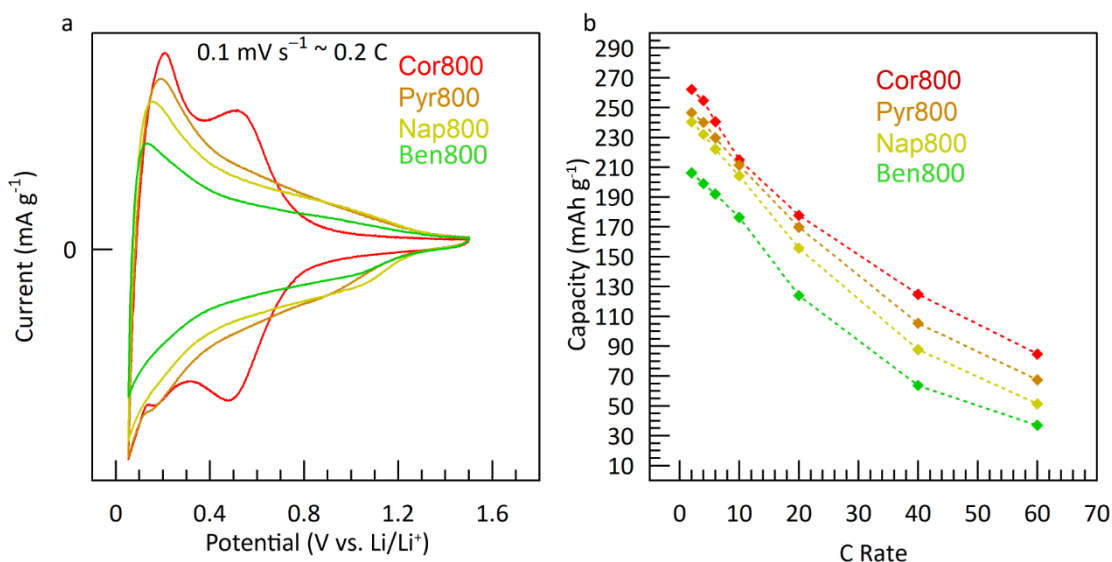


Figure S6. (a) CV profiles (at a 0.1 mV s^{-1} scan rate) and (b) GCD rate capability (between 0.4-30 A g⁻¹ or ~ 1 -60 C) of Ben800, Nap800, Pyr800, and Cor800.

Further Electrochemical Characterization of Primary Materials: The first cycle CV profiles of the four primary materials in this study, AG20, Cor800, ZTC, and Super P; at a scan rate of 0.02 mV s^{-1} are shown in Figure S7a, starting at open-circuit voltage (OCV, ~ 3.4 V vs. Li/Li⁺) and cycling down to 0.05 V, then returning to 0.4 V. The relative magnitude of the solvent-accessible surface area of each material can be observed by noting the total current upon reduction from OCV to 0.05 V. Cor800 shows only negligible current associated with the formation of solid-electrolyte interphase (SEI) during the first cycle, further confirming the confined nature of its “hydrogen-

type” sites. The reversible CV profile of each primary material between 0.05-0.4 V vs. Li/Li⁺ is shown in Figure S7b, at the same scan rate of 0.02 mV s⁻¹. AG20 exhibits distinct redox events that correspond to the formation of staging compounds. All three other materials appear to exhibit similar CV profiles, making it difficult to discern between wide interlayer intercalation and capacitive adsorption in this range.

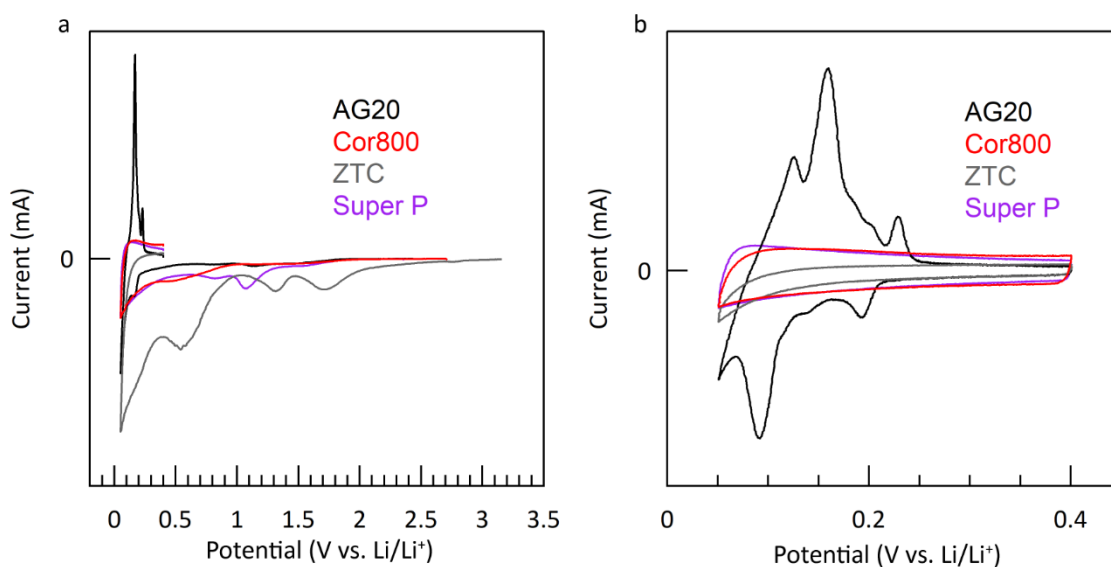


Figure S7. CV profiles (at a 0.02 mV s⁻¹ scan rate) of AG20, Cor800, ZTC, and Super P between 0.05-0.4 V vs. Li/Li⁺ (a) during the first cycle and (b) after extended cycling.

References

- (1) Yoshio, M.; Brodd, R. J.; Kozawa, A. *Lithium-Ion Batteries*; Springer, 2009; Vol. 1.
- (2) Yoshino, A. The Birth of the Lithium-Ion Battery. *Angew. Chem. Int. Ed.* **2012**, *51* (24), 5798–5800.
- (3) Nelson, P. A.; Ahmed, S.; Gallagher, K. G.; Dees, D. W. Modeling the Performance and Cost of Lithium-Ion Batteries for Electric-Drive Vehicles, Third Edition. Electrochemical Energy Storage Theme Chemical Sciences and Engineering Division Argonne National Laboratory **2019**.
- (4) Wu, Y. P.; Jiang, C.; Wan, C.; Holze, R. Modified Natural Graphite as Anode Material for Lithium Ion Batteries. *Journal of Power Sources* **2002**, *111* (2), 329–334.

- (5) von Lüders, C.; Zinth, V.; Erhard, S. V.; Osswald, P. J.; Hofmann, M.; Gilles, R.; Jossen, A. Lithium Plating in Lithium-Ion Batteries Investigated by Voltage Relaxation and in Situ Neutron Diffraction. *Journal of Power Sources* **2017**, *342*, 17–23.
- (6) Kim, D. S.; Kim, Y. E.; Kim, H. Improved Fast Charging Capability of Graphite Anodes via Amorphous Al₂O₃ Coating for High Power Lithium Ion Batteries. *Journal of Power Sources* **2019**, *422*, 18–24.
- (7) Xu, K. Nonaqueous Liquid Electrolytes for Lithium-Based Rechargeable Batteries. *Chem. Rev.* **2004**, *104* (10), 4303–4418.
- (8) Persson, K.; Sethuraman, V. A.; Hardwick, L. J.; Hinuma, Y.; Meng, Y. S.; van der Ven, A.; Srinivasan, V.; Kostecki, R.; Ceder, G. Lithium Diffusion in Graphitic Carbon. *J. Phys. Chem. Lett.* **2010**, *1* (8), 1176–1180.
- (9) Jow, T. R.; Delp, S. A.; Allen, J. L.; Jones, J.-P.; Smart, M. C. Factors Limiting Li⁺ Charge Transfer Kinetics in Li-Ion Batteries. *J. Electrochem. Soc.* **2018**, *165* (2), A361–A367.
- (10) Park, J. H.; Yoon, H.; Cho, Y.; Yoo, C.-Y. Investigation of Lithium Ion Diffusion of Graphite Anode by the Galvanostatic Intermittent Titration Technique. *Materials* **2021**, *14* (16), 4683.
- (11) Weiss, M.; Ruess, R.; Kasnatscheew, J.; Levartovsky, Y.; Levy, N. R.; Minnmann, P.; Stolz, L.; Waldmann, T.; Wohlfahrt-Mehrens, M.; Aurbach, D.; Winter, M.; Ein-Eli, Y.; Janek, J. Fast Charging of Lithium-Ion Batteries: A Review of Materials Aspects. *Advanced Energy Materials* **2021**, *11* (33), 2101126.
- (12) Xu, W.; Welty, C.; Peterson, M. R.; Read, J. A.; Stadie, N. P. Exploring the Limits of the Rapid-Charging Performance of Graphite as the Anode in Lithium-Ion Batteries. *J. Electrochem. Soc.* **2022**, *169* (1), 010531.
- (13) Dubey, R.; Zwahlen, M.; Shynkarenko, Y.; Yakunin, S.; Fuerst, A.; Kovalenko, M. V.; Kravchyk, K. V. Laser Patterning of High-Mass-Loading Graphite Anodes for High-Performance Li-Ion Batteries. *Elec. Soc. C* **2020**, *4* (3), 464–468.
- (14) Kottegoda, I. R. M.; Kadoma, Y.; Ikuta, H.; Uchimoto, Y.; Wakihara, M. High-Rate-Capable Lithium-Ion Battery Based on Surface-Modified Natural Graphite Anode and Substituted Spinel Cathode for Hybrid Electric Vehicles. *J. Electrochem. Soc.* **2005**, *152* (8), A1595.
- (15) Yao, J.; Wang, G. X.; Ahn, J.; Liu, H. K.; Dou, S. X. Electrochemical Studies of Graphitized Mesocarbon Microbeads as an Anode in Lithium-Ion Cells. *J. Power Sources* **2003**, *114* (2), 292–297.
- (16) Peng, C.; Liao, M. D.; Lv, X. L.; Chen, L.; Hou, S. P.; Min, D.; Chen, J.; Wang, H.-L.; Lin, J.-H. Large-Scale Synthesis of Highly Structural-Connecting Carbon Nanospheres as an Anodes Material for Lithium-Ion Batteries with High-Rate Capacity. *Chem. Eng. J* **2020**, *2*, 100014.

- (17) Yao, F.; Pham, D. T.; Lee, Y. H. Carbon-Based Materials for Lithium-Ion Batteries, Electrochemical Capacitors, and Their Hybrid Devices. *ChemSusChem* **2015**, *8* (14), 2284–2311.
- (18) Dahn, J. R.; Zheng, T.; Liu, Y.; Xue, J. S. Mechanisms for Lithium Insertion in Carbonaceous Materials. *Science* **1995**, *270* (5236), 590–593.
- (19) Xing, W.; Xue, J. S.; Zheng, T.; Gibaud, A.; Dahn, J. R. Correlation Between Lithium Intercalation Capacity and Microstructure in Hard Carbons. *J. Electrochem. Soc.* **1996**, *143* (11), 3482–3491.
- (20) Zheng, T.; Xing, W.; Dahn, J. R. Carbons Prepared from Coals for Anodes of Lithium-Ion Cells. *Carbon* **1996**, *34* (12), 1501–1507.
- (21) Mathis, T. S.; Kurra, N.; Wang, X.; Pinto, D.; Simon, P.; Gogotsi, Y. Energy Storage Data Reporting in Perspective—Guidelines for Interpreting the Performance of Electrochemical Energy Storage Systems. *Adv. Energy Mater.* **2019**, *9* (39), 1902007.
- (22) Enoki, T.; Miyajima, S.; Sano, M.; Inokuchi, H. Hydrogen-Alkali-Metal-Graphite Ternary Intercalation Compounds. *J. Mater. Res.* **1990**, *5* (2), 435–466.
- (23) Zheng, T.; Liu, Y.; Fuller, E. W.; Tseng, S.; von Sacken, U.; Dahn, J. R. Lithium Insertion in High Capacity Carbonaceous Materials. *J. Electrochem. Soc.* **1995**, *142* (8), 2581–2590.
- (24) Nishihara, H.; Kyotani, T. Zeolite-Templated Carbons – Three-Dimensional Microporous Graphene Frameworks. *Chem. Commun.* **2018**, *54* (45), 5648–5673.
- (25) Taylor, E. E.; Garman, K.; Stadie, N. P. Atomistic Structures of Zeolite-Templated Carbon. *Chem. Mater.* **2020**, *32* (7), 2742–2752.
- (26) Ferrari, A. C.; Basko, D. M. Raman Spectroscopy as a Versatile Tool for Studying the Properties of Graphene. *Nature Nanotechnol.* **2013**, *8* (4), 235–246.
- (27) McGlamery, D.; Baker, A. A.; Liu, Y.-S.; Mosquera, M. A.; Stadie, N. P. Phonon Dispersion Relation of Bulk Boron-Doped Graphitic Carbon. *J. Phys. Chem. C* **2020**, *124* (42), 23027–23037.
- (28) Diana, N.; Yamada, Y.; Gohda, S.; Ono, H.; Kubo, S.; Sato, S. Carbon Materials with High Pentagon Density. *J Mater Sci* **2021**, *56* (4), 2912–2943.
- (29) Levi, M. D.; Aurbach, D. The Mechanism of Lithium Intercalation in Graphite Film Electrodes in Aprotic Media. Part 1. High Resolution Slow Scan Rate Cyclic Voltammetric Studies and Modeling. *J. Electroanal. Chem.* **1997**, *421* (1–2), 79–88.
- (30) Peng, C.; Mercer, M. P.; Skylaris, C.-K.; Kramer, D. Lithium Intercalation Edge Effects and Doping Implications for Graphite Anodes. *J. Mater. Chem. A* **2020**, *8* (16), 7947–7955.
- (31) Augustyn, V.; Come, J.; Lowe, M. A.; Kim, J. W.; Taberna, P.-L.; Tolbert, S. H.; Abruña, H. D.; Simon, P.; Dunn, B. High-Rate Electrochemical Energy Storage through Li⁺ Intercalation Pseudocapacitance. *Nature Mater* **2013**, *12* (6), 518–522.

- (32) Gogotsi, Y.; Penner, R. M. Energy Storage in Nanomaterials – Capacitive, Pseudocapacitive, or Battery-Like? *ACS Nano* **2018**, *12* (3), 2081–2083.
- (33) Fleischmann, S.; Mitchell, J. B.; Wang, R.; Zhan, C.; Jiang, D.; Presser, V.; Augustyn, V. Pseudocapacitance: From Fundamental Understanding to High Power Energy Storage Materials. *Chem. Rev.* **2020**, *120* (14), 6738–6782.
- (34) Simon, P.; Gogotsi, Y.; Dunn, B. Where Do Batteries End and Supercapacitors Begin? *Science* **2014**, *343* (6176), 1210–1211.
- (35) Yin, J.; Jin, J.; Chen, C.; Lei, Y.; Tian, Z.; Wang, Y.; Zhao, Z.; Emwas, A.-H.; Zhu, Y.; Han, Y.; Schwingenschlögl, U.; Zhang, W.; Alshareef, H. N. Preferential Pyrolysis Construction of Carbon Anodes with 8400 h Lifespan for High-Energy-Density K-ion Batteries. *Angew Chem Int Ed* **2023**.
- (36) Langford, J. I.; Wilson, A. J. C. Seherrer after Sixty Years: A Survey and Some New Results in the Determination of Crystallite Size. *J. Appl. Cryst.* **1978**, No. 11, 102–113.
- (37) Ferrari, A. C.; Basko, D. M. Raman Spectroscopy as a Versatile Tool for Studying the Properties of Graphene. *Nature Nanotech* **2013**, *8* (4), 235–246.
- (38) McGlamery, D.; Baker, A. A.; Liu, Y.-S.; Mosquera, M. A.; Stadie, N. P. Phonon Dispersion Relation of Bulk Boron-Doped Graphitic Carbon. *J. Phys. Chem. C* **2020**, *124* (42), 23027–23037.

CHAPTER FOUR

PHONON DISPERSION RELATION OF
BULK BORON-DOPED GRAPHITIC CARBONContribution of Authors

Manuscript in Chapter 4

Author: Devin McGlamery

Contributions: Synthesized materials, collected data, analyzed data, produced figures, and wrote the manuscript.

Co-Author: Alexander A. Baker

Contributions: Assisted in collecting XAS data, aided in interpretation of XAS

Co-Author: Yi-Sheng Liu

Contributions: Assisted in collecting XAS data

Co-Author: Martín A. Mosquera

Contributions: Performed phonon dispersion calculation, and assisted in interpreting results

Co-Author: Nicholas P. Stadie

Contributions: Oversaw experimental designed, aided in interpretation of results, and assisted in writing and editing the manuscript.

Manuscript Information

Devin McGlamery[†], Alexander A. Baker[‡], Yi-Sheng Liul, Martín A. Mosquera[†], and Nicholas P. Stadie[†]

[†]Department of Chemistry & Biochemistry, Montana State University, Bozeman, Montana, 59717, United States

[‡]Materials Science Division, Lawrence Livermore National Laboratory, Livermore, California, 94550, United States

||Advanced Light Source, Lawrence Berkeley National Laboratory, Berkeley, California, 94720, United States

Status of Manuscript:

Prepared for submission to a peer-reviewed journal

Officially submitted to a peer-reviewed journal

Accepted by a peer-reviewed journal

Published in a peer-reviewed journal

ACS Journal of Physical Chemistry C

Volume 124, Issue 42

<https://doi.org/10.1021/acs.jpcc.0c06918>

Abstract

Bulk turbostratic graphitic carbon of varying levels of disorder and chemical compositions has been synthesized by a direct synthesis method in the temperature range of 750–1100 °C, with a focus on boron incorporation within the graphitic lattice. The atomistic and electronic/vibrational structures were characterized by X-ray diffraction, energy-dispersive X-ray spectroscopy, Auger electron spectroscopy, X-ray absorption spectroscopy, and Raman spectroscopy. The phonon dispersion relation of graphitic carbon was found to be uniquely sensitive to substitutional boron doping, which perturbs the phonon structure while leaving the lattice structure unchanged. The dispersion relation of the D peak measured by Raman spectroscopy can be used to uniquely identify bulk graphitic materials containing a large content of ordered trigonal planar g-BC₃ units, which are of high interest in applications ranging from hydrogen storage to lithium-ion batteries.

Introduction

Substitutional boron doping of graphite has proven to be an effective method to improve thermoelectric power,¹ oxidation resistance,²⁻⁵ the capture of thermal neutrons,⁶ and the ability to accept alkali metal intercalants (e.g., Li, Na, and K).⁷⁻¹¹ Numerous theoretical studies have shown great promise for high boron-content graphitic solutions, notably BC₃' (25 at. % boron), as an electrode material in electrochemical energy storage devices,¹²⁻¹⁴ as well as for reversible solid-state hydrogen storage at near ambient conditions.¹⁵⁻¹⁹ This latter proposal, in particular, has motivated great efforts to synthesize and characterize high boron-content graphitic carbon approaching the composition BC₃ as a bulk, free-standing material in order to assess boron's role in increasing the strength of interaction of graphite-like materials toward H₂.^{9,10,20} The first systematic experiments to incorporate boron within graphite were reported by Lowell in 1967 and established the equilibrium limit of boron substitutional doping as 2.35 at. %.²¹ Dresselhaus and co-workers investigated boron-implanted graphite (at low doping concentrations) in 1981, elegantly decoupling the effects of substitutional doping as opposed to structural defects (e.g., vacancies) on the Raman spectrum of graphitic carbon.²² This was followed by a synthetic breakthrough in 1986 when Kouvetakis and co-workers reported a novel route to high boron-content thin-films with a composition of BC₃.⁸ This metastable thin-film material was accessed through the reaction of benzene and boron trichloride at relatively low temperatures (800 °C) compared to those required to prepare equilibrium solid solutions (up to 2350 °C). Dahn and co-workers,^{7,23} among several other groups,^{4,5,24} were able to reproducibly synthesize and thoroughly characterize similar thin-film materials with tunable compositions up to BC₅. In 2012, Dresselhaus and co-workers followed up previous work by exfoliating low boron-content (equilibrium)

graphite to obtain boron-doped graphene (~ 0.22 at. % substitutional boron) and characterized the materials using Raman spectroscopy.²⁵ Most recently, bulk graphitic materials of composition $\sim \text{BC}_3$ (including some oxygen contamination) have been reported by two synthetic routes: a molecular tiling route based on a single organic precursor⁹ and the direct synthesis from a tunable solution of two commercially available liquid precursors.¹⁰ Such materials are free-standing forms of metastable graphitic carbon with a high concentration of boron but also a contribution from oxygen as well as halide contaminants; neither is highly crystalline, but both contain boron chemical environments like that expected for pristine BC_3' .

The quantification and characterization of boron inclusion in graphitic carbon is challenging, owing to the fundamental similarities in size and scattering cross section of boron, carbon, and lattice vacancies. Methods to quantify boron content in carbon-based materials include Auger electron spectroscopy (AES),^{7,23,24} elastic recoil detection analysis (ERDA),¹⁰ electron probe microanalysis,⁵ digestion followed by volumetric titration,²¹ combustion in fluorine gas to allow for the quantitative detection of BF_3 , and CF_4 by infrared spectroscopy,⁸ or by indirect comparison to previous work.^{22,26} Characterization of the boron chemical environment is typically performed by X-ray absorption spectroscopy (XAS),⁷ solid-state ^{11}B NMR,^{9,10} electron energy-loss spectroscopy,²⁷ or X-ray photoelectron spectroscopy.^{9,25,28} This class of materials ranges widely in terms of crystallinity and boron content; the crystalline nature of low boron-content materials reduces the challenge of probing the distinct boron environments. On the other hand, higher concentrations of boron are in all cases inherently accompanied by severe structural disorder, and hence, characterization is significantly more challenging. In this work, we focus on Raman spectroscopy as a versatile and widely available tool for the characterization of high boron-

content graphitic materials and the sensitive relationship it reveals between boron inclusions and defects in the graphitic lattice. The Raman spectrum of graphite has been a subject of active investigation since 1970 when Tuinstra and Koenig first reported and assigned the E_{2g} Raman-active mode of crystalline graphite and noticed a lower frequency mode that was only present in defective samples.²⁹ Several other features, especially a high-frequency overtone at $\sim 2700\text{ cm}^{-1}$, were also observed and discussed, with their assignments remaining somewhat disputed for many years owing to the complexity of their physical origin and the unique electronic properties of graphene/graphite. A thorough account of the major developments in and current understanding of the Raman spectrum of graphene and graphite was given by Ferrari and Basko in 2013.³⁰ Pristine graphite has two formally allowed Raman active modes, both with E_{2g} symmetry. The most well-known is the higher frequency mode associated with the optical branches of the phonon structure, being degenerate at the Γ point. It arises because of the relative in-plane motion of all sp^2 -hybridized carbon atoms, occurring at a Raman shift of $\sim 1580\text{ cm}^{-1}$, and is commonly referred to as the G mode. The second is a low-frequency shearing mode in which the two graphene layers within the unit cell slip with respect to each other, appearing at a Raman shift of $\sim 40\text{ cm}^{-1}$, and referred to as the C mode. Both vibrational modes occur at the Γ point in the first Brillouin zone, where the phonon wavevector is zero, thus satisfying the fundamental Raman selection rule. In addition to these formally allowed modes, more complex resonant processes (enabled by the unusual Dirac cone in the phonon structure of graphene/graphite) can also occur, in which electron scattering by defects results in a net conservation of momentum and thus an observed Raman process. This leads to the appearance of a multitude of formally forbidden transitions such as the D, D', and D'' modes in graphite that contains defects.^{30,31} These defect-activated modes can

provide a wealth of information on the nature and type of defects within graphitic systems. Other combinations and overtone modes involving two such phonons, for example, the $D + D''$, $2D$, and $2D'$ modes, are also present in the Raman spectrum of graphitic carbon, even in the absence of defects and become significant because of resonance enhancement. Formally, the individual phonons involved in these combination modes are forbidden because of their nonzero wavevectors; however, when two phonons with opposite wavevectors are combined, momentum can be conserved and the Raman process is observed, resulting in the significant presence of these combination modes even in pristine graphite and graphene when probed at optical incident frequencies.

Changing the excitation energy of the Raman scattering event (a common capability in the modern analytical laboratory) permits the examination of phonon dispersion and other excitation energy-dependent phenomena. The positions of Raman peaks that originate from double resonance processes, such as the D mode, show a strong dependence on excitation energy.^{30,32,33} This dispersion relation of the D peak is referred to as $\text{Disp}(D)$ and reported in units of $\text{cm}^{-1} \text{eV}^{-1}$, and the change in observed peak position [$\text{Pos}(D)$, in cm^{-1}] as a function of Raman excitation energy (E_L , in eV). The E_L dependence of $\text{Pos}(D)$ originates from the slope of the in-plane transverse optical (TO) phonon branch around the Kohn anomaly at the K point in the first Brillouin zone and is a fundamental material property of the graphitic system. In many materials, this is found to be a linear relation within the typical range of E_L accessible to a benchtop spectrometer,³⁴ providing a convenient metric for assessing the phonon structure of a variety of disordered graphitic materials with varying atomistic structure and composition.

The interpretation of the Raman spectrum of graphite, graphene, and disordered carbon materials is readily extended to graphitic systems containing substitutional boron doping. In such materials, boron doping and structural defects both give rise to the development of the defect-activated D peak. Low boron-content graphitic materials show that even when structural order is unperturbed, the presence of substitutional boron atoms within the graphitic lattice results in a Raman spectrum that is highly influenced by defect-activated modes.³⁵ By combining information gleaned from other analytical techniques with Raman spectroscopy, it is possible to separate the effects of structural and chemical defects, elucidating the role boron substitution plays on the electronic, vibrational, and physical structure of boron-doped graphitic carbon. In this work, we explore the effect of boron doping within bulk turbostratic graphitic carbon on the phonon dispersion (E_L dependence) of the D mode.

Using the recently established direct synthesis method,¹⁰ two series of bulk boron-doped graphitic materials were synthesized. The first series focuses on the effect of synthesis temperature: a series of boron-doped graphitic carbon materials with a nominal composition of 25 at. % boron (referred to herein as BC_3') was synthesized at 750–1100 °C in 50 °C increments. Benzene and tribromobenzene-derived graphitic carbon materials (referred to as C' and CBr_x') were also synthesized in a temperature series to elucidate the role of synthesis temperature on the materials properties of boron-free turbostratic carbon, with and without a bromine-containing leaving group. The second series focuses on the effect of boron composition: a series of increasing boron content within turbostratic graphitic carbon (referred to as BC_x') was synthesized at 800 °C, where the nominal composition was varied such that $x = 3, 5, 10, 20, 30,$ and ∞ . The material denoted by $x = \infty$ corresponds to a pure carbon material without any boron precursor (and is hence

a variety of C'). Both series were characterized by Raman spectroscopy, as well as several complementary techniques: X-ray diffraction (XRD), AES, energy-dispersive X-ray spectroscopy (EDX), and XAS. The so-obtained materials of highest importance are summarized in Figure 1. Of particular interest is the dispersion of the D peak in the Raman spectrum and its dependence on the structural and chemical properties of the graphitic lattice. A direct correlation between the presence of ordered BC_3 domains and a reduced phonon dispersion relation of the D peak is observed and corroborated by first-principles calculations of the vibrational structure of high boron-content graphene.

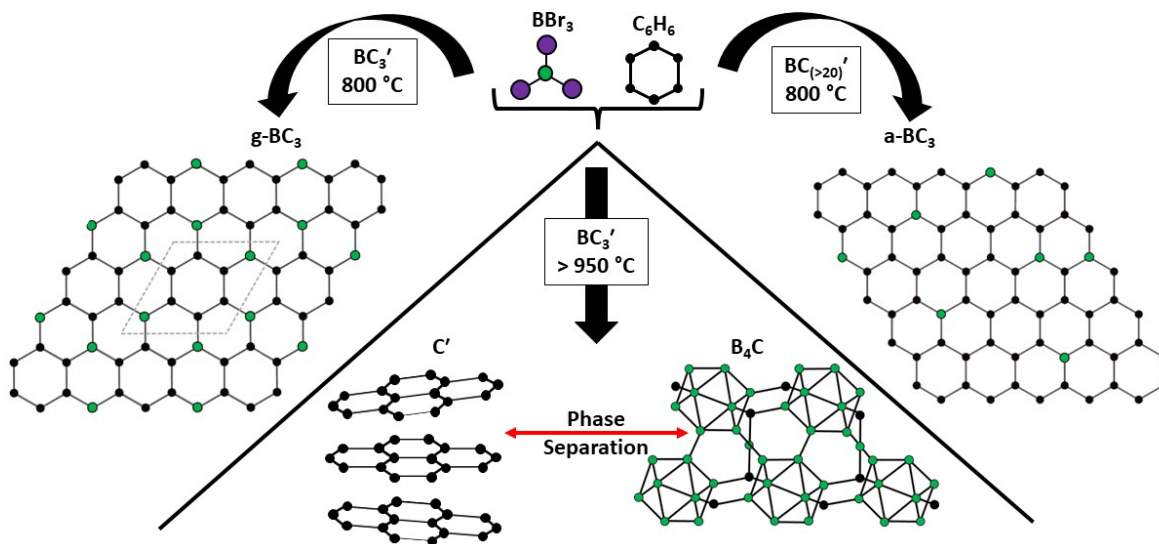


Figure 1. Schematic depiction of the pyrolysis products of boron tribromide and benzene depending on synthesis temperature and nominal composition (C/B ratio, x). Solid solutions of boron in turbostratic graphitic carbon are referred to as BC_x' , while pure turbostratic graphitic carbon is referred to as C' .

Experimental Methods

Direct Synthesis of Bulk C', CBr_x', and BC_x'

A solution of boron tribromide (99.99%, Sigma-Aldrich) and benzene (99.8%, Sigma-Aldrich), or a neat solution of either benzene or 1,3,5-tribromobenzene (98%, Alfa Aesar), was charged into a quartz ampule (15 cm length, 1 cm inner diameter, closed at one end) inside a glovebox under an inert argon atmosphere (<0.5 ppm of H₂O, <0.5 ppm of O₂). The amounts of the reagents used were determined by selecting the desired stoichiometry (nominal composition) of the product and by limiting the maximum pressure at the synthesis temperature to 20 bar within the quartz ampule, assuming that all of the bromine and/or hydrogen atoms would be evolved as diatomic ideal gases (e.g., 85.1 μL of BBr₃ and 40 μL of C₆H₆ to achieve a nominal composition of BC₃ in a 14 mL ampule at a maximum temperature of 800 °C). The open end of the ampule was closed with a Swagelok Ultra-Torr adapter and removed from the glovebox. The lower half of the ampule was submerged in liquid nitrogen to solidify the precursors. In this state, the ampule was connected to a stainless steel Schlenk line and evacuated to 10⁻² mbar. The ampule was flame-sealed under active vacuum. The sealed ampule was then placed in the center of a chamber furnace (Carbolite RWF 12/13) and heated to the temperature setpoint (750–1100 °C) via a 1 °C min⁻¹ ramp. The set temperature was held for 1 h and then allowed to gradually cool to ambient temperature. The ampule was carefully scored with a diamond-bladed saw and snapped open within a nitrile rubber enclosure, releasing the overpressure of gaseous byproducts into a fume hood. The solid product was collected and washed three times with deionized water, washed three times with acetone, and finally dried in air at 80 °C. The as-synthesized flakes were in some cases

investigated without further manipulation or were reduced to powder by ultrasonication in acetone for 5 min prior to drying at 80 °C, as denoted below.

Powder XRD

Powder XRD was performed on sonicated materials using a Rigaku Ultima IV diffractometer with Cu $K\alpha_{1,2}$ radiation ($\lambda = 1.54 \text{ \AA}$) in reflection geometry. Samples were spread thinly on the surface of a zero-background holder constructed of oriented silicon. Analysis of the raw data is described in the Supporting Information.

Raman Spectroscopy

As-synthesized flakes were investigated with a Raman spectrometer (LabRAM HR Evolution, Horiba Scientific Ltd.) equipped with a confocal microscope and three excitation sources: a 532 nm (2.33 eV) frequency doubled Nd:YAG laser with an incident power of 10 mW, a 633 nm (1.96 eV) HeNe laser with an incident power of 1.7 mW, and a 785 nm (1.58 eV) diode laser with an incident power of 25 mW. All measurements were performed at room temperature. Analysis of the raw data is described in the Supporting Information.

X-ray Absorption Spectroscopy

The boron and carbon environment of boron-containing materials was examined by XAS using synchrotron radiation at the Advanced Light Source (Lawrence Berkeley National Laboratory). Sonicated samples were mounted on carbon tape and transferred into an ultrahigh vacuum (10^{-9} mbar) chamber for analysis. The total fluorescence yield was measured allowing for probing depths of ~ 175 nm into the bulk of the sample. Boron oxide (99.999%, Sigma-Aldrich), amorphous boron (98%, Alfa Aesar), boron carbide (98%, Sigma-Aldrich), and hexagonal boron

nitride (99.5%, Alfa Aesar) were also analyzed under the same conditions as standard references. Analysis of the raw data (including additional C K-edge spectra) is described in the Supporting Information.

Elemental Analysis

AES and EDX were performed using a scanning electron microscope (PHI 710 Scanning Auger NanoProbe, Physical Electronics Inc.) under a highly focused electron beam with a well-defined energy of 10 kV operating at 10 nA. Samples were prepared by pressing the as-synthesized flakes into indium foil. The samples were sputtered for 3 min under a 3 keV argon ion beam to clean the surface for AES analysis. For EDX, a windowless X-ray detector (XFlash 6|10, Bruker Corp.) was used, permitting the detection of boron. Analysis of the raw data as well as several representative scanning electron micrographs of the samples is given in the Supporting Information. In the present work, the boron/ carbon ratio (e.g., BC₃') is used specifically to indicate the stoichiometry of the initial reaction mixture and is thus the “nominal composition.” On the other hand, the measured boron content of a material is reported as a percentage of boron to carbon in molar, dimensionless “at.%”.

Phonon Structure Calculations

Phonon dispersion calculations were performed using plane wave density functional theory (DFT) implemented by the Quantum ESPRESSO package.^{36,37} Rappe–Rabe–Kaxiras–Joannopoulos³⁸ ultrasoft pseudopotentials were employed to describe the core electrons of carbon and boron. The Perdew–Burke–Ernzerhof (PBE) exchange correlation functional³⁹ was selected. Supercells consisting of eight atoms in a single plane were optimized at the PBE level: C₈ (graphene), BC₇, and B₂C₆ (single-layer BC₃). The optimized in-plane lattice

constants (a) were found to be 4.930, 5.038, and 5.170 Å, respectively. To minimize the interaction between monolayers, the interlayer lattice constant (c) was set as 15 Å. For the electronic energy calculations and atomic position relaxations, the convergence thresholds were 1×10^{-12} Ry and 1×10^{-7} au, respectively, employing a $16 \times 16 \times 1$ k-grid. The phonon dispersion calculations were performed with a 1×10^{-14} Ry threshold, employing an $8 \times 8 \times 1$ q-grid. To interpret the phonon behavior of these materials, unfolding of the phonon structure was applied; the unfolded phonon dispersion diagrams reported in this work were generated with the Phonon Unfolding program.⁴⁰

Results

Structural Characterization

XRD patterns and Raman spectra ($E_L = 532$ nm) of the temperature series of BC_3' , C' , and CBr_x' materials synthesized in 50 °C increments ranging from 750 to 1100 °C are shown in Figure 2. The XRD patterns exhibit two broad reflections corresponding to a weakly ordered turbostratic graphitic structure: an intense (002) reflection centered between 24 and 26° as well as a family of (10) reflections centered at ~43° composed of (100) and (101) contributions. Tribromobenzene-derived graphitic carbon (CBr_x') exhibits broad (002) and (10) reflections at all synthesis temperatures. This very poor crystallinity is also observed in the broadness of the D and G peaks in the Raman spectrum, where little change is observed over the range of synthesis temperatures explored. Benzene-derived graphitic carbon (C') exhibits increasing order of the graphitic structure with increasing synthesis temperature, as revealed by a narrowing of the (002) reflection in the XRD patterns. Raman spectroscopy reveals more detailed information about the developing order. The intensity ratio (as defined in the Supporting Information) of the D and G peaks, referred to as $I(D)/I(G)$, is a common metric used to assess the quality of graphitic systems. For turbostratic

graphite, an increase in $I(D)/I(G)$, narrowing of all peaks, and the appearance of a well-defined 2D region are evidence of increasing graphitic ordering and the removal of defects within the graphitic lattice.⁴¹ This occurs for all C' materials synthesized above 950 °C in this work. Interestingly, the BC_3' materials show similar reflections in XRD compared to the C' materials; yet, their Raman spectra show much more subtle development as a function of increasing synthesis temperature. The $I(D)/I(G)$ of BC_3' decreases with increasing synthesis temperature, opposite to the C' material, and there is only slight narrowing of both the D and G peaks. Even at the highest synthesis temperature explored (1100 °C), BC_3' does not exhibit a well-defined 2D region.

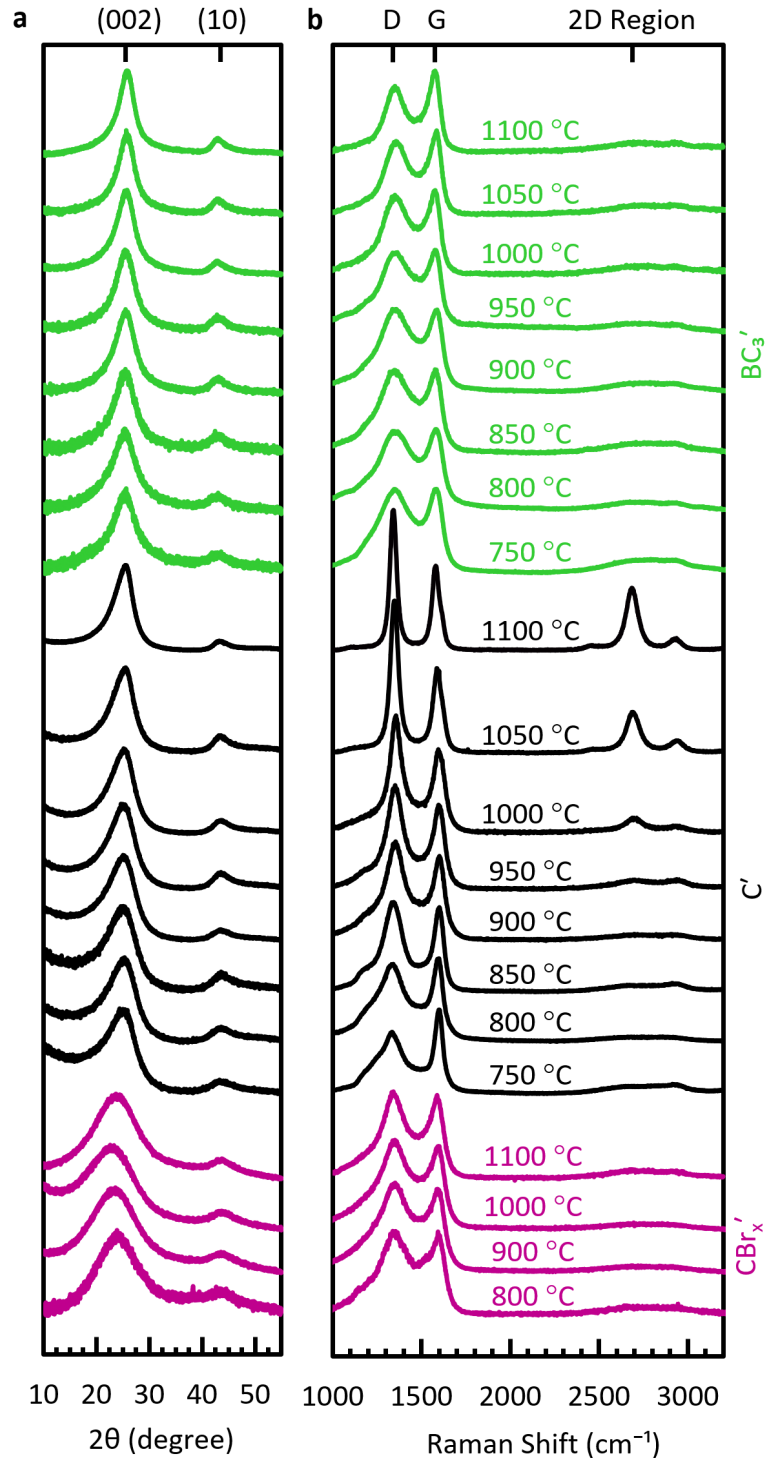


Figure 2. Structural characterization as a function of temperature. (a) XRD patterns and (b) Raman spectra ($E_L = 532$ nm) of CBr_x' (bottom, magenta), C' (middle, black), and BC_3' (top, green). Samples were synthesized by the direct method in 50 °C increments between 750 and 1100 °C.

XRD patterns and Raman spectra ($E_L = 532 \text{ nm}$) of the BC_x' composition series synthesized by the direct method at $800 \text{ }^\circ\text{C}$ are shown in Figure 3. The nominal compositions of BC_x' ($x = 3, 5, 10, 20, 30,$ and ∞) were set by varying the ratio of boron tribromide to benzene in the initial reaction mixture. The XRD patterns of BC_x' do not change significantly with increasing boron content. The Raman spectra, however, show subtle developments as a result of increasing boron concentration. In the absence of boron doping ($x = \infty$), the D peak is rather pronounced with an obvious shoulder between 1100 and 1200 cm^{-1} ; the G peak is comparatively narrow, and the 2D region is broad and very weak. As the boron content increases (up to $x = 3$), both the D and G peaks broaden, and overall intensity in the 2D region increases.

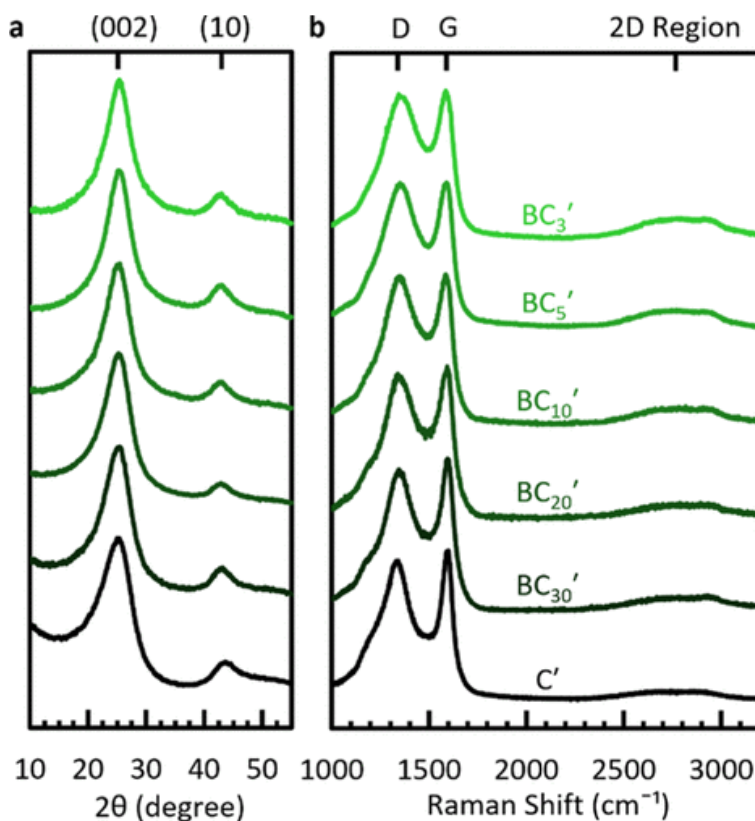


Figure 3. Structural characterization as a function of boron content. (a) XRD patterns and (b) Raman spectra ($E_L = 532 \text{ nm}$) of BC_x' ($x = 3, 5, 10, 20, 30,$ and ∞) synthesized by the direct method at $800 \text{ }^\circ\text{C}$.

Chemical Composition

The boron content of BC_x' as a function of nominal composition, as independently determined by AES and EDX techniques, is shown in Figure 4. The measured boron content is less than the nominal boron content at all compositions. This is likely due to a combination of several effects: incomplete reaction of the boron precursor (BBr_3), side reactions with the quartz ampule during synthesis, formation of soluble boron compounds such as oxide phases, and/or poor boron/carbon resolution inherent to the analytical methods. The latter issue has been remedied in previous work by use of ERDA,¹⁰ an analytical technique that is well-suited to resolving the boron concentration in carbon-based materials based on the signal arising from ^{10}B . In that case, similar materials showed a boron content roughly equivalent to the nominal composition. Nevertheless, in the present work there appears to be a limit to boron incorporation (~ 12 at. % according to AES and EDX results) reached at the nominal composition of BC_5' , corresponding to an actual stoichiometry of $\sim BC_8$. This observation of a limit to boron inclusion at a nominal composition of $\sim BC_5$ is consistent with previous results for thin-film boron-doped graphitic materials.⁷

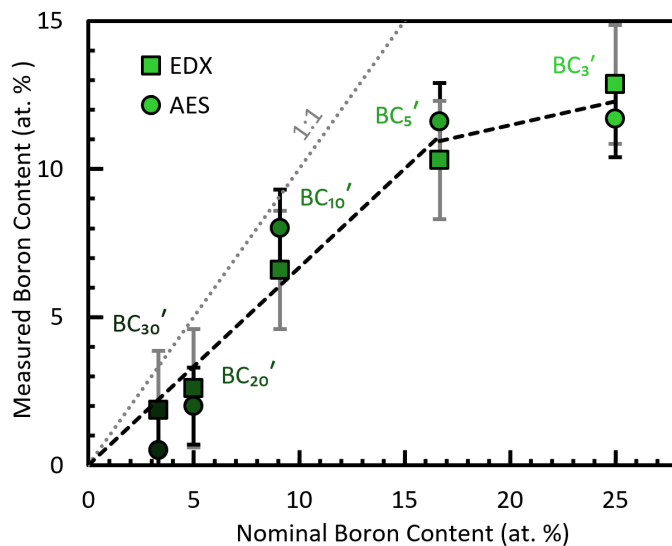


Figure 4. Elemental analysis. Boron content of BC_x' as measured by AES (circles) and EDX (squares) as a function of nominal composition determined by the B/C ratio of the initial reaction mixture.

Boron Chemical Environments

The boron chemical environments in the BC_3' temperature series and the BC_x' composition series were investigated by XAS, as shown in Figure 5. Several standards measured under identical conditions, as well as relevant literature references, are shown in Figure 5a to represent the possible chemical bonding environments in directly synthesized BC_x' . Boron oxide exhibits a very strong absorption associated with the σ^* transition of the BO_3 -type boron environments at 193.7 eV. Amorphous boron shows a broad, featureless absorption edge with an onset at 187–190 eV. Boron carbide (B_4C) exhibits a characteristic absorption associated with the σ^* transition of icosahedral boron environments at 190.6 eV. Hexagonal boron nitride, in polycrystalline powder form, shows a strong absorption associated with the π^* transition of trigonal planar BN_3 type boron at 191.6 eV, and a weaker absorption associated with the σ^* transition between 197 and 200 eV. The XAS spectrum of a thin-film material of reported composition $B_{0.25}C_{0.75}$ (TF-BC3) is also shown for comparison; this spectrum was originally reported by Caretti and co-workers in 2008⁴² and later

reinterpreted by Pallier and co-workers in 2013.⁴³ Four distinct boron environments are present in TF-BC₃: in ascending energy, Pallier et al. interpret these as trigonal planar mixed BC_{3-x}B_x environments in an amorphous lattice labeled as a-BC₃ (189.4 eV), an icosahedral B₄C-like environment (190.6 eV), a trigonal planar BC₃ environment with long range graphitic order labeled g-BC₃ (192.0 eV), and a boron oxide environment (193.7 eV). The g-BC₃ environment was also observed by Way and co-workers in their studies of thin-film BC_x, whose intensity was shown to depend on the angle of incidence.⁷ This supports the assignment of this peak as being due to a π^* transition in a graphitic lattice with a long-range order (similar to oriented pristine graphite which shows a π^* transition that exhibits strong angular dependence^{42,44}). All XAS spectra of boron-containing materials exhibit at least a weak contribution from BO₃ type boron environments consistent with the boron oxide standard.

The boron K-edge region of the XAS spectrum of the BC₃' temperature series synthesized between 750 and 1100 °C is shown in Figure 5b and enlarged in Figure 5e. Boron oxide environments can be seen in all samples, most likely because of a surface oxide layer present on the sonicated materials, formed during handling. The material synthesized at 750 °C shows little evidence of boron-carbon bonding. The BC₃' materials synthesized between 800 and 900 °C show a distinct g-BC₃ environment as well as a minor contribution from a-BC₃ environments. Between 950 and 1050 °C, the g-BC₃ environment becomes less distinguishable because of greater spectral weight from a broad feature corresponding to boron carbide environments. At 1100 °C, the g-BC₃ structure is completely obscured by the presence of B₄C as well as two other environments (marked with asterisks) that appear at 191.3 and 193.0 eV which have not yet been assigned. These latter contributions are suspected to be related to sub-stoichiometric boron carbide domains.⁴³

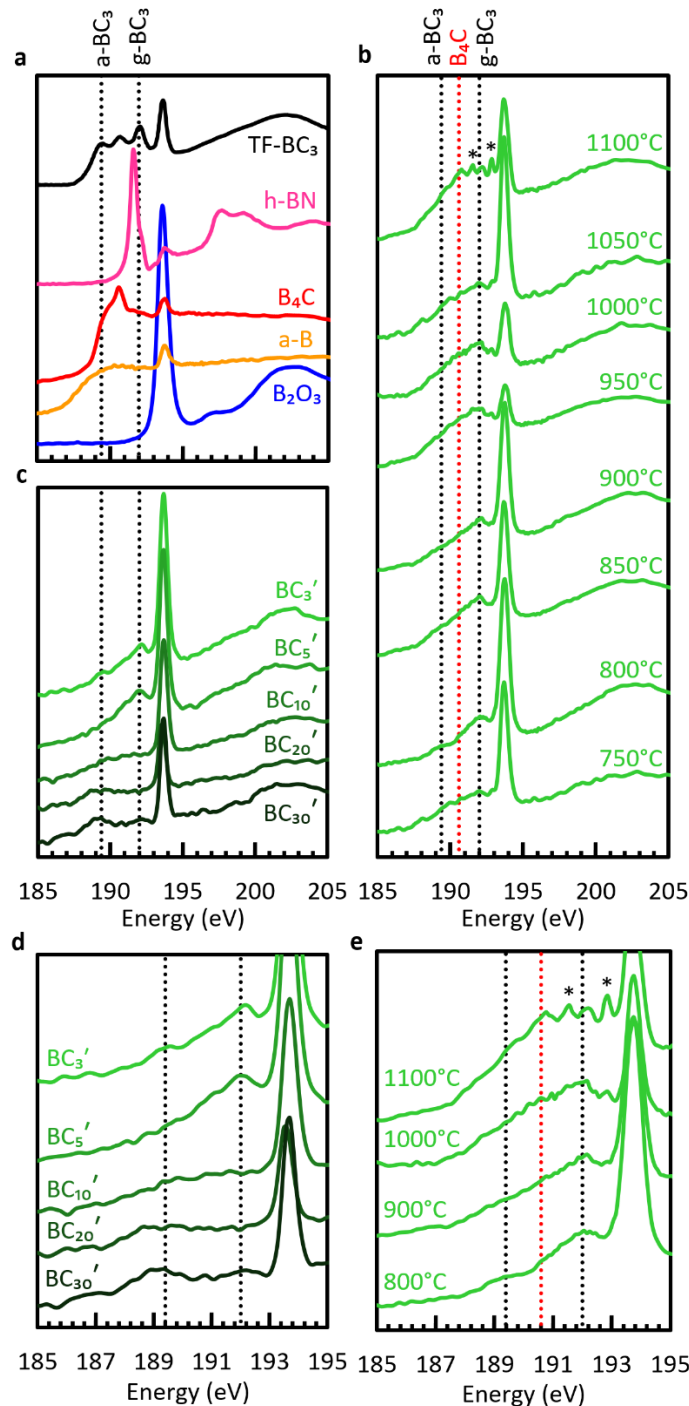


Figure 5. Boron chemical environment. XAS spectra near the B Kedge of BC_x' synthesized by the direct method and related materials: (a) boron oxide, amorphous boron, and hexagonal boron nitride, chosen as standards, and thin film BC_3 (TF- BC_3) for reference⁴³, (b) BC_x' composition series, and (c) BC_3' temperature series. The near-edge region is expanded for (d) BC_x' composition and (e) BC_3' temperature series.

Discussion

XRD, Raman spectroscopy, and XAS of boron-doped graphitic carbon synthesized by the direct method (BC_x') combine to yield an illuminative picture as to the interplay between structural defects (e.g., vacancies, edge sites, and stacking mismatch) and boron substitutions on overall disorder within the graphitic lattice. For BC_x' materials, XRD probes atomic periodicities without significant regard for elemental composition (boron and carbon have similar atomic form factors toward X-rays). Meanwhile, Raman spectroscopy is highly sensitive to bonding symmetry and therefore to elemental composition within the underlying graphitic lattice, the unique Raman spectrum of graphite especially so. A peculiarity of the characterization of graphitic carbon materials by Raman spectroscopy is that the resonance enhancement effect (which occurs at all excitation energies) renders any other present phases less prominent in the measured spectrum. Therefore, non-crystalline secondary phases may remain undetected by both XRD and Raman characterization; this is addressed herein by XAS, which reveals all boron-containing chemical environments in each material.

X-ray Diffraction

The evolution of the underlying graphitic structural regularity of BC_x' , C' , and CBr_x' as a function of the boron content or synthesis temperature as revealed by XRD is shown in Figure 5. The average d_{002} spacing was determined by applying Bragg's law to the position of the (002) reflection. The average crystallite size along the c and a-axes, referred to as L_c and L_a , respectively, were estimated by applying the Scherrer equation to the full-width at half-maximum (fwhm) of the (002) and (100) reflections.⁴⁵ Further details related to XRD pattern analysis can be found in the Supporting Information. The effects of temperature on the graphitic structure of directly

synthesized BC_3' , C' , and CBr_x' are shown in Figure 6a–c. Directly synthesized BC_3' exhibits the largest graphitic crystallites (in both L_c and L_a) and simultaneously the smallest d_{002} spacing (closest to pristine graphite). With an increase in synthesis temperature, the crystallites become larger and exhibit narrower interlayer spacing. Hence, the average number of layers per crystallite is the highest for BC_3' synthesized at 1100 °C: ~ 6 layers per crystallite. Pure graphitic carbon derived from benzene (C') also exhibits measurable increases in L_c and L_a as synthesis temperature increases, although with less change in the interlayer spacing. For C' , the maximum number of layers per crystallite is also observed for the material synthesized at 1100 °C: ~ 5 layers per crystallite. Hence, XRD analysis confirms that BC_x' is, overall, more ordered than C' synthesized by the same method.

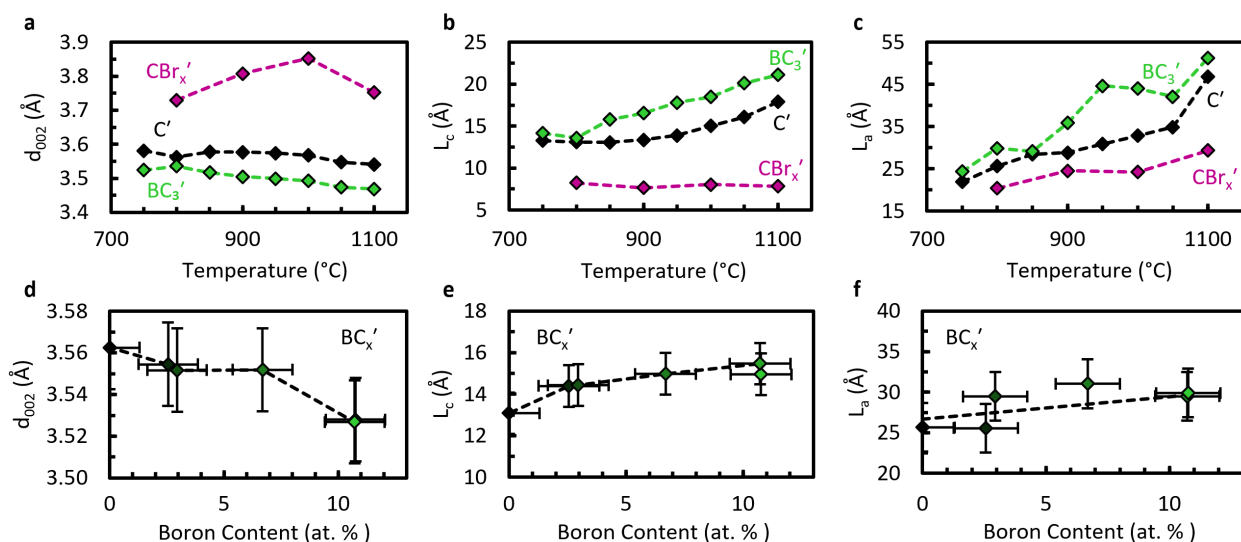


Figure 6. Interlayer spacing and crystallite size. The development of (a) d_{002} , (b) L_c , and (c) L_a as a function of synthesis temperature within the BC_3' , C' , and CBr_x' temperature series. The development of (d) d_{002} , (e) L_c , and (f) L_a as a function of boron content measured by AES within the BC_x' composition series.

The CBr_x' materials exhibit the weakest ordering (smallest crystallite size) and the largest interlayer spacing of all the materials investigated: $>3.7 \text{ \AA}$. CBr_x' was investigated to assess the effect of bromine as opposed to hydrogen on the structure of the resulting graphitic materials. The low crystallinity of CBr_x' confirms that the presence of boron within the reaction mixture to produce BC_x' is responsible for its higher crystallinity (consistent with earlier results^{46,47}) and contradicts that the presence of bromine in the boron precursor drives the reaction toward a higher crystalline graphitic product. This issue had previously hindered the direct comparison of nonhalide precursor-derived pure carbon materials (e.g., C') with boron trihalide-derived materials (e.g., BC_x'), which always exhibit higher crystallinity under equivalent synthesis conditions. The graphitic structure of the composition series, BC_x' synthesized at $800 \text{ }^\circ\text{C}$ is shown in Figure 6d–f. An increase in L_c and L_a (15% and up to 20%, respectively) are observed as a function of the boron content; this catalytic effect of boron on the formation of graphite is consistent across the literature.^{11,46,47} The average d_{002} spacing is $\sim 3.55 \text{ \AA}$ for all nominal compositions up to BC_{10} (corresponding to measured boron contents of $<10 \text{ at. \%}$) and decreases to $\sim 3.53 \text{ \AA}$ for BC_5' and BC_3' (corresponding to measured boron contents of $\sim 12 \text{ at. \%}$). The reduction in d_{002} spacing between BC_{10}' and BC_5' is directly correlated with the evolution of the g- BC_3 environments observed by XAS (see Figure 5d). Although the d_{002} spacing in directly synthesized BC_x' is larger than that of high boron-content thin films prepared by chemical vapor deposition methods ($3.48\text{--}3.34 \text{ \AA}$), the trend of decreasing interlayer spacing with increasing boron content remains consistent with previous observations for both equilibrium solid solutions of boron in graphite as well as disordered boron-doped graphitic materials.^{7,21,23,48}

Raman Spectroscopy

Further insights into the graphitic structure as well as the role of chemical defects were deduced by analysis of the Raman spectrum of BC_x' as compared to C' and CBr_x' . Four simple metrics to describe structural development/deterioration within the graphitic carbon amorphization trajectory proposed by Ferrari and Robertson⁴¹ were extracted from each individual Raman spectrum, as shown in Figure 7. The first metric described in their work is the intensity ratio of the D and G peaks, referred to as $I(D)/I(G)$. As graphitic carbon degrades from crystalline graphite (stage 1) to defective turbostratic graphite (stage 2) and eventually into amorphous carbon (stage 3), $I(D)/I(G)$ is nonmonotonically related to graphitic ordering. It first increases as a result of interruptions in symmetry of the graphitic lattice, resulting in an increase in the number of sixfold rings that have been isolated from the bulk by defects. $I(D)/I(G)$ reaches a maximum at the transition from stage 1 to stage 2 and then decreases as sixfold rings are destroyed in the material. This is due to the opening of sixfold rings into chains that only express the formally allowed Raman-active G mode. The second metric is the (apparent) position of the G peak, referred to as $Pos(G)$, observed at $\sim 1580\text{ cm}^{-1}$ for pristine graphite (stage 1). As defects are introduced and the crystallites reduce in size, $Pos(G)$ increases to $\sim 1600\text{ cm}^{-1}$ for turbostratic graphite at the transition from stage 1 to stage 2. This is a result of an increasing $FWHM(G)$ combined with the appearance of the neighboring defect-activated D' mode at $\sim 1620\text{ cm}^{-1}$; the merging of these two peaks results in an apparent shift in $Pos(G)$ to higher frequencies for turbostratic graphite. If the material degrades further into amorphous carbon (stage 3), the D' mode is no longer active because of the total destruction of the graphitic structure, resulting in an apparent reversal in the shift of $Pos(G)$. The third and fourth metrics are the $FWHM$ of the D and G peaks, referred to as $FWHM(D)$ and

FWHM(G), respectively. FWHM(D) and FWHM(G) always increase with increasing defects and disorder, making it possible to distinguish between stage 1 and stage 2 of the proposed amorphization trajectory. When boron is incorporated into the graphite lattice, the local symmetry around each lattice site is broken, resulting in the appearance of “defect-activated” modes and the broadening of features even when the lattice is pristinely ordered. At first, this seems to be an inconvenience as substitutional dopants lend a similar contribution to the Raman spectrum as defects. However, when the Raman spectrum of BC_3' is compared to that of C' and the results are combined with structural and chemical information obtained by XRD and XAS, the two contributions (boron doping vs lattice defects) can be effectively decoupled.

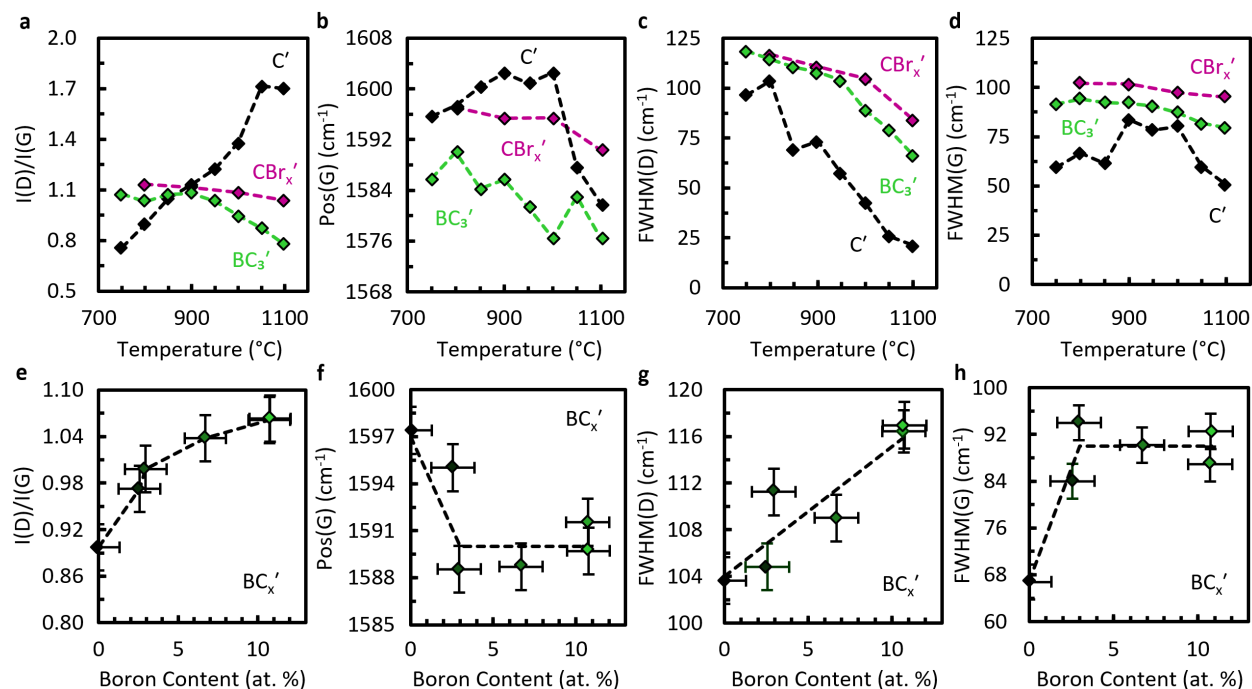


Figure 7. Raman spectroscopy analysis ($E_L = 532$ nm). The (a) $I(D)/I(G)$ ratio, (b) $Pos(G)$, (c) $FWHM(D)$, and (d) $FWHM(G)$ as a function of synthesis temperature within the BC_3' , C' , and CBr_x' temperature series. The (e) $I(D)/I(G)$ ratio, (f) $Pos(G)$, (g) $FWHM(D)$, and (h) $FWHM(G)$ as a function of measured boron content by AES within the BC_x' composition series.

Temperature and Graphitic Structure

Analysis of the Raman spectra of the BC_3' , C' , and CBr_x' temperature series as well as the BC_x' composition series by the aforementioned four metrics is shown in Figure 7a–d. The $I(D)/I(G)$, $Pos(G)$, and $FWHM(D)$ of the low-temperature variants of C' indicate it to be stage 2 nanocrystalline graphitic carbon, referring to the stages of the amorphization trajectory as proposed by Ferrari and Robertson.⁴¹ Directly synthesized C' undergoes a transition to stage 1 nanocrystalline graphitic carbon as synthesis temperature is increased. This is determined by the maximum reached in $I(D)/I(G)$ as well as in $Pos(G)$ and is corroborated by examining the crystallite size along the c-axis as determined by XRD, where L_c increases from 1.3 to 1.7 nm. Interestingly, BC_3' does not show the same maximum in $I(D)/I(G)$ and $Pos(G)$ even though the crystallite size in the c-axis is larger, increasing from 1.4 to 2.1 nm with increasing synthesis temperature. This can be explained by the high boron content within the graphitic lattice that presents as substitutional defects, resulting in a Raman spectrum that reflects a more disordered system compared to its C' counterparts, despite having larger crystallites as detected by XRD. There is a reduction in $FWHM(D)$ with increasing synthesis temperature for all samples, indicating an overall ordering of the material at higher temperatures. The decrease in $FWHM(D)$ for the C' materials is roughly linear over the entire temperature range with a slope of -24 cm^{-1} per $100\text{ }^\circ\text{C}$. The BC_3' material shows two distinct regions for the evolution of $FWHM(D)$. Between 750 and 950 $^\circ\text{C}$, $FWHM(D)$ changes little with synthesis temperature, having a slope of -7 cm^{-1} per $100\text{ }^\circ\text{C}$. However, from 950 to 1100 $^\circ\text{C}$, the D peak narrows at the same rate as the C' materials, having a slope of -24 cm^{-1} per $100\text{ }^\circ\text{C}$. Hence, this is an important transition temperature that indicates significantly different structural properties of directly synthesized BC_3' ; at 950 $^\circ\text{C}$ and above, the

material transitions into graphitic carbon with similar spectral behavior as found in boron-free graphitic carbon.

The above results indicate that boron leaves the graphitic BC_x' phase at high temperatures, whereupon temperature plays a similar role in improving the graphitic ordering, as for the C' counterparts. The same two regions are also observed for the CBr_x' material. This is proposed to be a result of bromine atoms that have not been expelled from the material until it is heated above 950 °C. Bromine can form stable intercalation compounds within graphite.^{49,50} This process is only partially reversible in that the last 5–10% of the intercalated bromine can only be removed by strong heating to form volatile carbon derivatives that incorporate bromine.⁵¹ In the present work, intercalated bromine and its destructive deintercalation process likely explains the larger d_{002} and low values of L_c and L_a observed over the CBr_x' temperature series, as seen in Figure 6a–c.

Boron Content and Graphitic Structure

The effect of boron doping within the graphitic lattice on key features of the Raman spectra of the BC_x' composition series is shown in Figure 7e–h. The overall effect is an increased ordering as a result of increasing boron content, being consistent with previous studies of boron-doped graphitic thin-films.²³ This is most clearly observed by inspection of $\text{Pos}(G)$ (Figure 7f); $\text{Pos}(G)$ initially decreases with increasing boron content and then settles at $\sim 1590 \text{ cm}^{-1}$. Hence, low boron content BC_x' initially exhibits a nanocrystalline graphitic structure near the transition from stage 2 to stage 1 of the amorphization trajectory, shifting further into stage 1 for $x \leq 20$. This trend is corroborated by XRD analysis, showing a decrease in d_{002} and an increase in L_c and L_a as a function of increasing boron content (Figure 6d–f). Despite increasing ordering, increasing boron content results in an increase in $I(D)/I(G)$, until the composition saturates (at ~ 12 at. % boron as measured

by AES), as shown in Figure 7e. This is a direct result of boron incorporation within the material, as the substitutional boron atoms act as defects that break symmetry and activate the D mode.²³ The G mode, on the other hand, arises from the relative motion of all sp^2 -hybridized lattice site occupants and its intensity is not expected to be greatly affected by the boron content. Hence, an increasing $I(D)/I(G)$ with increasing boron content is associated exclusively with an increased contribution from the D mode that has been activated by substitutional boron atoms. $FWHM(D)$ also increases with boron content because of an increase in the number and type of defects (e.g., a- BC_3 , $BC_{3-x}B_x$, g- BC_3 , or BO_3). Last, $FWHM(G)$ increases as a function of boron content, which can be explained by two phenomena: increasing intensity of the D' peak that presents as a high-frequency shoulder of the G peak and the difference in mass of boron and carbon that leads to slight perturbations of the phonon frequency.²³

Phonon Dispersion Relation

Many features of the Raman spectrum of graphitic materials are sensitively dependent on the excitation energy, E_L . In particular, $I(D)/I(G)$ increases as excitation energy decreases (see Figure S2b).^{34,52,53} This significantly changes the appearance of the Raman spectrum and emphasizes that $I(D)/I(G)$ is only a useful metric for the comparison of graphitic materials when measured with the same E_L . Of particular interest in this work is the E_L dependence of $Pos(D)$, a relation referred to as $Disp(D)$ that probes the phonon structure of the highest optical branch around the K point. In highly crystalline graphitic systems, the introduction of a low concentration of defects leads to a well-defined $Disp(D)$ of $50\text{--}60\text{ cm}^{-1}\text{ eV}^{-1}$.⁵⁴ Similar values of $Disp(D)$ are observed across a plethora of other graphitic systems exhibiting a variety of defect types and concentrations.^{25,34} The dispersion of the D peak is a result of the steep slope of the Kohn anomaly

located on the TO phonon branch near the first Brillouin zone corner K (see Figure S7). On the other hand, the TO branch for single-layer BC₃, the highest boron content investigated in this work, shows no evidence for a Kohn anomaly at the K point, and it would therefore be expected that pure, crystalline BC₃' exhibits no dependence of Pos(D) on excitation energy, E_L.

The phonon dispersion relation of the D peak in the BC₃' temperature series and the BC_x' composition series is shown in Figure 8. Boron-free materials (C' and CBr_x') and low boron content materials (BC_x' with x = 20 and 30) show a Disp(D) of ~45 to 55 cm⁻¹ eV⁻¹. Similarly, BC₃' materials synthesized at ≥1000 °C exhibit a dispersion of ~55 cm⁻¹ eV⁻¹ or larger. On the other hand, BC₃' materials synthesized at 950 °C or lower exhibit a distinctly lower Disp(D) between 30 and 40 cm⁻¹ eV⁻¹. It should be noted that the dispersion of the G peak in all materials was found to be ~0, supporting the classification of these materials as stage 1 and 2 graphitic carbon in the Ferrari amorphization trajectory, composed primarily of sp²-hybridized lattice sites.⁴¹

The temperature series of CBr_x' materials was examined to determine if the presence of bromine is a cause of the observed shift in Disp(D). However, these materials show an even higher Disp(D) of ~60 cm⁻¹ eV⁻¹ over the entire temperature range studied herein. This demonstrates that the presence of bromine is not responsible for the unusually low Disp(D) of the BC₃' materials synthesized at or below 950 °C. The C' materials do have a somewhat lower dispersion of ~43 cm⁻¹ eV⁻¹ when synthesized at very low temperatures (only at 750 °C in this work). However, such materials are poorly crystalline and exhibit a D peak that is not well defined (a broad low-energy shoulder complicates the fitting analysis). At 800 °C, the Disp(D) of C' is ~50 cm⁻¹ eV⁻¹ and further heating to 1000 °C continues to increase the Disp(D) to a maximum of ~65 cm⁻¹ eV⁻¹,

similar to highly defected CBr_x' . Above 1000 °C, the Disp(D) of C' returns to $\sim 50 \text{ cm}^{-1} \text{ eV}^{-1}$, as expected for typical forms of nanocrystalline graphitic carbon.

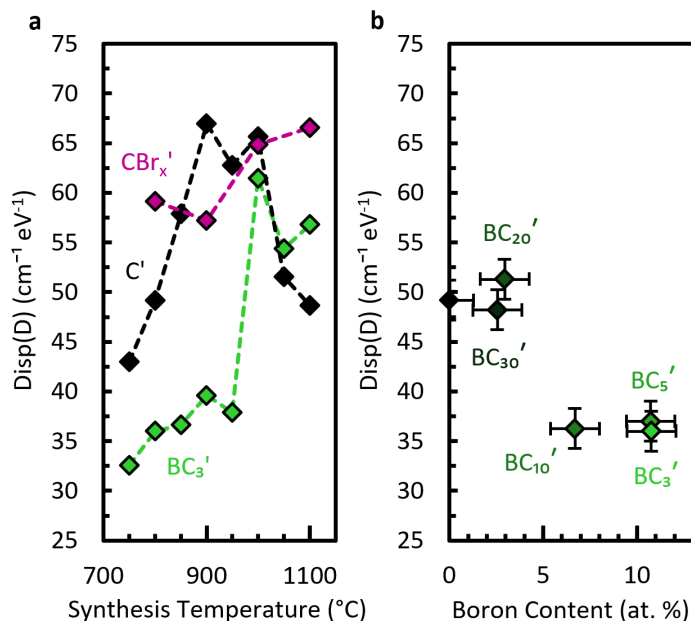


Figure 8. Phonon dispersion of the D mode. (a) Disp(D) as a function of synthesis temperature for BC_3' , C' , and CBr_x' temperature series materials. (b) Disp(D) as a function of the measured boron content within the BC_x' composition series synthesized at 800 °C.

Unlike C' and CBr_x' , directly synthesized BC_3' has an unusually low Disp(D) of ~ 30 to $40 \text{ cm}^{-1} \text{ eV}^{-1}$ when synthesized between 750 and 950 °C, as seen in Figure 8a. This temperature range favors the prevalence of trigonal planar g- BC_3 environments (as evidenced by XAS, Figure 5e). Hence, g- BC_3 environments are likely responsible for the distinctly low value of Disp(D) observed in high boron-content BC_x' synthesized at or below 950 °C. At or above 1000 °C, the boron in any would-be g- BC_3 environments is subject to phase separation into low boron-content graphitic domains (with $< 3 \text{ at.}\% \text{ B}$) and boron carbide, as indicated by XAS. The low boron-content disordered graphitic carbon exhibits a Disp(D) of $\sim 50 \text{ cm}^{-1} \text{ eV}^{-1}$, consistent with many other varieties of graphitic carbon. Disp(D) as a function of boron content for the BC_x' materials

synthesized at 800 °C is shown in Figure 8b. At low boron compositions ($x = 20$ and 30), Disp(D) is $\sim 50 \text{ cm}^{-1} \text{ eV}^{-1}$. According to XAS results, the boron in these materials is mainly composed of a- BC_3 environments (Figure 5d) that do not have a large influence on the phonon structure of the graphitic nanocrystals. At higher boron compositions ($x = 10, 5,$ and 3), Disp(D) is $\sim 36 \text{ cm}^{-1} \text{ eV}^{-1}$ and g- BC_3 is the dominant boron carbon bonding environment indicated by XAS (Figure 5d).

A reduced Disp(D) of $37 \text{ cm}^{-1} \text{ eV}^{-1}$ has also been observed for highly ordered boron-doped graphene produced by the exfoliation of equilibrium solid-solution boron-doped graphite formed at 2450 °C (corresponding to a substitutional boron content of 0.22 at. %). This effect can be explained by electron–hole doping of the pristine graphene lattice, resulting from the dilute presence of electron deficient boron substitutions.^{25,55} The high boron content in bulk BC_x' produced herein, however, prohibits an explanation of the reduced Disp(D) because of hole doping.⁵⁵ Instead, DFT calculated phonon dispersion diagrams of single-layer BC_3 reveal a ring breathing mode with similar A_{1g} symmetry to the well-known D mode in graphite/graphene (see Figure S7 and Figure S8). This phonon originates from a flat optical branch around K, resulting in a lower observed Disp(D) for the breathing mode in BC_3' (which exhibits a mixed character between BC_3' and pure graphite). The breathing mode in BC_3' is also calculated to exhibit a higher frequency than the D mode in graphite, resulting in an increase in Pos(D) at all E_L , in excellent agreement with experimental results (see Figure S2b). The Disp(D) of $30\text{--}40 \text{ cm}^{-1} \text{ eV}^{-1}$ observed in BC_3' , BC_5' , and BC_{10}' can be explained by a hindered phase separation of the developing metastable material and therefore the presence of a significant population of g- BC_3 structures that are required to exhibit the phonons responsible for the distinctly lower value of Disp(D) . In BC_{20}' and BC_{30}' , the concentration of boron is not sufficient to form g- BC_3 units under the synthesis

conditions explored; instead, there is a random distribution of a-BC₃ within the graphitic lattice that exhibits the standard D mode of defected boron-free graphite. Once the boron concentration reaches a threshold, observed herein between BC₂₀' and BC₁₀', the majority of the boron exists in g-BC₃ domains that facilitate the phonon responsible for the observed dispersion relation of ~30 to 40 cm⁻¹ eV⁻¹.

Conclusions

Directly synthesized bulk boron-doped graphitic carbon exhibits a uniquely reduced D peak dispersion relation of 30–40 cm⁻¹ eV⁻¹ when the concentration of boron within the graphitic lattice exceeds ~3 at.%, a condition that favors ordered, trigonal planar BC₃ chemical environments. This has been confirmed by complementary XRD, Raman spectroscopy, and XAS studies that decouple the effects of boron doping on the structure and composition of the underlying lattice. The unique, metastable phase of high boron-content graphitic carbon is only accessible between synthesis temperatures of 800–950 °C; at temperatures of ≥1000 °C, a phase separation between boron carbide and the graphitic solution occurs, resulting in a leaching of boron from the graphitic phase. Bulk graphitic materials prepared without substitutional boron (or with undetectable quantities of g-BC₃ environments), while exhibiting many similar features in their respective XRD patterns and Raman spectra, exhibit a higher D peak dispersion relation of ~50 cm⁻¹ eV⁻¹, characteristic of common graphite. Hence, the D peak dispersion can be used to uniquely identify bulk graphitic materials with a substitutional boron content approaching BC₃, which are of high interest in applications ranging from hydrogen storage to lithium-ion batteries.

Associated ContentSupporting Information

X-Ray Diffraction (XRD): Analysis of the as-measured XRD patterns (RD) was accomplished by direct subtraction of the background (BGD) based on an identical experiment performed without any sample. The resulting pattern (BGSD) was fitted to the combination of a linear background (BG), a single Lorentzian for the (002) reflection (referred to as L_1), and two Lorentzians for the (10) region (referred to as L_2 and L_3) comprised of the (100) and (101) reflections of crystalline graphite. A representative example is shown in Figure S1.

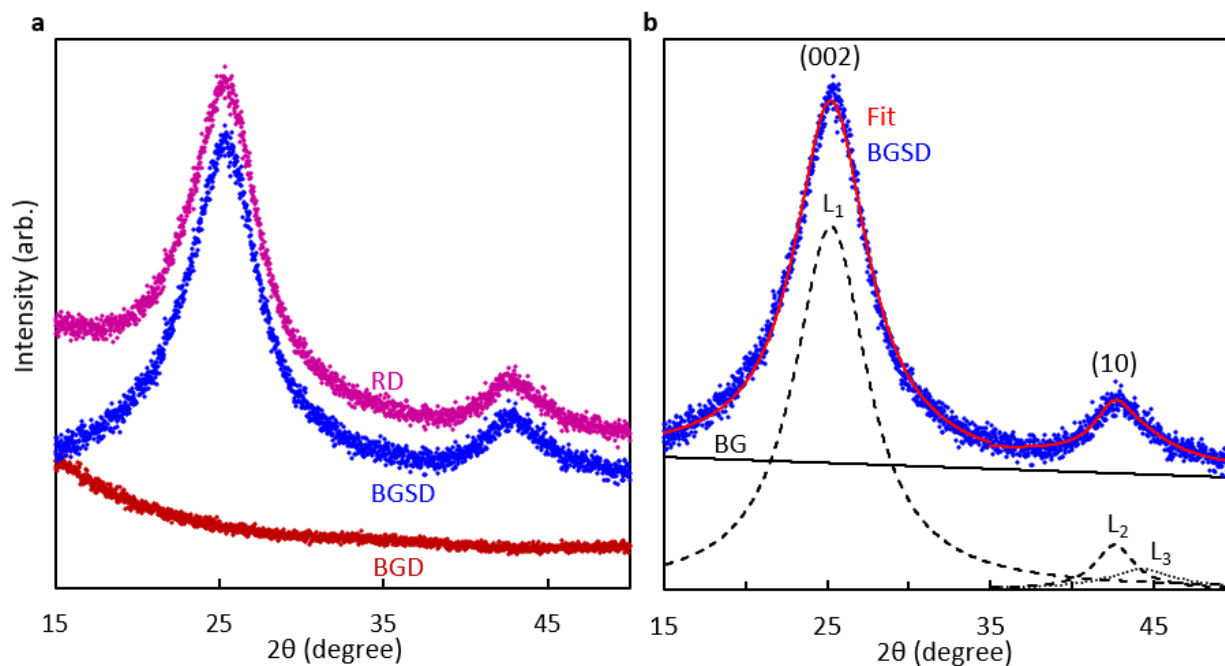


Figure S1. XRD pattern analysis. (a) The raw data (RD), measured background data (BGD), and background-subtracted data (BGSD) of BC_3' synthesized at 800 °C as a representative graphitic carbon material. (b) The BGSD fitted to the combination of a linear background (BG), a single Lorentzian (L_1) for the (002) reflection, and two Lorentzians for the (10) family of reflections (L_2 and L_3).

The peak center of L_1 was related to the d-spacing via Bragg's law, Equation 1, and the full-width at half-maxima (FWHM) of L_1 and L_2 were used to estimate the crystallite size in the c and a axes (referred to as L_c and L_a , respectively) via the Scherrer equation, Equation 2. The d-spacing and Scherrer size estimates based on the (002) reflection correspond to c-axis (layer-to-layer) ordering whereas the size estimate based on the (10) reflections corresponds to a-axis (in-plane) ordering.⁵⁶

$$d = \frac{1.54 \text{ \AA}}{2 \sin \theta} \quad (1)$$

$$L = \frac{0.9 \lambda}{(\text{FWHM}) \cos \theta} \quad (2)$$

The FWHM in the Scherrer equation corresponds to the width of the reflection in 2θ , in radians. When plotting the resulting XRD patterns for comparison (Figure 2a and Figure 3a of the main text), the intensity of each pattern was normalized based on the maximum of the (002) reflection.

Raman Spectroscopy: The region containing the D and G peaks in each Raman spectrum was fitted using a previously established method based on the combination of a Lorentzian and a Breit-Wigner-Fano (BWF) line shape.⁵³ The D peak was fitted to a single Lorentzian (referred to as L_4), the G peak was fitted to a single BWF, and the baseline was approximated by a linear background (BG), as shown in Figure S2a. The combination of a Lorentzian and a BWF provides a profile with minimal fitting parameters that can effectively fit the Raman spectrum of a wide range of graphitic carbon materials. The BWF line shape is given by Equation 3:

$$I(\omega) = \frac{I_0 [1 + 2(\omega - \omega_0/Q\Gamma)]^2}{1 + [2(\omega - \omega_0)/\Gamma]^2} \quad (3)$$

Where I_0 is the peak intensity, ω_0 is the peak position, Γ is the FWHM, and Q is the BWF coupling coefficient. A negative Q value tails the BWF toward lower frequency and accounts for residual intensity between the D and G peaks. Due to the asymmetry of the BWF line shape, ω_0 does not lie at the frequency of the peak maximum (ω_{\max}) as in a simple Lorentzian or Gaussian function. To correct for this, Equation 4 was applied to determine ω_{\max} . Since Q is negative, ω_{\max} lies at a lower wavenumber than ω_0 .

$$\omega_{\max} = \omega_0 + \frac{\Gamma}{2Q} \quad (4)$$

$I(D)/I(G)$ was determined for each material based on the ratio of the peak maximum (I_0) of L_4 to that of the BWF. $\text{FWHM}(D)$ and $\text{FWHM}(G)$ were determined based on Γ of the L_4 and BWF fits, respectively. $\text{Pos}(D)$ was determined based on ω_0 of L_4 and $\text{Pos}(G)$ was determined by applying Equation 4 to ω_0 of the BWF fit. The process for determining $\text{Disp}(D)$ from a set of Raman spectra of varying E_L is demonstrated in Figure S2b-d. In this work, Raman spectra were collected at $E_L = 532, 633, \text{ and } 785 \text{ nm}$. The shift in $\text{Pos}(D)$ as E_L decreases in energy is shown. The change in $\text{Pos}(D)$ as a function of E_L is approximately linear, and the slope of this line is $\text{Disp}(D)$ in units of $\text{cm}^{-1} \text{ eV}^{-1}$. When plotting the Raman spectra for comparison (Figure S2c-d as well as Figure 2b and Figure 3b of the main text), the intensity was normalized based on the maximum of the G peak.

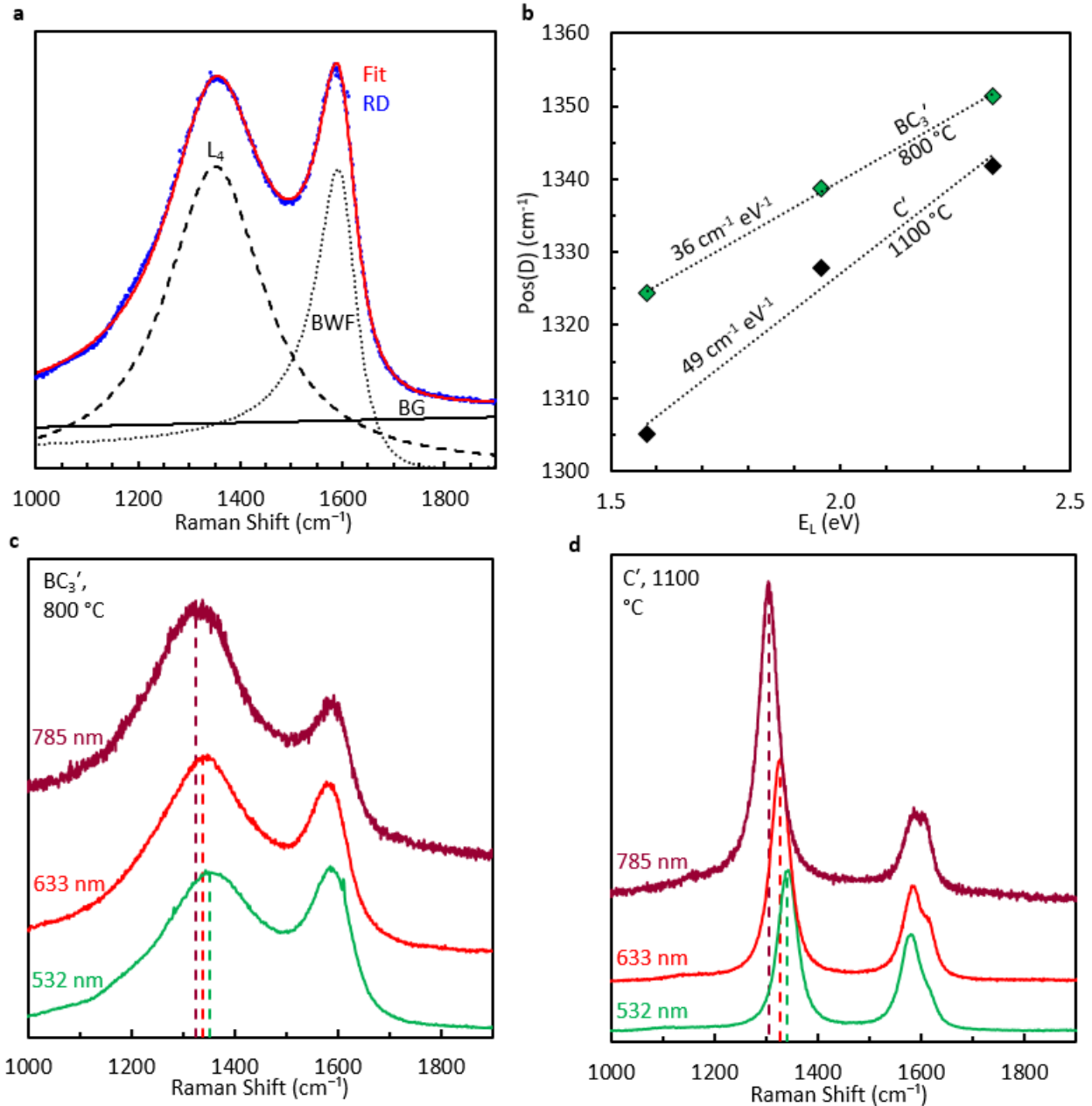


Figure S2. Raman spectrum analysis. (a) The raw data (RD) fitted to the combination of a linear background (BG), a single Lorentzian (L_4) for the D peak, and a single BWF for the G peak. The Raman spectrum of BC_3' synthesized at 800°C (analyzed at $E_L = 532 \text{ nm}$) is shown as a representative example. (b) The E_L dependence of $\text{Pos}(D)$ used to calculate $\text{Disp}(D)$ for two materials: (c) BC_3' synthesized at 800°C and (d) C' synthesized at 1100°C .

X-Ray Absorption Spectroscopy (XAS): Analysis of the XAS spectra was accomplished by dividing the measured total fluorescence yield (TFY) by the intensity of the incident X-ray beam. This accounts for fluctuations in beam intensity. The corrected spectrum was then normalized based on the pre- and post-edge step height. This provides a physically meaningful comparison between spectra since the pre-edge intensity corresponds to the minimum fluorescence observed and the post-edge intensity results from the excitation of a continuum of states within the bulk material and is expected to be relatively constant. The observed intensities of XAS features should not be directly related to concentrations of specific species within the sample since the scattering cross-sections for different excitations must be considered. As a result, the boron oxide signal observed in all materials investigated is disproportionately large.

The carbon K-edge of the BC₃' temperature series was also investigated to confirm the graphitic nature of the materials and is shown in Figure S3. The development of a strong angle dependent π^* absorption at 285.5 eV as well as a pronounced σ^* transition at ~292 eV is evident of the improving hexagonal graphitic structure as synthesis temperature increases.

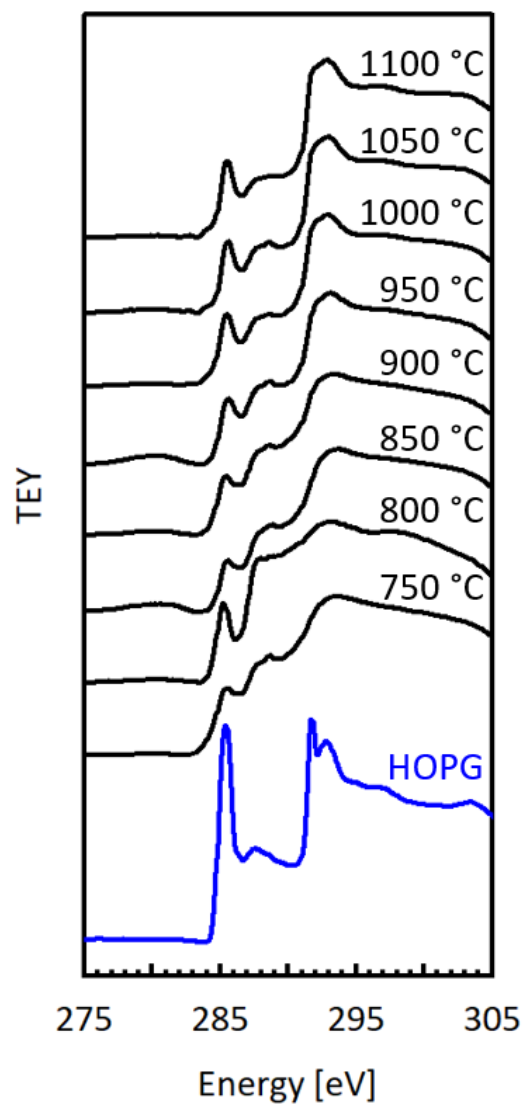


Figure S3. Carbon chemical environment. XAS spectrum near the C K-edge of the BC₃' temperature series (Black), and HOPG (Blue) as a standard.

Energy Dispersive X-Ray Spectroscopy (EDX): The raw EDX spectra of the BC_x' composition series are shown in Figure S4a. The intensities of the B $K\alpha$ transition as well as the O $K\alpha$ and Br $L\alpha$ transitions increase as a function of nominal boron content. The boron content was determined using sensitivity factors for B, C, O, and Br as implemented by Bruker ESPRIT microanalysis software. As seen in Figure S4b, the raw data (RD) overestimate the amount of boron in the material at low compositions; as a result, it is necessary to apply a baseline subtraction (BGSD) to the measured boron content. A correction factor is then applied to the BGSD to bring the measured boron content of the boron carbide (B_4C) standard up to 80 at. %. The corrected data (CD) show an incorporation limit of boron in carbon at ~ 11 at.%. The maximum amount of bromine measured in any BC_x' material was < 0.5 at.%.

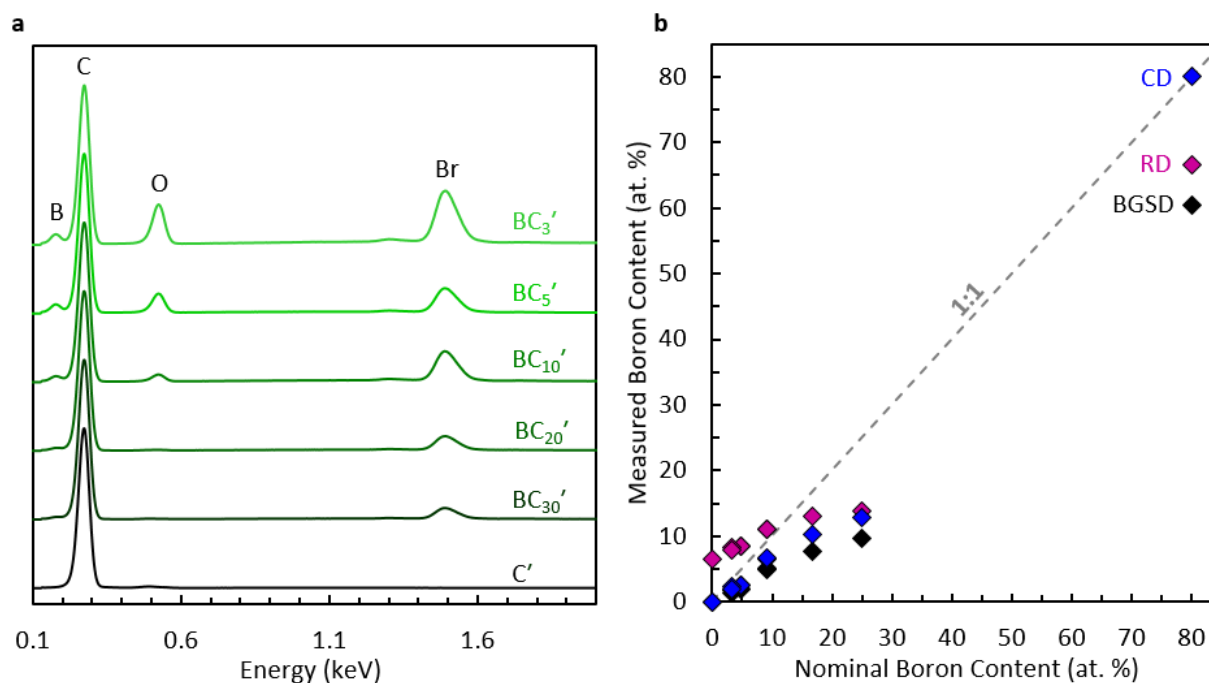


Figure S4. EDX spectrum analysis. (a) EDX spectrum of the BC_x' composition series. (b) The boron content was determined for the BC_x' composition series as well as a boron carbide standard.

Auger Electron Spectroscopy (AES): Auger electron spectra (AES) of the BC_x' composition series are shown in Figure S5a-c. In qualitative agreement with EDX results, the intensity of the B KLL and O KLL transitions increase with increasing nominal boron content. Quantification of the smoothed and differentiated AES spectra was performed using sensitivity factors as implemented by PHI MultiPak analysis software. The raw data (RD) and background subtracted data (BGSD) are shown in Figure S5d. A correction factor was applied to bring the measured boron content of a boron carbide standard (B_4C) up to 80 at.%, shown as corrected data (CD).

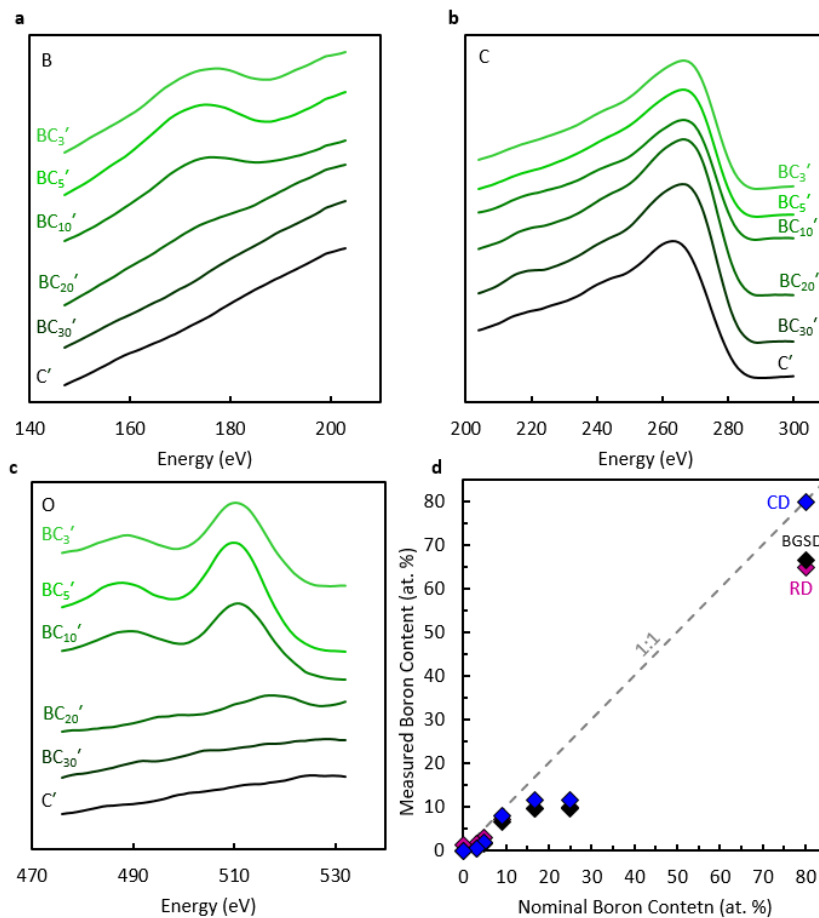


Figure S5. AES spectrum analysis. Raw AES spectra for the (a) B K-LL, (b) C K-LL, and (c) O K-LL transitions of the BC_x' composition series. (b) The boron content was determined for the BC_x' composition series as well as a boron carbide standard.

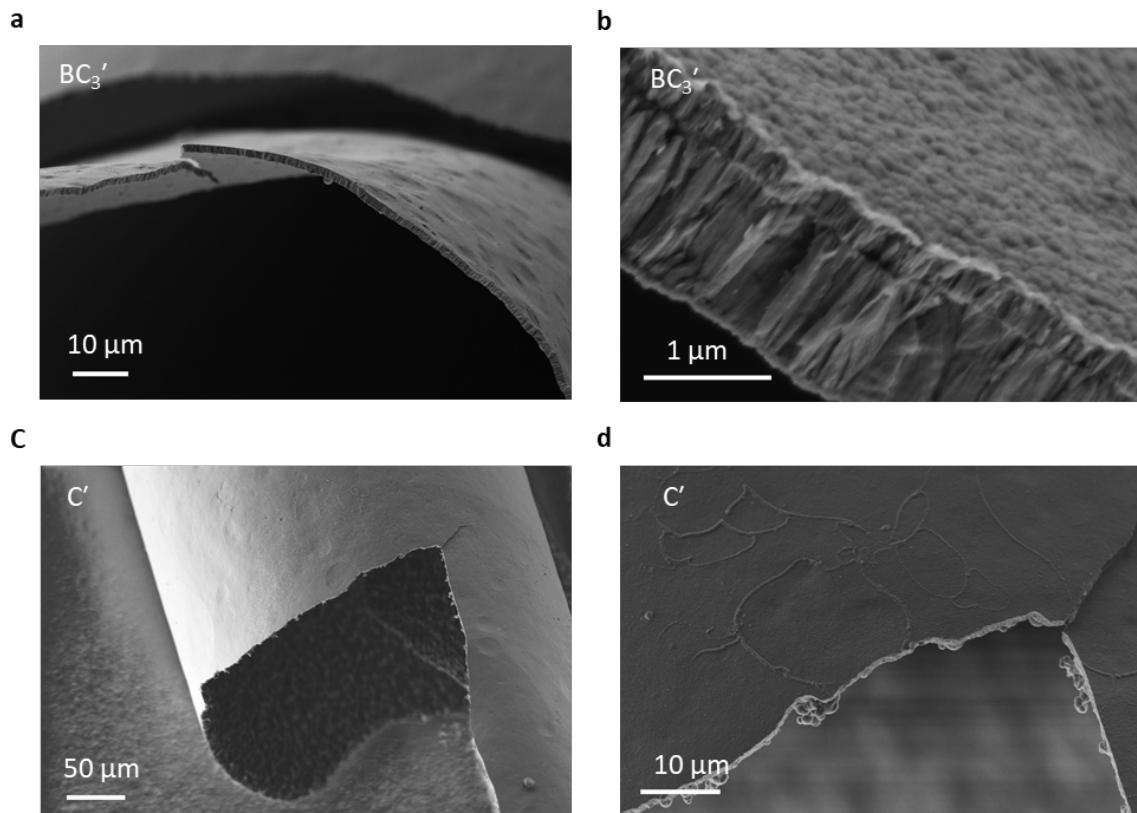
Scanning Electron Microscopy (SEM):

Figure S6. Scanning electron microscopy. SEM images of BC₃' (a) and (b), as well as SEM images of C' material (c) and (d).

Phonon Dispersion Calculations: The unfolded phonon dispersion diagrams along the high-symmetry directions of the Brillouin zone for graphene, BC₇, and BC₃, calculated at the PBE level of DFT, are shown in Figure S7. The lattice motion associated with the high frequency TO phonon at the K point is illustrated for four phonons of interest likely to contribute to the D peak in the Raman spectrum of BC_x' in Figure S8. The TO phonon in graphene (red circle, Figure S7a), referred to as a "ring breathing" mode, exhibits A_{1g} symmetry (Figure S8a). The frequency of this phonon is calculated to be 1281 cm⁻¹ at the K point, but exhibits a distinct Kohn anomaly and therefore gives rise to a D peak with a strong dispersion relation. We note that the phonon

dispersion diagram for graphene was calculated based on a supercell containing 8 atoms, and hence exhibits a number of spurious branches even after unfolding (including some apparent higher optical modes at the K point that are not physically meaningful).

A similar “ring breathing” mode is not present in single-layer BC₇ owing to reduced symmetry; there are no six-membered carbon rings exhibiting bonding environments with hexagonal symmetry. The six-fold axis of symmetry has been replaced by a three-fold axis. The highest symmetry vibrational mode at the K-point in this range of frequency shows breathing-like “ring distortion:” the three carbon-carbon bonds around the three-fold rotational axes elongate, while the three carbon-boron bonds remain stationary (Figure S8b). This mode exhibits a frequency of 1289 cm⁻¹ at the K point (purple circle, Figure S7b). Both types of modes appear for single-layer BC₃ owing to the reemergence of six-fold axes of symmetry at the center of each pure carbon ring (blue circles, Figure S7c): a “ring breathing” mode at 1363 cm⁻¹ (Figure S8c) and a “ring distorting” mode at 1304 cm⁻¹ (Figure S8d). By symmetry considerations, only the “ring breathing” modes in graphene and BC₃’ are truly comparable in their contributions to the position, intensity, and dispersion of the D peak measured in the Raman spectrum of graphitic BC_x’ materials. The “ring breathing” mode at 1363 cm⁻¹ in BC₃’ is flat at near the K point and hence would give rise to a D peak with a negligible dispersion relation.

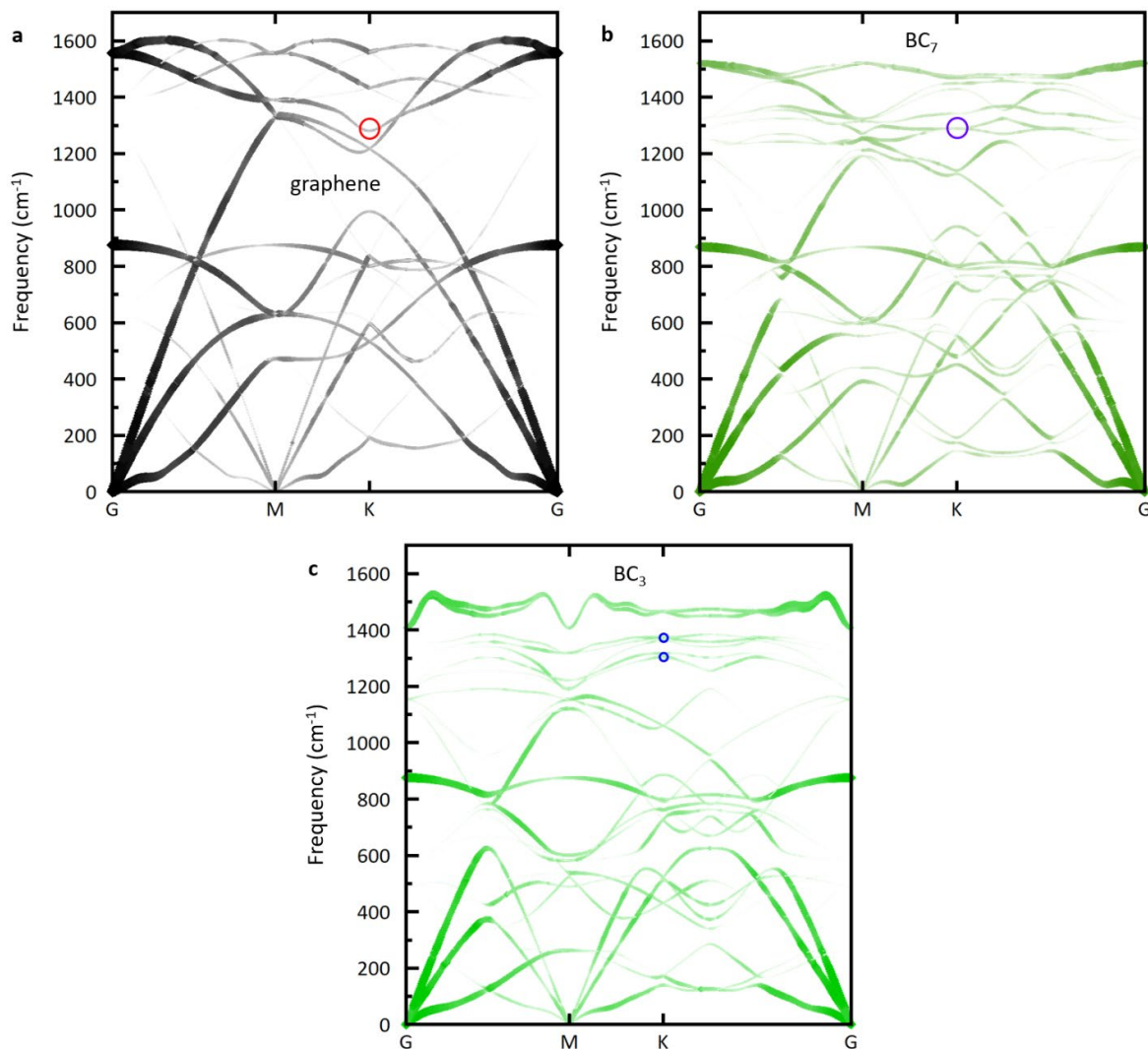


Figure S7. Calculated phonon dispersion diagrams for (a) graphene, (b) single-layer BC₇, and (c) single-layer BC₃'. The optical modes (possibly) contributing to the D peak in the Raman spectrum of BC_x' are shown in the red, purple, and blue circles, respectively.

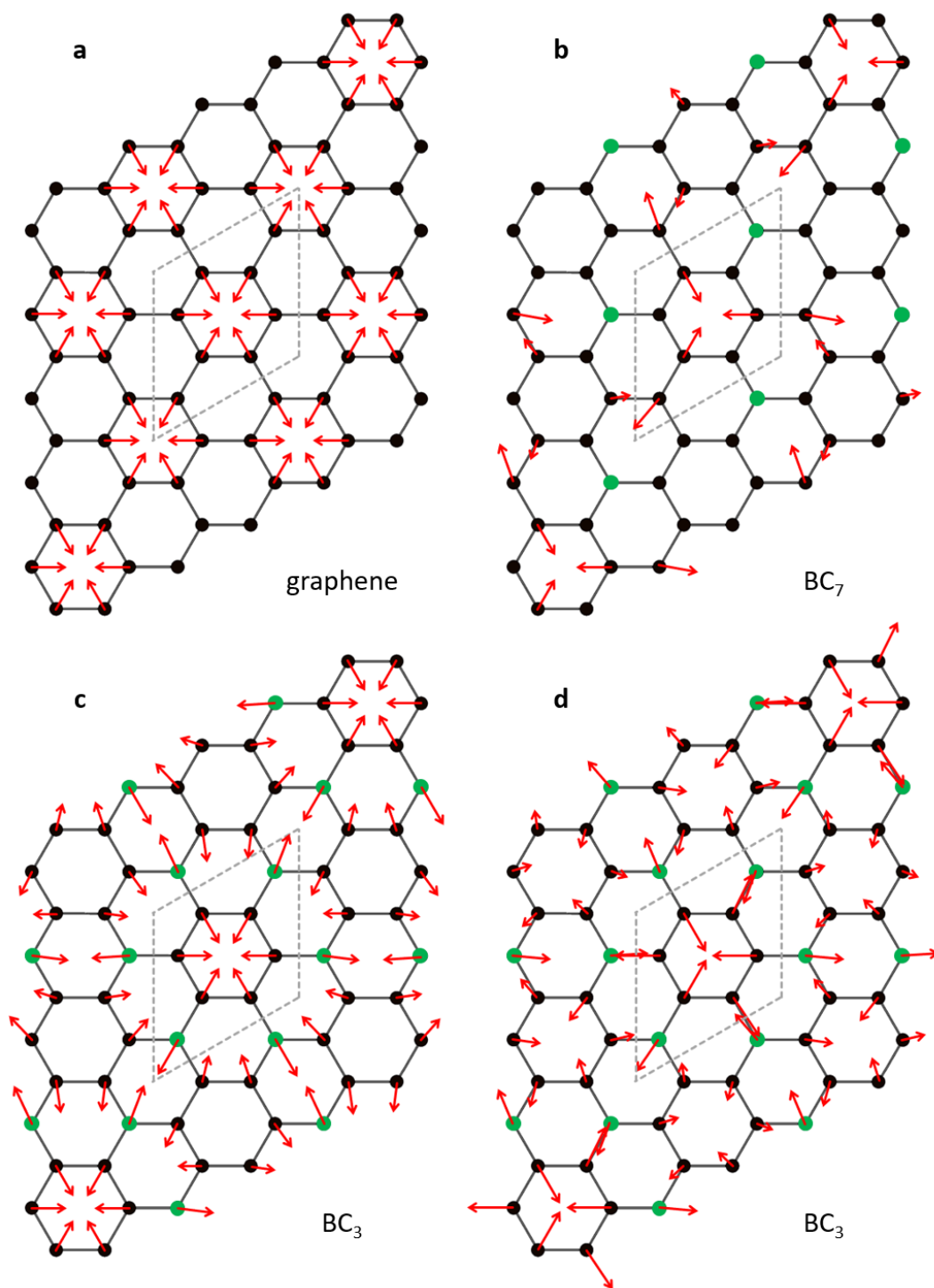


Figure S8. Vibrational modes corresponding to phonon branches of (a) graphene, (b) single-layer BC_7 , and (c-d) single-layer BC_3' at near the measured D peak frequency in graphitic BC_x' materials, at frequencies of 1281, 1289, 1363, and 1304 cm^{-1} , respectively. Carbon is shown in black, boron in green, and the 8-atom cell used for calculations in gray.

Corresponding Author

Nicholas P. Stadie – Department of Chemistry & Biochemistry, Montana State University, Bozeman, Montana 59717, United States; orcid.org/0000-0002-1139-7846;
Email: nstadie@montana.edu

Authors

Devin McGlamery – Department of Chemistry & Biochemistry, Montana State University, Bozeman, Montana 59717, United States

Alexander A. Baker – Materials Science Division, Lawrence Livermore National Laboratory, Livermore, California 94550, United States; orcid.org/0000-0003-0700-0858

Yi-Sheng Liu – Advanced Light Source, Lawrence Berkeley National Laboratory, Berkeley, California 94720, United States; orcid.org/0000-0002-1085-1947

Martín A. Mosquera – Department of Chemistry & Biochemistry, Montana State University, Bozeman, Montana 59717, United States; orcid.org/0000-0003-2170-5651

Complete contact information is available at: <https://pubs.acs.org/10.1021/acs.jpcc.0c06918>

Author Contributions The manuscript was written through contributions of all authors.

Notes: The authors declare no competing financial interest.

Acknowledgments

We thank Nicholas J. Borys for insightful discussions. We acknowledge the donors of the American Chemical Society Petroleum Research Fund for support of this research. We thank the Montana Nanotechnology Facility (MONT, an NNCI facility supported by National Science Foundation grant ECCS-1542210) for the use of their instrumentation. We acknowledge research support from the U.S. Department of Energy (DOE), Office of Energy Efficiency and Renewable

Energy, Fuel Cell Technologies Office through the Hydrogen Storage Materials Advanced Research Consortium (HyMARC). This research employed resources of the Advanced Light Source (Beamline 8.0.1) which is a DOE Office of Science User Facility under Contract no. DE-AC0205CH11231. Portions of this work were performed under the auspices of the DOE by Lawrence Livermore National Laboratory under Contract no. DE-AC52-07NA27344.

References

- (1) Breckenridge, R. G. *Thermoelectric Materials Final Report*; Union Carbide Corp.: Parma, OH, 1960.
- (2) Woodley, R. E. The Oxidation of Boronated Graphite. *Carbon* **1968**, *6*, 617–626.
- (3) Fecko, D. L.; Jones, L. E.; Thrower, P. A. The formation and oxidation of BC₃, a new graphitelike material. *Carbon* **1993**, *31*, 637–644.
- (4) Cermignani, W.; Paulson, T. E.; Onneby, C.; Pantano, C. G. Synthesis and Characterization of Boron-Doped Carbons. *Carbon* **1995**, *33*, 367–374.
- (5) Shirasaki, T.; Derré, A.; Mé né trier, M.; Tressaud, A.; Flandrois, S. Synthesis and characterization of boron-substituted carbons. *Carbon* **2000**, *38*, 1461–1467.
- (6) Davidson, J. M.; Gates, L. O.; Nightingale, R. E. Radiation Damage Effects in Borated Graphite. *Nucl. Sci. Eng.* **1966**, *26*, 90–98.
- (7) Way, B. M.; Dahn, J. R.; Tiedje, T.; Myrtle, K.; Kasrai, M. Preparation and characterization of B_xC_{1-x} thin films with the graphite structure. *Phys. Rev. B: Condens. Matter Mater. Phys.* **1992**, *46*, 1697–1702.
- (8) Kouvetakis, J.; Kaner, R. B.; Sattler, M. L.; Bartlett, N. A novel graphite-like material of composition BC₃, and nitrogen–carbon graphites. *J. Chem. Soc., Chem. Commun.* **1986**, 1758–1759.
- (9) King, T. C.; Matthews, P. D.; Glass, H.; Cormack, J. A.; Holgado, J. P.; Leskes, M.; Griffin, J. M.; Scherman, O. A.; Barker, P. D.; Grey, C. P.; et al. Theory and practice: bulk synthesis of C3B and its H₂- and Li-storage capacity. *Angew. Chem., Int. Ed.* **2015**, *54*, 5919–5923.
- (10) Stadie, N. P.; Billeter, E.; Piveteau, L.; Kravchyk, K. V.; Döbeli, M.; Kovalenko, M. V. Direct Synthesis of Bulk Boron-Doped Graphitic *Carbon. Chem. Mater.* **2017**, *29*, 3211–3218.

- (11) Endo, M.; Kim, C.; Karaki, T.; Nishimura, Y.; Matthews, M. J.; Brown, S. D. M.; Dresselhaus, M. S. Anode performance of a Li ion battery based on graphitized and B-doped milled mesophase pitchbased carbon fibers. *Carbon* **1999**, *37*, 561–568.
- (12) Liu, Y.; Artyukhov, V. I.; Liu, M.; Harutyunyan, A. R.; Yakobson, B. I. Feasibility of Lithium Storage on Graphene and Its Derivatives. *J. Phys. Chem. Lett.* **2013**, *4*, 1737–1742.
- (13) Joshi, R. P.; Ozdemir, B.; Barone, V.; Peralta, J. E. Hexagonal BC₃: A Robust Electrode Material for Li, Na, and K Ion Batteries. *J. Phys. Chem. Lett.* **2015**, *6*, 2728–2732.
- (14) Fitzhugh, W.; Li, X. Modulation of Ionic Current Limitations by Doping Graphite Anodes. *J. Electrochem. Soc.* **2018**, *165*, A2233–A2238.
- (15) Zhang, C.; Alavi, A. Hydrogen absorption in bulk BC₃: a firstprinciples study. *J. Chem. Phys.* **2007**, *127*, 214704.
- (16) Firlej, L.; Kuchta, B.; Wexler, C.; Pfeifer, P. Boron substituted graphene: energy landscape for hydrogen adsorption. *Adsorption* **2009**, *15*, 312.
- (17) Zhu, Z. H.; Lu, G. Q.; Hatori, H. New Insights into the Interaction of Hydrogen Atoms with Boron-Substituted Carbon. *J. Phys. Chem. B* **2006**, *110*, 1249–1255.
- (18) Sha, X.; Cooper, A. C.; Bailey, W. H.; Cheng, H. Revisiting Hydrogen Storage in Bulk BC₃. *J. Phys. Chem. C* **2010**, *114*, 3260–3264.
- (19) Nayyar, I.; Ginovska, B.; Karkamkar, A.; Gennett, T.; Autrey, T. Physi-Sorption of H₂ on Pure and Boron-Doped Graphene Monolayers: A Dispersion-Corrected DFT Study. *C* **2020**, *6*, 15.
- (20) Bult, J. B.; Lee, J.; O'Neill, K.; Engtrakul, C.; Hurst, K. E.; Zhao, Y.; Simpson, L. J.; Parilla, P. A.; Gennett, T.; Blackburn, J. L. Manipulation of Hydrogen Binding Energy and Desorption Kinetics by Boron Doping of High Surface Area Carbon. *J. Phys. Chem. C* **2012**, *116*, 26138–26143.
- (21) Lowell, C. E. Solid Solution of Boron in Graphite. *J. Am. Ceram. Soc.* **1967**, *50* (3), 142–144.
- (22) Elman, B. S.; Dresselhaus, M. S.; Dresselhaus, G.; Maby, E. W.; Mazurek, H. Raman scattering from ion-implanted graphite. *Phys. Rev. B: Condens. Matter Mater. Phys.* **1981**, *24*, 1027–1034.
- (23) Naeini, J. G.; Way, B. M.; Dahn, J. R.; Irwin, J. C. Raman scattering from boron-substituted carbon films. *Phys. Rev. B: Condens. Matter Mater. Phys.* **1996**, *54*, 144–151.
- (24) Kouvetakis, J.; McElfresh, M. W.; Beach, D. B. Chemical vapor deposition of highly conductive boron-doped graphite from triphenyl boron. *Carbon* **1994**, *32*, 1129–1132.

- (25) Kim, Y. A.; Fujisawa, K.; Muramatsu, H.; Hayashi, T.; Endo, M.; Fujimori, T.; Kaneko, K.; Terrones, M.; Behrends, J.; Eckmann, A.; et al. Raman Spectroscopy of Boron-Doped Single-Layer Graphene. *ACS Nano* **2012**, *6*, 6293–6300.
- (26) Hagio, T.; Nakamizo, M.; Kobayashi, K. Studies on X-ray diffraction and Raman spectra of B-doped natural graphite. *Carbon* **1989**, *27*, 259–263.
- (27) Serin, V.; Brydson, R.; Scott, A.; Kihn, Y.; Abidate, O.; Maquin, B.; Derré, A. Evidence for the solubility of boron in graphite by electron energy loss spectroscopy. *Carbon* **2000**, *38*, 547–554.
- (28) Kim, E.; Oh, I.; Kwak, J. Atomic structure of highly ordered pyrolytic graphite doped with boron. *Electrochem. Commun.* **2001**, *3*, 608–612.
- (29) Tuinstra, F.; Koenig, J. L. Raman Spectrum of Graphite. *J. Chem. Phys.* **1970**, *53*, 1126–1130.
- (30) Ferrari, A. C.; Basko, D. M. Raman spectroscopy as a versatile tool for studying the properties of graphene. *Nat. Nanotechnol.* **2013**, *8*, 235.
- (31) Dresselhaus, M. S.; Jorio, A.; Saito, R. Characterizing Graphene, Graphite, and Carbon Nanotubes by Raman Spectroscopy. *Annu. Rev. Condens. Matter Phys.* **2010**, *1*, 89–108.
- (32) Thomsen, C.; Reich, S. Double Resonant Raman Scattering in Graphite. *Phys. Rev. Lett.* **2000**, *85*, 5214–5217.
- (33) Maultzsch, J.; Reich, S.; Thomsen, C.; Requardt, H.; Ordejón, P. Phonon Dispersion in Graphite. *Phys. Rev. Lett.* **2004**, *92*, 075501.
- (34) Matthews, M. J.; Pimenta, M. A.; Dresselhaus, G.; Dresselhaus, M. S.; Endo, M. Origin of dispersive effects of the Raman D band in carbon materials. *Phys. Rev. B: Condens. Matter Mater. Phys.* **1999**, *59*, R6585.
- (35) Endo, M.; Hayashi, T.; Hong, S.-H.; Enoki, T.; Dresselhaus, M. S. Scanning tunneling microscope study of boron-doped highly oriented pyrolytic graphite. *J. Appl. Phys.* **2001**, *90*, 5670–5674.
- (36) Giannozzi, P.; Baroni, S.; Bonini, N.; Calandra, M.; Car, R.; Cavazzoni, C.; Ceresoli, D.; Chiarotti, G. L.; Cococcioni, M.; Dabo, I.; et al. QUANTUM ESPRESSO: a modular and open-source software project for quantum simulations of materials. *J. Phys.: Condens. Matter* **2009**, *21*, 395502.
- (37) Giannozzi, P.; Andreussi, O.; Brumme, T.; Bunau, O.; Buongiorno Nardelli, M.; Calandra, M.; Car, R.; Cavazzoni, C.; Ceresoli, D.; Cococcioni, M.; et al. Advanced capabilities for materials modelling with Quantum ESPRESSO. *J. Phys.: Condens. Matter* **2017**, *29*, 465901.

- (38) Rappe, A. M.; Rabe, K. M.; Kaxiras, E.; Joannopoulos, J. D. Optimized pseudopotentials. *Phys. Rev. B: Condens. Matter Mater. Phys.* **1990**, *41*, 1227–1230.
- (39) Perdew, J. P.; Burke, K.; Ernzerhof, M. Generalized Gradient Approximation Made Simple. *Phys. Rev. Lett.* **1996**, *77*, 3865–3868.
- (40) Zheng, F.; Zhang, P. Phonon Unfolding: A program for unfolding phonon dispersions of materials. *Comput. Phys. Commun.* **2017**, *210*, 139–144.
- (41) Ferrari, A. C.; Robertson, J. Interpretation of Raman spectra of disordered and amorphous carbon. *Phys. Rev. B: Condens. Matter Mater. Phys.* **2000**, *61*, 14095–14107.
- (42) Caretti, I.; Gago, R.; Albella, J. M.; Jiménez, I. Boron carbides formed by coevaporation of B and C atoms: Vapor reactivity, B_xC_{1-x} composition, and bonding structure. *Phys. Rev. B: Condens. Matter Mater. Phys.* **2008**, *77*, 174109.
- (43) Pallier, C.; Leyssale, J.-M.; Truflandier, L. A.; Bui, A. T.; Weisbecker, P.; Gervais, C.; Fischer, H. E.; Sirotti, F.; Teyssandier, F.; Chollon, G. Structure of an Amorphous Boron Carbide Film: An Experimental and Computational Approach. *Chem. Mater.* **2013**, *25*, 2618–2629.
- (44) Brühwiler, P. A.; Maxwell, A. J.; Puglia, C.; Nilsson, A.; Andersson, S.; Mårtensson, N. π^* and σ^* Excitons in C 1s Absorption of Graphite. *Phys. Rev. Lett.* **1995**, *74*, 614–617.
- (45) Langford, J. I.; Wilson, A. J. C. Scherrer after sixty years: A survey and some new results in the determination of crystallite size. *J. Appl. Crystallogr.* **1978**, *11*, 102–113.
- (46) Murty, H. N.; Biederman, D. L.; Heintz, E. A. Apparent catalysis of graphitization. 3. Effect of boron. *Fuel* **1977**, *56*, 305–312.
- (47) Ōya, A.; Yamashita, R.; Otani, S. Catalytic graphitization of carbons by borons. *Fuel* **1979**, *58*, 495.
- (48) Turnbull, J. A.; Stagg, M. S.; Eeles, W. T. Annealing studies of boron-doped graphite by electron microscopy and X-ray diffraction. *Carbon* **1966**, *3*, 387–392.
- (49) Young, D. A. The intercalation process in graphite-bromine. *Carbon* **1977**, *15*, 373–377.
- (50) Chung, D. D. L. Structure and phase transitions of graphite intercalated with bromine. *Phase Transitions* **1986**, *8*, 35–57.
- (51) Lalancette, J.-M.; Roussel, R. Metals intercalated in graphite. V. A concentration cell with intercalated bromine. *Can. J. Chem.* **1976**, *54*, 3541.
- (52) Sood, A. K.; Gupta, R.; Asher, S. A. Origin of the unusual dependence of Raman D band on excitation wavelength in graphitelike materials. *J. Appl. Phys.* **2001**, *90*, 4494–4497.

- (53) Ferrari, A. C.; Robertson, J. Resonant Raman spectroscopy of disordered, amorphous, and diamondlike carbon. *Phys. Rev. B: Condens. Matter Mater. Phys.* **2001**, 64, 075414.
- (54) Pócsik, I.; Hundhausen, M.; Kócs, M.; Ley, L. Origin of the D peak in the Raman spectrum of microcrystalline graphite. *J. Non-Cryst. Solids* **1998**, 227–230, 1083–1086.
- (55) Attacalite, C.; Wirtz, L.; Lazzeri, M.; Mauri, F.; Rubio, A. Doped Graphene as Tunable Electron–Phonon Coupling Material. *Nano Lett.* **2010**, 10, 1172–1176.
- (56) Langford, J. I.; Wilson, A. J. C. Scherrer after sixty years: A survey and some new results in the determination of crystallite size. *J. Appl. Crystallogr.* **1978**, 11, 102–113.

CHAPTER FIVE

PRECURSOR DECOMPOSITION COMPATIBILITY AS THE KEY TO
THE HALIDE-FREE SYNTHESIS OF METASTABLE BC₃'Contribution of Authors

Manuscript in Chapter 4

Author: Devin McGlamery

Contributions: Synthesized materials, collected data, analyzed data, produced figures, and wrote the manuscript.

Co-Author: Charles McDaniel

Contributions: Assisted in material synthesis and conducted thermochemical calculations

Co-Author: Dylan M. Ladd

Contributions: Assisted in the synthesis of decaborane derived carbons

Co-Author: Yang Ha

Contributions: performed XAS experiments

Co-Author: Martín A. Mosquera

Contributions: Performed thermochemical calculations calculation.

Co-Author: Michael T. Mock

Contributions: Assisted in organic synthesis of NBD precursor

Co-Author: Nicholas P. Stadie

Contributions: Oversaw experimental designed, aided in interpretation of results, and assisted in writing and editing the manuscript.

Manuscript Information

Devin McGlamery[‡], Charles McDaniel[‡], Dylan M. Ladd^{‡†}, Yang Ha[‡], Martín A. Mosquera[‡], Michael T. Mock[‡], and Nicholas P. Stadie[‡]

[‡]Department of Chemistry & Biochemistry, Montana State University, Bozeman, Montana 59717, United States

‡Advanced Light Source, Lawrence Berkeley National Laboratory, Berkeley, California, 94720, United States

† Department of Materials Science & Engineering, University of Colorado, Boulder, Colorado, 80309, United States.

Status of Manuscript:

Prepared for submission to a peer-reviewed journal

Officially submitted to a peer-reviewed journal

Accepted by a peer-reviewed journal

Published in a peer-reviewed journal

Journal of the American Chemical Society

Abstract

Layered BC_3' , a metastable phase within the binary boron-carbon system that is composed of graphite-like sheets with hexagonally symmetric C_6B_6 units, has never been successfully crystallized. Instead, poorly-crystalline BC_3 -like materials with significant stacking disorder have been isolated, based on the co-pyrolysis of a boron trihalide precursor with benzene at around 800 °C. The halide leaving group (-X) is a significant driving force of these reactions, but the subsequent evolution of gaseous HX species at such high temperatures hampers their scaling up and also prohibits their further use in the presence of hard-casting templates such as ordered silicates. Herein, we report a novel halide-free synthesis route to turbostratic BC_3' with long-range in-plane ordering, as evidenced by multi-wavelength Raman spectroscopy. Judicious pairing of the two molecular precursors is crucial to achieving B-C bond formation and preventing phase-segregation into the thermodynamically favored products. A simple computational method used herein to evaluate the compatibility of bottom-up molecular precursors can be generalized to guide the future synthesis of other metastable materials beyond the boron-carbon system.

Introduction

Boron and carbon each exhibit uniquely complex elemental chemistry.¹ In particular, boron has been crystallized in a plethora of allotropic forms owing to the rich chemistry that results from its lack of electrons compared to its number of ground state atomic orbitals.² The vast number of carbon allotropes and their exceptional properties are well-known.³ When combined, boron and carbon give rise to a phase space that is both enormous and often difficult to accurately characterize, owing to the nearly identical size and hybridization states of the two elements. The single thermodynamically-stable binary phase at ambient conditions is boron carbide (nominally B_4C), a structure comprised of the dominant B_{12} icosahedral unit prevalent in boron's elemental phases. However, as might be expected, this phase exhibits wide compositional variability and there remains disagreement as to its formal description as $B_{12}C_3$ or $B_{13}C_2$ ⁴ in its most carbon-rich form.⁵

Numerous theoretical studies⁶⁻⁹ support growing experimental evidence¹⁰⁻¹² for the existence of a high symmetry graphite-like phase of composition BC_3 (Figure 1b). Indeed, the equilibrium solubility of boron in graphite is established to be relatively high: 2.35 at.% at 2375 °C.¹³ Hence, many researchers have reported strategies to isolating metastable¹⁴ BC_3' at ambient conditions,^{12,15-21} an effort that has been intensified owing to the promising theoretical applications of BC_3' for energy storage applications.²²⁻²⁷

Our previous work¹² culminated in the synthesis of a bulk (free-standing) graphite-like material of composition BC_3' via the bottom-up reaction of two molecular precursors: boron tribromide (BBr_3) and benzene (C_6H_6). At that time, previous efforts had only succeeded to produce either thin-films (led by Kouvetakis, Bartlett and coworkers)^{10,16} or oxygen-contaminated

bulk flakes (led by King, Wright, and coworkers)¹¹; our approach combined these two strategies by leveraging the high-purity nature of combining only two commercially-available precursors (similar to the BCl_3 and benzene chosen for the thin-film synthesis) and the liquid miscibility associated with a Br-terminated boron precursor (as inspired by the 1,3-bis-(dibromoboryl)benzene precursor chosen to produce the first free-standing BC_3 -like flakes). The crystalline quality of the resulting products is low, especially with respect to ordering in the stacking direction, but our direct synthesis approach has been shown to yield long-range ordered in-plane structures with a vibrational structure that is consistent with BC_3 '.²¹

The investigation of directly-synthesized BC_3 -like materials for hydrogen storage and for electrochemical energy storage applications has remained severely limited by its inherent release of HBr at elevated temperatures, typically 800 °C, in closed-reactor conditions, preventing the use of stainless steel reaction vessels or their equivalent. Therefore, two important synthetic goals of research in this area became (1) to achieve higher crystallinity of bulk BC_3 ' and (2) to devise halide-free routes to the synthesis of bulk BC_3 ' in order to prevent the release of corrosive HX or X_2 gases (X = halogen) at elevated temperatures. Our natural hypothesis was that diborane (B_2H_6), the smallest borane species and a reactive gas at ambient pressure, would be well-suited to reactions with benzene to produce bulk BC_3 ' with only the release of H_2 as a side-product.

Results and Discussion

The resulting studies of the reaction between diborane and benzene within a custom-designed apparatus comprising a closed, stainless steel reaction vessel at up to 800 °C (see Supporting Information for details) consistently revealed a heterogeneous mixture of products, a hodgepodge compounded by the presence of metal particle-catalyzed graphitic fibers which are

known to be characteristic of carbon soots produced under similar conditions.^{28,29} Control reactions (e.g., of liquid mixtures of condensed diborane and benzene) in the absence of catalytic effects from the metal-walled reactor were not safe enough to conduct within the scope of this work. Meanwhile, benzene remained the optimal hydrocarbon precursor owing mainly to the desire to preserve its ring structure within the planar layers of BC_3' (Figure 1), and hence we set out to identify a compatible, halide-free boron precursor to pair it with in our efforts to achieve the goals listed above.

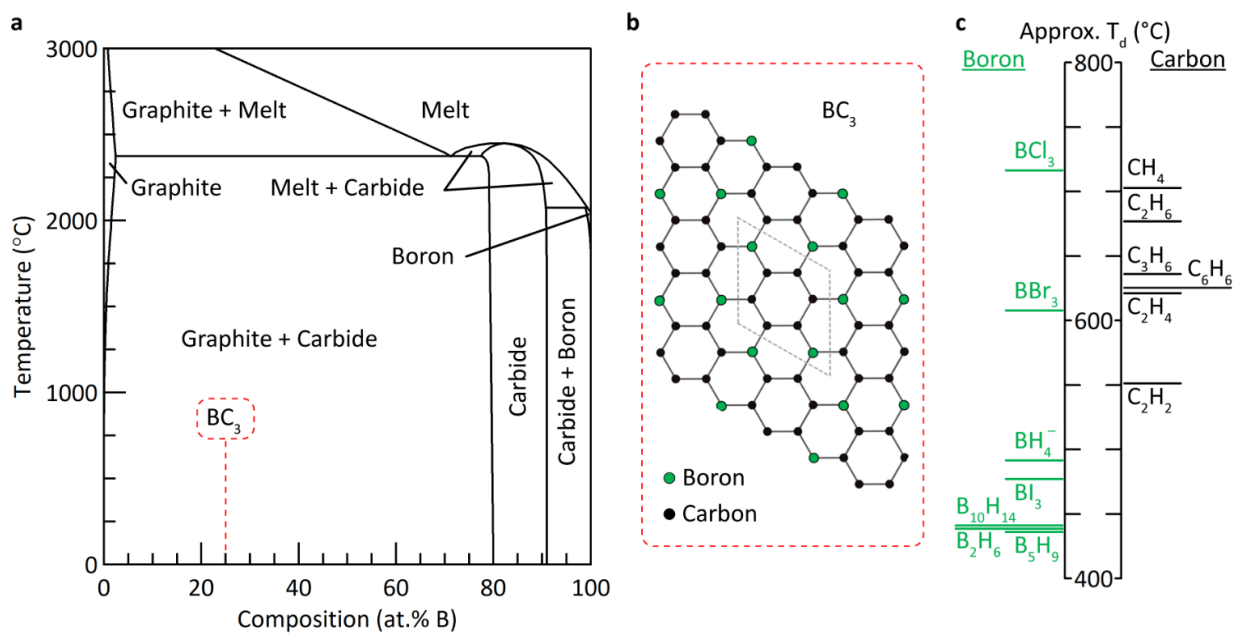


Figure 1. (a) Binary phase diagram of the boron-carbon system.³⁰ The region of interest for the formation of metastable BC_3' is highlighted. (b) The proposed in-plane structure and unit cell of BC_3' .^{7,10} (c) Thermochemical ranking of boron and carbon precursors based on their estimated temperature of decomposition (T_d).

Two additional halide-free molecular boron precursors were then explored as candidates toward elucidation of the synthesis of bulk BC_3' : decaborane ($B_{10}H_{14}$) and a bespoke polyaromatic carborane species (1,8-naphthalenediyl-bridged diborane, NDB)³¹. The former, a readily available

commercial compound, is obtainable as a high-purity crystalline solid at ambient conditions and is miscible in benzene up to the desired B:C ratio of 1:3. However, reactions between decaborane and benzene at up to 800 °C always generated carbon-rich flakes with a colorful (iridescent) thin surface layer of amorphous boron, and with no discernible content of BC₃' (see Supporting Information). The latter precursor, NDB, itself requires a multi-step organic synthesis that, even under strict air-free handling, inevitably leads to the introduction of impurities such as oxygen, chlorine, and aluminum in the eventual high-temperature pyrolysis product (see Supporting Information). Scanning electron microscopy (SEM) studies of this product revealed the existence of a rippled, carbide-like film on the surface of carbon-rich flakes. The overall maximum boron content of such products is in any case limited to ~17 at.% owing to its stoichiometry of B₂C₁₀H₁₀ (B:C of 1:5), preventing the realization of BC₃'. No other planar carboranes exist with a higher content of boron, and hence a halide-free single precursor "tiling" route to bulk BC₃' was also abandoned. The products of the attempted syntheses of bulk BC₃' from diborane (II), decaborane (III), and NDB (IV) are compared to that from boron tribromide (I), the previously established route, in Figure 2. In summary, a systematic approach to identifying a compatible halide-free boron precursor for reactions with benzene at near 800 °C was needed.

The heterogeneity of each of the products of the aforementioned reactions can likely be explained by a mismatch in the decomposition or cracking temperatures of the boron and carbon species within each reaction. In order to realize a homogeneous metastable phase within a binary system, the thermodynamically favored phases (enriched in one or the other of the two elements, in this case graphite and boron carbide) must be prevented from forming, which requires the simultaneous decomposition of the corresponding precursors: i.e., co-pyrolysis. We undertook to

estimate the relative decomposition temperatures (T_d) of an expansive library of boron and carbon precursors using a simple density functional theory (DFT) method, described in detail in the Supporting Information. In short, the change in energy of simplified decomposition reactions were calculated at the MN15/def2-QZVPP^{32,33} level (recently benchmarked for studies of small molecular systems of composed of boron, carbon, and hydrogen).^{34,35} The normalized change in electronic energy, ΔE^{SCF} , where the Δ refers to decomposition into B or C and the relevant diatomic gases, was found to be highly correlated with the experimental decomposition temperature of each precursor (Figure S26). The results revealed that among all of the precursors investigated, borohydride (BH_4^-) exhibited the closest energetic match to benzene, without the presence of borohalide (B–X) bonds (Figure 1c).

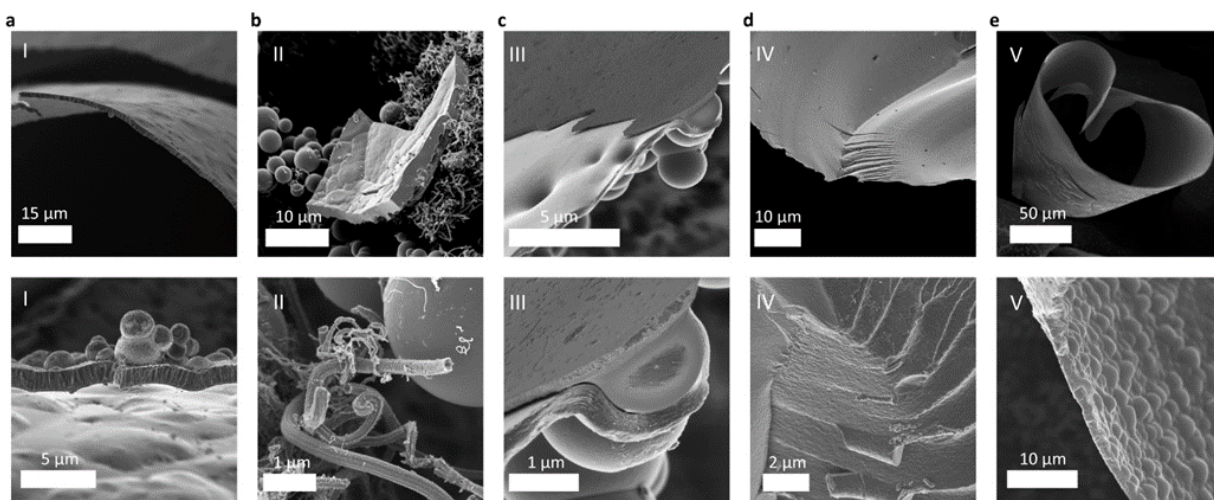


Figure 2. SEM images of the graphitic BC_x pyrolysis products resulting from five different synthesis routes: (a) route I via boron tribromide, (b) route II via diborane, (c) route III via decaborane, (d) route IV via NDB, and (e) route V via sodium borohydride.

Borohydride salts are widely available in high purity, and their decomposition temperatures are known to be directly related to the electronegativity of the counter ion (M^+).³⁶ However, no previous studies of even common borohydrides ($\text{M} = \text{Li}, \text{Na}, \text{or Mg}$) with simple hydrocarbon

precursors such as benzene have been reported. Many of the less-stable borohydrides are known to emit diborane at modest temperatures (e.g., as low as ~ 61 °C for $\text{Al}(\text{BH}_4)_3$) during decomposition.^{36,37} On the other hand, the stable borohydrides such as $\text{Li}(\text{BH}_4)$ do not produce detectable diborane upon decomposition, leading to polymeric B–B bond formation and the eventual formation of higher boranes such as $\text{B}_{12}\text{H}_{12}^{2-}$.³⁸ The similar decomposition temperatures of NaBH_4 (~ 600 °C)³⁶ and benzene (~ 750 °C)³⁹ led us to predict that reactions between these two precursors could result in the formation of BC_3' .

A stoichiometric mixture of benzene and sodium borohydride (with a B:C ratio of 1:3) was charged into a quartz ampule under argon, solidified by submersion in liquid nitrogen, and then flame-sealed within the ampule under active vacuum (referred to herein as “synthesis route V,” see Supporting Information). Pyrolysis was carried out at 800 °C for 1 h, and the sample was then collected in air at room temperature. To prevent the formation of sodium metal and/or reactions of the sodium with the walls of the quartz reactor, a sodium-ion-trapping agent should also be added to the mixture (e.g., I_2 , Se, or Te) to form a water-soluble salt that can be easily separated during workup of the product. Dark lustrous flakes were collected, showing very little tendency to adhere to the inner walls of the ampule, a characteristic feature of bulk polycrystalline BC_3' derived from BBr_3 (referred to herein as “synthesis route I”).¹² SEM imaging further supports that sodium borohydride-derived BC_3' (route V) exhibits a homogeneous, flake-like morphology (~ 2 μm in width) with the same “cratered” texture (Figure 2e) as that derived from boron tribromide (Figure 2a).

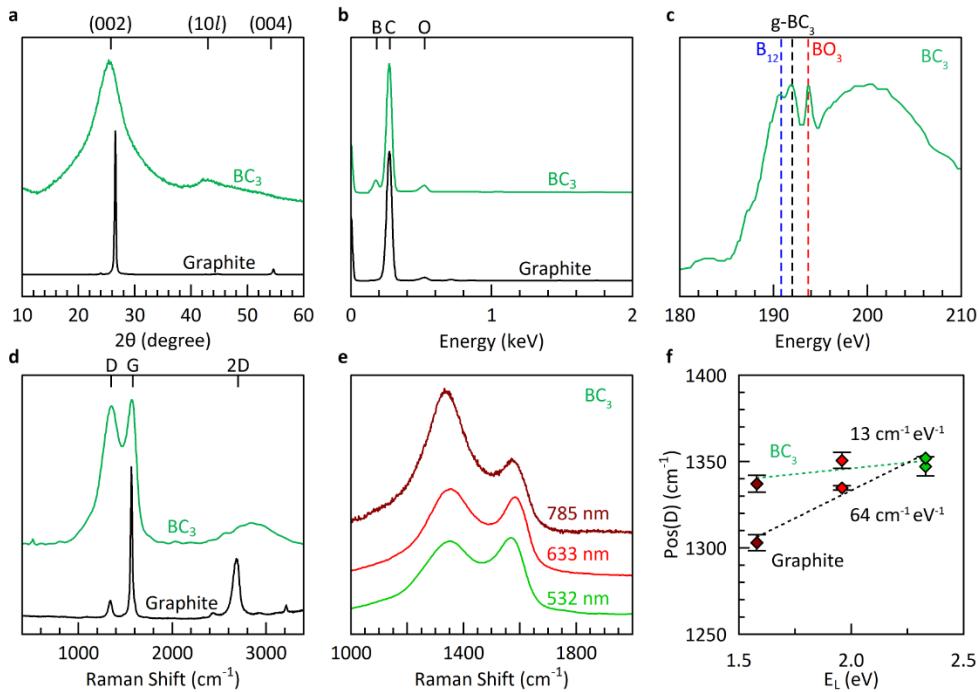


Figure 3. Materials characterization of borohydride-derived BC_3' compared to graphite: (a) XRD patterns, (b) EDX spectra, (c) XAS spectra at the B K-edge, and (d) Raman spectra at 532 nm. (e-f) Dispersion relation of the D peak as revealed by multi-wavelength Raman spectroscopy.

Further materials characterization (Figure 3) reveals borohydride-derived bulk BC_3' (route V) to be similar in structure and composition to that derived from boron tribromide (route I). The underlying structure is exclusively graphitic, as evidenced by powder X-ray diffraction (XRD), with significant misalignment (turbostratic disorder) along the stacking direction as shown by the broad reflection at $2\theta = 25.4^\circ$ corresponding to an interlayer spacing of 3.5 Å. This broadness is in agreement with theoretical predictions for crystalline BC_3' which show that its various high-symmetry stacking sequences all lie within a narrow range of formation energies (± 0.011 eV atom $^{-1}$),⁷ indicating the strong likelihood of stacking misalignment. The in-plane structure is revealed to be more ordered, with an average domain size of 42 Å according to a Scherrer analysis of the (10 l) peak at $2\theta = \sim 42^\circ$. The elemental composition measured using energy dispersive X-ray spectroscopy (EDX) is estimated to be $\sim BC_5$, identical to equivalent measurements of the products

of synthesis route I. It must be noted that past work has shown EDX to underestimate the boron content compared to more sensitive methods such as elastic recoil detection analysis (ERDA).¹²

The boron chemical environments present in borohydride-derived BC₃' were investigated by a combination of X-ray absorption spectroscopy (XAS) and multi-wavelength Raman spectroscopy (Figure 3c-f). The presence of planar g-BC₃ units in long-range ordered, hexagonal symmetry is evidenced by a dominant absorption feature in the B K-edge at 192.0 eV.⁴⁰ Some icosahedral B₁₂ environments are also detected at 190.8 eV, likely due to the small degree of mismatch between the decomposition temperatures of benzene and BH₄⁻ which favors the slightly earlier formation of boron rich phases prior to the desired reaction to form BC₃'. Most importantly, the Raman spectrum exhibits the characteristic features of bulk BC₃': a broad and intense D peak at Pos(D) = ~1350 cm⁻¹, exhibiting almost no dispersion as a function of the energy of irradiation (E_L), and a broad, intense, and modulated 2D region associated with two-phonon intervalley scattering.⁴¹ The non-dispersive nature of the D peak of borohydride-derived BC₃' is the ultimate evidence for its long-range, in-plane ordering consisting of C₆B₆ "flower-like" units integral to the structure of BC₃'.²¹

Conclusions

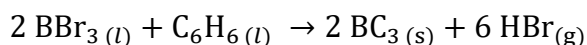
In conclusion, we report a novel borohalide-free route to turbostratic BC₃' with exceptional in-plane ordering via the reaction of benzene with sodium borohydride at 800 °C. The computational method developed herein can be extended to identify candidate precursors for other bottom-up synthesis efforts toward binary metastable phases. The limited set of experimental conditions explored herein compels future work to tune the decomposition profile of the borohydride precursor by varying the counter ion and/or matching a given salt with a hydrocarbon

of similar stability, opening an abundance of possible chemical routes to more crystalline forms of graphite-like BC₃'.

Associated Content

Supporting Information

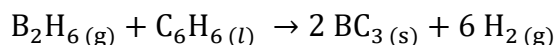
Direct Synthesis of BC₃' from BBr₃ (Route I): The idealized reaction in the previously established¹² direct synthesis of bulk BC₃' (referred to herein as route I) is:



A 2:1 molar solution of boron tribromide (liquid, 99.99%, Sigma-Aldrich) and benzene (liquid, 99.8%, Sigma-Aldrich) was charged into a ~35 mL quartz ampule inside a glovebox under an inert argon atmosphere (<0.5 ppm of H₂O, <0.5 ppm of O₂). The total volume of solution added was 313 μL, limiting the maximum pressure to <20 bar at 800 °C. The open end of the ampule was closed with a Swagelok Ultra-Torr adapter and removed from the glovebox. The lower half of the ampule was submerged in liquid nitrogen to solidify the precursors. In this state, the ampule was connected to a stainless-steel Schlenk line, evacuated to 10⁻² mbar, and flame-sealed under active vacuum. The sealed ampule was then placed in the center of a chamber furnace (RWF 12/13, Carbolite Gero Ltd.) and heated to 800 °C at 1 °C min⁻¹. The ampule was held at 800 °C for 1 h and then allowed to gradually cool to ambient temperature. The ampule was carefully scored with a diamond-bladed saw and snapped open within a nitrile rubber enclosure, releasing the over-pressure of gaseous byproducts into a fume hood. The solid product was collected and washed three times with deionized water, washed three times with acetone, and finally dried in air at 80 °C. The as-synthesized flakes (referred to herein as BC₃', reflecting their nominal composition)

were in some cases investigated without further manipulation; in other experiments, they were reduced to powder by grinding in a dry mortar and pestle for 15 min, as denoted below.

Synthesis of BC₃' from B₂H₆ (Route II): A novel synthesis route to BC₃' via B₂H₆ as the boron precursor (route II) was carried out, based on the following idealized reaction:



A stainless-steel reactor (4651 high-pressure vessel, Parr Instrument Company) with a gas inlet port and an internal volume of 250 mL was thoroughly dried in air at 80 °C. A stainless-steel gasket (44HC7AD, Parr Instrument Company) was placed in the pre-lubricated sealing groove of the reactor body and all components were then transferred into a glovebox under inert argon atmosphere (<0.5 ppm of H₂O, <0.5 ppm of O₂); the reactor was charged with 0.62 mL of benzene (liquid, 99.8%, Sigma-Aldrich), sealed using a torque wrench, and transferred out of the glovebox. The main body of the sealed reactor was cooled by submersion in an acetone and dry ice bath for 60 min. It was then connected to a previously dried and evacuated gas/vacuum manifold via a metal gasket face-seal fitting (VCR, stainless steel, Swagelok Co.) and evacuated for 10 s using a dry scroll vacuum pump (10⁻² mbar ultimate pressure, ACP 15, Pfeiffer Vacuum GmbH). After a brief evacuation, a gas mixture containing 30% diborane in hydrogen (99.99% purity B₂H₆ in 99.9999% purity H₂, Air Liquide Electronics U.S. LP) was filled into the reactor headspace up to a pressure of 2.0 bar (6.6 mmol or 180 mg of diborane). The reactor was then resealed, disconnected from the gas/vacuum manifold, removed from the cooling bath, and allowed to warm to room temperature. After thorough drying of the outer walls from condensation, the reactor was placed within a custom chamber furnace (Parr Instrument Company) and heated to 700 °C at 1 °C min⁻¹. The reactor was held at 700 °C for 4 h and then allowed to gradually cool to ambient

temperature. During pyrolysis, the pressure within the closed reactor was monitored using an integrated transducer (G2, Ashcroft Inc.). Upon completion, the gaseous byproducts were vented into a fume hood to just above ambient pressure. The reactor was transferred into an argon glovebox and opened, and the product was collected from the bottom of the vessel; the solid product was investigated without further manipulation.

Safety Note (Route II): Diborane is a pyrophoric compound and is also toxic at low concentrations (LC50 values for inhalation at <100 ppm). Therefore, it is crucial that any gas manifold exposed to diborane at greater than atmospheric pressure (e.g., 2 bar) be leak-tight and sufficiently purged with argon prior to the introduction of diborane to remove any trace water or oxygen. Leak testing at elevated pressures using pure hydrogen or helium and a suitable leak detector (used herein with H₂: Sensistor XRS9012, INFICON Inc.) is highly recommended prior to introducing diborane to the system. Abatement is also crucially important; in this work, all waste diborane contained within the manifold (i.e., which was not closed within the reactor) was quenched by exhausting through a series of two Dreschel washing flasks filled with methanol at a flow rate of 20 sccm (Figure S4). The system was then completely purged of diborane by flushing with excess argon at 100 sccm for 30 min.

Experimental Setup (Route II): A stainless-steel reactor equipped with a pressure transducer was custom-designed and fabricated over three versions to carry out synthesis route II. The ultimate design comprised a 250 mL reactor outfitted with a digital pressure transducer, allowing for monitoring and post-synthesis analysis of the reaction. By converting the pressure to a total amount of gaseous species present (using the ideal gas law and the known fixed volume and temperature), leaks and/or the change in amount of gaseous species could be plotted as a function

of time (Figure S1). In the co-pyrolysis of diborane with benzene, analysis of the pressure profile reveals three distinct steps: (1) gasification of benzene, (2) decomposition of diborane followed by condensation of higher-order boranes, and (3) decomposition of benzene. In the neat pyrolysis of benzene, only two steps are observed: (1) gasification of benzene and (3) decomposition of benzene.

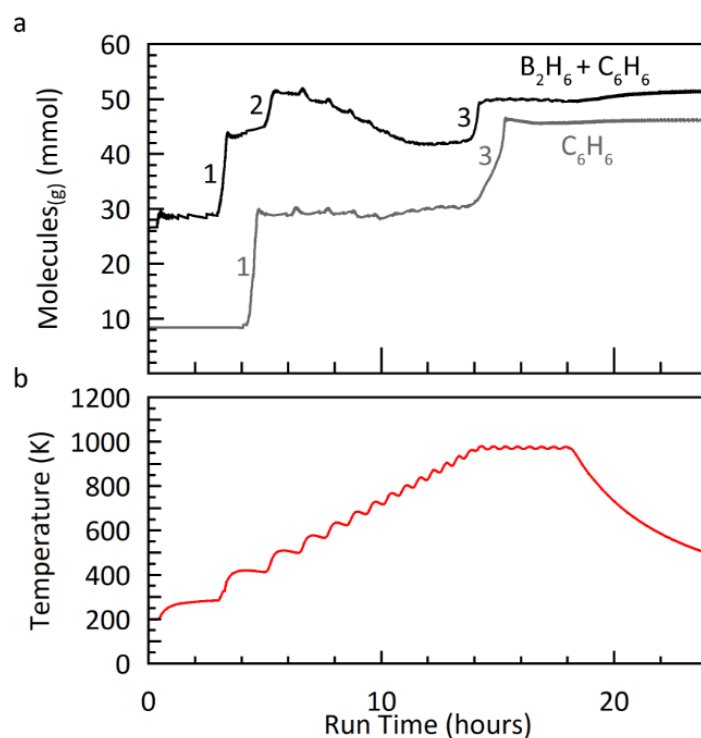


Figure S1. Gas evolution during pyrolysis in a custom metal reactor. (a) Change in amount of gaseous species present as a function of reaction time during the co-pyrolysis of B_2H_6 and C_6H_6 (route II) or pure C_6H_6 , under closed, inert conditions and (b) the corresponding temperature profile.



Figure S2. Experimental apparatus for filling and sealing the custom metal reactor within a glovebox: the reactor body affixed to a vise (center), the head of the reactor (bottom center), and the split-ring sealing cuff (top right) are shown.



Figure S3. Experimental apparatus for storage and delivery of diborane: lecture bottle containing the B₂H₆/H₂ mixture (center) within a freezer held at -20 °C, a purgeable regulator (right), pressure transducer controller (top center), and purge, vent, and delivery gas lines (right and top right) inside a fume hood.

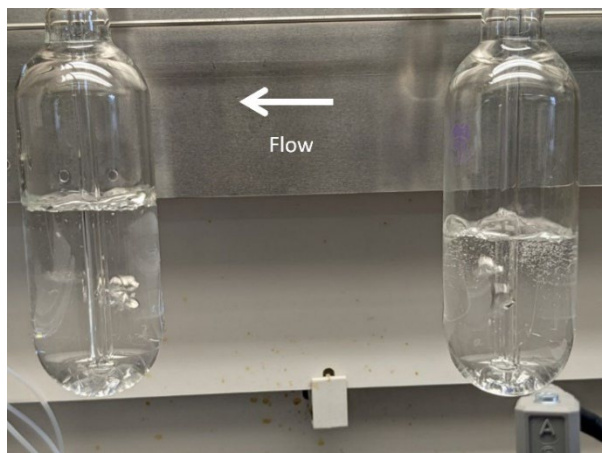


Figure S4. Experimental apparatus for diborane abatement: two Dreschel flasks (left and right) filled with methanol (clear liquid) showing exhaust flow from right to left. In contact with methanol, diborane is converted into trimethoxyborane and hydrogen is evolved (small bubbles are shown in both flasks, but less evolution occurs in the downstream flask on the left).



Figure S5. Experimental apparatus for diborane/benzene co-pyrolysis reactions (route II): custom metal reactor (center), furnace (center right), freezer containing the B_2H_6/H_2 mixture (left), purgeable regulator (center left), gas manifold (Teflon and stainless steel), vacuum outlet (right), and abatement system (top center). The reactor is shown submerged in an acetone and dry ice bath at $-78\text{ }^\circ\text{C}$.



Figure S6. Custom metal reactor removed from the furnace, shown post reaction and prior to opening.



Figure S7. Custom metal reactor head and thermowell, shown post reaction (benzene pyrolysis at 700 °C) and after opening.

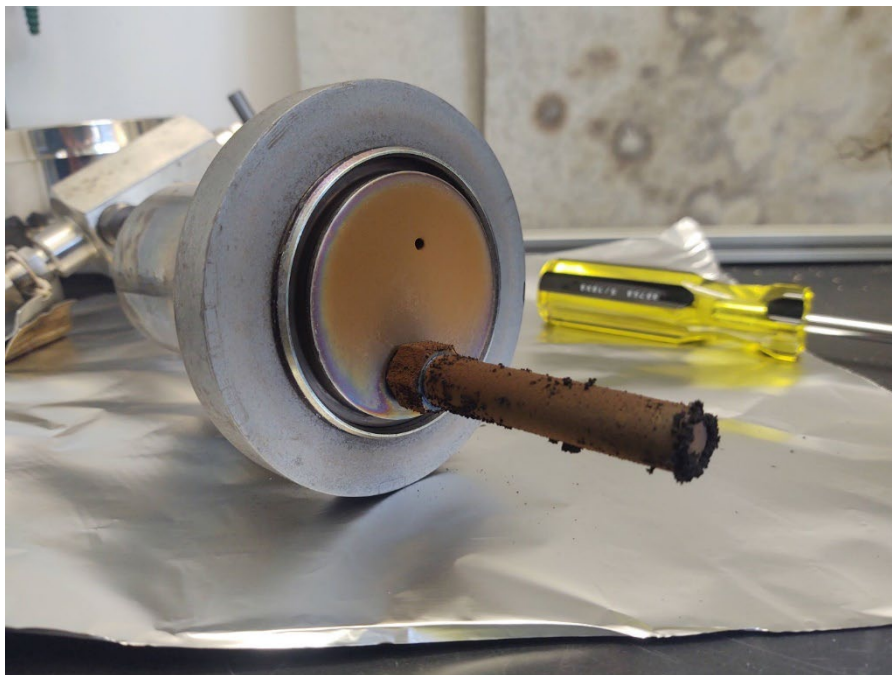
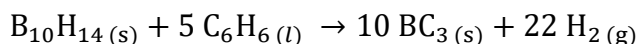


Figure S8. Custom metal reactor head and thermowell, shown post reaction (diborane/benzene pyrolysis at 700 °C) and after opening.

Synthesis of BC₃' from B₁₀H₁₄ (Route III): A novel synthesis route to BC₃' via B₁₀H₁₄ as the boron precursor (route III) was carried out, based on the following idealized reaction:



A 1:5 molar solution of decaborane (solid, technical grade, Sigma-Aldrich) and benzene (liquid, 99.8%, Sigma-Aldrich) was charged into a ~12 mL quartz ampule inside a glovebox under an inert argon atmosphere (<0.5 ppm of H₂O, <0.5 ppm of O₂). The total volume of solution added was 40 μL, limiting the maximum pressure to <20 bar at 800 °C. The open end of the ampule was closed with a Swagelok Ultra-Torr adapter and removed from the glovebox. Pyrolysis was carried out in an identical procedure as described in route I. The solid product was collected and washed three times with deionized water, washed three times with acetone, and finally dried in air at 80 °C. The as-synthesized flakes (referred to herein as BC₃', reflecting their nominal composition)

were in some cases investigated without further manipulation; in other experiments, they were reduced to powder by grinding in a dry mortar and pestle for 15 min, as denoted below.

Synthesis of NDB (Route IV Precursor): Methods to synthesize 1,8-naphthalenediyl-bridged diborane(6) (NDB) were adapted from those reported by Scholz and coworkers.³¹ The materials, general procedures, and multi-step synthesis of NDB that were used herein follow.

Organic Synthesis Materials: Me₃SiCl and B(OMe)₃ were distilled over CaH₂ and Na, respectively. The following reagents were purchased from commercial vendors and used as received: CDCl₃ (99.8%, Cambridge Isotope Labs), 1,8-diiodonaphthalene (≥98.0%, Sigma Aldrich), *n*-BuLi (1.5 M in *n*-hexane, Thermo Scientific), CH₂Cl₂ (>99.9%, Honeywell), KOH (97.8%, Mallinckrodt Chemicals), HCl (Acros Organics), MgSO₄ (Oakwood Products, Inc.), LiAlH₄ (1.0 M in Et₂O, Sigma Aldrich). C₆D₆ was purchased from Cambridge Isotope Labs, degassed by three freeze-pump-thaw cycles, and stored in a N₂- or Ar-filled glovebox over activated molecular sieves.

Organic Synthesis General Procedures: All synthetic procedures were performed under N₂ or Ar using standard glovebox or Schlenk line techniques, unless otherwise noted. The solvents used for synthetic procedures (diethyl ether, Et₂O, and *n*-hexane) were sparged and stored under ultrahigh purity (UHP) Ar before being dried via passing through a solvent purification system (CHEMBLY, formerly JC Meyer Solvent Systems) using UHP argon as the working gas. All glassware was heated to 160 °C overnight prior to use.

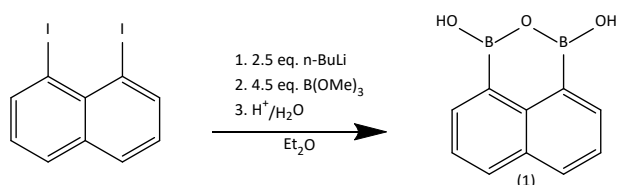
Synthesis of 1,8-Naphthalic Boronic Acid Anhydride, 1:

Figure S9. Synthesis of 1,8-Naphthalic Boronic Acid Anhydride, 1.

1,8-Diiodonaphthalene (5.0 g, 13.13 mmol, 1 eq.) was added to a 250 mL Schlenk flask containing a stir bar. The solid was dissolved in dry Et₂O (~80 mL) and the solution was cooled to 0 °C. In this state, *n*-BuLi (1.5 M in *n*-hexane; 21 mL, 31.5 mmol, 2.5 eq.) was added dropwise via a syringe while the solution was stirred. The solution was allowed to warm to room temperature over the course of 3 h after which it was cooled to -78 °C and B(OMe)₃ (7.1 mL, 63 mmol, 4.5 eq.) was added dropwise. The solution was removed from the cooling bath and allowed to warm to room temperature over the course of 12 h. HCl (2 M in H₂O; 23.5 mL) was added, and the solution was stirred for an additional 2 h at room temperature. The two phases were separated, and the aqueous phase was extracted with CH₂Cl₂ (4×10 mL). The organic phases were combined and **1** was extracted into aqueous KOH (2 M; 4×10 mL). The aqueous phases were combined and washed with CH₂Cl₂. HCl (33 M in H₂O) was added dropwise to the aqueous phase until the solution became acidic, whereupon a precipitate formed. The precipitate was collected by vacuum filtration and washed with H₂O on the frit. The solid product was dissolved in ethyl acetate and dried over MgSO₄. The solution was filtered, and the filtrate was obtained as an off-white solid by drying under reduced pressure to yield **1** (1.95 g, 9.87 mmol, 74% yield). ¹H NMR (300 MHz, CDCl₃): δ = 8.20 (dd, 3J(H,H) = 6.8 Hz, 4J(H,H) = 0.9 Hz, 2H), δ = 8.06 (dd, 3J(H,H) = 8.3 Hz, 4J(H,H) = 0.9 Hz, 2H), δ = 7.60 (dd, 3J(H,H) = 8.3 Hz, 3J(H,H) = 6.8 Hz, 2H), δ = 4.75 (br, 2H; O–H).

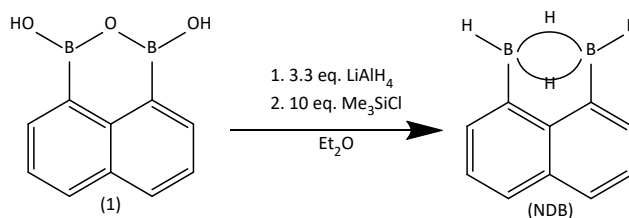
Synthesis of 1,8-Naphthalenediyl-Bridged Diborane(6) (NDB):

Figure S10. Synthesis of 1,8-Naphthalenediyl-Bridged Diborane(6) (NDB).

1 (0.5 g, 2.53 mmol, 1 eq.) was added to a 100 mL Schlenk flask equipped with a stir bar. The solid was dissolved in dry Et₂O (~50 mL) and cooled to 0 °C. In this state, a solution of LiAlH₄ (1M in Et₂O, 8.4 mL, 8.4 mmol, 3.3 eq.) was added dropwise via a syringe while the solution was stirred, during which a colorless precipitate formed along with the evolution of a colorless gas. The solution was stirred for 30 min at 0 °C then allowed to warm to room temperature where it was stirred for an additional 12 h. The solution was cooled to -78 °C and neat Me₃SiCl (3.2 mL, 25.3 mmol, 10 eq.) was added dropwise via a syringe, resulting in the formation of a colorless precipitate. The mixture was stirred for 10 min at -78 °C then allowed to warm to room temperature where it was stirred for an additional 12 h. The mixture was evaporated under reduced pressure to a yellow paste. This paste was thoroughly triturated with *n*-hexanes to assist in the removal of coordinated solvent molecules, then evaporated to dryness under reduced pressures. The NDB product was isolated in high purity by three subsequent vacuum sublimations (80 °C, 10⁻² mbar) and collected as a clear crystalline sublimate to yield NDB (245 mg, 1.61 mmol, 64% yield). **¹H NMR (500 MHz, C₆D₆):** δ = 7.87 (d, 3J(H,H) = 6.7 Hz, 2H), δ = 7.71 (dd, 3J(H,H) = 8.3 Hz, 4J(H,H) = 0.6 Hz, 2H), δ = 7.38 (dd, 3J(H,H) = 8.3 Hz, 3J(H,H) = 6.7 Hz, 2H), δ = 4.78 (q, 1J(H,B) ≈ 130 Hz, 2H), δ = 1.61 (s, br, 2H). **¹³C NMR (125 MHz, C₆D₆):** δ = 144.8, δ = 138.7 (br), δ = 133.5, δ = 130.0, δ = 130.0, δ = 126.9.

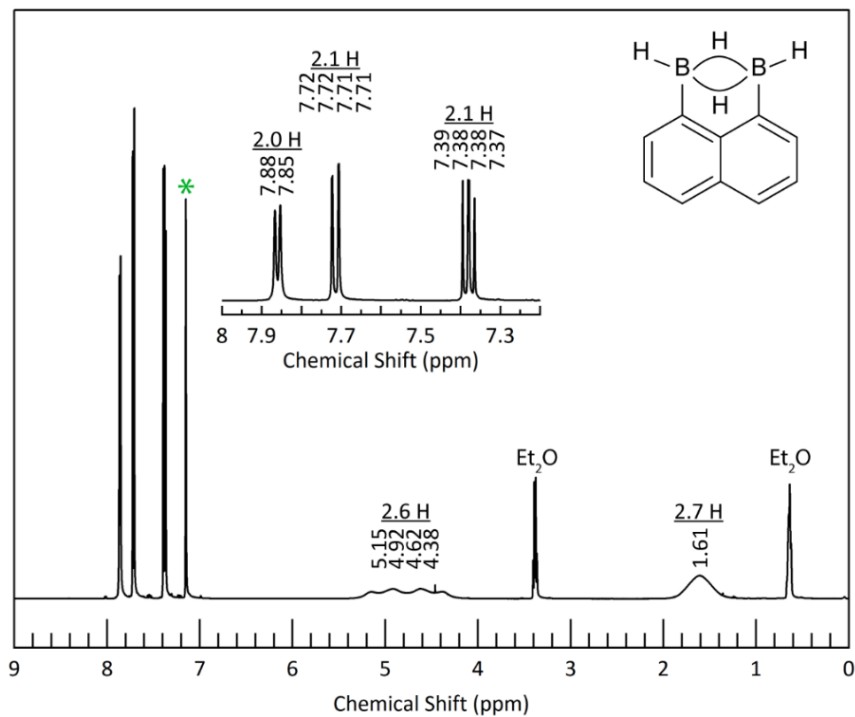


Figure S11. ^1H NMR spectrum of NDB dissolved in C_6D_6 (*) using a 500 MHz spectrometer.

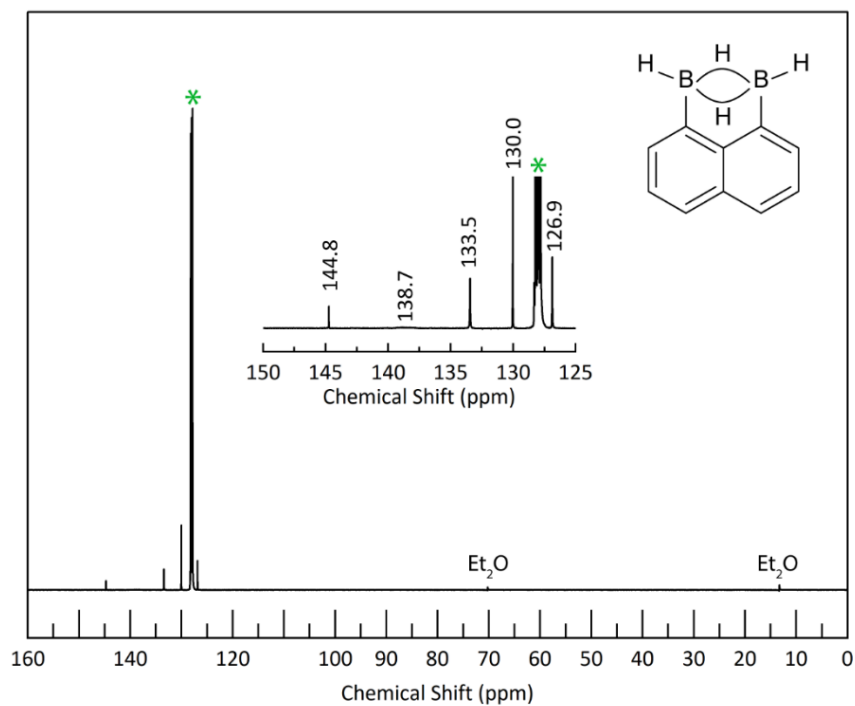
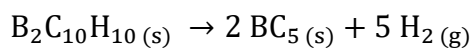


Figure S12. ^{13}C NMR spectrum of NDB dissolved in C_6D_6 (*) using a 500 MHz spectrometer.

Synthesis of BC₅ from the Molecular Tile B₂C₁₀H₁₀ (Route IV): A novel synthesis route to BC₅ via the neat pyrolysis of 1,8-naphthalenediyl-bridged diborane(6) (NDB, B₂C₁₀H₁₀, route IV) was carried out, based on the following idealized decomposition reaction:



The product was purified three times by sublimation and then charged into a ~30 mL quartz ampule inside a glovebox under an inert argon atmosphere (<0.5 ppm of H₂O, <0.5 ppm of O₂). The total amount of NDB added was 200 mg, limiting the maximum pressure to <20 bar at 800 °C. The open end of the ampule was closed with a Swagelok Ultra-Torr adapter and removed from the glovebox. Pyrolysis was carried out in an identical procedure as described in routes I and III. The solid product was collected and washed three times with deionized water, washed three times with acetone, and finally dried in air at 80 °C. The as-synthesized material (referred to herein as BC₅, reflecting its nominal composition) was in some cases investigated without further manipulation; in other experiments, it was reduced to powder by grinding in a dry mortar and pestle for 15 min, as denoted below.

Separation of Pyrolysis Products: Upon pyrolysis of the NDB precursor, two morphologies were generated and separated by density. The minor flakes were suspended in ethanol and poured off while the majority solid (see Figure S13) was collected for further characterization.



Figure S13. Two solid products generated by the pyrolysis of $B_2C_{10}H_{14}$ (NDB) at 800 °C (route IV) can be seen: a suspension of flakes (left) and the remaining mound of the majority solid (right).

Synthesis of BC_3' from $NaBH_4$ (Route V): A novel synthesis route to BC_3' via $NaBH_4$ as the boron precursor (route V) was carried out, based on the following idealized reaction:



Sodium borohydride (powder, 99%, Sigma-Aldrich), iodine (solid crystals, >99%, purified by sublimation, Sigma-Aldrich), and benzene (liquid, 99.8%, Sigma-Aldrich) were charged into a ~35 mL quartz ampule inside a glovebox under an inert argon atmosphere (<0.5 ppm of H_2O , <0.5 ppm of O_2). A typical mixture contained 65.5 mg of $NaBH_4$, 439.9 mg of I_2 , and 77.2 μL of C_6H_6 to achieve a nominal stoichiometry of BC_3' at <20 bar at 800 °C. The open end of the ampule was closed with a Swagelok Ultra-Torr adapter and removed from the glovebox. Pyrolysis was carried out in an identical procedure as described in routes I, III, and IV. The solid product was collected and washed three times with deionized water, three times with acetone, once with a 50% aqueous HF solution, three additional times with deionized water, and finally three additional times with acetone; this product was dried in air at 80 °C.

The addition of elemental iodine to synthesis route V was necessary for the scavenging of sodium. While other sodium scavengers could be used (e.g., Se or Te), iodine was chosen herein. The decomposition of sodium borohydride in the presence of iodine produces reactive borane

species at high temperatures that can be incorporated into the forming graphitic material to form BC_3' . This is accompanied by the formation of sodium iodide (NaI) as a byproduct that can easily be separated from the reaction products by washing with water. The presence of any remaining sodium iodide in the product of route V is detectable by XRD. Upon further washing, the sodium iodide can be completely removed. The mother liquor from an aqueous wash was dried by evaporation to produce a white solid; analysis of this water-soluble solid is shown in Figure S14.

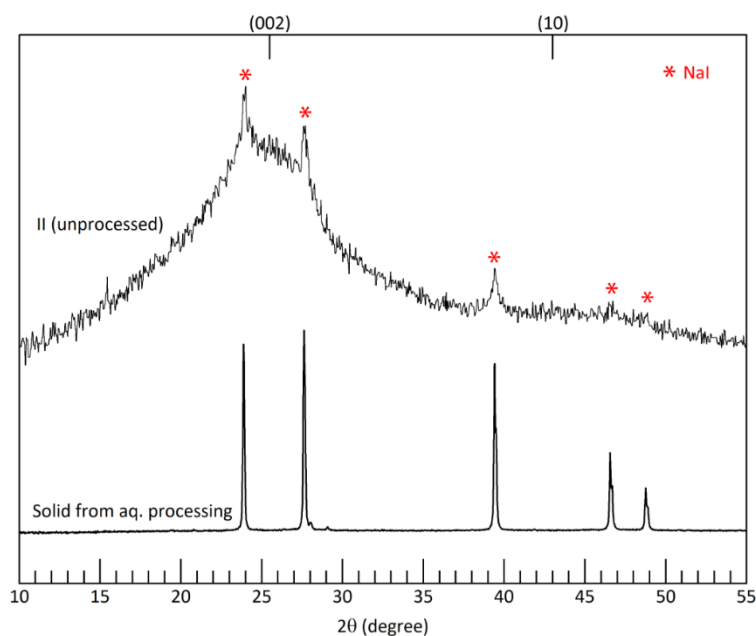


Figure S14. XRD patterns of the as-collected solid products generated by the co-pyrolysis of $NaBH_4$, I_2 , and C_6H_6 under inert conditions within a quartz ampule at $800\text{ }^\circ\text{C}$ (route V), and of the solid recovered after concentrating wash water from processing the graphitic material.

Compositional mapping of the as-synthesized product of synthesis route V via EDX reveals a mixture of boron-doped graphite, sodium iodide crystals, and sodium silicate fibers (see Figure S15). The sodium silicates can be effectively separated from the graphitic product by dissolution in hydrofluoric acid.

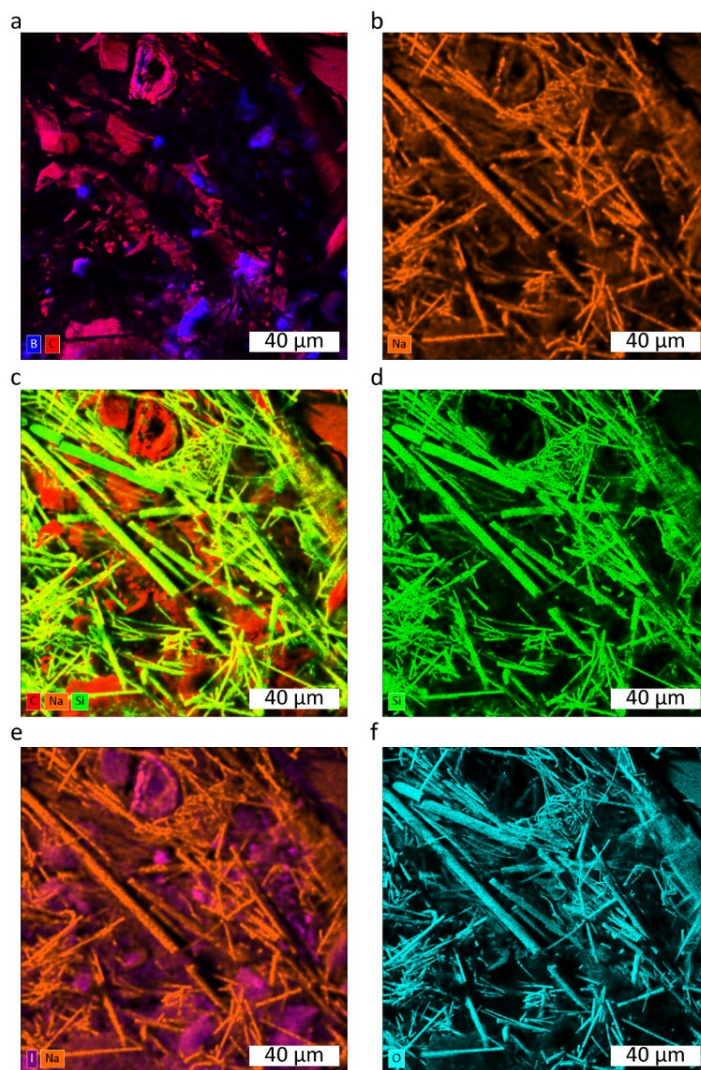


Figure S15. EDX maps of the as-collected solid products generated by the co-pyrolysis of NaBH_4 , I_2 , and C_6H_6 at $800\text{ }^\circ\text{C}$ (route V). The color-coded maps are generated from the signals of (a) boron and carbon, (b) sodium, (c) carbon, sodium, and silicon, (d) silicon, (e) iodine and sodium, and (f) oxygen.

X-Ray Diffraction: Powder X-ray diffraction (XRD) was performed on hand-ground samples using a laboratory diffractometer (D8 ADVANCE, Bruker Corp.) equipped with a $\text{Cu K}\alpha_{1,2}$ radiation source ($\lambda = 1.54\text{ \AA}$) in reflection geometry. All measurements were performed at room temperature using a recessed-well sample holder (25 mm diameter well, Bruker Corp.); the

sample was rotated at 15 rev min⁻¹ and sampled in 0.02° increments for 0.5 s each from 2θ = 10°–60°.

Raman Spectroscopy: As-synthesized materials were investigated with a benchtop Raman spectrometer (LabRAM HR Evolution, Horiba Scientific Ltd.) equipped with a confocal microscope and three excitation sources: a 532 nm (2.33 eV) frequency doubled Nd:YAG laser with an incident power of 10 mW, a 633 nm (1.96 eV) HeNe laser with an incident power of 17 mW, and a 785 nm (1.58 eV) diode laser with an incident power of 25 mW. All measurements were performed at room temperature.

Fitting Raman Spectral Data: The region containing peaks associated to the D and G modes in each Raman spectrum were fitted using a previously established method based on the combination of a Lorentzian and a Breit-Wigner-Fano (BWF) lineshape.^{21,41} The main D peak was fitted to a single Lorentzian and the low frequency shoulder of the D peak was fitted to another Lorentzian to account for hydrogen edge character and denoted as (*C-H). The G peak was fitted to a single BWF, and the baseline was approximated by a linear background, as shown in Figure S16. The combination of two Lorentzian functions and a BWF provided a profile with minimal fitting parameters that could effectively fit the Raman spectrum of the wide range of carbon materials with varying hydrogen content explored in this work. The BWF lineshape is given by:

$$I(\omega) = I_0 \frac{[1 + (\omega - \omega_0/Q\Gamma)]^2}{1 + [(\omega - \omega_0)/\Gamma]^2} \quad (\text{Equation 1})$$

where I_0 is the peak intensity, ω_0 is the peak position, Γ is the FWHM, and Q is the BWF coupling coefficient. A negative Q value tails the BWF toward lower frequency and helps accounts for residual intensity between the D and G peaks. Due to the asymmetry of the BWF lineshape, ω_0

does not lie at the frequency of the peak maximum (ω_{\max}) as in a simple Lorentzian or Gaussian function. To correct for this, the following equation was applied to determine ω_{\max} :

$$\omega_{\max} = \omega_0 + \frac{\Gamma}{2Q} \quad (\text{Equation 2})$$

Since Q is negative, ω_{\max} lies at a lower frequency than ω_0 . FWHM(D) and FWHM(G) were determined based on FWHM of the Lorentzian associated with the D Peak and BWF fits, respectively. The position of the D peak (Pos(D)) was determined based on ω_0 of the Lorentzian associated with the D Peak, and Pos(G) was determined based on ω_{\max} of the BWF associated with the G peak by applying Equation 2.

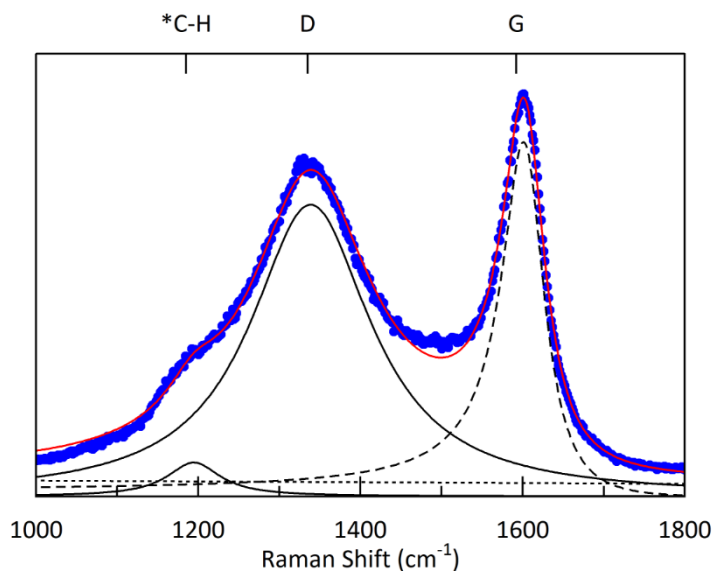


Figure S16. Representative fitting profile for the Raman spectrum of graphitic carbon. One Lorentzian (*C-H) is used to account for hydrogen edge character, a second Lorentzian (D) accounts for the D mode, and a BWF lineshape (G) accounts for the G mode.

X-Ray Absorption Spectroscopy: The boron chemical environments in each material were investigated by X-ray absorption spectroscopy (XAS) using synchrotron radiation at beam line BL8.0.1.4 at the Advanced Light Source (Lawrence Berkeley National Laboratory). The hand-

ground samples were mounted on carbon tape and transferred into an ultrahigh vacuum (10^{-9} mbar) chamber for analysis. The total fluorescence yield (TFY) was measured to probe ~ 175 nm into the bulk of the sample, and the total electron yield (TEY) was measured for analysis of the surface chemical environments. As reference materials, boron oxide (B_2O_3 , 99.999%, Sigma-Aldrich), amorphous boron (98%, Alfa Aesar), hexagonal boron nitride (BN, 99.5%, Alfa Aesar), and boron carbide ($\sim B_4C$, 98%, Sigma-Aldrich) were also examined under identical conditions.

Scanning Electron Microscopy: Scanning electron microscopy (SEM) of the as-synthesized materials was performed for imaging using a field emission scanning electron microscope (SUPRA 55VP, ZEISS Group) operating at 1 kV with a working distance of < 5 mm. Samples were prepared by mounting onto conductive carbon tape.

Decomposition Energy Estimations: The energy of decomposition of each molecular precursor, a proxy for its temperature of decomposition, was approximated as the difference in quantum mechanical electronic energy at 0 K (E^{SCF}) between the original precursor alone as compared to the sum of its elements in their standard state molecular form (e.g., H_2 gas for H, Cl_2 gas for Cl) or as monatomic gases for the solids (e.g., C gas for C, B gas for B):

$$\Delta E^{SCF} = \left(\sum_i^{elements} E_i^{SCF} \right) - E_{precursor}^{SCF} \quad (\text{Equation 3})$$

Hence, the Δ prefix carries the meaning of “decomposition” into the elements, typically either boron or carbon and the relevant diatomic gas (either hydrogen or halogen). Geometry optimization of each species was performed independently, at a level of density functional theory (DFT) previously benchmarked³⁴ for investigations of adsorption systems containing carbon, boron, and hydrogen: the MN15 functional,³² a meta nonseparable gradient approximation (meta-

NGA) global hybrid for the exchange-correlation energy, combined with the def2-QZVPP basis set,³³ a high-quality quadruple zeta basis with two polarization functions, using a commercial computational chemistry software package (Gaussian 16⁴²). Vibrational frequencies were then determined, which guaranteed the stability of the molecular structures and provided the electronic energies of the compounds of interest; standard thresholds for the single-point calculations, optimization, and frequency simulations were used. The final decomposition energy (ΔE^{SCF}) was then divided by the number of “solid” atoms (either B or C) in the sum to provide an estimate of the decomposition energy per atom, reported in units of eV atom⁻¹.

Morphology and Composition: The pyrolysis products of synthesis routes I–V varied significantly in terms of morphology and homogeneity. Representative SEM micrographs of the resulting morphologies of each product are shown in Figure 2 of the main text. Likewise, the chemical compositions of the various morphologies produced during each pyrolysis reaction also varied, indicating different degrees of phase segregation (Table S1). As the benchmark for comparison, the co-pyrolysis of boron tribromide and benzene at 800 °C (route I) primarily results in free-standing flakes with a thickness of $\sim 2 \mu\text{m}$ (Figure 2a), typically formed completely free from the walls of the quartz ampule. The surfaces of the flakes exhibit a cratered/dimpled topology that is characteristic of highly boron-doped graphitic carbons and other boron-rich phases.^{12,18,21,43} Spheres with a diameter of $\sim 2 \mu\text{m}$ are also present in minor abundance in route I. The boron-to-carbon ratio of both morphologies is ~ 0.21 ($\sim \text{BC}_5$) as measured using EDX, with only minor oxygen and bromine impurities ($< 5 \text{ at.}\%$), consistent with previous studies.^{12,21} We note that accurately determining the B:C ratio is challenging, and previous reports showing compositions closer to BC_3 were evidenced by data collected using elastic recoil detection analysis (ERDA)

which is highly suited to the quantification of light-element compositions compared to EDX.^{12A} A comparable halide-free synthesis product to that of route I is achieved via the co-pyrolysis of sodium borohydride and benzene at 800 °C (route V). Using borohydride as a boron precursor requires a counter-ion, in this case sodium. To prevent the formation of metallic sodium, a sodium scavenger must be used. While a number of scavengers could be used, the additive used herein was iodine, leading to the formation of sodium iodide salt which is water soluble and hence easy to separate from the BC_x product. Route V also primarily produces flakes with a thickness of ~2 μm with a similar texture to those produced via route I, and which are also accompanied by spheres that range in diameter from 1–5 μm in minor abundance. The chemical composition of both flakes and spheres was effectively identical to that of the products of route I, with a boron to carbon ratio of ~0.22 (~BC₅ stoichiometry) and with little oxygen, sodium, or other contamination.

Table S1. Elemental composition (as determined by EDX) of each morphology of the BC_x products of synthesis routes I–V.

	Boron Precursor	Flakes	Spheres	Fibers	Film	Carbide
I	BBr ₃	BC ₅ (3% O, 3% Br)	BC ₅ (3% O, 3% Br)	-	-	
II	B ₂ H ₆	BC ₃ (8% O)	B ₂ C (7% O)	BC ₃₂ (2% O)	-	
III	B ₁₀ H ₁₄	BC ₁₉ (2% O)	BC ₁₀ (1% O)	-	B ₅ C ₂ (4% O)	
IV	NDB	BC ₇ (6% Cl, 3% O, 2% Al)	-	-	-	BC ₅ (17% O, 5% Cl, 2% Al)
V	BH ₄ ⁻	BC ₅ (4% O, 2% I)	BC ₅ (1% O, 0.3% Na, 3% I)	-	-	

The products of synthesis route II (the co-pyrolysis of diborane and benzene at 700 °C) depart significantly from those of routes I and V, largely owing to the nature of the stainless-steel

reactor. Route II yields a product with the largest degree of morphological variation of all synthesis routes explored herein. Fibers, spheres, and flakes, in order of descending contribution, are present in all parts of the product, regardless of whether collected exclusively from the thermowell (a cold head) or from the reactor base or walls. The fibers are likely a byproduct of metal-catalyzed side reactions on the stainless-steel body of the reactor, as described for other pyrolysis reactions carried out in the presence of Ni-containing steels.^{28,29,44} The spheres produced by this synthesis are smooth in texture and vary in diameter from 1–5 μm . Contrary to routes I and V, these spheres are found to be composed primarily of boron, with a boron to carbon ratio of ~ 2 (B_2C) and a moderate oxygen content of 7 at.%. While fibers and spheres are the major morphologies generated by route II, flakes with a thickness of ~ 4 μm are also observed as a minor phase. These flakes are similar in appearance to those produced by routes I and V, exhibiting a cratered/dimpled texture and a boron to carbon ratio of ~ 0.4 , close to that of BC_3 .

Synthesis routes III and IV also lead to the formation of multiple morphologies. A colorful boron-rich film with a composition approaching B_4C is found on the surface of the layered graphitic flakes produced in route III. This layered structure is easily seen in the SEM images in Figure 2c of the main text. The underlying graphitic flakes contain only ~ 5 at.% boron (with very little oxygen incorporation). Meanwhile, the pyrolysis of NDB (route IV) also leads to the formation of two morphologies, one that is flake-like and another that exhibits the characteristic folded/crinkled textures indicative of boron carbide.⁴⁵ Interestingly, despite the outward appearance of the folded/crinkled regions, the elemental composition of both morphologies is close to that of the original NDB precursor molecule (BC_5), except with a large impurity content from not only oxygen (3-17 at.%) but also chlorine and aluminum (an additional 5-7 at.%). The large

amount of oxygen contamination is typical of the products of other “molecular tiling” routes, owing to the susceptibility of exposure to air during the requisite multistep organic synthesis of the tile; this disadvantage of tiling type synthesis routes has been previously discussed.¹²

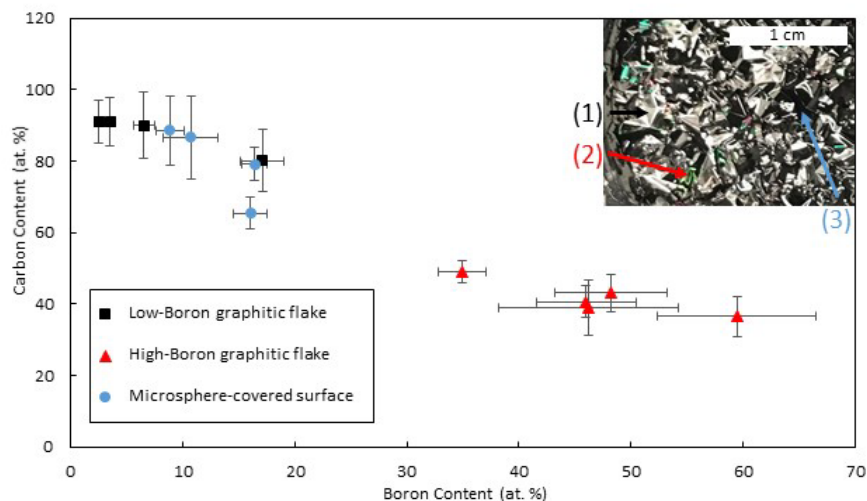


Figure S17. Compositional analysis of decaborane-derived BC_x (route III). Three morphologies can be seen: (1) low-boron content flakes with a grey metallic luster, (2) high-boron content flakes with a colorful metallic luster, and (3) microsphere-covered surfaces that appear dull black.

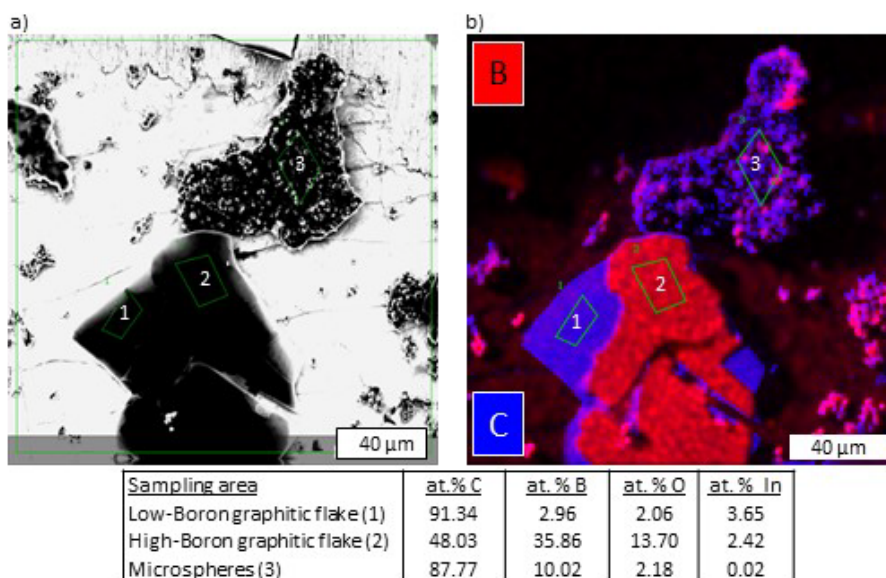


Figure S18. (a) SEM image and (b) EDX elemental map of decaborane-derived BC_x (route III). The same heterogeneity observed by eye (Figure S17) can be quantifiably differentiated in terms of boron content.

Structure: XRD patterns and Raman spectra (EL = 532 nm) of the pyrolysis products from synthesis routes I–V are shown in Figure S19. With the exception of route II, the “crystalline” products of all routes exhibit broad features consistent with that of turbostratic, nanocrystalline graphite. All of the products exhibit two dominant XRD peaks both consistent with graphite: the characteristic (002) reflection between $2\theta = 25\text{--}26^\circ$ that represents layer-to-layer ordering and a peak comprising the (10*l*) family of reflections centered at $2\theta = 42\text{--}43^\circ$ that is associated with in-plane ordering. Synthesis route II produces higher quality graphite, shown in XRD by the higher angle (002) reflection with a narrower FWHM compared to the other samples. This higher level of graphitic order is attributable to the catalytic activity of the metal reactor. All of the products also exhibit features primarily indicative of poorly-crystalline graphite: a G peak centered between $1570\text{--}1590\text{ cm}^{-1}$, a D peak centered between $1335\text{--}1360\text{ cm}^{-1}$, and a broad 2D region between $2500\text{--}3200\text{ cm}^{-1}$. The products of routes III and IV also exhibit a low-frequency shoulder of the D peak between $1125\text{--}1250\text{ cm}^{-1}$ attributable to edge features of graphitic sheets terminated with hydrogen.¹⁵ The product of route II is again an exception; two distinct types of Raman spectra were found upon spatial exploration of the heterogeneous morphologies present. The first spectral type (solid trace in Figure S19b) is consistent with that of other forms of graphitic BC_x phase-mixed with some content of elemental boron (as indicated by a series of peaks between $500\text{--}900\text{ cm}^{-1}$). The second spectral type (dashed trace in Figure S19b) is consistent with a more ordered and lower boron-content graphitic carbon, consistent with the more ordered graphitic phase apparent in its XRD pattern. The D:G intensity ratio of this latter spectral type (~2:1) differs significantly from that of all other products and its 2D region comprises well-defined peaks centered at 2675 and 2930 cm^{-1} , revealing that synthesis route II produces a mixture of higher-

quality low-boron-content graphite, and high-boron-content graphitic BC_x together with elemental boron.

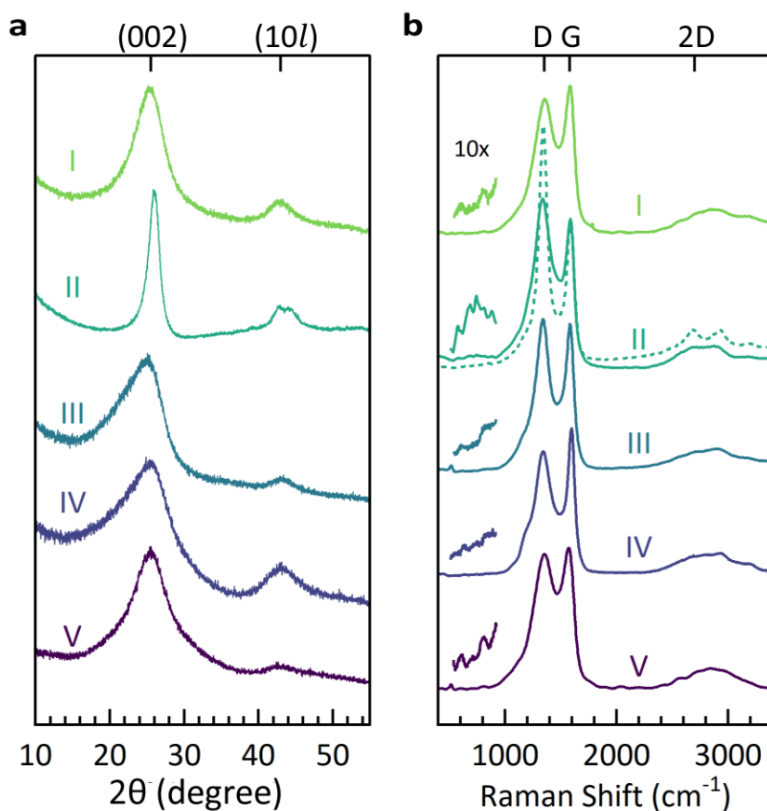


Figure S19. Structural analysis of the pyrolysis products from routes I-V. (a) XRD patterns and (b) Raman spectra ($E_L = 532$ nm) of boron tribromide- (I), diborane- (II), decaborane- (III), NDB- (IV), and sodium borohydride- (V) derived BC_x .

Boron Chemical Environments: The boron chemical environments produced in synthesis routes I-V were investigated by XAS, as shown in Figure S20. Several standard materials containing relevant boron chemical environments are shown in Figure S20c for reference. Hexagonal boron nitride (g-BN) contains ordered trigonal planar boron environments that are characterized by an intense π^* transition at 191.6 eV, and a weaker σ^* transition between 197–200 eV.⁴⁶ Amorphous boron (a-B) exhibits a broad, featureless absorption edge with an onset at 187–190 eV. Boron carbide (B_4C) exhibits the characteristic σ^* transition originating from icosahedral

boron (B_{12}) units at 190.6 eV.⁴⁷ Boron oxide (B_2O_3) exhibits an intense σ^* transition associated with trigonal planar (BO_3) environments at 193.7 eV. This boron oxide environment is also observed in the other standard materials due to surface oxidation resulting from the extremely negative bond association energy of boron-oxygen bonds.

The boron K-edge XAS spectra of the products of routes I-V are shown in Figure S20a (enlarged in Figure S20b). Like the standards, all products exhibit a prominent boron oxide peak at 193.7 eV that is more intense in the TEY signal, consistent with the formation of a surface oxide layer. Synthesis route I primarily results in hexagonally-ordered trigonal planar BC_3 environments (g- BC_3) at 192.0 eV with a small contribution from amorphous BC_3 (a- BC_3) at 189.4 eV, in agreement with previous studies.²¹ The surface (TEY) and bulk (TFY) signals are highly consistent, indicating a homogeneous single-phase product. Synthesis route V produces a similar distribution of boron environments as route I, with a primary contribution from g- BC_3 at 192.0 eV. The product of route V produces a small but detectable contribution from icosahedral B_{12} environments centered at 190.6 eV and a smaller contribution from boron oxide type environments than for the product of route I.

Synthesis routes II-IV produce drastically different chemical environments at the surface compared to within the bulk of the sample, consistent with the morphological heterogeneity revealed by SEM, XRD, and Raman spectroscopy. By comparison of the TEY and TFY spectra of the product of route II, a core-shell structure with a core consisting of elemental boron and a shell of graphitic carbon that contains an array of substitutional boron atoms is revealed. Synthesis route III also produces XAS features consistent with a core-shell structure. The surface spectrum exhibits a sloping edge with a feature at 190.8 eV associated with icosahedral B_{12} environments

as well as a distinct feature at 192.3 eV that is associated with sub-stoichiometric boron carbide domains arising from the inclusion of carbon into the nest-like structure of the decaborane precursor.⁴⁰ The bulk of the sample is a combination of elemental boron, boron carbide (indicated by a subtle feature at 190.8 eV), and sub-stoichiometric boron carbide domains. Synthesis route IV produces a prominent feature from boron oxide at 193.7 eV throughout its core-shell structure, containing predominantly a-BC₃ and sub-stoichiometric boron carbide environments in the core with almost exclusively sub-stoichiometric carbide in the shell.

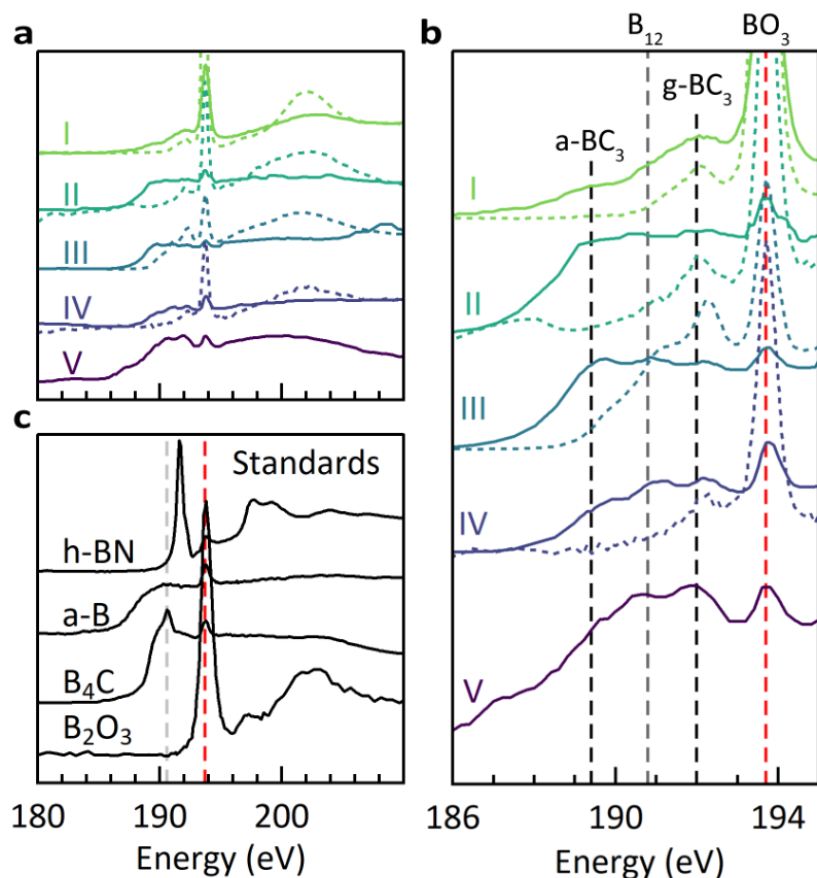


Figure S20. XAS spectra near the B K-edge of the pyrolysis products from routes I-V and related reference materials. The samples shown are boron tribromide- (I), diborane- (II), decaborane- (III), NDB- (IV), and sodium borohydride- (V) derived BC_x, hexagonal boron nitride, amorphous boron, boron carbide, and boron oxide. TEY spectra (surface) are shown as dashed lines, and TFY spectra (bulk) as solid lines.

Raman spectroscopy at multiple wavelengths was used to determine the magnitude of the dispersion of the D peak in the products of routes I-V, as shown in Figure S21–Figure S25 and summarized in Table S2. A lower dispersion of the D peak is indicative of higher contents of C₆B₆ “flower-like” units within the planar structure of the graphitic parts of a given BC_x product. Raman and XAS analysis of the products of synthesis routes I and V both corroborate a large contribution from g-BC₃ environments throughout the bulk of the sample; the D peak dispersion (Disp(D)) of the product of route V is the lowest of all samples measured herein. The products of route II (from diborane) showed two distinct Raman spectral types, each with a distinct Disp(D) as well. One environment is remarkably similar to that of the products of routes I and V and appears to be akin to bulk BC₃'; this is in agreement with the XAS spectrum (Figure S20) which reveals that the surface of the product of route II exhibits a high density of g-BC₃ environments. The other environment is typical of ordered, boron-poor graphitic carbon, likely catalyzed by the metal walls of the reactor. The Raman spectra of the product of synthesis route III (derived from B₁₀H₁₄) were spatially homogeneous and exhibit a Disp(D) of 33 cm⁻¹ eV⁻¹ indicating a detectable presence of g-BC₃. The core-shell nature of this sample is strongly evidenced by the XAS results (see above). Lastly, the product of synthesis route IV exhibits a Raman spectrum that resembles that of a standard disordered carbon, with a Disp(D) of 44 cm⁻¹ eV⁻¹. This is expectable on the basis of the fact that the naphthalene moiety of the NDB precursor would need to be at least partially decomposed to produce hexagonally ordered g-BC₃ environments; the B–C bonds in the original molecular structure are not in the correct position for true molecular tiling. The pyrolysis temperature of route IV (800 °C) is likely too low to decompose the aromatic structure of naphthalene. The XAS spectra of the route IV product also show discrepancies between the surface

and bulk boron environments, indicating the likely liberation of the bridging diborane during pyrolysis.

Table S2. Raman D peak dispersion of the products from synthesis routes I-V.

	Boron Precursor	Disp(D) ($\text{cm}^{-1} \text{eV}^{-1}$)
I	BBr_3	32
II	B_2H_6	21, 43
III	$\text{B}_{10}\text{H}_{14}$	33
IV	NDB	44
V	BH_4^-	13

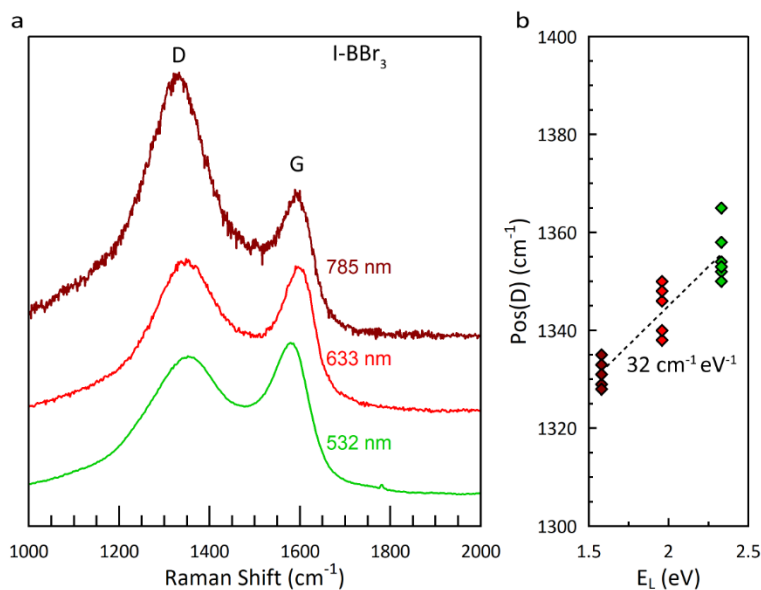


Figure S21. Raman analysis of the D peak dispersion of the product of the co-pyrolysis of BBr_3 and C_6H_6 at $800\text{ }^\circ\text{C}$ (route I). (a) Representative Raman spectra at 532 nm, 633 nm, and 785 nm. (b) D peak position as a function of excitation wavelength, and the least-squares fit dispersion relation.

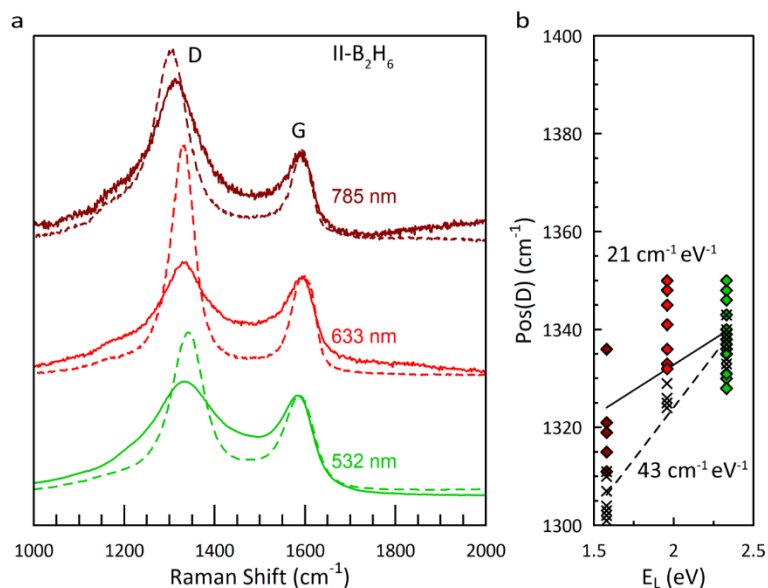


Figure S22. Raman analysis of the D peak dispersion of the product of the co-pyrolysis of B₂H₆ and C₆H₆ at 700 °C (route II). (a) Representative Raman spectra at 532 nm, 633 nm, and 785 nm. (b) D peak position as a function of excitation wavelength, and the least-squares fit dispersion relation.

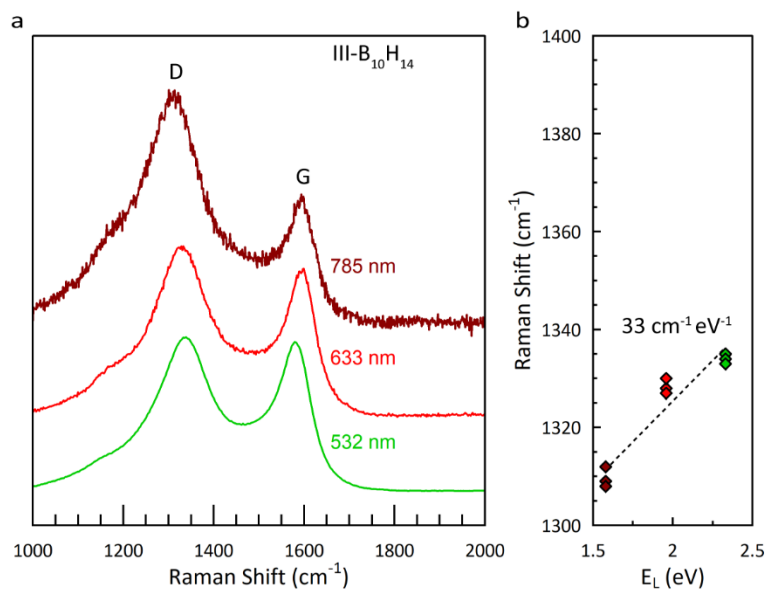


Figure S23. Raman analysis of the D peak dispersion of the product of the co-pyrolysis of B₁₀H₁₄ and C₆H₆ at 800 °C (route III). (a) Representative Raman spectra at 532 nm, 633 nm, and 785 nm. (b) D peak position as a function of excitation wavelength, and the least-squares fit dispersion relation.

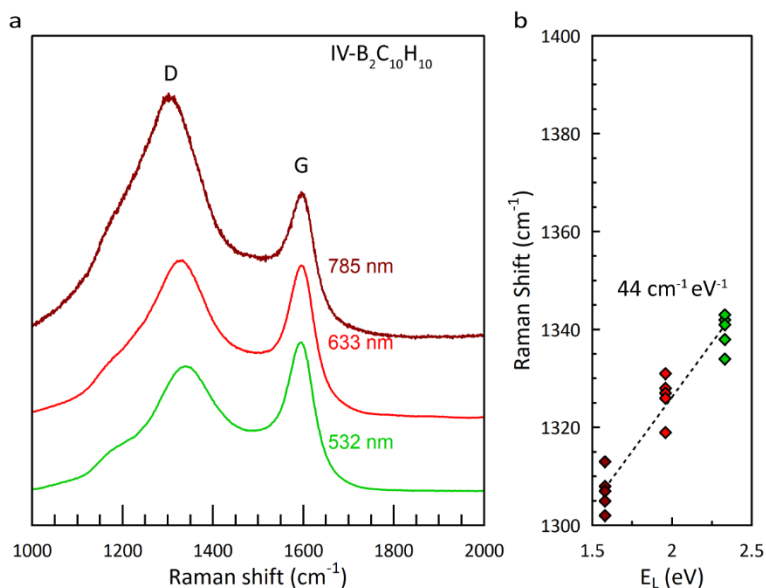


Figure S24. Raman analysis of the D peak dispersion of the product of the pyrolysis of B₂C₁₀H₁₄ (NDB) at 800 °C (route IV). (a) Representative Raman spectra at 532 nm, 633 nm, and 785 nm. (b) D peak position as a function of excitation wavelength, and the least-squares fit dispersion relation.

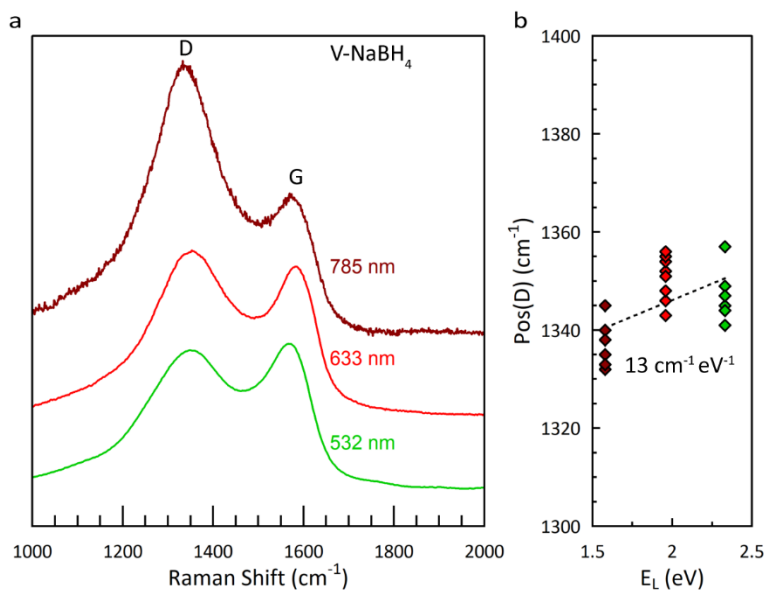


Figure S25. Raman analysis of the D peak dispersion of the product of the co-pyrolysis of NaBH₄ and C₆H₆ at 800 °C (route V). (a) Representative Raman spectra at 532 nm, 633 nm, and 785 nm. (b) D peak position as a function of excitation wavelength, and the least-squares fit dispersion relation.

Decomposition Energy/Temperature Correlation: The relative thermochemical stabilities of the precursor molecules explored in this work were roughly approximated by the simple DFT approach described above. The resulting decomposition energies (ΔE^{SCF}) of several common B- and C-containing precursors are shown in Table S3. The relationship between ΔE^{SCF} and the experimental decomposition temperature (T_d) of the same precursors is shown in Figure S26. Benzene is calculated to exhibit a decomposition energy of 9.1 eV per carbon atom, which corresponds to an experimental decomposition temperature of ~ 750 °C.³⁹ The decomposition energy of boron tribromide is similar to that of benzene: 8.8 eV per boron atom. Of the halide-free precursors, borohydride exhibits the most similar decomposition energy to benzene: 7.0 eV per boron atom. Diborane and decaborane are found to be less stable, at 6.2 and 6.3 eV per boron atom, respectively. These values are consistent with the low stability and high reactivity characteristic of the entire family of lower boranes.⁴⁸ Notably the decomposition energy of NDB ($\text{B}_2\text{C}_{10}\text{H}_{10}$) is significantly higher at 8.5 eV per atom, normalized to the sum of both boron and carbon within the single precursor; this gives rise to an expected decomposition temperature of ~ 600 °C according to the fit over all precursors investigated (dashed line).

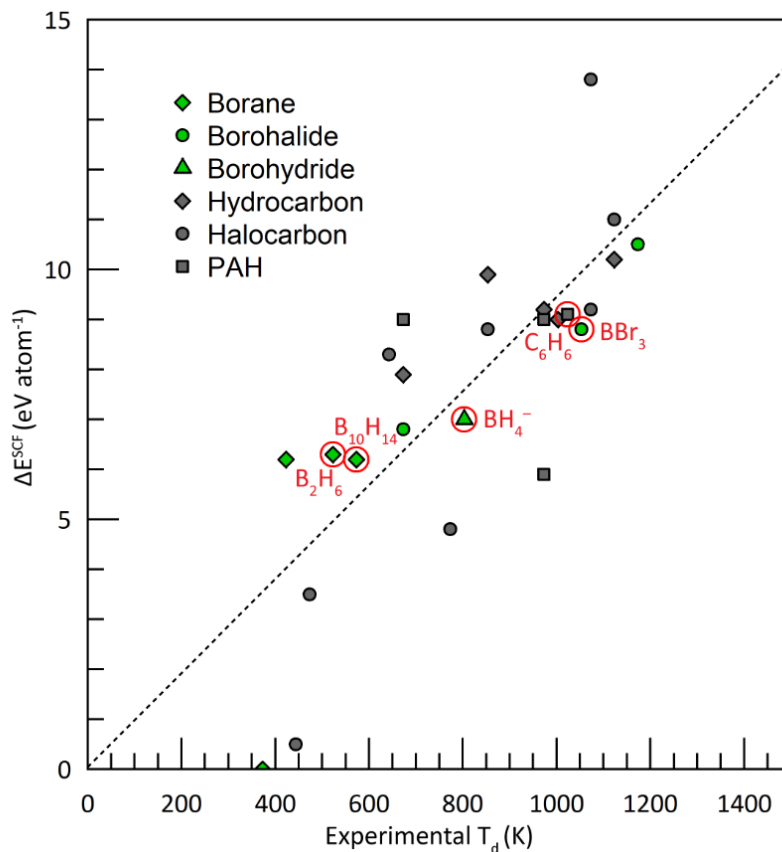


Figure S26. Thermochemical decomposition energy/temperature correlation. Calculated decomposition energy (ΔE^{SCF}), normalized to the number of atoms of relevance (B or C), as a function of experimental decomposition temperature (T_d), showing an expectable correlation that passes close to the origin. The precursors explored in this work are circled in red and indicated with their molecular formula. Note: the “decomposition temperature” of any species is highly dependent on the experimental method/apparatus used, as well as the definition of decomposition itself.

Table S3. Decomposition energies (ΔE^{SFC}), experimental decomposition temperatures, and corresponding references for small molecules of interest in co-pyrolysis reactions to produce boron- and carbon-containing products.

Decomposition Reaction	ΔE^{SFC} (eV atom ⁻¹)	Experimental T _d (°C)	Experimental SI Reference
$\text{BF}_3 \rightarrow \text{B} + 3/2 \text{F}_2$	18.3	-	-
$\text{CF}_4 \rightarrow \text{C} + 2 \text{F}_2$	13.8	800	49
$\text{C}_6\text{F}_6 \rightarrow 6 \text{C} + 3 \text{F}_2$	11.0	850	50
$\text{BCl}_3 \rightarrow \text{B} + 3/2 \text{Cl}_2$	10.5	900	51
$\text{CH}_4 \rightarrow \text{C} + 2 \text{H}_2$	10.2	850	52,53
$\text{C}_2\text{H}_6 \rightarrow 2 \text{C} + 3 \text{H}_2$	9.9	580	54
$\text{C}_3\text{H}_6 \rightarrow 3 \text{C} + 3 \text{H}_2$	9.2	700	55
$\text{C}_6\text{Cl}_6 \rightarrow 6 \text{C} + 3 \text{Cl}_2$	9.2	800	56
$\text{C}_6\text{H}_6 \rightarrow 6 \text{C} + 3 \text{H}_2$	9.1	750	39
$\text{C}_{10}\text{H}_{10} \rightarrow 10 \text{C} + 5 \text{H}_2$	9.0	400	57
$\text{C}_2\text{H}_4 \rightarrow 2 \text{C} + 2 \text{H}_2$	9.0	730	58
$\text{C}_{24}\text{H}_{12} \rightarrow 24 \text{C} + 6 \text{H}_2$	9.0	700	this work
$\text{C}_6\text{Br}_6 \rightarrow 6 \text{C} + 3 \text{Br}_2$	8.8	580	59
$\text{BBr}_3 \rightarrow \text{B} + 3/2 \text{Br}_2$	8.8	780	60
$\text{C}_6\text{I}_6 \rightarrow 6 \text{C} + 3 \text{I}_2$	8.3	370	61
$\text{C}_2\text{H}_2 \rightarrow 2 \text{C} + \text{H}_2$	7.9	400	62
$\text{BH}_4^- \rightarrow \text{B} + 2 \text{H}_2 + \text{e}^-$	7.0	530	63
$\text{BI}_3 \rightarrow \text{B} + 3/2 \text{I}_2$	6.8	400	64,65
$\text{B}_{10}\text{H}_{14} \rightarrow 10 \text{B} + 7 \text{H}_2$	6.3	250	66
$\text{B}_5\text{H}_9 \rightarrow 5 \text{B} + 9/2 \text{H}_2$	6.2	150	66
$\text{B}_2\text{H}_6 \rightarrow 2 \text{B} + 3 \text{H}_2$	6.2	100-300	55,67,68
$\text{C}_{10}\text{H}_8 \rightarrow 10 \text{C} + 4 \text{H}_2$	5.9	700	69
$\text{CCl}_4 \rightarrow \text{C} + 2 \text{Cl}_2$	4.8	500	70
$\text{CBr}_4 \rightarrow \text{C} + 2 \text{Br}_2$	3.5	200	71
$\text{Cl}_4 \rightarrow \text{C} + 2 \text{I}_2$	0.5	-	-

*Note: total decomposition energy is normalized per heteroatom of relevance (C, B, or P)

Funding Sources

We acknowledge the donors of the American Chemical Society Petroleum Research Fund (PRF) as well as support from the U.S. Department of Energy's Office of Energy Efficiency and Renewable Energy (EERE) under the Hydrogen and Fuel Cell Technologies and Vehicle Technologies Offices (award DE-EE0008815). The XAS experiments were performed at beam line BL8.0.1.4 at the Advanced Light Source (ALS), which is a DOE Office of Science User Facility (contract DE-AC02-05CH11231). The NMR experiments were performed using equipment supported by the National Science Foundation (awards MRI:DBI-1532078 and MRI:CHE-2018388) and the Murdock Charitable Trust Foundation (2015066:MNL).

Acknowledgments

We thank Tom Autrey for many exciting and helpful conversations. We also thank Steven Christensen for assistance with developing the safety protocols related to handling diborane.

References

- (1) Greenwood, N. N., Earnshaw, A., *Chemistry of the Elements*, 2nd ed.; Butterworth-Heinemann. Oxford, 1997.
- (2) Albert, B.; Hillebrecht, H. Boron: Elementary Challenge for Experimenters and Theoreticians. *Angew. Chem. Int. Ed.* **2009**, *48* (46), 8640–8668.
- (3) Hirsch, A. The Era of Carbon Allotropes. *Nat. Mater.* **2010**, *9* (11), 868–871.
- (4) Will, G.; Kossobutzki, K. H. An X-Ray Diffraction Analysis of Boron Carbide, $B_{13}C_2$. *J. Less Common Met.* **1976**, *47*, 43–48.
- (5) Thévenot, F. Boron Carbide—A Comprehensive Review. *J. Eur. Ceram. Soc.* **1990**, *6* (4), 205–225.
- (6) Wang, Q.; Chen, L.-Q.; Annett, J. F. Ab Initio Calculation of Structural Properties of C_3B and C_5B Compounds. *Phys. Rev. B* **1997**, *55* (1), 8–10.
- (7) Sun, H.; Ribeiro, F. J.; Li, J.-L.; Roundy, D.; Cohen, M. L.; Louie, S. G. Ab Initio Pseudopotential Studies of Equilibrium Lattice Structures and Phonon Modes of Bulk BC_3 . *Phys. Rev. B* **2004**, *69* (2), 024110.
- (8) Luo, X.; Yang, J.; Liu, H.; Wu, X.; Wang, Y.; Ma, Y.; Wei, S.-H.; Gong, X.; Xiang, H. Predicting Two-Dimensional Boron–Carbon Compounds by the Global Optimization Method. *J. Am. Chem. Soc.* **2011**, *133* (40), 16285–16290.
- (9) M. Dieb, T.; Hou, Z.; Tsuda, K. Structure Prediction of Boron-Doped Graphene by Machine Learning. *J. Chem. Phys.* **2018**, *148* (24), 241716.
- (10) Kouvetakis, J.; Kaner, R. B.; Sattler, M. L.; Bartlett, N. A novel graphite-like material of composition BC_3 , and nitrogen–carbon graphites. *J. Chem. Soc., Chem. Commun.* **1986**, 1758–1759.
- (11) King, T. C.; Matthews, P. D.; Glass, H.; Cormack, J. A.; Holgado, J. P.; Leskes, M.; Griffin, J. M.; Scherman, O. A.; Barker, P. D.; Grey, C. P.; et al. Theory and practice: bulk synthesis of C_3B and its H_2 - and Li-storage capacity. *Angew. Chem., Int. Ed.* **2015**, *54*, 5919–5923.
- (12) Stadie, N. P.; Billeter, E.; Piveteau, L.; Kravchyk, K. V.; Döbeli, M.; Kovalenko, M. V. Direct Synthesis of Bulk Boron-Doped Graphitic Carbon. *Chem. Mater.* **2017**, *29* (7), 3211–3218.
- (13) Lowell, C. E. Solid Solution of Boron in Graphite. *J. Am. Ceram. Soc.* **1967**, *50* (3), 142–144.

- (14) The difference in formation energies between BC_3 and equivalent quantities of graphite and boron carbide is not currently known, but is likely small compared to the thermal energies present at the temperatures characteristic of graphite and carbide synthesis.
- (15) Kaner, R. B.; Kouvetakis, J.; Warble, C. E.; Sattler, M. L.; Bartlett, N. Boron-Carbon-Nitrogen Materials of Graphite-like Structure. *Mater. Res. Bull.* **1987**, *22* (3), 399–404.
- (16) Kouvetakis, J.; Sasaki, T.; Shen, C.; Hagiwara, R.; Lerner, M.; Krishnan, K. M.; Bartlett, N. Novel Aspects of Graphite Intercalation by Fluorine and Fluorides and New B/C, C/N and B/C/N Materials Based on the Graphite Network. *Synth. Met.* **1989**, *34* (1), 1–7.
- (17) Way, B. M.; Dahn, J. R.; Tiedje, T.; Myrtle, K.; Kasrai, M. Preparation and Characterization of B_xC_{1-x} Thin Films with the Graphite Structure. *Phys. Rev. B* **1992**, *46* (3), 1697–1702.
- (18) Cermignani, W.; Paulson, T. E.; Onneby, C.; Pantano, C. G. Synthesis and Characterization of Boron-Doped Carbons. *Carbon* **1995**, *33*, 367–374.
- (19) Naeini, J. G.; Way, B. M.; Dahn, J. R.; Irwin, J. C. Raman Scattering from Boron-Substituted Carbon Films. *Phys. Rev. B* **1996**, *54* (1), 144–151.
- (20) Shirasaki, T.; Derré, A.; Mé né trier, M.; Tressaud, A.; Flandrois, S. Synthesis and characterization of boron-substituted carbons. *Carbon* **2000**, *38*, 1461–1467.
- (21) McGlamery, D.; Baker, A. A.; Liu, Y.-S.; Mosquera, M. A.; Stadie, N. P. Phonon Dispersion Relation of Bulk Boron-Doped Graphitic Carbon. *J. Phys. Chem. C* **2020**, *124* (42), 23027–23037.
- (22) Zhang, C.; Alavi, A. Hydrogen Absorption in Bulk BC_3 : A First-Principles Study. *J. Chem. Phys.* **2007**, *127* (21), 214704.
- (23) Sha, X.; Cooper, A. C.; Bailey, W. H.; Cheng, H. Revisiting Hydrogen Storage in Bulk BC_3 . *J. Phys. Chem. C* **2010**, *114*, 3260–3264.
- (24) Joshi, R. P.; Ozdemir, B.; Barone, V.; Peralta, J. E. Hexagonal BC_3 : A Robust Electrode Material for Li, Na, and K Ion Batteries. *J. Phys. Chem. Lett.* **2015**, *6*, 2728–2732.
- (25) Kuzubov, A. A.; Fedorov, A. S.; Eliseeva, N. S.; Tomilin, F. N.; Avramov, P. V.; Fedorov, D. G. High-Capacity Electrode Material BC_3 for Lithium Batteries Proposed by *Ab Initio* Simulations. *Phys. Rev. B* **2012**, *85* (19), 195415.
- (26) Belasfar, K.; Houmad, M.; Boujnah, M.; Benyoussef, A.; Kenz, A. E. First-Principles Study of BC_3 Monolayer as Anodes for Lithium-Ion and Sodium-Ion Batteries Applications. *J. Phys. Chem. Solids* **2020**, *139*, 109319.

- (27) Zhao, L.; Li, Y.; Zhou, G.; Lei, S.; Tan, J.; Lin, L.; Wang, J. First-Principles Calculations of Stability of Graphene-like BC₃ Monolayer and Its High-Performance Potassium Storage. *Chinese Chem. Lett.* **2021**, *32* (2), 900–905.
- (28) Toebes, M. Impact of the Structure and Reactivity of Nickel Particles on the Catalytic Growth of Carbon Nanofibers. *Catal. Today* **2002**, *76* (1), 33–42.
- (29) De Jong, K. P.; Geus, J. W. Carbon Nanofibers: Catalytic Synthesis and Applications. *Catal. Rev.* **2000**, *42* (4), 481–510.
- (30) Okamoto, H. B-C (Boron-Carbon). *J. Phase Equilib.* **1992**, *13* (4), 436–436.
- (31) Scholz, A. S.; Massoth, J. G.; Bursch, M.; Mewes, J.-M.; Hetzke, T.; Wolf, B.; Bolte, M.; Lerner, H.-W.; Grimme, S.; Wagner, M. BNB-Doped Phenalenyls: Modular Synthesis, Optoelectronic Properties, and One-Electron Reduction. *J. Am. Chem. Soc.* **2020**, *142* (25), 11072–11083.
- (32) Yu, H. S.; He, X.; Li, S. L.; Truhlar, D. G. MN15: A Kohn–Sham Global-Hybrid Exchange–Correlation Density Functional with Broad Accuracy for Multi-Reference and Single-Reference Systems and Noncovalent Interactions. *Chem. Sci.* **2016**, *7* (8), 5032–5051.
- (33) Weigend, F.; Ahlrichs, R. Balanced Basis Sets of Split Valence, Triple Zeta Valence and Quadruple Zeta Valence Quality for H to Rn: Design and Assessment of Accuracy. *Phys. Chem. Chem. Phys.* **2005**, *7* (18), 3297–3305.
- (34) Rowsey, R.; Taylor, E. E.; Irle, S.; Stadie, N. P.; Szilagy, R. K. Methane Adsorption on Heteroatom-Modified Maquettes of Porous Carbon Surfaces. *J. Phys. Chem. A* **2021**, *125* (28), 6042–6058.
- (35) Rowsey, R.; Taylor, E. E.; Hinson, R. W.; Compton, D.; Stadie, N. P.; Szilagy, R. K. Does Boron or Nitrogen Substitution Affect Hydrogen Physisorption on Open Carbon Surfaces? *Phys. Chem. Chem. Phys.* **2022**, *24* (46), 28121–28126.
- (36) Nakamori, Y.; Miwa, K.; Ninomiya, A.; Li, H.; Ohba, N.; Towata, S.; Züttel, A.; Orimo, S. Correlation between Thermodynamical Stabilities of Metal Borohydrides and Cation Electronegativities: First-Principles Calculations and Experiments. *Phys. Rev. B* **2006**, *74* (4), 045126.
- (37) Callini, E.; Borgschulte, A.; Ramirez-Cuesta, A. J.; Züttel, A. Diborane Release and Structure Distortion in Borohydrides. *Dalton Trans.* **2012**, *42* (3), 719–725.
- (38) Pitt, M. P.; Paskevicius, M.; Brown, D. H.; Sheppard, D. A.; Buckley, C. E. Thermal Stability of Li₂B₁₂H₁₂ and Its Role in the Decomposition of LiBH₄. *J. Am. Chem. Soc.* **2013**, *135* (18), 6930–6941.

- (39) Zanetti, J. E.; Egloff, G. The Thermal Decomposition of Benzene. *J. Ind. Eng. Chem.* **1917**, *9* (4), 350–356.
- (40) Pallier, C.; Leyssale, J.-M.; Truflandier, L. A.; Bui, A. T.; Weisbecker, P.; Gervais, C.; Fischer, H. E.; Sirotti, F.; Teyssandier, F.; Chollon, G. Structure of an Amorphous Boron Carbide Film: An Experimental and Computational Approach. *Chem. Mater.* **2013**, *25*, 2618–2629.
- (41) Ferrari, A. C.; Basko, D. M. Raman Spectroscopy as a Versatile Tool for Studying the Properties of Graphene. *Nat. Nanotech.* **2013**, *8* (4), 235–246.
- (42) Frisch, M. J.; Trucks, G. W.; Schlegel, H. B.; Scuseria, G. E.; Robb, M. A.; Cheeseman, J. R.; Scalmani, G.; Barone, V.; Petersson, G. A.; Nakatsuji, H.; Li, X.; Caricato, M.; Marenich, A. V.; Bloino, J.; Janesko, B. G.; Gomperts, R.; Mennucci, B.; Hratchian, H. P.; Ortiz, J. V.; Izmaylov, A. F.; Sonnenberg, J. L.; Williams-Young, D.; Ding, F.; Lipparini, F.; Egidi, F.; Goings, J.; Peng, B.; Petrone, A.; Henderson, T.; Ranasinghe, D.; Zakrzewski, V. G.; Gao, J.; Rega, N.; Zheng, G.; Liang, W.; Hada, M.; Ehara, M.; Toyota, K.; Fukuda, R.; Hasegawa, J.; Ishida, M.; Nakajima, T.; Honda, Y.; Kitao, O.; Nakai, H.; Vreven, T.; Throssell, K.; Montgomery, J. A., Jr.; Peralta, J. E.; Ogliaro, F.; Bearpark, M. J.; Heyd, J. J.; Brothers, E. N.; Kudin, K. N.; Staroverov, V. N.; Keith, T. A.; Kobayashi, R.; Normand, J.; Raghavachari, K.; Rendell, A. P.; Burant, J. C.; Iyengar, S. S.; Tomasi, J.; Cossi, M.; Millam, J. M.; Klene, M.; Adamo, C.; Cammi, R.; Ochterski, J. W.; Martin, R. L.; Morokuma, K.; Farkas, O.; Foresman, J. B.; Fox, D. J. *Gaussian 16*, **2016**.
- (43) Wallenberger, F. T.; Nordine, P. C. Strong, Small Diameter, Boron Fibers by LCVD. *Mater. Lett.* **1992**, *14* (4), 198–202.
- (44) Tzeng, S.-S.; Hung, K.-H.; Ko, T.-H. Growth of Carbon Nanofibers on Activated Carbon Fiber Fabrics. *Carbon* **2006**, *44* (5), 859–865.
- (45) Sha, W.; Liu, Y.; Zhou, Y.; Huang, Y.; Huang, Z. Effect of Carbon Content on Mechanical Properties of Boron Carbide Ceramics Composites Prepared by Reaction Sintering. *Materials* **2022**, *15* (17), 6028.
- (46) Jiménez, I.; Sutherland, D. G. J.; van Buuren, T.; Carlisle, J. A.; Terminello, L. J.; Himpsel, F. J. Photoemission and X-Ray-Absorption Study of Boron Carbide and Its Surface Thermal Stability. *Phys. Rev. B* **1998**, *57* (20), 13167–13174.
- (47) Caretti, I.; Gago, R.; Albella, J. M.; Jiménez, I. Boron carbides formed by coevaporation of B and C atoms: Vapor reactivity, B_xC_{1-x} composition, and bonding structure. *Phys. Rev. B: Condens. Matter Mater. Phys.* **2008**, *77*, 174109.
- (48) Long, L. H. The Mechanisms of Thermal Decomposition of Diborane and of Interconversion of the Boranes: A Reinterpretation of the Evidence. *J. Inorg. Nucl. Chem.* **1970**, *32* (4), 1097–1115.

- (49) *carbon tetrafluoride*. <https://www.chembk.com/en/chem/carbon%20tetrafluoride> (accessed 2023-07-01).
- (50) Dibeler, V. H.; Reese, R. M.; Mohler, F. L. Ionization and Dissociation of Hexafluorobenzene by Electron Impact. *J. Chem. Phys.* **1957**, *26* (2), 304–305.
- (51) Muroi, M.; Otani, M.; Habuka, H. Boron-Silicon Film Chemical Vapor Deposition Using Boron Trichloride, Dichlorosilane and Monomethylsilane Gases. *ECS J. Solid State Sci. Technol.* **2021**, *10* (6), 064006.
- (52) Yousefi, M.; Donne, S. Experimental Study for Thermal Methane Cracking Reaction to Generate Very Pure Hydrogen in Small or Medium Scales by Using Regenerative Reactor. *Front. Energy Res.* **2022**, *10*, 971383.
- (53) Guéret, C.; Daroux, M.; Billaud, F. Methane Pyrolysis: Thermodynamics. *Chem. Eng. Sci.* **1997**, *52* (5), 815–827.
- (54) Laidler, K. J.; Wojciechowski, B. W.; Steacie, E. W. R. Kinetics and Mechanisms of the Thermal Decomposition of Ethane - I. The Uninhibited Reaction. *Proc. R. Soc. Lond. A* **1961**, *260* (1300), 91–102.
- (55) Hurd, D. T. The Reactions of Diborane with Hydrocarbons. *J. Am. Chem. Soc.* **1948**, *70* (6), 2053–2055.
- (56) Ahling, B.; Lindskog, A. Thermal Destruction of PCB and Hexachlorobenzene. *Sci. Total Environ.* **1978**, *10* (1), 51–59.
- (57) Straus, S.; Madorsky, S. L. Thermal Stability of Polydivinylbenzene and of Copolymers of Styrene With Divinylbenzene and With Trivinylbenzene. *J. Res. NBS A Phys. Chem.* **1961**, *65A* (3), 243–248.
- (58) Towell, G. D.; Martin, J. J. Kinetic Data from Nonisothermal Experiments: Thermal Decomposition of Ethane, Ethylene, and Acetylene. *AIChE J.* **1961**, *7* (4), 693–698.
- (59) Jiang, L.; Niu, T.; Lu, X.; Dong, H.; Chen, W.; Liu, Y.; Hu, W.; Zhu, D. Low-Temperature, Bottom-Up Synthesis of Graphene via a Radical-Coupling Reaction. *J. Am. Chem. Soc.* **2013**, *135* (24), 9050–9054.
- (60) Sugaya, T.; Takeuchi, Y.; Watanabe, O. Preparation and Crystal Structure of Solid Boron Grown from the BBr₃-H₂ Mixture. *J. Common Met.* **1976**, *47*, 49–54.
- (61) Mattern, D. L. Periodination of Benzene with Periodate/Iodide. *J. Org. Chem.* **1983**, *48* (24), 4772–4773.
- (62) Cullis, C. F.; Franklin, N. H.; Gaydon, A. G. The Pyrolysis of Acetylene at Temperatures from 500 to 1000 °C. *Proc. R. Soc. Lond. A* **1964**, *280* (1380), 139–152.

- (63) Jubert Tomasso, C.; Pham, A. L.; Mattox, T. M.; Urban, J. J. Using Additives to Control the Decomposition Temperature of Sodium Borohydride. *J. Energy Power Technol.* **2020**, *2* (2), 1–20.
- (64) Moore, R. E.; Ownby, P. D. Thermal Decomposition of Boron Triiodide on Molybdenum Field Emitter Surfaces. *Jpn. J. Appl. Phys.* **1974**, *13* (S2), 71.
- (65) Gao, W. Crystal Growth of Alpha-Rhombohedral Boron. Thesis, Kansas State University, 2010. <https://krex.k-state.edu/handle/2097/4171> (accessed 2023-07-01).
- (66) Owen, J. The Pyrolysis of Decaborane. *J. Chem. Soc.* **1961**, 5438–5444.
- (67) Travers, M. W. On the New View of the Nature of the Covalent Linkage, and the Formation of Free Radicals. *Trans. Faraday Soc.* **1934**, *30* (0), 100–102.
- (68) Mazaheri, A.; Javadi, M.; Abdi, Y. Chemical Vapor Deposition of Two-Dimensional Boron Sheets by Thermal Decomposition of Diborane. *ACS Appl. Mater. Interfaces* **2021**, *13* (7), 8844–8850.
- (69) Gai, C.; Dong, Y.; Yang, S.; Zhang, Z.; Liang, J.; Li, J. Thermal Decomposition Kinetics of Light Polycyclic Aromatic Hydrocarbons as Surrogate Biomass Tar. *RSC Adv.* **2016**, *6* (86), 83154–83162.
- (70) Tonnoir, H.; Huo, D.; Davoisne, C.; Celzard, A.; Fierro, V.; Saurel, D.; El Marssi, M.; Benyoussef, M.; Meunier, P.; Janot, R. Pyrolysis Temperature Dependence of Sodium Storage Mechanism in Non-Graphitizing Carbons. *Carbon* **2023**, *208*, 216–226.
- (71) Hoke, W. E.; Weir, D. G.; Lemonias, P. J.; Hendriks, H. T. Carbon Tetrabromide Carbon Doping of Molecular Beam Epitaxial (GaAs) Films. *Appl. Phys. Lett.* **1994**, *64* (2), 202–204.

CHAPTER SIX

CONCLUSIONS

Summary of Results

The studies presented in this work are motivated by the ever-growing need for alternative energy carriers in today's rapidly evolving society. Energy storage materials constructed from first row elements are ideal due to their inherent low densities and relatively high abundance, as well as the large library of structures that can be accessed from carbons bonding motifs. This work's main focus revolves around understanding the synthesis and characterization of high boron content nanocrystalline graphitic carbon as a bulk free-standing material with the long-term goal of accessing highly crystalline graphitic BC_3' . Though today we are still limited to the nanocrystalline regime, this work has made great strides in understanding the transition from molecular precursors to bulk materials. Through a bottom-up synthesis approach, a new pair of boron and carbon precursors has been identified, permitting the halide-free synthesis and characterization of graphitic materials resembling BC_3' . In addition, discovered new characterization methods for the detection of graphitic BC_3 chemical environments have been developed via Raman spectroscopy. The synthetic progress described herein has shed fundamental insight into the importance of decomposition compatibility of boron and carbon precursors for the generation of homogeneous metastable BC_3' . The materials investigated in this work have practical applications related to energy storage in the form of high-rate anode materials for lithium-ion batteries as well as for the solid-state storage of hydrogen at near ambient conditions.

This work addresses the three main objectives outlined in Chapter 1. These discoveries have led to a wealth of new testable hypotheses that will be discussed as avenues for future studies.

Objective 1

Through the exploration of the relative decomposition mechanisms of carbon precursor molecules in the temperature range of relevance for the formation of BC_3' , we have revealed that the decomposition of PAH molecules proceeds via the evolution of edge hydrogens and that the shape of the original carbon molecule is well preserved. This finding establishes that the framework of the final material is determined by the geometry of the carbon precursor molecule. To arrive at a hexagonally-ordered BC_3' material, benzene is likely the ideal carbon-containing precursor molecule, as it will facilitate the formation of C_6B_6 flower-like units in the final structure, as seen in Figure 1.

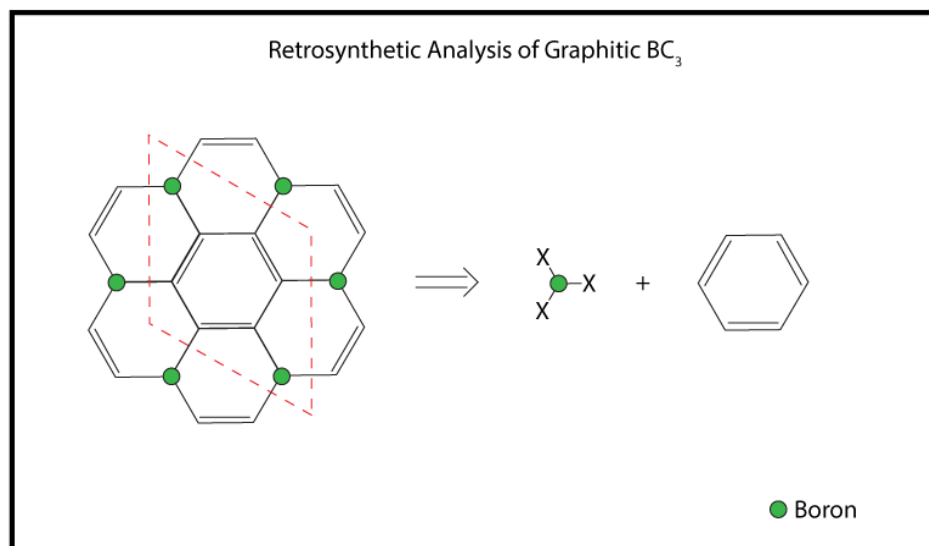


Figure 1. Retrosynthetic analysis of the in-plane structure of graphitic BC_3' .

In the pursuit of Objective 1, we have arrived at another serendipitous discovery of a novel type of lithiation mechanism of carbon materials. This lithiation event was observed for a coronene-derived graphitic carbon material pyrolyzed at 800 °C, referred to herein as Cor800. This novel lithiation event has been thoroughly characterized by electrochemical techniques and theorized to be associated with the large amount of internal hydrogen edge character found in this material. Cor800 is graphitic in nature and exhibits a low surface area, while at the same time contains a high content of hydrogen. Coupling these two observations evidences the existence of extensive edge character buried within the bulk of the material. The unique combination of wide interlayer graphitic stacking and internal hydrogen-type sites allows for rapid insertion and de-insertion of lithium at ultra-fast current rates up to 60 C (1 min charging time) with excellent reversibility and stability of the redox event at ~ 0.5 V vs. Li/Li⁺. The buried nature of these lithiation sites renders them protected from solvent during the first cycle lithiation, permitting high first-cycle efficiency, that has proven to be elusive for other high-rate LIB anode materials.

Objective 2

We have developed a new method for identifying g-BC₃ chemical environments within BC₃' that is accessible by benchtop characterization techniques. By utilizing multiple wavelength Raman spectroscopy, we have discovered a unique phonon dispersion relation of the D mode in graphitic carbons that contain a significant amount of hexagonally-ordered BC₃ chemical environments. Such materials exhibit a reduced D peak dispersion relation as low as 13 cm⁻¹ eV⁻¹. This can be explained by the flattening of optical phonon branch associated with ring-breathing around the K point in the first Brillouin zone for BC₃' compared to that of graphite. The highly dispersive D peak in disordered graphite originates from the Kohn anomaly at the K point and is

distinctly different from what is experimentally observed for graphitic BC_3' . Hence, the D peak dispersion can be used to identify bulk graphitic materials with substitutional boron doping that is inherent to the structure of BC_3' and is expected to be zero for a single crystal.

This study also elucidates the conditions needed for the formation of the metastable phase of high boron-content graphitic carbon that is only accessible between synthesis temperatures of 800–950 °C; at temperatures of ≥ 1000 °C, phase separation between boron carbide and the low boron content graphitic solution results in the leaching of boron from the graphitic phase.

Objective 3

We have explored new synthetic routes to access bulk BC_3' that circumvent the use of boron halide reagents such as boron tribromide (BBr_3) or boron trichloride (BCl_3). Upon examination of the materials generated from the co-pyrolysis of benzene with sodium borohydride, diborane, or decaborane, we have arrived at the conclusion that not only must the precursor geometry be considered to generate trigonal planer BC_3 chemical environments within a graphitic product, but also the relative decomposition energies of the precursor molecules must be sufficiently close to allow for the simultaneous pyrolysis of both reactants. It was found that the energies of decomposition of the co-pyrolysis reagents must be sufficiently close to allow for both species to interact during the pyrolysis reaction and form a homogeneous product. Boron tribromide and sodium borohydride are two promising reagents to be used with benzene for the generation of graphitic BC_3' . This is due to two main factors: first, these reagents effectively isolate the boron atom, preventing the formation of B–B bonds, and second, these reagents have relatively high thermochemical stabilities, comparable to that of benzene. These two factors work in conjunction to prevent the decomposition of the boron species into higher order boranes and allows the reactive

species to be present at the same synthesis temperature, allowing the formation of trigonal planar BC_3 chemical environments. When the various boranes are used, such as diborane or decaborane, the reaction proceeds first by the expected decomposition and formation of larger boron clusters at a relatively low temperature of ~ 100 °C, followed by a later and isolated decomposition of benzene into a low boron content graphite at temperatures at or above 700 °C. Thus, not only must the geometry of the carbon and boron precursor be considered, but also the relative decomposition energies of the molecular reagents.

This work has led to the development of a DFT framework to assess the thermochemical stability of small molecules for co-pyrolysis reactions. This computational method serves to guide future work in this field (e.g., by elevating other combinations of precursors such as C_2H_2 and B_2H_6) and can be easily extended beyond the boron-carbon system to other bottom-up gas- or liquid-phase reactions that involve the co-pyrolysis of p-block elements toward novel metastable phases.

Future Work

This scientific journey led to a wealth of testable hypotheses. While the studies presented in this work have addressed the three objectives outlined in chapter one, they have also generated additional questions regarding synthetic conditions, materials characterization, and the application of these materials for energy storage. Some future directions stemming from the three objectives will be highlighted in the following sections.

H-Type Binding Sites

The discovery of H-type binding sites in Cor800 was a serendipitous finding that arose from the systematic investigation of the pyrolysis reactions of various PAH molecules. The initial synthesis was conducted at 800 °C, and no further exploration into the synthesis temperature was conducted. It remains to be seen if H-type sites can be accessed and their performance enhanced by conducting the pyrolysis reaction at lower temperatures or by changing the PAH molecule used for synthesis. We proposed that smaller PAH molecules will require a lower synthesis temperature to preserve their internal hydrogen content and allow access to H-type sites. There is also the possibility that increasing the precursor size will afford a greater hydrogen content within the pyrolysis products at low synthesis temperatures.

Detailed characterization and elucidation of the atomistic structure of H-type binding sites is still needed. The Raman spectrum of Cor800 shows unique and well-defined features on the low frequency shoulder of the D peak. These features are associated with C–H edge character within the graphitic crystallite³ and could be the regions where charge transfer between the lithium ion and Cor800 is occurring. If lithium binds to these locations, it is proposed that the shoulder features of the D peak in the Raman spectrum would be eliminated, resulting from the altered edge character. These experiments would necessitate the fabrication and commissioning of an operando electrochemical cell that would allow for examination of the carbonaceous anode at various states of charge by Raman spectroscopy.

It remains to be definitively proven that the redox event of Cor800 is associated with the hydrogen edge character and not with intercalation of lithium between the widely-spaced molecular fragments of the large PAH molecule that persist through the pyrolysis reaction. To elucidate the effect of hydrogen on the system, it is proposed that a study should be conducted to

replace the hydrogens in coronene with chlorine. This could be performed by synthesizing 1,2,3,4,5,6,7,8,9,10,11,12-dodecakischlorocoronene ($C_{24}Cl_{12}$) by the synthetic procedures outlined by Dong and coworkers.⁴ This chlorinated coronene product could then be pyrolyzed to obtain a material with a similar carbon framework to Cor800 but without any hydrogens present in the material, this would be referred to as Cl–Cor800. We predicted that the electrochemical lithiation of Cl–Cor800 would proceed without the redox event centered at 0.5 V vs. Li/Li⁺ and, instead, only show the low voltage feature associated with the intercalation of lithium within the widely spaced interlayer galleries of the material. This would be substantial evidence for the existence of interactions between lithium and hydrogen within the novel material Cor800.

Diborane-Derived BC₃'

Based on the results presented herein, spanning extensive studies of the diborane-benzene pyrolysis reaction, coupled with the insight on decomposition temperatures gleaned from thermochemical calculations of the isolated precursor molecules, it can be concluded that alternative carbon precursors are needed to form graphitic BC₃' with diborane as the boron source. If another brave researcher wishes to undertake this task, our thermochemical calculations indicate that acetylene (C₂H₂) would have a similar decomposition temperature to that of diborane. This would facilitate the formation of a single homogeneous phase likely leading to the formation of BC₃' in higher purity than was accessible by the reaction of diborane and benzene. The proposed reaction of acetylene and diborane brings about many challenges, mainly the controlled mixing of the acetylene and diborane feed stock to achieve an overall ratio of BC₃ in the final product. This coupled with the safety concerns associated with the reactive species acetylene and the toxic and pyrophoric nature of diborane would most certainly complicate the synthetic endeavor. However,

with appropriate planning, adequate equipment, and thoughtful experiment design and execution, this route would likely lead to the formation of a high boron content graphitic carbon at temperatures well below 700 °C.

References

- (1) King, T. C.; Matthews, P. D.; Glass, H.; Cormack, J. A.; Holgado, J. P.; Leskes, M.; Griffin, J. M.; Scherman, O. A.; Barker, P. D.; Grey, C. P.; et al. Theory and practice: bulk synthesis of C3B and its H₂- and Li-storage capacity. *Angew. Chem., Int. Ed.* **2015**, 54, 5919–5923.
- (2) Stadie, N. P.; Billeter, E.; Piveteau, L.; Kravchyk, K. V.; Döbeli, M.; Kovalenko, M. V. Direct Synthesis of Bulk Boron-Doped Graphitic Carbon. *Chem. Mater.* **2017**, 29 (7), 3211–3218.
- (3) Yamada, Y.; Kawai, M.; Yorimitsu, H.; Otsuka, S.; Takanashi, M.; Sato, S. Carbon Materials with Zigzag and Armchair Edges. *ACS Appl. Mater. Inter.* **2018**, 10 (47), 40710–40739.
- (4) Dong, R.; Pfeffermann, M.; Skidin, D.; Wang, F.; Fu, Y.; Narita, A.; Tommasini, M.; Moresco, F.; Cuniberti, G.; Berger, R.; Müllen, K.; Feng, X. Persulfurated Coronene: A New Generation of “Sulflower.” *J. Am. Chem. Soc.* **2017**, 139 (6), 2168–2171.

APPENDICES

APPENDIX A:

AMPOLES AND SCHLENK LINE

Ampule Fabrication

Large ampules for synthesis are fabricated in house from stock quartz tubing (19 mm OD, 16 mm ID, 122.5 cm length, Technical Glass Products, Inc.). The stock quartz tube is cut to a length of 60 cm, with a diamond bladed Dremel tool running on the slowest speed setting. During the cutting process one should be equipped with an N95 dust mask. The quartz dust that is generated from cutting the stock tubing is immediately cleaned up by wiping the benchtop down with a damp paper towel. Once the tubing is cut to length, the quartz dust is removed from the interior and exterior of the tube with compressed air. The tube is then marked at 30 cm, the halfway point, and an oxy-hydrogen torch is used to collapse the tubing in on itself to separate the 60 cm length into two 30 cm lengths, each with one closed end. The flame of the torch should form an inner blue cone and have sufficient intensity to quickly soften the quartz tube, see Figure A1. Care is taken to maintain the thickness of the quartz end by letting the quartz collapse in on itself and by refraining from pulling the two halves apart. Once the end of the ampule is closed, the neck of the ampule is formed. The ampule is marked 21 cm from the closed end. At this mark the neck is formed with the oxy-hydrogen torch by allowing the walls to collapse inward, again preserving the thickness of the walls by refraining from pulling the two sides of the ampule apart. The neck is collapsed until the inner diameter of the orifice is ~ 0.5 cm at its smallest point, and the length of the neck is ~ 4 cm. At this point the rim of the open end is softened with the torch by briefly applying the flame to the rim on the open end of the ampule. Care must be taken to prevent deformation of the ampule and only to soften any sharp surfaces.

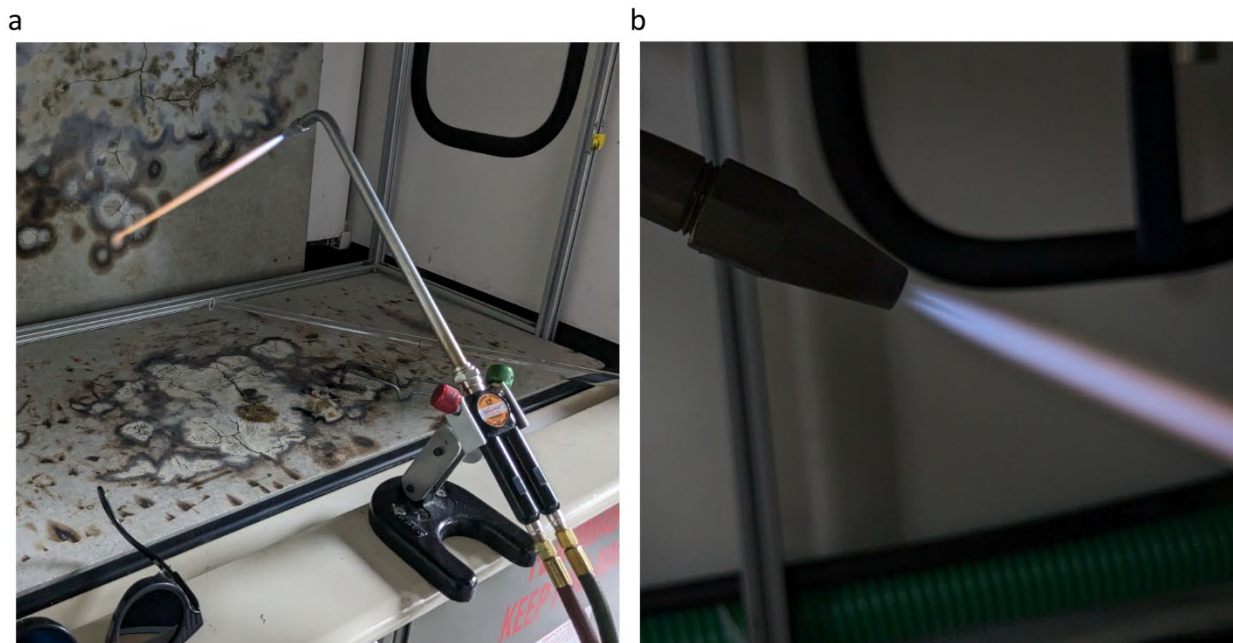


Figure A1. Oxy-Hydrogen torch flame intensity. (a) The flame should be relatively intense to effectively soften and move the quartz. (b) the ratio of hydrogen to oxygen should be adjusted so the flame forms a sharp inner cone.

The process of forming the ampule generates silicon dioxide dust on the surface of the ampule resulting from interactions with the flame. This dust is removed by holding the ampule upside down and washing it thoroughly with deionized water. Once the exterior is clean the interior is rinsed at least three times with deionized water. The ampule is then dried overnight in an oven at 120 °C. Figure A2 shows the progression from a cut segment of quartz tubing to the dry and clean large ampule.

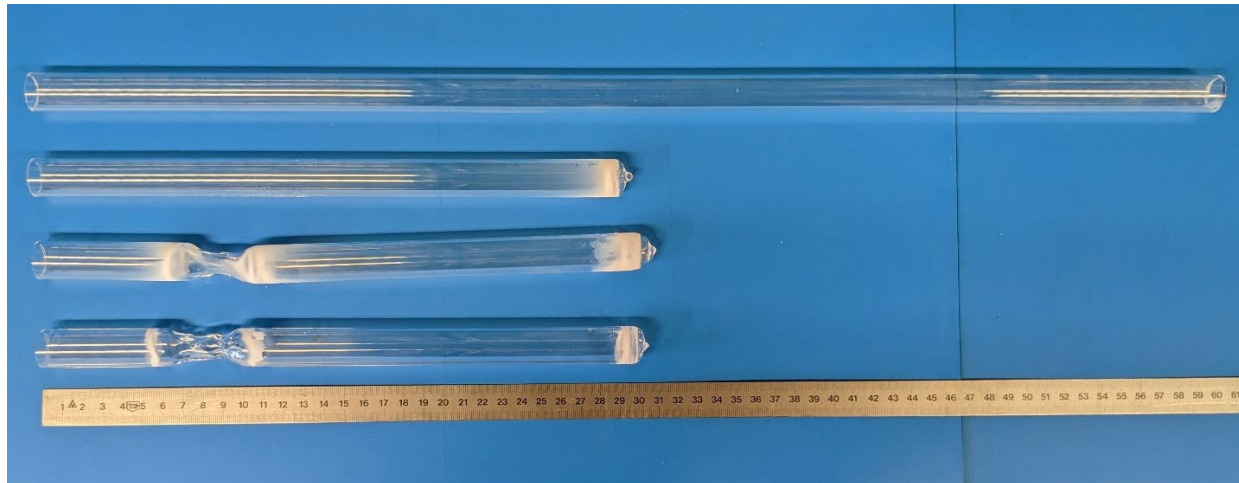


Figure A2. The evolution of a quartz tube into a finished large ampule. The top tube is a cut segment of the stock tubing, below that is a partially generated ampule where the bottom has been closed off. Third from the top is an ampule with a neck that has not been cleaned, note the white silicon dioxide dust around the neck and base. Bottom is a synthesis ready ampule that has been washed and dried.

Ampule synthesis

The clean and dry ampule is then transferred into a glovebox to be filled with reagents. Within the glovebox the appropriate quantity of reagents is precisely charged into the ampule being careful to add the reagent past the neck of the ampule. The quantity of reagents should not produce more than 20 bar of pressure within the ampule at the maximum synthesis temperature, assuming all the evolved species are diatomic ideal gasses. The ampule is then temporarily sealed with a custom Schlenk adapter and removed from the glovebox. The custom stainless-steel Schlenk adapter consists of an Ultra-Torr vacuum fitting (SS-12-UT-6, Swagelok) coupled to a quick connect (SS-QC8-D1-810, Swagelok), as seen in Figure A3.



Figure A3. Male $\frac{3}{4}$ inch Schlenk adapter. The assembled Schlenk adapter can be seen on top and the exploded view on bottom. The O-rings often need to be replaced to achieve an acceptable seal. The small stem O-ring (k-EP-70-OR-008, Swagelok) can be seen on the left, and the two Ultra-Torr O-rings (VT-7-OR-116, Swagelok) can be seen on the right of the assembly.

The custom stainless-steel Schlenk line is prepared by closing the ball valve on the stainless-steel cold trap (P108558, Ideal Vacuum Products), turning on the vacuum pump (RZ 2.5, Vacubrand) and allowing it to warm up for ~ 30 minutes, then the stainless-steel cold trap is filled with liquid nitrogen. The Schlenk connection consists of a female Quick connect (SS-QC8-B1-810, Swagelok), as seen in Figure A4.



Figure A4. Female Schlenk adapter. The assembled Schlenk adapter can be seen on the top and the exploded view on bottom. The O-rings often need to be changed to achieve an acceptable seal; from left to right the valve O-ring (VT-7-OR-012, Swagelok), insert O-ring (K-FC-75-OR-015, Swagelok), and stem seal O-ring (VT-7-OR-014, Swagelok) can be seen.

Within a fume hood, the contents of the ampule are frozen out by submerging the lower half of the ampule in a liquid nitrogen bath. The ampule is then immediately connected to the custom stainless steel Schlenk line, with the lower half still submerged in the liquid nitrogen bath and the ampule is evacuated to 1×10^{-2} mbar. In this state the ampule is promptly flame sealed under active vacuum using the oxy-hydrogen torch harboring a well-prepared flame, as seen in Figure A1. With a properly formed ampule, sufficient flame intensity, and good technique the neck of the ampule can be sealed off in a matter of seconds. The sealed ampule drops into the liquid nitrogen dewar and is immediately removed and set aside to warm to room temperature. The ampule is then cooked within the center of a chamber furnace (RWF 12/13, Carbolite Gero Ltd.) programed with the desired rap rate, maximum temperature, and hold time. The Schleck line is then decommissioned by turning off the vacuum pump and venting the system via the ball valve on the cold trap. The cold head is then removed from the cold trap, washed with soap and water, rinsed with deionized water and acetone, and finally dried in an oven at 80 °C.

Sample Collection

Once the furnace has cooled to room temperature, the ampule is carefully removed and placed in a fume hood. The ampule is carefully scored, roughly in the middle, with a diamond bladed Dremel tool running at the slowest speed setting. The scored ampule is gently placed in a beaker and the ampule is then gently washed with deionized water and acetone to remove any quartz dust generated during cutting. The floor of the fume hood is also wiped down with a damp paper towel to remove the quartz dust generated from scoring the ampule. Once clean, the ampule is inserted into an XL nitrile glove and the open end of the glove is closed with an alligator clip. The ampule, contained within the nitrile glove, is then clamped into a vise with the score line

resting on a knife edge that is affixed to the end of the vise. The overhanging portion of the ampule is struck with a small hammer to crack open the ampule on the score line, releasing the gaseous byproducts into the fume hood. The glove is then cut open with a scalpel and the contents of the ampule are collected with deionized water, as seen in Figure A5.

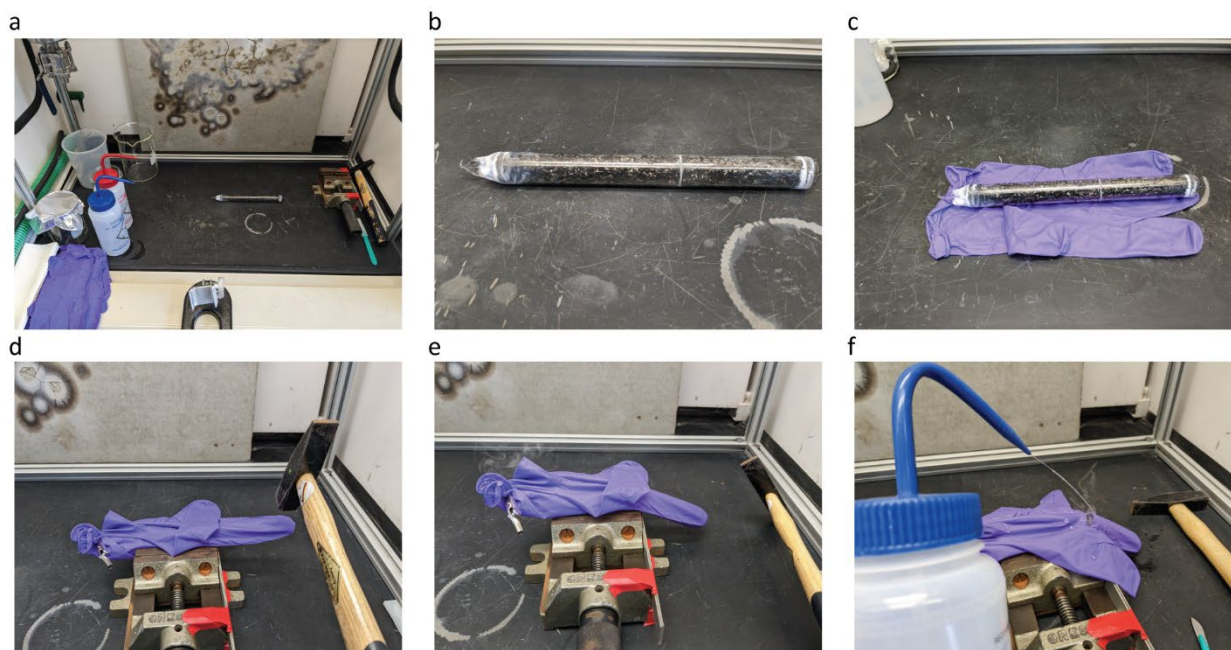


Figure A5. Ampule opening procedure. a) The workspace is clean and prepared with the ampule sitting in the center of the fume hood. b) The ampule has been carefully scored with a diamond bladed saw. c) After cleaning the ampule, it is prepared to be placed within the nitrile enclosure. d) The ampule is secured within the vise with the score line resting on the knife edge that is affixed to the right side of the vise. e) The ampule releases its gaseous byproducts into the fume hood after it has been snapped open. (Note the white fumes exiting the nitrile enclosure) f) The nitrile enclosure is cut open and the contents of the ampule are wetted to assist in collection.

With some materials it is necessary to etch the walls of the ampule with hydrofluoric acid (HF) to free the synthesized material. In these situations, the ampule is placed vertically within a Teflon beaker and ~20 % HF in water (v/v) is added. The ampule is allowed to soak overnight then the contents are poured into a second Teflon beaker and diluted with deionized water. The dilute HF solution containing the product is filtered over a frit to collect the product. The product is then

washed three times with deionized water to remove any trace amounts of HF. When handling HF one should be equipped with a Teflon apron, face shield, nitrile gloves as well as elbow length AlpTec® Solvex® nitrile gloves (37-185, Ansell Healthcare Products LLC).

The collected product is washed three times with deionized water over a frit then washed three times with acetone, as seen in Figure A6. The washed product is transferred into a vial and dried in an oven overnight at 40°C or 80 °C depending on the sensitivity of the product.



Figure A6. Collection and washing of synthesized material. (a–b) The material is collected with deionized water. (c–d) the collected material is washed over a filter frit.

APPENDIX B:

HYDROGEN UPTAKE MEASUREMENTS IN BC₃'

Graphitic BC_3' is predicted to chemisorb hydrogen within the bulk of the material at near ambient condition.^{1,2} These computational studies were motivated by previous studies that show enhanced hydrogen release by boron-doped graphitic thin-films at temperatures between 400-1200 K.³⁻⁵ The development of the direct synthesis route to BC_3' established by Stadie and coworkers in 2017 allowed access to gram quantities of nanocrystalline BC_3' in high purity.⁶ Although these materials are highly disordered and nanocrystalline in nature, it has been shown that this bulk material indeed contains a large portion of hexagonally ordered BC_3 chemical environments that are the origin of the increased hydrogen uptake predicted for the idealized single crystal variant.^{6,7} Although the crystallinity of BC_3' that is accessible today is far from that of the material explored in the computational works, it serves as a means to validate high hydrogen uptake that is predicted for BC_3' compared to the negligible uptake expressed by graphite.

We present preliminary hydrogen uptake measurements on BC_3' prepared by the direct synthesis method. In this, hydrogen sorption measurements were conducted at elevated temperatures of 87 °C. This temperature was chosen based on theoretical results that suggest both hydrogen intercalation and dissociation are thermodynamically and kinetically favorable at near ambient conditions (~70–140 °C).^{1,2} The hydrogen uptake in BC_3' is compared to physisorption of hydrogen on three high surface area carbon scaffolds; a coconut shell derived activated carbon (CNS-201) with an N_2 accessible surface area of 1095 m^2g^{-1} , a super activated carbon (MSC-30) with an N_2 accessible surface area of 3244 m^2g^{-1} , and a zeolite templated carbon (ZTC) with an ultra-high surface area of 3600 m^2g^{-1} . To obtain reasonable physisorption of hydrogen on the high surface area materials, uptake measurements were conducted at 25 °C.⁸ The hydrogen uptake of

BC₃' collected at 87 °C is compared to the room temperature adsorption measurements of the three high surface area carbons in Figure B1.^{8,9}

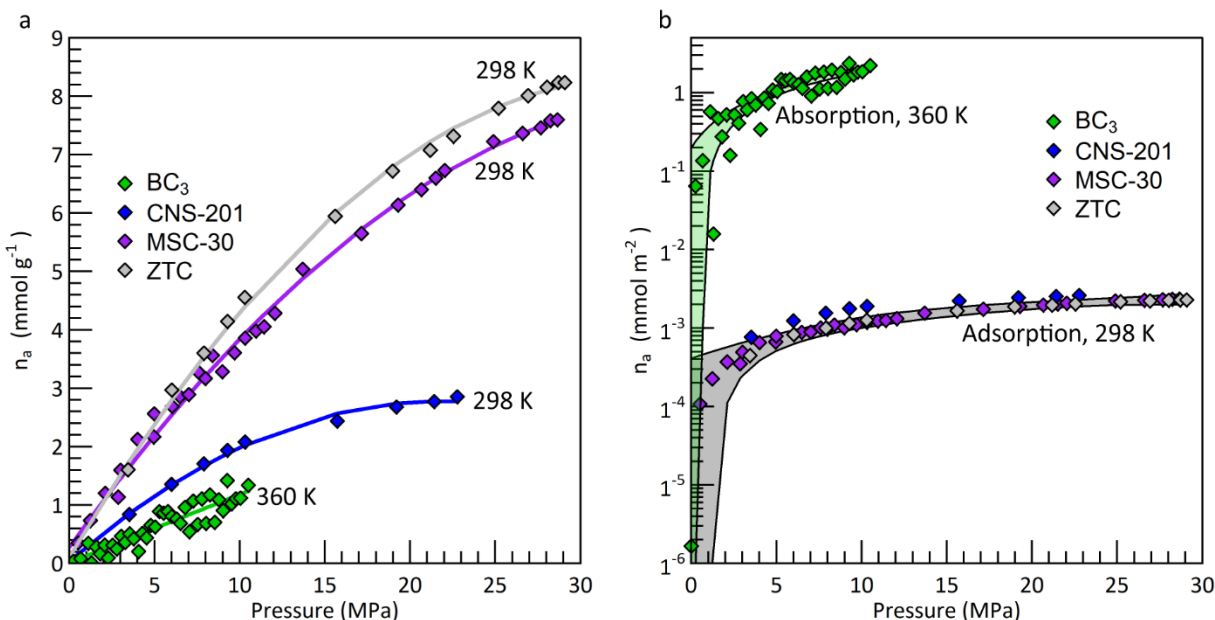


Figure B1. (a) Gravimetric hydrogen uptake, and (b) hydrogen uptake normalized to the materials surface area, BC₃' collected at 87 °C, and CNS-201, MSC-30, and ZTC collected at 25 °C^{8,9}

From Figure B1b it is evident that the observed hydrogen uptake in BC₃' cannot be accounted for by surface adsorption alone, thus hydrogen is being stored within the bulk of the material, consistent with theoretical predictions. This observation proves that hydrogen uptake in BC₃' is not associated with simple surface adsorption. Chahine's rule predicts that surface area and maximum excess hydrogen adsorption on a material are linearly related.¹⁰ If we were to assume a purely physisorptive storage mechanism, ~1 wt.% Hydrogen per 500 m² of N₂ accessible surface area would be adsorbed at ~77 K. Due to the low surface area of BC₃' and disproportionately large hydrogen uptake seen at the high temperature of 360 K, it is evident that an alternative storage mechanism is being utilized, most likely chemisorption of hydrogen within the bulk. While these results only show 0.27 wt% reversible hydrogen uptake in BC₃', well below the predictions of

reversible chemisorption of hydrogen up to H_3BC_3 (~6 wt. %) within the single crystal,^{1,2} these preliminary results set the groundwork for future studies on hydrogen uptake in BC_3' .

Future studies should focus on utilizing large quantities of high-quality bulk BC_3' that have been synthesized by the direct synthesis method. To improve the signal to noise of the measurement the graphitic material should be densely packed within the sampling chamber. Based on these results as well as the predicted binding and activation energies of hydrogen dissociation, migration, and bond formation, it is recommended that adsorption should be conducted in the temperature range of (~70–140 °C).^{1,2}

References

- (1) Zhang, C.; Alavi, A. Hydrogen Absorption in Bulk BC_3 : A First-Principles Study. *J. Chem. Phys.* **2007**, *127* (21), 214704.
- (2) Sha, X.; Cooper, A. C.; Bailey, W. H.; Cheng, H. Revisiting Hydrogen Storage in Bulk BC_3 . *J. Phys. Chem. C* **2010**, *114*, 3260–3264.
- (3) Ferro, Y.; Marinelli, F.; Allouche, A.; Brosset, C. Density Functional Theory Investigation of H Adsorption on the Basal Plane of Boron-Doped Graphite. *J. Chem. Phys.* **2003**, *118* (12), 5650–5657.
- (4) Ferro, Y.; Marinelli, F.; Jelea, A.; Allouche, A. Adsorption, Diffusion, and Recombination of Hydrogen on Pure and Boron-Doped Graphite Surfaces. *J. Chem. Phys.* **2004**, *120* (24), 11882–11888.
- (5) Ferro, Y.; Brosset, C.; Allouche, A. Quantum Study of Hydrogen Interaction with Plasma-Facing Graphite and Boron Doped Graphite Surfaces. *Phys. Scr.* **2004**, *2004* (T108), 76.
- (6) Stadie, N. P.; Billeter, E.; Piveteau, L.; Kravchyk, K. V.; Döbeli, M.; Kovalenko, M. V. Direct Synthesis of Bulk Boron-Doped Graphitic Carbon. *Chem. Mater.* **2017**, *29* (7), 3211–3218.
- (7) McGlamery, D.; Baker, A. A.; Liu, Y.-S.; Mosquera, M. A.; Stadie, N. P. Phonon Dispersion Relation of Bulk Boron-Doped Graphitic Carbon. *J. Phys. Chem. C* **2020**, *124* (42), 23027–23037.

- (8) Stadie, N. P.; Vajo, J. J.; Cumberland, R. W.; Wilson, A. A.; Ahn, C. C.; Fultz, B. Zeolite-Templated Carbon Materials for High-Pressure Hydrogen Storage. *Langmuir* **2012**, *28* (26), 10057–10063.
- (9) Putnam, S., T. Thermodynamic Studies of Hydrogen Storage Materials, Montana State University, Bozeman, Montana, 2021.
- (10) Stadie, N. P. Synthesis and Thermodynamic Studies of Physisorptive Energy Storage Materials. phd, California Institute of Technology, 2013.

REFERENCES

- Dahn, J. R.; Zheng, T.; Liu, Y.; Xue, J. S. Mechanisms for Lithium Insertion in Carbonaceous Materials. *Science* **1995**, *270* (5236), 590–593.
- Stevens, D. A.; Dahn, J. R. The Mechanisms of Lithium and Sodium Insertion in Carbon Materials. *J. Electrochem. Soc.* **2001**, *148* (8), A803.
- Stadie, N. P.; Billeter, E.; Piveteau, L.; Kravchyk, K. V.; Döbeli, M.; Kovalenko, M. V. Direct Synthesis of Bulk Boron-Doped Graphitic Carbon. *Chem. Mater.* **2017**, *29*, 3211–3218.
- Ferrari, A. C.; Robertson, J. Interpretation of Raman spectra of disordered and amorphous carbon. *Phys. Rev. B: Condens. Matter Mater. Phys.* **2000**, *61*, 14095–14107.
- Dresselhaus, M. S.; Jorio, A.; Saito, R. Characterizing Graphene, Graphite, and Carbon Nanotubes by Raman Spectroscopy. *Annu. Rev. Condens. Matter Phys.* **2010**, *1*, 89–108.
- Ferrari, A. C.; Basko, D. M. Raman Spectroscopy as a Versatile Tool for Studying the Properties of Graphene. *Nat. Nanotech.* **2013**, *8* (4), 235–246.
- Langford, J. I.; Wilson, A. J. C. Seherrer after Sixty Years: A Survey and Some New Results in the Determination of Crystallite Size. *J. Appl. Cryst.* **1978**, No. 11, 102–113.
- Yamada, Y.; Kawai, M.; Yorimitsu, H.; Otsuka, S.; Takanashi, M.; Sato, S. Carbon Materials with Zigzag and Armchair Edges. *ACS Appl. Mater. Inter.* **2018**, *10* (47), 40710–40739.
- Naeini, J. G.; Way, B. M.; Dahn, J. R.; Irwin, J. C. Raman Scattering from Boron-Substituted Carbon Films. *Phys. Rev. B* **1996**, *54* (1), 144–151.
- Cloutis, E.; Szymanski, P.; Applin, D.; Goltz, D. Identification and Discrimination of Polycyclic Aromatic Hydrocarbons Using Raman Spectroscopy. *Icarus* **2016**, *274*, 211–230.
- Ingemarsson, L.; Halvarsson, M. SEM/EDX Analysis of Boron, 2011.
- Madden, H. H.; Nelson, G. C. Auger-Electron Spectra from Boron Carbide. *Phys. Rev. B* **1985**, *31* (6), 3667–3671.
- Matejovic, I. Determination of Carbon, Hydrogen, and Nitrogen in Soils by Automated Elemental Analysis (Dry Combustion Method). *Commun. Soil Sci. Plant Anal.* **1993**, *24*, 213–222.
- Ravel, B. *Introduction to X-ray Absorption Spectroscopy*. Synchrotron Science Group National Institute of Standards and Technology & Beamline for Materials Measurements National Synchrotron Light Source II.
- Way, B. M.; Dahn, J. R.; Tiedje, T.; Myrtle, K.; Kasrai, M. Preparation and Characterization of B_xC_{1-x} Thin Films with the Graphite Structure. *Phys. Rev. B* **1992**, *46* (3), 1697–1702.

- Pallier, C.; Leyssale, J.-M.; Truflandier, L. A.; Bui, A. T.; Weisbecker, P.; Gervais, C.; Fischer, H. E.; Sirotti, F.; Teyssandier, F.; Chollon, G. Structure of an Amorphous Boron Carbide Film: An Experimental and Computational Approach. *Chem. Mater.* **2013**, *25*, 2618–2629.
- Caretti, I.; Gago, R.; Albella, J. M.; Jiménez, I. Boron carbides formed by coevaporation of B and C atoms: Vapor reactivity, B_xC_{1-x} composition, and bonding structure. *Phys. Rev. B: Condens. Matter Mater. Phys.* **2008**, *77*, 174109.
- Islamoglu, T.; Idrees, K. B.; Son, F. A.; Chen, Z.; Lee, S.-J.; Li, P.; Farha, O. K. Are You Using the Right Probe Molecules for Assessing the Textural Properties of Metal–Organic Frameworks? *J. Mater. Chem. A* **2021**, *10* (1), 157–173.
- Lowell, C. E. Solid Solution of Boron in Graphite. *J. Am. Ceram. Soc.* **1967**, *50* (3), 142–144.
- McQuarrie, D. A.; Simon, J. D. *Physical Chemistry: A Molecular Approach*; University Science Books, 1997.
- Sanna, S.; Esposito, V.; Andreasen, J. W.; Hjelm, J.; Zhang, W.; Kasama, T.; Simonsen, S. B.; Christensen, M.; Linderoth, S.; Pryds, N. Enhancement of the Chemical Stability in Confined δ - Bi_2O_3 . *Nat. Mater.* **2015**, *14* (5), 500–504.
- Nagabhushana, G. P.; Shivaramaiah, R.; Navrotsky, A. Direct Calorimetric Verification of Thermodynamic Instability of Lead Halide Hybrid Perovskites. *P. Natl. Acad. Sci. USA* **2016**, *113* (28), 7717–7721.
- Kuech, T. F.; Babcock, S. E.; Mawst, L. Growth Far from Equilibrium: Examples from III-V Semiconductors. *Appl. Phys. Rev.* **2016**, *3* (4), 040801.
- Sclafani, A.; Herrmann, J. M. Comparison of the Photoelectronic and Photocatalytic Activities of Various Anatase and Rutile Forms of Titania in Pure Liquid Organic Phases and in Aqueous Solutions. *J. Phys. Chem.* **1996**, *100* (32), 13655–13661.
- Davis, M. E.; Lobo, R. F. Zeolite and Molecular Sieve Synthesis. *Chem. Mater.* **1992**, *4* (4), 756–768.
- Stadie, N. P.; Murialdo, M.; Ahn, C. C.; Fultz, B. Anomalous Isothermic Enthalpy of Adsorption of Methane on Zeolite-Templated Carbon. *J. Am. Chem. Soc.* **2013**, *135* (3), 990–993.
- Sun, W. Theoretical Advancements towards Understanding Crystalline Metastability during Materials Synthesis. Thesis, Massachusetts Institute of Technology, 2016.
- Ribeiro, T. R.; Ferreira Neto, J. B.; Takano, C.; Pocić, J. G. R.; Kolbeinsen, L.; Ringdalen, E. C-O-H₂ Ternary Diagram for Evaluation of Carbon Activity in CH₄-Containing Gas Mixtures. *Materials Research and Technology* **2021**, *13*, 1576–1585.

Parija, A.; Waetzig, G. R.; Andrews, J. L.; Banerjee, S. Traversing Energy Landscapes Away from Equilibrium: Strategies for Accessing and Utilizing Metastable Phase Space. *J. Phys. Chem. C* **2018**, *122* (45), 25709–25728.

Sun, W.; Dacek, S. T.; Ong, S. P.; Hautier, G.; Jain, A.; Richards, W. D.; Gamst, A. C.; Persson, K. A.; Ceder, G. The Thermodynamic Scale of Inorganic Crystalline Metastability. *Science Advances* **2016**, *2* (11), e1600225.

Kouvetakis, J.; McElfresh, M. W.; Beach, D. B. Chemical vapor deposition of highly conductive boron-doped graphite from triphenyl boron. *Carbon* **1994**, *32*, 1129–1132.

Shirasaki, T.; Derré, A.; Mé né trier, M.; Tressaud, A.; Flandrois, S. Synthesis and characterization of boron-substituted carbons. *Carbon* **2000**, *38*, 1461–1467.

Kouvetakis, J.; Kaner, R. B.; Sattler, M. L.; Bartlett, N. A novel graphite-like material of composition BC₃, and nitrogen–carbon graphites. *J. Chem. Soc., Chem. Commun.* **1986**, 1758–1759.

XFlash 6-10 detector. <https://www.bruker.com/en/products-and-solutions/elemental-analyzers/eds-wds-ebds-SEM-Micro-XRF/detectors/xflash-6-10-detector.html> (accessed 2023-05-11).

Statham, P. J. Prospects for Improvement in EDX Microanalysis. *J. Microsc.-Oxford* **1983**, *130* (2), 165–176.

Parkin, G. Representation of Three-Center–Two-Electron Bonds in Covalent Molecules with Bridging Hydrogen Atoms. *J. Chem. Educ.* **2019**, *96* (11), 2467–2475.

McGlamery, D.; Baker, A. A.; Liu, Y.-S.; Mosquera, M. A.; Stadie, N. P. Phonon Dispersion Relation of Bulk Boron-Doped Graphitic Carbon. *J. Phys. Chem. C* **2020**, *124* (42), 23027–23037.

King, T. C.; Matthews, P. D.; Glass, H.; Cormack, J. A.; Holgado, J. P.; Leskes, M.; Griffin, J. M.; Scherman, O. A.; Barker, P. D.; Grey, C. P.; et al. Theory and practice: bulk synthesis of C₃B and its H₂- and Li-storage capacity. *Angew. Chem., Int. Ed.* **2015**, *54*, 5919–5923.

Serin, V.; Brydson, R.; Scott, A.; Kihn, Y.; Abidate, O.; Maquin, B.; Derré, A. Evidence for the solubility of boron in graphite by electron energy loss spectroscopy. *Carbon* **2000**, *38*, 547–554.

Kim, Y. A.; Fujisawa, K.; Muramatsu, H.; Hayashi, T.; Endo, M.; Fujimori, T.; Kaneko, K.; Terrones, M.; Behrends, J.; Eckmann, A.; et al. Raman Spectroscopy of Boron-Doped Single-Layer Graphene. *ACS Nano* **2012**, *6*, 6293–6300.

Kim, E.; Oh, I.; Kwak, J. Atomic structure of highly ordered pyrolytic graphite doped with boron. *Electrochem. Commun.* **2001**, *3*, 608–612.

Lithium-Ion Batteries: Science and Technologies; Yoshio, M., Brodd, R. J., Kozawa, A., Eds.; Springer: New York, NY, 2009.

Li, M.; Lu, J.; Chen, Z.; Amine, K. 30 Years of Lithium-Ion Batteries. *Adv. Mater.* **2018**, *30* (33), 1800561.

Kim, T.; Song, W.; Son, D.-Y.; K. Ono, L.; Qi, Y. Lithium-Ion Batteries: Outlook on Present, Future, and Hybridized Technologies. *J. Mater. Chem. A* **2019**, *7* (7), 2942–2964.

Continuing Our Investment in Nevada. Tesla. <https://www.tesla.com/blog/continuing-our-investment-nevada> (accessed 2023-05-12).

Mohr, S. H.; Mudd, G. M.; Giurco, D. Lithium Resources and Production: Critical Assessment and Global Projections. *Minerals* **2012**, *2* (1), 65–84.

Gruber, P. W.; Medina, P. A.; Keoleian, G. A.; Kesler, S. E.; Everson, M. P.; Wallington, T. J. Global Lithium Availability. *J. Ind. Ecol.* **2011**, *15* (5), 760–775.

Swain, B. Recovery and Recycling of Lithium: A Review. *Sep. Purif. Technol.* **2017**, *172*, 388–403.

Schlapbach, L.; Züttel, A. Hydrogen-Storage Materials for Mobile Applications. *Nature* **2001**, *414* (6861), 353–358.

Allendorf, M. D.; Hulvey, Z.; Gennett, T.; Ahmed, A.; Autrey, T.; Camp, J.; Cho, E. S.; Furukawa, H.; Haranczyk, M.; Head-Gordon, M.; Jeong, S.; Karkamkar, A.; Liu, D.-J.; Long, J. R.; Meihaus, K. R.; Nayyar, I. H.; Nazarov, R.; Siegel, D. J.; Stavila, V.; Urban, J. J.; Veccham, S. P.; Wood, B. C. An Assessment of Strategies for the Development of Solid-State Adsorbents for Vehicular Hydrogen Storage. *Energy Environ. Sci.* **2018**, *11* (10), 2784–2812.

Physical Hydrogen Storage. Energy.gov. <https://www.energy.gov/eere/fuelcells/physical-hydrogen-storage> (accessed 2023-05-22).

Toray Advanced Composites to lead research consortium for development of liquid hydrogen composite tanks for civil aviation - Toray Advanced Composites. <https://www.toraytac.com/media/news-item/2021/12/14/Toray-Advanced-Composites-to-lead-research-consortium-for-development-of-liquid-hydrogen-composite-tanks-for-civil-aviation> (accessed 2023-05-22).

Züttel, A. Materials for Hydrogen Storage. *Mater. Today* **2003**, *6* (9), 24–33.

Stadie, N. P.; Vajo, J. J.; Cumberland, R. W.; Wilson, A. A.; Ahn, C. C.; Fultz, B. Zeolite-Templated Carbon Materials for High-Pressure Hydrogen Storage. *Langmuir* **2012**, *28* (26), 10057–10063.

Huong, T. T. T.; Thanh, P. N.; Son, D. N. Metal – Organic Frameworks: State-of-the-Art Material for Gas Capture and Storage. *VNU Journal of Science: Mathematics - Physics* **2016**, *32* (1).

Hydrogen Storage. Energy.gov. <https://www.energy.gov/eere/fuelcells/hydrogen-storage> (accessed 2023-05-22).

Orimo, S.; Nakamori, Y.; Eliseo, J. R.; Züttel, A.; Jensen, C. M. Complex Hydrides for Hydrogen Storage. *Chem. Rev.* **2007**, *107* (10), 4111–4132.

Zhang, C.; Alavi, A. Hydrogen Absorption in Bulk BC₃: A First-Principles Study. *J. Chem. Phys.* **2007**, *127* (21), 214704.

Ferro, Y.; Marinelli, F.; Allouche, A.; Brosset, C. Density Functional Theory Investigation of H Adsorption on the Basal Plane of Boron-Doped Graphite. *J. Chem. Phys.* **2003**, *118* (12), 5650–5657.

Ferro, Y.; Marinelli, F.; Jelea, A.; Allouche, A. Adsorption, Diffusion, and Recombination of Hydrogen on Pure and Boron-Doped Graphite Surfaces. *J. Chem. Phys.* **2004**, *120* (24), 11882–11888.

Ferro, Y.; Brosset, C.; Allouche, A. Quantum Study of Hydrogen Interaction with Plasma-Facing Graphite and Boron Doped Graphite Surfaces. *Phys. Scr.* **2004**, *2004* (T108), 76.

Sha, X.; Cooper, A. C.; Bailey, W. H.; Cheng, H. Revisiting Hydrogen Storage in Bulk BC₃. *J. Phys. Chem. C* **2010**, *114*, 3260–3264.

Hurd, D. T. The Reactions of Diborane with Hydrocarbons. *J. Am. Chem. Soc.* **1948**, *70* (6), 2053–2055.

Elman, B. S.; Dresselhaus, M. S.; Dresselhaus, G.; Maby, E. W.; Mazurek, H. Raman scattering from ion-implanted graphite. *Phys. Rev. B: Condens. Matter Mater. Phys.* **1981**, *24*, 1027–1034.

Kouvetakis, J.; Sasaki, T.; Shen, C.; Hagiwara, R.; Lerner, M.; Krishnan, K. M.; Bartlett, N. Novel Aspects of Graphite Intercalation by Fluorine and Fluorides and New B/C, C/N and B/C/N Materials Based on the Graphite Network. *Synth. Met.* **1989**, *34* (1), 1–7.

Fecko, D. L.; Jones, L. E.; Thrower, P. A. The formation and oxidation of BC₃, a new graphitelike material. *Carbon* **1993**, *31*, 637–644.

Cermignani, W.; Paulson, T. E.; Onneby, C.; Pantano, C. G. Synthesis and Characterization of Boron-Doped Carbons. *Carbon* **1995**, *33*, 367–374.

Jacques, S.; Guette, A.; Bourrat, X.; Langlais, F.; Guimon, C.; Labrugere, C. LPCVD and Characterization of Boron-Containing Pyrocarbon Materials. *Carbon* **1996**, *34* (9), 1135–1143.

Jin, Z.; Sun, Z.; Simpson, L. J.; O'Neill, K. J.; Parilla, P. A.; Li, Y.; Stadie, N. P.; Ahn, C. C.; Kittrell, C.; Tour, J. M. Solution-Phase Synthesis of Heteroatom-Substituted Carbon Scaffolds for Hydrogen Storage. *J. Am. Chem. Soc.* **2010**, *132* (43), 15246–15251.

Yoshio, M.; Brodd, R. J.; Kozawa, A. *Lithium-Ion Batteries*; Springer, 2009; Vol. 1.

- Yoshino, A. The Birth of the Lithium-Ion Battery. *Angew. Chem. Int. Ed.* **2012**, *51* (24), 5798–5800.
- Nelson, P. A.; Ahmed, S.; Gallagher, K. G.; Dees, D. W. Modeling the Performance and Cost of Lithium-Ion Batteries for Electric-Drive Vehicles, Third Edition. Electrochemical Energy Storage Theme Chemical Sciences and Engineering Division Argonne National Laboratory **2019**.
- Wu, Y. P.; Jiang, C.; Wan, C.; Holze, R. Modified Natural Graphite as Anode Material for Lithium Ion Batteries. *Journal of Power Sources* **2002**, *111* (2), 329–334.
- von Lüders, C.; Zinth, V.; Erhard, S. V.; Osswald, P. J.; Hofmann, M.; Gilles, R.; Jossen, A. Lithium Plating in Lithium-Ion Batteries Investigated by Voltage Relaxation and in Situ Neutron Diffraction. *Journal of Power Sources* **2017**, *342*, 17–23.
- Kim, D. S.; Kim, Y. E.; Kim, H. Improved Fast Charging Capability of Graphite Anodes via Amorphous Al₂O₃ Coating for High Power Lithium Ion Batteries. *Journal of Power Sources* **2019**, *422*, 18–24.
- Xu, K. Nonaqueous Liquid Electrolytes for Lithium-Based Rechargeable Batteries. *Chem. Rev.* **2004**, *104* (10), 4303–4418.
- Persson, K.; Sethuraman, V. A.; Hardwick, L. J.; Hinuma, Y.; Meng, Y. S.; van der Ven, A.; Srinivasan, V.; Kostecki, R.; Ceder, G. Lithium Diffusion in Graphitic Carbon. *J. Phys. Chem. Lett.* **2010**, *1* (8), 1176–1180.
- Jow, T. R.; Delp, S. A.; Allen, J. L.; Jones, J.-P.; Smart, M. C. Factors Limiting Li⁺ Charge Transfer Kinetics in Li-Ion Batteries. *J. Electrochem. Soc.* **2018**, *165* (2), A361–A367.
- Park, J. H.; Yoon, H.; Cho, Y.; Yoo, C.-Y. Investigation of Lithium Ion Diffusion of Graphite Anode by the Galvanostatic Intermittent Titration Technique. *Materials* **2021**, *14* (16), 4683.
- Weiss, M.; Ruess, R.; Kasnatscheew, J.; Levartovsky, Y.; Levy, N. R.; Minnmann, P.; Stolz, L.; Waldmann, T.; Wohlfahrt-Mehrens, M.; Aurbach, D.; Winter, M.; Ein-Eli, Y.; Janek, J. Fast Charging of Lithium-Ion Batteries: A Review of Materials Aspects. *Advanced Energy Materials* **2021**, *11* (33), 2101126.
- Xu, W.; Welty, C.; Peterson, M. R.; Read, J. A.; Stadie, N. P. Exploring the Limits of the Rapid-Charging Performance of Graphite as the Anode in Lithium-Ion Batteries. *J. Electrochem. Soc.* **2022**, *169* (1), 010531.
- Dubey, R.; Zwahlen, M.; Shynkarenko, Y.; Yakunin, S.; Fuerst, A.; Kovalenko, M. V.; Kravchyk, K. V. Laser Patterning of High-Mass-Loading Graphite Anodes for High-Performance Li-Ion Batteries. *Elec. Soc. C* **2020**, *4* (3), 464–468.
- Kottegoda, I. R. M.; Kadoma, Y.; Ikuta, H.; Uchimoto, Y.; Wakihara, M. High-Rate-Capable Lithium-Ion Battery Based on Surface-Modified Natural Graphite Anode and Substituted Spinel Cathode for Hybrid Electric Vehicles. *J. Electrochem. Soc.* **2005**, *152* (8), A1595.

- Yao, J.; Wang, G. X.; Ahn, J.; Liu, H. K.; Dou, S. X. Electrochemical Studies of Graphitized Mesocarbon Microbeads as an Anode in Lithium-Ion Cells. *J. Power Sources* **2003**, *114* (2), 292–297.
- Peng, C.; Liao, M. D.; Lv, X. L.; Chen, L.; Hou, S. P.; Min, D.; Chen, J.; Wang, H.-L.; Lin, J.-H. Large-Scale Synthesis of Highly Structural-Connecting Carbon Nanospheres as an Anodes Material for Lithium-Ion Batteries with High-Rate Capacity. *Chem. Eng. J* **2020**, *2*, 100014.
- Yao, F.; Pham, D. T.; Lee, Y. H. Carbon-Based Materials for Lithium-Ion Batteries, Electrochemical Capacitors, and Their Hybrid Devices. *ChemSusChem* **2015**, *8* (14), 2284–2311.
- Xing, W.; Xue, J. S.; Zheng, T.; Gibaud, A.; Dahn, J. R. Correlation Between Lithium Intercalation Capacity and Microstructure in Hard Carbons. *J. Electrochem. Soc.* **1996**, *143* (11), 3482–3491.
- Zheng, T.; Xing, W.; Dahn, J. R. Carbons Prepared from Coals for Anodes of Lithium-Ion Cells. *Carbon* **1996**, *34* (12), 1501–1507.
- Mathis, T. S.; Kurra, N.; Wang, X.; Pinto, D.; Simon, P.; Gogotsi, Y. Energy Storage Data Reporting in Perspective—Guidelines for Interpreting the Performance of Electrochemical Energy Storage Systems. *Adv. Energy Mater.* **2019**, *9* (39), 1902007.
- Enoki, T.; Miyajima, S.; Sano, M.; Inokuchi, H. Hydrogen-Alkali-Metal-Graphite Ternary Intercalation Compounds. *J. Mater. Res.* **1990**, *5* (2), 435–466.
- Zheng, T.; Liu, Y.; Fuller, E. W.; Tseng, S.; von Sacken, U.; Dahn, J. R. Lithium Insertion in High Capacity Carbonaceous Materials. *J. Electrochem. Soc.* **1995**, *142* (8), 2581–2590.
- Nishihara, H.; Kyotani, T. Zeolite-Templated Carbons – Three-Dimensional Microporous Graphene Frameworks. *Chem. Commun.* **2018**, *54* (45), 5648–5673.
- Taylor, E. E.; Garman, K.; Stadie, N. P. Atomistic Structures of Zeolite-Templated Carbon. *Chem. Mater.* **2020**, *32* (7), 2742–2752.
- Levi, M. D.; Aurbach, D. The Mechanism of Lithium Intercalation in Graphite Film Electrodes in Aprotic Media. Part 1. High Resolution Slow Scan Rate Cyclic Voltammetric Studies and Modeling. *J. Electroanal. Chem.* **1997**, *421* (1–2), 79–88.
- Peng, C.; Mercer, M. P.; Skylaris, C.-K.; Kramer, D. Lithium Intercalation Edge Effects and Doping Implications for Graphite Anodes. *J. Mater. Chem. A* **2020**, *8* (16), 7947–7955.
- Augustyn, V.; Come, J.; Lowe, M. A.; Kim, J. W.; Taberna, P.-L.; Tolbert, S. H.; Abruña, H. D.; Simon, P.; Dunn, B. High-Rate Electrochemical Energy Storage through Li⁺ Intercalation Pseudocapacitance. *Nature Mater* **2013**, *12* (6), 518–522.
- Gogotsi, Y.; Penner, R. M. Energy Storage in Nanomaterials – Capacitive, Pseudocapacitive, or Battery-Like? *ACS Nano* **2018**, *12* (3), 2081–2083.

- Fleischmann, S.; Mitchell, J. B.; Wang, R.; Zhan, C.; Jiang, D.; Presser, V.; Augustyn, V. Pseudocapacitance: From Fundamental Understanding to High Power Energy Storage Materials. *Chem. Rev.* **2020**, *120* (14), 6738–6782.
- Simon, P.; Gogotsi, Y.; Dunn, B. Where Do Batteries End and Supercapacitors Begin? *Science* **2014**, *343* (6176), 1210–1211.
- Yin, J.; Jin, J.; Chen, C.; Lei, Y.; Tian, Z.; Wang, Y.; Zhao, Z.; Emwas, A.-H.; Zhu, Y.; Han, Y.; Schwingenschlögl, U.; Zhang, W.; Alshareef, H. N. Preferential Pyrolysis Construction of Carbon Anodes with 8400 h Lifespan for High-Energy-Density K-ion Batteries. *Angew Chem Int Ed* **2023**.
- Ferrari, A. C.; Basko, D. M. Raman Spectroscopy as a Versatile Tool for Studying the Properties of Graphene. *Nature Nanotech* **2013**, *8* (4), 235–246.
- Breckenridge, R. G. *Thermoelectric Materials Final Report*; Union Carbide Corp.: Parma, OH, 1960.
- Woodley, R. E. The Oxidation of Boronated Graphite. *Carbon* **1968**, *6*, 617–626.
- Davidson, J. M.; Gates, L. O.; Nightingale, R. E. Radiation Damage Effects in Borated Graphite. *Nucl. Sci. Eng.* **1966**, *26*, 90–98.
- Endo, M.; Kim, C.; Karaki, T.; Nishimura, Y.; Matthews, M. J.; Brown, S. D. M.; Dresselhaus, M. S. Anode performance of a Li ion battery based on graphitized and B-doped milled mesophase pitchbased carbon fibers. *Carbon* **1999**, *37*, 561–568.
- Liu, Y.; Artyukhov, V. I.; Liu, M.; Harutyunyan, A. R.; Yakobson, B. I. Feasibility of Lithium Storage on Graphene and Its Derivatives. *J. Phys. Chem. Lett.* **2013**, *4*, 1737–1742.
- Joshi, R. P.; Ozdemir, B.; Barone, V.; Peralta, J. E. Hexagonal BC₃: A Robust Electrode Material for Li, Na, and K Ion Batteries. *J. Phys. Chem. Lett.* **2015**, *6*, 2728–2732.
- Fitzhugh, W.; Li, X. Modulation of Ionic Current Limitations by Doping Graphite Anodes. *J. Electrochem. Soc.* **2018**, *165*, A2233–A2238.
- Firlej, L.; Kuchta, B.; Wexler, C.; Pfeifer, P. Boron substituted graphene: energy landscape for hydrogen adsorption. *Adsorption* **2009**, *15*, 312.
- Zhu, Z. H.; Lu, G. Q.; Hatori, H. New Insights into the Interaction of Hydrogen Atoms with Boron-Substituted Carbon. *J. Phys. Chem. B* **2006**, *110*, 1249–1255.
- Nayyar, I.; Ginovska, B.; Karkamkar, A.; Gennett, T.; Autrey, T. Physi-Sorption of H₂ on Pure and Boron-Doped Graphene Monolayers: A Dispersion-Corrected DFT Study. *C* **2020**, *6*, 15.

- Bult, J. B.; Lee, J.; O'Neill, K.; Engtrakul, C.; Hurst, K. E.; Zhao, Y.; Simpson, L. J.; Parilla, P. A.; Gennett, T.; Blackburn, J. L. Manipulation of Hydrogen Binding Energy and Desorption Kinetics by Boron Doping of High Surface Area Carbon. *J. Phys. Chem. C* **2012**, 116, 26138–26143.
- Hagio, T.; Nakamizo, M.; Kobayashi, K. Studies on X-ray diffraction and Raman spectra of B-doped natural graphite. *Carbon* **1989**, 27, 259–263.
- Tuinstra, F.; Koenig, J. L. Raman Spectrum of Graphite. *J. Chem. Phys.* **1970**, 53, 1126–1130.
- Thomsen, C.; Reich, S. Double Resonant Raman Scattering in Graphite. *Phys. Rev. Lett.* **2000**, 85, 5214–5217.
- Maultzsch, J.; Reich, S.; Thomsen, C.; Requardt, H.; Ordejón, P. Phonon Dispersion in Graphite. *Phys. Rev. Lett.* **2004**, 92, 075501.
- Matthews, M. J.; Pimenta, M. A.; Dresselhaus, G.; Dresselhaus, M. S.; Endo, M. Origin of dispersive effects of the Raman D band in carbon materials. *Phys. Rev. B: Condens. Matter Mater. Phys.* **1999**, 59, R6585.
- Endo, M.; Hayashi, T.; Hong, S.-H.; Enoki, T.; Dresselhaus, M. S. Scanning tunneling microscope study of boron-doped highly oriented pyrolytic graphite. *J. Appl. Phys.* **2001**, 90, 5670–5674.
- Giannozzi, P.; Baroni, S.; Bonini, N.; Calandra, M.; Car, R.; Cavazzoni, C.; Ceresoli, D.; Chiarotti, G. L.; Cococcioni, M.; Dabo, I.; et al. QUANTUM ESPRESSO: a modular and open-source software project for quantum simulations of materials. *J. Phys.: Condens. Matter* **2009**, 21, 395502.
- Giannozzi, P.; Andreussi, O.; Brumme, T.; Bunau, O.; Buongiorno Nardelli, M.; Calandra, M.; Car, R.; Cavazzoni, C.; Ceresoli, D.; Cococcioni, M.; et al. Advanced capabilities for materials modelling with Quantum ESPRESSO. *J. Phys.: Condens. Matter* **2017**, 29, 465901.
- Rappe, A. M.; Rabe, K. M.; Kaxiras, E.; Joannopoulos, J. D. Optimized pseudopotentials. *Phys. Rev. B: Condens. Matter Mater. Phys.* **1990**, 41, 1227–1230.
- Perdew, J. P.; Burke, K.; Ernzerhof, M. Generalized Gradient Approximation Made Simple. *Phys. Rev. Lett.* **1996**, 77, 3865–3868.
- Zheng, F.; Zhang, P. Phonon Unfolding: A program for unfolding phonon dispersions of materials. *Comput. Phys. Commun.* **2017**, 210, 139–144.
- Brühwiler, P. A.; Maxwell, A. J.; Puglia, C.; Nilsson, A.; Andersson, S.; Mårtensson, N. π^* and σ^* Excitons in C 1s Absorption of Graphite. *Phys. Rev. Lett.* **1995**, 74, 614–617.
- Murty, H. N.; Biederman, D. L.; Heintz, E. A. Apparent catalysis of graphitization. 3. Effect of boron. *Fuel* **1977**, 56, 305–312.

- Ōya, A.; Yamashita, R.; Otani, S. Catalytic graphitization of carbons by borons. *Fuel* **1979**, *58*, 495.
- Turnbull, J. A.; Stagg, M. S.; Eeles, W. T. Annealing studies of boron-doped graphite by electron microscopy and X-ray diffraction. *Carbon* **1966**, *3*, 387–392.
- Young, D. A. The intercalation process in graphite-bromine. *Carbon* **1977**, *15*, 373–377.
- (Chung, D. D. L. Structure and phase transitions of graphite intercalated with bromine. *Phase Transitions* **1986**, *8*, 35–57.
- Lalancette, J.-M.; Roussel, R. Metals intercalated in graphite. V. A concentration cell with intercalated bromine. *Can. J. Chem.* **1976**, *54*, 3541.
- Sood, A. K.; Gupta, R.; Asher, S. A. Origin of the unusual dependence of Raman D band on excitation wavelength in graphitelike materials. *J. Appl. Phys.* **2001**, *90*, 4494–4497.
- Ferrari, A. C.; Robertson, J. Resonant Raman spectroscopy of disordered, amorphous, and diamondlike carbon. *Phys. Rev. B: Condens. Matter Mater. Phys.* **2001**, *64*, 075414.
- Pócsik, I.; Hundhausen, M.; Koós, M.; Ley, L. Origin of the D peak in the Raman spectrum of microcrystalline graphite. *J. Non-Cryst. Solids* **1998**, *227–230*, 1083–1086.
- Attacalite, C.; Wirtz, L.; Lazzeri, M.; Mauri, F.; Rubio, A. Doped Graphene as Tunable Electron–Phonon Coupling Material. *Nano Lett.* **2010**, *10*, 1172–1176.
- Langford, J. I.; Wilson, A. J. C. Scherrer after sixty years: A survey and some new results in the determination of crystallite size. *J. Appl. Crystallogr.* **1978**, *11*, 102–113.
- Greenwood, N. N., Earnshaw, A., *Chemistry of the Elements*, 2nd ed.; Butterworth-Heinemann. Oxford, 1997.
- Albert, B.; Hillebrecht, H. Boron: Elementary Challenge for Experimenters and Theoreticians. *Angew. Chem. Int. Ed.* **2009**, *48* (46), 8640–8668.
- Hirsch, A. The Era of Carbon Allotropes. *Nat. Mater.* **2010**, *9* (11), 868–871.
- Will, G.; Kossobutzki, K. H. An X-Ray Diffraction Analysis of Boron Carbide, B₁₃C₂. *J. Less Common Met.* **1976**, *47*, 43–48.
- Thévenot, F. Boron Carbide—A Comprehensive Review. *J. Eur. Ceram. Soc.* **1990**, *6* (4), 205–225.
- Wang, Q.; Chen, L.-Q.; Annett, J. F. Ab Initio Calculation of Structural Properties of C₃B and C₅B Compounds. *Phys. Rev. B* **1997**, *55* (1), 8–10.
- Sun, H.; Ribeiro, F. J.; Li, J.-L.; Roundy, D.; Cohen, M. L.; Louie, S. G. Ab Initio Pseudopotential Studies of Equilibrium Lattice Structures and Phonon Modes of Bulk BC₃. *Phys. Rev. B* **2004**, *69* (2), 024110.

- Luo, X.; Yang, J.; Liu, H.; Wu, X.; Wang, Y.; Ma, Y.; Wei, S.-H.; Gong, X.; Xiang, H. Predicting Two-Dimensional Boron–Carbon Compounds by the Global Optimization Method. *J. Am. Chem. Soc.* **2011**, *133* (40), 16285–16290.
- M. Dieb, T.; Hou, Z.; Tsuda, K. Structure Prediction of Boron-Doped Graphene by Machine Learning. *J. Chem. Phys.* **2018**, *148* (24), 241716.
- Kaner, R. B.; Kouvetakis, J.; Warble, C. E.; Sattler, M. L.; Bartlett, N. Boron-Carbon-Nitrogen Materials of Graphite-like Structure. *Mater. Res. Bull.* **1987**, *22* (3), 399–404.
- Kuzubov, A. A.; Fedorov, A. S.; Eliseeva, N. S.; Tomilin, F. N.; Avramov, P. V.; Fedorov, D. G. High-Capacity Electrode Material BC₃ for Lithium Batteries Proposed by *Ab Initio* Simulations. *Phys. Rev. B* **2012**, *85* (19), 195415.
- Belasfar, K.; Houmad, M.; Boujnah, M.; Benyoussef, A.; Kenz, A. E. First-Principles Study of BC₃ Monolayer as Anodes for Lithium-Ion and Sodium-Ion Batteries Applications. *J. Phys. Chem. Solids* **2020**, *139*, 109319.
- Zhao, L.; Li, Y.; Zhou, G.; Lei, S.; Tan, J.; Lin, L.; Wang, J. First-Principles Calculations of Stability of Graphene-like BC₃ Monolayer and Its High-Performance Potassium Storage. *Chinese Chem. Lett.* **2021**, *32* (2), 900–905.
- Toebe, M. Impact of the Structure and Reactivity of Nickel Particles on the Catalytic Growth of Carbon Nanofibers. *Catal. Today* **2002**, *76* (1), 33–42.
- De Jong, K. P.; Geus, J. W. Carbon Nanofibers: Catalytic Synthesis and Applications. *Catal. Rev.* **2000**, *42* (4), 481–510.
- Okamoto, H. B-C (Boron-Carbon). *J. Phase Equilib.* **1992**, *13* (4), 436–436.
- Scholz, A. S.; Massoth, J. G.; Bursch, M.; Mewes, J.-M.; Hetzke, T.; Wolf, B.; Bolte, M.; Lerner, H.-W.; Grimme, S.; Wagner, M. BNB-Doped Phenalenyls: Modular Synthesis, Optoelectronic Properties, and One-Electron Reduction. *J. Am. Chem. Soc.* **2020**, *142* (25), 11072–11083.
- Yu, H. S.; He, X.; Li, S. L.; Truhlar, D. G. MN15: A Kohn–Sham Global-Hybrid Exchange–Correlation Density Functional with Broad Accuracy for Multi-Reference and Single-Reference Systems and Noncovalent Interactions. *Chem. Sci.* **2016**, *7* (8), 5032–5051.
- Weigend, F.; Ahlrichs, R. Balanced Basis Sets of Split Valence, Triple Zeta Valence and Quadruple Zeta Valence Quality for H to Rn: Design and Assessment of Accuracy. *Phys. Chem. Chem. Phys.* **2005**, *7* (18), 3297–3305.
- Rowsey, R.; Taylor, E. E.; Irle, S.; Stadie, N. P.; Szilagy, R. K. Methane Adsorption on Heteroatom-Modified Maquettes of Porous Carbon Surfaces. *J. Phys. Chem. A* **2021**, *125* (28), 6042–6058.

Rowsey, R.; Taylor, E. E.; Hinson, R. W.; Compton, D.; Stadie, N. P.; Szilagy, R. K. Does Boron or Nitrogen Substitution Affect Hydrogen Physisorption on Open Carbon Surfaces? *Phys. Chem. Chem. Phys.* **2022**, *24* (46), 28121–28126.

Nakamori, Y.; Miwa, K.; Ninomiya, A.; Li, H.; Ohba, N.; Towata, S.; Züttel, A.; Orimo, S. Correlation between Thermodynamical Stabilities of Metal Borohydrides and Cation Electronegativities: First-Principles Calculations and Experiments. *Phys. Rev. B* **2006**, *74* (4), 045126.

Callini, E.; Borgschulte, A.; Ramirez-Cuesta, A. J.; Züttel, A. Diborane Release and Structure Distortion in Borohydrides. *Dalton Trans.* **2012**, *42* (3), 719–725.

Pitt, M. P.; Paskevicius, M.; Brown, D. H.; Sheppard, D. A.; Buckley, C. E. Thermal Stability of $\text{Li}_2\text{B}_{12}\text{H}_{12}$ and Its Role in the Decomposition of LiBH_4 . *J. Am. Chem. Soc.* **2013**, *135* (18), 6930–6941.

Zanetti, J. E.; Egloff, G. The Thermal Decomposition of Benzene. *J. Ind. Eng. Chem.* **1917**, *9* (4), 350–356.

Frisch, M. J.; Trucks, G. W.; Schlegel, H. B.; Scuseria, G. E.; Robb, M. A.; Cheeseman, J. R.; Scalmani, G.; Barone, V.; Petersson, G. A.; Nakatsuji, H.; Li, X.; Caricato, M.; Marenich, A. V.; Bloino, J.; Janesko, B. G.; Gomperts, R.; Mennucci, B.; Hratchian, H. P.; Ortiz, J. V.; Izmaylov, A. F.; Sonnenberg, J. L.; Williams-Young, D.; Ding, F.; Lipparini, F.; Egidi, F.; Goings, J.; Peng, B.; Petrone, A.; Henderson, T.; Ranasinghe, D.; Zakrzewski, V. G.; Gao, J.; Rega, N.; Zheng, G.; Liang, W.; Hada, M.; Ehara, M.; Toyota, K.; Fukuda, R.; Hasegawa, J.; Ishida, M.; Nakajima, T.; Honda, Y.; Kitao, O.; Nakai, H.; Vreven, T.; Throssell, K.; Montgomery, J. A., Jr.; Peralta, J. E.; Ogliaro, F.; Bearpark, M. J.; Heyd, J. J.; Brothers, E. N.; Kudin, K. N.; Staroverov, V. N.; Keith, T. A.; Kobayashi, R.; Normand, J.; Raghavachari, K.; Rendell, A. P.; Burant, J. C.; Iyengar, S. S.; Tomasi, J.; Cossi, M.; Millam, J. M.; Klene, M.; Adamo, C.; Cammi, R.; Ochterski, J. W.; Martin, R. L.; Morokuma, K.; Farkas, O.; Foresman, J. B.; Fox, D. J. *Gaussian 16*, **2016**.

Wallenberger, F. T.; Nordine, P. C. Strong, Small Diameter, Boron Fibers by LCVD. *Mater. Lett.* **1992**, *14* (4), 198–202.

Tzeng, S.-S.; Hung, K.-H.; Ko, T.-H. Growth of Carbon Nanofibers on Activated Carbon Fiber Fabrics. *Carbon* **2006**, *44* (5), 859–865.

Sha, W.; Liu, Y.; Zhou, Y.; Huang, Y.; Huang, Z. Effect of Carbon Content on Mechanical Properties of Boron Carbide Ceramics Composites Prepared by Reaction Sintering. *Materials* **2022**, *15* (17), 6028.

Jiménez, I.; Sutherland, D. G. J.; van Buuren, T.; Carlisle, J. A.; Terminello, L. J.; Himpsel, F. J. Photoemission and X-Ray-Absorption Study of Boron Carbide and Its Surface Thermal Stability. *Phys. Rev. B* **1998**, *57* (20), 13167–13174.

- Long, L. H. The Mechanisms of Thermal Decomposition of Diborane and of Interconversion of the Boranes: A Reinterpretation of the Evidence. *J. Inorg. Nucl. Chem.* **1970**, 32 (4), 1097–1115.
- carbon tetrafluoride. <https://www.chembk.com/en/chem/carbon%20tetrafluoride> (accessed 2023-07-01).
- Dibeler, V. H.; Reese, R. M.; Mohler, F. L. Ionization and Dissociation of Hexafluorobenzene by Electron Impact. *J. Chem. Phys.* **1957**, 26 (2), 304–305.
- Muroi, M.; Otani, M.; Habuka, H. Boron-Silicon Film Chemical Vapor Deposition Using Boron Trichloride, Dichlorosilane and Monomethylsilane Gases. *ECS J. Solid State Sci. Technol.* **2021**, 10 (6), 064006.
- Yousefi, M.; Donne, S. Experimental Study for Thermal Methane Cracking Reaction to Generate Very Pure Hydrogen in Small or Medium Scales by Using Regenerative Reactor. *Front. Energy Res.* **2022**, 10, 971383.
- Guéret, C.; Daroux, M.; Billaud, F. Methane Pyrolysis: Thermodynamics. *Chem. Eng. Sci.* **1997**, 52 (5), 815–827.
- Laidler, K. J.; Wojciechowski, B. W.; Steacie, E. W. R. Kinetics and Mechanisms of the Thermal Decomposition of Ethane - I. The Uninhibited Reaction. *Proc. R. Soc. Lond. A* **1961**, 260 (1300), 91–102.
- Ahling, B.; Lindskog, A. Thermal Destruction of PCB and Hexachlorobenzene. *Sci. Total Environ.* **1978**, 10 (1), 51–59.
- Straus, S.; Madorsky, S. L. Thermal Stability of Polydivinylbenzene and of Copolymers of Styrene With Divinylbenzene and With Trivinylbenzene. *J. Res. NBS A Phys. Chem.* **1961**, 65A (3), 243–248.
- Towell, G. D.; Martin, J. J. Kinetic Data from Nonisothermal Experiments: Thermal Decomposition of Ethane, Ethylene, and Acetylene. *AIChE J.* **1961**, 7 (4), 693–698.
- Dong, R.; Pfeffermann, M.; Skidin, D.; Wang, F.; Fu, Y.; Narita, A.; Tommasini, M.; Moresco, F.; Cuniberti, G.; Berger, R.; Müllen, K.; Feng, X. Persulfurated Coronene: A New Generation of “Sulflower.” *J. Am. Chem. Soc.* **2017**, 139 (6), 2168–2171.
- Sugaya, T.; Takeuchi, Y.; Watanabe, O. Preparation and Crystal Structure of Solid Boron Grown from the BBr₃-H₂ Mixture. *J. Common Met.* **1976**, 47, 49–54.
- Mattern, D. L. Periodination of Benzene with Periodate/Iodide. *J. Org. Chem.* **1983**, 48 (24), 4772–4773.
- Cullis, C. F.; Franklin, N. H.; Gaydon, A. G. The Pyrolysis of Acetylene at Temperatures from 500 to 1000 °C. *Proc. R. Soc. Lond. A* **1964**, 280 (1380), 139–152.

- Jubert Tomasso, C.; Pham, A. L.; Mattox, T. M.; Urban, J. J. Using Additives to Control the Decomposition Temperature of Sodium Borohydride. *J. Energy Power Technol.* **2020**, *2* (2), 1–20.
- Moore, R. E.; Ownby, P. D. Thermal Decomposition of Boron Triiodide on Molybdenum Field Emitter Surfaces. *Jpn. J. Appl. Phys.* **1974**, *13* (S2), 71.
- Gao, W. Crystal Growth of Alpha-Rhombohedral Boron. Thesis, Kansas State University, 2010. <https://krex.k-state.edu/handle/2097/4171> (accessed 2023-07-01).
- Owen, J. The Pyrolysis of Decaborane. *J. Chem. Soc.* **1961**, 5438–5444.
- Travers, M. W. On the New View of the Nature of the Covalent Linkage, and the Formation of Free Radicals. *Trans. Faraday Soc.* **1934**, *30* (0), 100–102.
- Mazaheri, A.; Javadi, M.; Abdi, Y. Chemical Vapor Deposition of Two-Dimensional Boron Sheets by Thermal Decomposition of Diborane. *ACS Appl. Mater. Interfaces* **2021**, *13* (7), 8844–8850.
- Gai, C.; Dong, Y.; Yang, S.; Zhang, Z.; Liang, J.; Li, J. Thermal Decomposition Kinetics of Light Polycyclic Aromatic Hydrocarbons as Surrogate Biomass Tar. *RSC Adv.* **2016**, *6* (86), 83154–83162.
- Tonnoir, H.; Huo, D.; Davoisne, C.; Celzard, A.; Fierro, V.; Saurel, D.; El Marssi, M.; Benyoussef, M.; Meunier, P.; Janot, R. Pyrolysis Temperature Dependence of Sodium Storage Mechanism in Non-Graphitizing Carbons. *Carbon* **2023**, *208*, 216–226.
- Hoke, W. E.; Weir, D. G.; Lemonias, P. J.; Hendriks, H. T. Carbon Tetrabromide Carbon Doping of Molecular Beam Epitaxial (GaAs) Films. *Appl. Phys. Lett.* **1994**, *64* (2), 202–204.
- Putnam, S., T. Thermodynamic Studies of Hydrogen Storage Materials, Montana State University, Bozeman, Montana, 2021.
- Stadie, N. P. Synthesis and Thermodynamic Studies of Physisorptive Energy Storage Materials. phd, California Institute of Technology, 2013.